Fabrication and Design of Sub-wavelength Periodic Textures for Improving Light Harvesting in Multi-junction III-V Photovoltaics

A Dissertation Presented to

the Faculty of the Department of Physics

University of Houston

In Partial Fulfillment

of the Requirements for the Degree

Doctor of Philosophy

By

Wei Wang

December 2015

Fabrication and Design of Sub-wavelength Periodic Textures for Improving Light Harvesting in Multi-junction III-V Photovoltaics

____

Wei Wang

APPROVED:

____

Prof. Alex Freundlich, Chair (Physics Department)

____

Prof. Wei-Kan Chu (Physics Department)

____

Prof. Donna Stokes (Physics Department)

____

Prof. Paul Ruchhoeft
(Electrical & Computer Engineering Department)

____

Prof. Lowell Wood (Physics Department)

____

Dean, College of Natural Sciences and Mathematics

Acknowledgments

I wish to thank all those who helped me. Without them, I could not have completed this project. I have to thank all the members in our group. Thanks to my supervisor Alex Freundlich for his wise and broad view guide; who not only served as my supervisor but also encouraged and challenged me throughout my academic program. Thanks to Akhil Mehrotra for patient explanation and detailed instruction; who urged me to speed up my progress. Thanks to Andenet Alemu for checking my beginning calculation results with his. Thanks to Michael Fitchette who helped me proofread my paper and dissertation. Thanks to Gopi Krishna V for his glowing example of independent thinking and solving problems. Thanks to Rabi Ebrahim for systematic technology for equipment. Thanks to two of our lab manager, Carlos Gramajo, Robert Keith who made so many of our lab smoothly run. Thanks to Manori Gunasekera for a shining model to set a neat lab and her sister-like regard. Thanks to Camden Kirkland for nice reviews of my papers. Thanks to Kaveh Shervin and Khim Kharel for sharing their ideas with me. Thanks to all the interns and high-school teachers who have been working with me, which gave me a chance to make sure I have clear logic on my work. Last but the most important, I thank all my committee members, who spent much effort in witnessing my growth in research, giving me valuable suggestions and reading my manuscript.

Fabrication and Design of Sub-wavelength Periodic Textures for Improving Light Harvesting in Multi-junction III-V Photovoltaics

----

An Abstract of a Dissertation

Presented to

the Faculty of the Department of Physics

University of Houston

In Partial Fulfillment

of the Requirements for the Degree

Doctor of Philosophy

By

Wei Wang

December 2015

Abstract

Optimization of non-planar antireflective coating and back- (or front-) surface texturing are widely studied to further reduce the reflection losses and increase the sunlight absorption path in solar cells.

In III-V concentrator applications sunlight is focused onto the surface of cell and consequently, light arrives with a wide angular distribution that limits the effectiveness of conventional thin-film antireflective coatings (ARCs). Furthermore, the transmission properties are generally degraded non-uniformly over the electromagnetic spectrum, which in the case of multi-junction solar cells, leads to additional sub-cell current matching-related losses. Here, and in an attempt to identify a better alternative to the conventional dual-layer ARCs, a systematic analysis is undertaken regarding the design of parameters and angular dependent antireflective properties of dielectric grating formed through the implementation of sub-wavelength arrays of 2D pyramidal and hemispherical textures. The study includes evaluation of these properties for several common dielectrics through a careful selection of dielectric material and design. These structures can significantly surpass the performance of planar dual-layer ARCs, and the total number of reflected photons over 380-2000 *nm* wavelength range can be reduced to less than 2%, by use of single-material textured dielectric. It is also shown that the implementation of these structures for a typical concentrated 3 or 4 junction solar cells with apertures ranging from 0-60 degrees reduces total losses of reflected photons for each sub-cell to less than 4%, and therefore reduces current degradation.

Back reflectors have been developed from perfect mirror to textured mirror in order to further increase light path, which can significantly improve the efficiency and allow for much-thinner devices. A Lambertian surface, which has the most random texture, can theoretically raise the light path to $4n^2$ times that of a smooth surface. It's a challenge however to fabricate ideal

Lambertian texture, especially in a fast and low-cost way. In this work, a method is developed to overcome this challenge that combines the use of laser interference lithography and selective wet etching. The approach allows for a rapid wafer-scale texture processing with subwavelength (nano-) scale control of the pattern and the pitch. The technique appears as being particularly attractive for the development of ultra-thin III-V devices, or in overcoming the weak sub-bandgap absorption in devices incorporating quantum dots or quantum wells (QWs). The design and fabrication process on the application of the technique for the development of back reflectors for MQWs solar cells are presented. Depending on the growth order (inverted or up-right growth), the two-side device-metallization incorporated with lift-off process are designed differently due to the fragile ultra-thin (~ 2 μm) active layer, and the strain from embedded QWs. Another approach is done through thinning the substrate (~ 15-20 μm), texturing the substrate as an incoherent reflector, and metallization, which won't affect active layers.

Contents

List of figures

Chapter 2

Chapter 3

Chapter 4

Chapter 5

Chapter 1 Introduction

This work focuses on light management for photovoltaic applications, including both the implementation of improved light coupling at the front surface for anti-reflective purpose, and the light trapping / recycling at the back surface by incoherent coupling. The conventional planar anti-reflective coating (ARC) has its advantage of easy fabrication and efficient coupling the light into devices, but limited by available materials to match the value of desired refractive index as we move to multi-layer ARC, especially for low index materials. To overcome this challenge, sub-wavelength textures have been proposed to gradually change the effective index from air to that of the textured material. Also the sub-wavelength textures are commonly used to minimize scattering effects and hence allow better sunlight coupling into solar cells rather than scattered back into air. The sub-wavelength anti-reflective texturing can broaden the low reflection spectrum region compared with conventional planar films, especially important for multi-junction application. It also demonstrates angular tolerant property even with large off normal incidence, which is unavoidable for high efficiency concentrated photovoltaic application. Scatterings or multi-reflection are preferred at the back surface for internal total reflection at the semiconductor-air interface so that light can be trapped inside the solar cells leading to an enhancement of the absorption path, so that it gives a chance to make devices thinner and lighter. Yet there is a challenge to produce the textured rare surface in large scale while keeping fast process. The cooperation between laser interference lithography and selective wet etching makes fabricating incoherent back reflector to increase effective light path in a fast and scalable way.

Chapter 2 introduces various approaches used in the literature to improve photovoltaic conversion efficiency. We will examine solar-cell-device enhancement and discuss design factors that affecting the conversion efficiency. Next, we will discuss in the light of intrinsic properties such as bandgap and absorption coefficient, strategies in selecting the right material for single-junction solar cells, followed by a discussion on different technology to further enhance light harvesting property, *i.e.* multi-junction multi-bandgap design to broaden the absorption spectrum range, or adding quantum well to absorb below-bandgap photons, light management at the front surface and back surface for low reflection loss and photon recycling which makes thinner device possible. Finally, we will also discuss few emerging technique like wafer bounding, substrate recycling designs for the purpose of lowering the fabrication costs.

Chapter 3 deals with the theoretical aspects of the work, in which a guidance is given of what are the desired texture for the front and back surface, and discussion of three simulation methods, the thin-film method (TFM), the rigorous coupled-wave analysis (RCWA), and the finite domain time domain (FDTD) has almost identical simulation results for sub-wavelength texture. We then aiming the potential of enhancing anti-reflective properties using a special explain on their implementation of multi-junction III-V devices for concentration application.

In chapter 4 we undertake an experimental demonstration of a fast, mask-less and scalable access to fabricated tunable-scale texture by laser interference lithography (LIL) and selective wet etching, which has been proven in literature that it can increase the effective light path in QW region up to 5 times of that from conventional devices. This technique makes texturing possible to large-scale industry application.

Chapter 5 explains how to implement light-management technology into solar-cell devices, with detailed post-process procedure according to specific grown structures.

Chapter 2 Approaches to Improve Photovoltaic Device Conversion Efficiency

Photovoltaic (PV) is a method to convert sunlight power directly into electricity, usually using semiconducting materials. With the main concern of reducing the cost of power; high conversion efficiency is a main strategy adopted to achieve this goal. Conversion efficiency is a critical attribute to define the quality of PV devices. The PV conversion efficiency can be improved by the device design, tailoring material properties and increasing their quality, replacement of direct solar radiation with concentrated light, using various technique to trap and harvest the sunlight into solar cells

2.1 Photovoltaic efficiency calculation

There are two commonly used methods for solar-cell efficiency calculation—the detail-balance approach and the drift-diffusion approach. The detail-balance model is a very optimistic model which assumes 100% absorption, 100% carrier-extraction efficiency, and 0% recombination; therefore, leading to an ultimate idealistic theoretical efficiency limit. The drift diffusion model, on the other hand, takes more practical material properties into account hence giving realistic efficiencies and perfectly matched device performance.

2.1.1 Detail balance efficiency limit

The detailed balance energy limit to model a single-junction solar cell was introduced by Shockley and Queisser in 1961 [1]. It establishes an ideal efficiency limit as a function of the bandgap and cell operating temperature. This efficiency limit is often referred to as the Shockley-Queisser limit, which is calculated by examining the amount of electrical energy that is extracted from incoming sunlight. It gives a prediction of an ideal single-junction solar cell for a given bandgap, which has several assumptions:

- Any photon with energy below the bandgap will not produce any electron-hole pair;
- Any photon with energy above bandgap will produce one electron-hole pair; (Assume internal quantum efficiency equals 1. In reality, due to absorption and recombination issues, this is not the case.)
- Photons with energy E above the bandgap E_g will convert energy equal to the bandgap E_g, and thermalize the remaining energy E-E_g.
- The number of photons emitted (both for solar cell and light source) is predicted by the Fermi-Dirac distribution

From sunlight spectrum properties, any material above absolute zero temperature will emit radiation through black-body radiation. Therefore, the solar cell receives N_r number of photons above bandgap (integrate photons from E_g to infinity) from the sun and emits photons N_e over the entire energy spectrum (integrate photons from zero to infinity) due to black-body radiation. Assuming the temperature of the sun is T_s, the temperature of solar cell is T_c, and the bandgap for solar cell is E_g, the net number of photons that solar cell can absorb is the difference between those received and those emitted $N_r(T_s, E_g,+\infty)$-$N_e(T_c,0,+\infty)$ photons. Notations are labeled in Fig. 2.1 (Detailed balance energy limit generally ignores reflection loss at the air-solar cell interface).

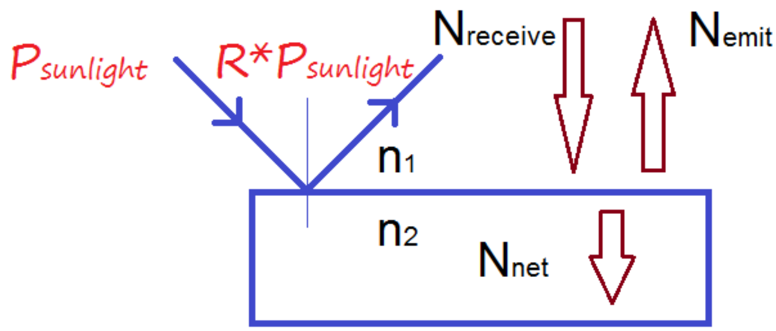

Fig. 2.1 Physical parameters relevant to single-junction conversion efficiency calculation

Since a solar cell is generally connected to an external load, which has potential difference on the two sides, the radiation term from the solar cell should be modified [2,3] by its chemical potential from energy $\hbar\omega$. The current generated by photons can be expressed by equation (2.1.4). The generated current *I(V)* is given by the electronic charge *q* multiplied by the net number of absorbed photons per second (*i.e.*, $N_{net} = N_{receive}$-N_{emit}). The number of photons received must be multiplied by an etendue coefficient, because the sun's surface and earth's surface are concentric spheres with different radii. The efficiency of the solar cell is defined as the power produced over the ratio of the power received from sun; which is expressed in equation (2.1.5). Set (a) in equation (2.1.3) refers to black body light source, while (b) is applicable for any spectrum source, like AM 0, AM 1.5G, *etc*. (Since available spectrum database are commonly provided as wavelength versus power intensity, the set (b) equations generally used)

The number of photons received from a black-body radiation spectrum

$$N_{receive} = \frac{\pi \cdot C \cdot \sin^2\theta \cdot n_1^{\,2}}{4\pi^3\hbar^3 c_0^{\,2}} \int_{E_g}^{\infty} \frac{(\hbar\omega)^2}{e^{\frac{\hbar\omega}{kT_s}} - 1} d(\hbar\omega) \qquad (2.1.1a)$$

The number of photons received by any spectrum with known power-wavelength relation

$$N_{receive} = C \cdot n_1^{\ 2} \int_{E_g}^{\infty} \frac{Power(\lambda)}{hc_0 / \lambda} d\lambda \tag{2.1.1b}$$

The number of photons emitted from solar cell devices

$$N_{emit}(V) = \frac{\pi \cdot n_2^{\ 2}}{4\pi^3 \hbar^3 c_0^{\ 2}} \int_{E_g}^{\infty} \frac{(\hbar\omega)^2}{e^{\frac{(\hbar\omega - qV)}{kT_c}} - 1} d(\hbar\omega) \tag{2.1.2}$$

The power of incoming sunlight as a black-body radiator

$$P_{sunlight} = \frac{\pi \cdot C \cdot \sin^2\theta \cdot n_1^{\ 2}}{4\pi^3 \hbar^3 c_0^{\ 2}} \int_0^{\infty} \frac{(\hbar\omega)^3}{e^{\frac{\hbar\omega}{kT_s}} - 1} d(\hbar\omega) \tag{2.1.3a}$$

The power of incoming sunlight as any spectrum with known power-wavelength relation

$$P_{sunlight} = C \cdot n_1^{\ 2} \int_0^{\infty} \frac{Power(\lambda)}{hc_0 / \lambda} d\lambda \tag{2.1.3b}$$

The current generated by devices, proportional to the net number of photons absorbed

$$I(V) = q(N_{receive} - N_{emit}) \tag{2.1.4}$$

The conversion efficiency of a device

$$\eta = \frac{I \cdot V}{P_{sunlight}} \tag{2.1.5}$$

where, C is the sun concentration, varying from 0 to 46500 [1] (Without any concentrators, $C = 1$);

θ is half angle of radiation (the angle of the view of the sun) ;

k is the Boltzmann constant;

$\hbar$ is the reduced Planck constant, or called the Dirac constant after Paul Dirac;

T_s is the temperature of sun;

---

[1] As the definition of etendue, if there was a concentrator with concentration factor C in front of solar cell, the maximum concentrating effect is the same as putting solar cell, which means etendue equals to π, so the limit of C is given by $\pi/(6.75 \times 10^{-5})=46500$.

T_c is the temperature of solar cell;

ω is circular frequency of incident photon;

c_0 is the velocity of photons in vacuum;

q is electron charge;

n_1, n_2 are the refractive index for the air and solar cell respectively.

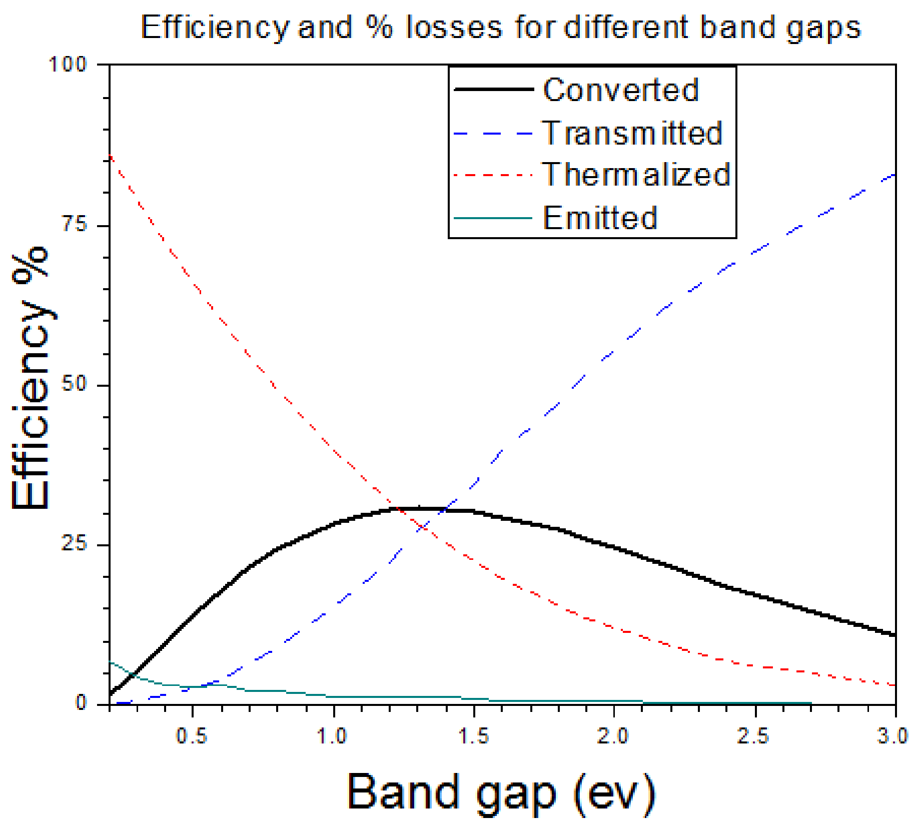

Fig. 2.2 Converted, transmitted, thermalized, and emitted photon efficiency as a function of bandgap

The incoming photons with energy below the bandgap will be transmitted through the solar cell, as shown by blue curve labeled "transmitted" in Fig. 2.2. The incoming photons with energy above the bandgap will be transformed into e-h pairs and the extra energy (E-E_g) will be lost in form of heat, as shown by red curve labeled "thermalized". The solar cell operating at a certain temperature will emit photons approximately as a black body, as shown by green curve labeled “emitted”. The amount of converted photons, shown by black curve labeled “converted”, is given by the total number of incident photons minus the sum of: emitted, transmitted, and thermalized photons. Fig. 2.2 shows the efficiencies of these different processes as a function of bandgap.

In the case of a solar cell operating at ambient room temperature, 300 *K*, the emitted energy is due to black-body radiation. This energy cannot be captured by the cell, and represents a loss of about 7% of the total available incoming energy. The efficiency is given by the ratio of current *I* generated multiplied by the external potential *V* over the incoming power *P*. The proper solar cell device design should have the biggest *IV* value.

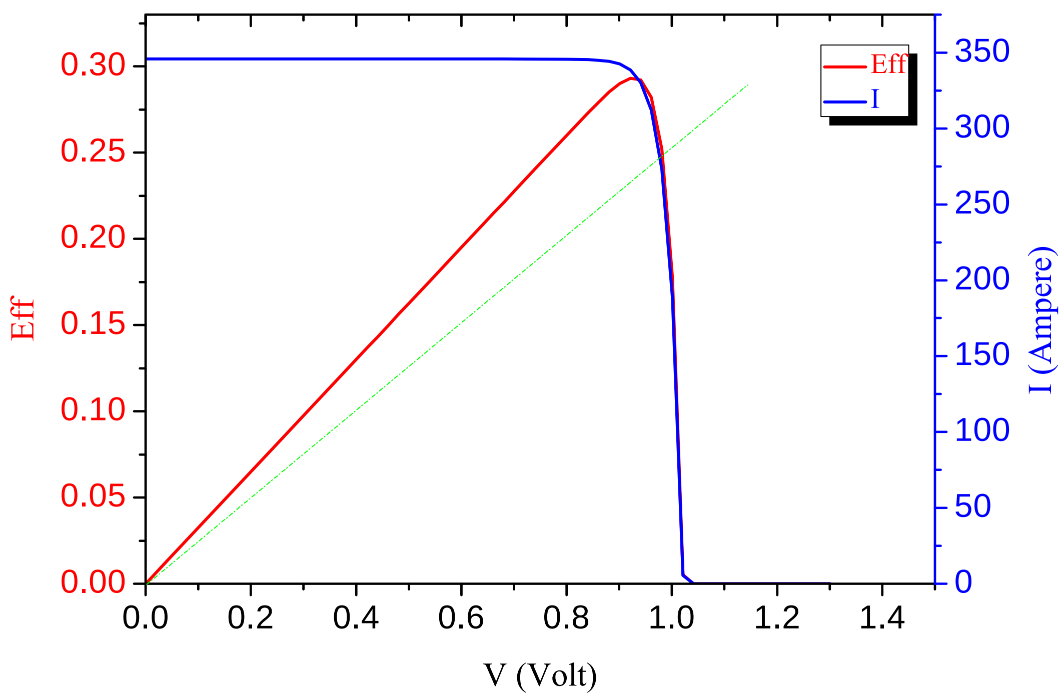

Fig. 2.3 I-V characteristic of single-junction solar cell with bandgap $Eg = 1.35\ eV$

Fig. 2.3 illustrates the external potential versus generating current relation for a fixed bandgap of 1.35 *eV*. It demonstrates that the maximum efficiency would be reached only at a specific point, corresponding to single set of current and external potential values (*Vmax,Imax*). So the highest-efficiency solar cell requires the external load to have a resistance equal to $R = Vmax/Imax$.

For terrestrial applications, the efficiency limit calculations use a standardized AM 1.5 G spectrums with realistic refractive indices rather than ideal black body radiation with refractive index of 1. Fig. 2.4 depicts several such efficiency calculations with a refractive index of 3.3 (*i.e.* GaAs) illustrating that the maximum attainable efficiency increases with concentration. This indicates that concentration is a good approach to increase efficiency, and the optimal value of the bandgap decreases as concentration is increased.

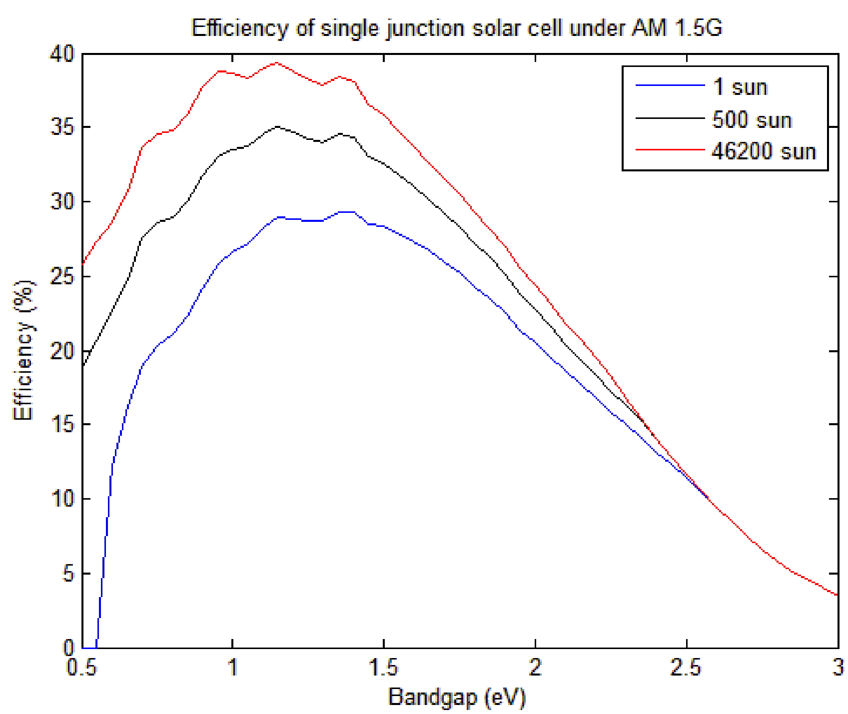

Fig. 2.4 Ideal single-junction efficiency versus bandgap under AM 1.5G for different sun concentrations

2.1.2 Drift-diffusion model

The drift-diffusion model takes more details into account such as: recombination (which includes minority carrier diffusion length, diffusion coefficient or minority carrier life time, surface recombination, and Shockley-Read-Hall (SRH) recombination [2] in depleted or i-region), doping for both acceptor and donor, sun spectrum (AM 1.5 G or AM 0 or ideal black body radiation), shadowing loss (caused by electrode coverage), reflection loss and absorption. The minority carrier diffusion length depends on doping; namely, increasing doping causes a reduction of the diffusion length, consequently e-h pairs will recombine in a shorter distance for highly doped p-n junctions. However, for low doping, the built in potential would be small which would decrease the operating voltage of the solar cell.

Like the detailed balance model, this model also takes into account the transmission losses below the bandgap. The photons whose energy E are less than bandgap E_g will just pass through semiconductor (so the extinction coefficient k and absorption coefficient follow $\alpha = \frac{4\pi k}{\lambda_0}$, and absorption is zero when $E<E_g$, where λ_0 is the wavelength in vacuum). Photons having energy E larger or equal to the bandgap energy E_g will contribute to the generation of e-h pairs. The extra energy E-E_g will be lost in the form of heat by lattice vibration (phonons). Since semiconductors' absorption represents how long

---

[2] SRH recombination occurs through defects. Thus, it does not occur in pure, defect free materials. This process contains two steps: 1) an electron (or hole) gets trapped in a forbidden band energy state, which results from crystal defects, and 2) if a hole (or electron) moves to the same energy state before the previous electron (or hole) is thermally re-emitted, the electron and hole would recombine.

the photons can travel before being generated into e-h pairs, a thicker semiconductor can guarantee that most of the photons are absorbed; however, semiconductor minority carriers have a finite diffusion length and life time, thus it is necessary to have a p-n junction of thickness generally smaller than diffusion length, so that maximum number of charge can be collected before recombination.

The surfaces of semiconductors contain interface traps, which act as recombination centers, reducing the number of e-h pairs extracted out of the device. This surface recombination can be reduced by using a passivation layer, which will be discussed in the later part of this chapter.

By solving drift-diffusion equations for p-n junction, equations (2.1.6) can be used to predict I-V characteristics of solar cells [4,5].

$$J = \left(J_{0p} + J_{0n}\right)\left(e^{\frac{qv}{kT}} - 1\right) - J_{1p} - J_{1n} - J_{dep} + J_r \tag{2.1.6}$$

where, J_{0p} is recombination in p type region due to applied voltage;

J_{0n} is recombination in n type region due to applied voltage;

J_{1p} is generation of e-h pairs in p type region;

J_{1n} is generation of e-h pairs in n type region;

J_{dep} is the current generated by photons in depleted region;

J_r is the Shockley-Read-Hall recombination in depleted region present due to defect trap at mid bandgap.

The calculation formulae of all the current terms (J_{0p}, J_{0n}, J_{1p}, J_{1n}, J_{dep}, J_r) in each region are explained below.

$$J_{0p} = -\left(\frac{qD_n}{L_n}\right)n_0\left[\frac{\left(\frac{S_nL_n}{D_n}\right)\cosh\left(\frac{x_s}{L_n}\right)+\sinh\left(\frac{x_s}{L_n}\right)}{\left(\frac{S_nL_n}{D_n}\right)\sinh\left(\frac{x_s}{L_n}\right)+\cosh\left(\frac{x_s}{L_n}\right)}\right] \tag{2.1.7}$$

$$J_{0n} = -\left(\frac{qD_p}{L_p}\right)p_0\left[\frac{\left(\frac{S_pL_p}{D_p}\right)\cosh\left(\frac{x_1}{L_p}\right)+\sinh\left(\frac{x_1}{L_p}\right)}{\left(\frac{S_pL_p}{D_p}\right)\sinh\left(\frac{x_1}{L_p}\right)+\cosh\left(\frac{x_1}{L_p}\right)}\right] \tag{2.1.8}$$

$$J_{1p} = -\left(\frac{q\phi e^{-\alpha(x_1+x_2)}}{1-\alpha^{-2}L_n^{-2}}\right)\left\{1-\alpha^{-1}L_n^{-1}\frac{\left(\frac{S_nL_n}{D_n}\right)\left[\cosh\left(\frac{x_s}{L_n}\right)-e^{-\alpha x_s}\right]+\sinh\left(\frac{x_s}{L_n}\right)+\alpha L_n e^{-\alpha x_s}}{\left(\frac{S_nL_n}{D_n}\right)\sinh\left(\frac{x_s}{L_n}\right)+\cosh\left(\frac{x_s}{L_n}\right)}\right\} \tag{2.1.9}$$

$$J_{1n} = -\left(\frac{q\phi}{1-\alpha^{-2}L_n^{-2}}\right)\left\{-e^{-\alpha x_1}+\frac{-e^{-\alpha x_1}\sinh\left(\frac{x_1}{L_p}\right)+\alpha D_p+S_p-e^{-\alpha x_1}\cosh\left(\frac{x_1}{L_p}\right)S_p}{\alpha\cosh\left(\frac{x_1}{L_p}\right)D_p+\alpha\sinh\left(\frac{x_1}{L_p}\right)L_pS_p}\right\} \tag{2.1.10}$$

$$J_{dep} = -q\phi e^{-\alpha x_1}\left(1-e^{-\alpha x_2}\right) \tag{2.1.11}$$

$$J_r = -\frac{qn_ix_2\pi}{2\sqrt{t_nt_p}}\left[\frac{2\sinh\left(\frac{qV}{2kT}\right)}{\frac{q\left(V_{bi}-L_p\right)}{kT}}\right] \tag{2.1.12}$$

where x_3, D_n, S_n, L_n are thickness, diffusion coefficient, surface recombination velocity, and minority carrier diffusion length in n type materials respectively. Similarly x_1, D_p, S_p, and L_p are thickness, diffusion coefficient, surface recombination velocity, and minority carrier diffusion length in p type materials respectively. (The minority carrier diffusion length is indirectly related to doping concentration. Highly doped materials result in shorter diffusion length.) The surface recombination velocity is reduced through the use of a passivation layer. α is absorption coefficient of the material and it depends on incident photon energy. ϕ is the solar flux which is arriving on the cell, x_2 is the depletion width, V_{bi} is the built in voltage, and V is the applied external voltage, t_p and t_n are recombination lifetimes for Shockley-Read-Hall effect in depletion region for holes and electrons respectively. These equations are valid for the p on n device configuration. For an n on p device, the same equations can be applied by switching the p and n terms. We can see that the drift diffusion model is quite a realistic model, which can optimize the thickness of each domain and can make efficiency predictions which are close to experimental results [6]. The defects, doping concentration, and external potentials are all directly or indirectly expressed in the data of diffusion length and life time.

2.2 Material optimization

Fig. 2.4 demonstrates that the bandgap of a material plays a significant role in the efficiency behavior among single junction devices. It's not only important in a single junction structure, but also critical in multi-junction devices as well. More on this, in the sub-chapter 2.3.

It can be seen that the detailed balance limit is for idealized solar cells which absorb all the energy above the bandgap and have a 1-to-1 conversion of photons to e-h pairs with no energy loss inside the solar cell itself. A practical device would have finite absorption, small minority carrier transport ability, and non-negligible surface recombination, surface reflection, shadowing losses, and resistance losses (from electrodes). Finite absorption and carrier transport problems are usually solved by carefully designing the thickness and doping concentrations in the device; surface recombination is reduced by surface passivation techniques (*i.e.*, inclusion of a highly doped thin window layer of a wider bandgap semiconductor); Front grid shadowing loss is reduced by proper design of front surface contact grid or/and use of transparent conductive electrodes ; resistive losses are reduced by using highly conductive electrode material (Au, Au-Ge); and reflection is reduced by incorporation of antireflection coatings or other light trapping schemes (texturing, plasmonics, *etc*.). Many of these loss-mitigation approaches have tradeoffs since often optimizing one parameter detrimentally affects another one. Issues pertaining to optimization of reflective losses as well as some more common approaches used in the literature will be discussed in detail in subsequent chapters. These losses originate between the detail balanced efficiency projections and practical realizations.

2.2.1 Bandgap

Fig. 2.5 shows the best theoretical efficiency projections and some confirmed best experimental efficiencies for single-junction solar cells.

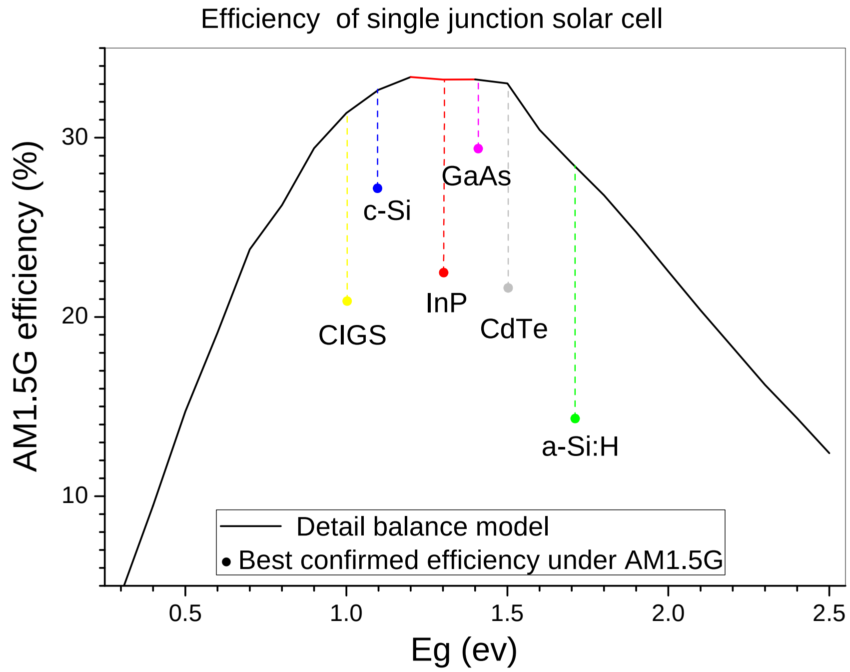

Fig. 2.5 Comparison of confirmed realistic solar cells efficiency with theoretical efficiency. Experimental data extracted from solar cell efficiency tables (version 45) [7]

Shockley and Queisser's work considered idealized devices; there are a number of other factors that further reduce the theoretical efficiency. These factors include: a finite probability for photons to generate e-h pairs, the fact that existing e-h pairs can recombine, finite absorption coefficients, and device thickness. The detail-balance model is an idealized model that doesn't take into account the physical properties of the semiconductor. Shockley and Queisser's efficiency is far higher than that of any state-of-the-art solar cells experimentally produced. The huge disparity between predicted and experimental efficiencies originates from ignoring finite absorption coefficient, finite diffusion length, and reflected photon loss in the front surface of solar cells, and demands a better model to explain the efficiencies more accurately.

Semiconductors with direct bandgap, such as GaAs, can directly absorb photons in one step (*i.e.*, without an accompanying photon). On the other hand, material with an indirect bandgap, such as Si, require a phonon to assist the absorption process; therefore its absorption coefficient suffers which, thus, requires a thicker absorber layer to complete this process.

2.2.2Absorption coefficient

The absorption coefficient describes by how easy or hard it is for photons to be converted into e-h pairs. Fig. 2.6 shows a few common solar cell material absorption coefficients. Indirect bandgap materials, like Si, have smaller absorption coefficients compared to direct bandgap materials, like GaAs. The intensity of light after passing through a certain material, whose absorption coefficient is α and thickness is l, is given by $exp(-\alpha*l)$. This indicates that a large absorption coefficient and/or long light path would generate more e-h pairs. However, the generated e-h pairs would recombine due to a finite minority carrier diffusion length (which is the average length a carrier would move between its generation and recombination). Hence, an optimized thickness is required to obtain maximum current; optimized via the tradeoff between diffusion and absorption.

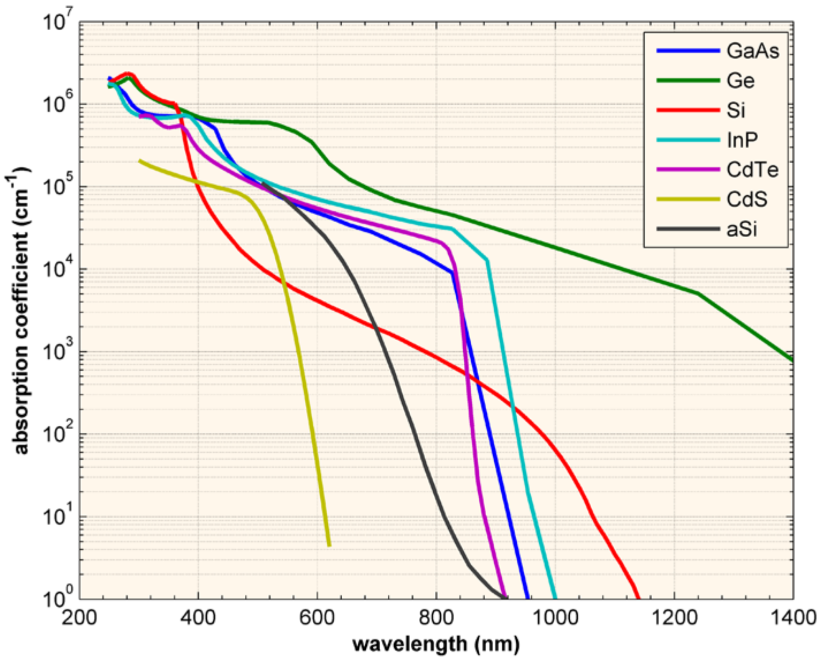

Fig. 2.6 Absorption coefficient of commonly used semiconductor materials

For a direct bandgap material, the absorption coefficient follows equation [8] (2.2.1).

$$\alpha \approx A^* \sqrt{h\nu - E_g} \text{, with } A^* = \frac{q^2 x_{vc}^{\ 2} (2m_r)^{3/2}}{\lambda_0 \varepsilon_0 \hbar^3 n} \tag{2.2.1}$$

where, v is the incident light's frequency

h is Planck's constant

$\hbar$ is reduced Planck constant

E_g is the bandgap energy

λ_0 is the wavelength in vacuum

m_r is the reduced mass $m_r = \dfrac{m_h^* m_e^*}{m_h^* + m_e^*}$, where m_e^* and m_h^* are the effective mass of electron and hole respectively.

q is the elementary charge

n is the (real) index of refraction

ε_0 is the vacuum permittivity

x_{vc} is a matrix element, in electric field cross polarization matrix, with units of length and typical values of the same order of magnitude as the lattice constant

For the indirect bandgap, the absorption coefficient can be approximated by [9]

$$\alpha \propto \frac{\left(h\nu - E_g + E_p\right)^2}{\exp\left(\frac{E_p}{kT}\right)-1} - \frac{\left(h\nu - E_g - E_p\right)^2}{\exp\left(-\frac{E_p}{kT}\right)-1} \tag{2.2.2}$$

where, E_p is the energy of the phonon that assists in the transition.

These two equations are valid only for photon energy being larger (but not by too much) than the bandgap (more specifically, assuming that the bands are approximately parabolic), and ignoring all other sources of absorption other than the band-to-band absorption in question as well as the electrical attraction between the newly created electron and hole. They are also invalid in the case that the direct transition is forbidden, or in the case that many of the states in the valence band are empty or the states in the conduction band are full.

2.3 Application of multi-junction

In an attempt to achieve higher efficiencies, two main approaches can be considered to increase photon absorption. One way is by spectrum splitting the source with beam splitters and connecting the cells in parallel while physically placing each cell in such a way that it will work in a narrow spectrum region, instead of the full spectrum, (which would result in higher thermalized losses. The other way is improving solar cell mechanism by piling up a few sub-cells vertically in one of two approaches: stack and monolithically integrated. The stack design has a shadowing/alignment challenge. For example, the front and back side of top cell's grid, and the front side of the second cell's grid need to exactly match in order to avoid shadowing losses. A more commonly used approach nowadays is monolithic integration as shown in Fig. 2.7, in which case there is no need to add a back contact on the top cell or front contact on the bottom cell. Series connected absorbers are widely used in order to increase the device voltage; while confronting current matching challenge. In a two-junction solar cell or tandem solar cell, transparency loss is reduced by adding another solar cell whose bandgap is below the first solar cell's bandgap. The efficiency of the device may be optimized by adjusting the sub-cell bandgaps to get the maximum efficiency. Multi-junction solar cells have multiple sub-cells which allow for the device to absorb a wider spectrum of light radiation. Using multiple sub-cells the transparency loss is further reduced.

From the efficiency calculation in previous sub-chapter 2.3.1, a solar cell's efficiency is determined by choosing the bandgap and applying a certain external potential. Hence, the efficiency for multi-junction solar cells is determined by the bandgap of each sub-cell and the externally applied potential applied to them individually.

Multi-junction solar cells divide a spectrum into several regions, and each sub-cell absorbs energies in their working region. For a two-junction solar cell, whose bandgaps for top and bottom sub-cells are E_{g1} and E_{g2} respectively, the current of the total device is determined by the smaller of the currents generates by the two sub-cells; and the voltage is the sum of two sub-cells. (In series, currents in both sub-cells are equal, where the larger current will be reduced by heat loss.) From the equation (2.1.1)-(2.1.5), we can find the current in each sub-cell, and the efficiency of whole device is determined by equation (2.3.1)-(2.3.5). i in equation (2.3.4) refers to the index of sub-cells. (Here, equations are using light source with a black body spectrum, which can be replaced by any realistic sources using equations in chapter 2.1.1 set (b).)

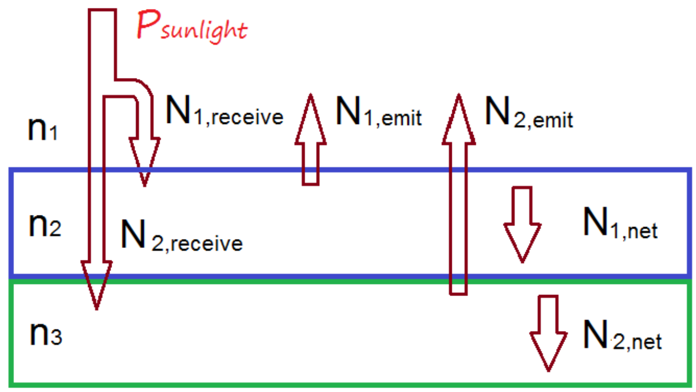

Fig. 2.7 Schematic of tandem solar cell showing different parameters used

The number of photons received in the top-cell from a black-body radiation spectrum

$$N_{1,receive} = \frac{\pi \cdot C \cdot \sin^2 \theta \cdot n_1^{\ 2}}{4\pi^3 \hbar^3 c_0^{\ 2}} \int_{E_{g1}}^{\infty} \frac{(\hbar\omega)^2}{e^{\frac{\hbar\omega}{kT_s}} - 1} d(\hbar\omega)$$

The number of photons received in the bottom-cell from a black-body radiation spectrum

$$N_{2,receive} = \frac{\pi \cdot C \cdot \sin^2 \theta \cdot n_1^{\ 2}}{4\pi^3 \hbar^3 c_0^{\ 2}} \int_{E_{g2}}^{E_{g1}} \frac{(\hbar\omega)^2}{e^{\frac{\hbar\omega}{kT_s}} - 1} d(\hbar\omega) \tag{2.3.1}$$

The number of photons emitted from the top-cell as a black-body radiator

$$N_{1,emit}(V_1) = \frac{\pi \cdot n_2^{\ 2}}{4\pi^3 \hbar^3 c_0^{\ 2}} \int_{E_{g1}}^{\infty} \frac{(\hbar\omega)^2}{e^{\frac{(\hbar\omega - qV_1)}{kT_c}} - 1} d(\hbar\omega)$$

The number of photons emitted from the bottom-cell as a black-body radiator

$$N_{2,emit}\left(V_2\right) = \frac{\pi \cdot {n_2}^2}{4\pi^3\hbar^3{c_0}^2}\int_{E_{g2}}^{\infty}\frac{\left(\hbar\omega\right)^2}{e^{\frac{\left(\hbar\omega - qV_2\right)}{kT_c}} - 1}d\left(\hbar\omega\right) \tag{2.3.2}$$

The power of incoming sunlight assuming the sun is a black-body radiator

$$P_{sunlight} = \frac{\pi \cdot C \cdot \sin^2\theta \cdot {n_1}^2}{4\pi^3\hbar^3{c_0}^2}\int_{0}^{\infty}\frac{\left(\hbar\omega\right)^3}{e^{\frac{\hbar\omega}{kT_s}} - 1}d\left(\hbar\omega\right) \tag{2.3.3}$$

The current generated in each sub-cell

$$I_i\left(V\right) = q\left(N_{i,receive} - N_{i,emit}\right) \tag{2.3.4}$$

The conversion efficiency of a tandem device

$$\eta = \frac{\min\left(I_1, I_2\right)\cdot\left(V_1 + V_2\right)}{P_{sunlight}} \tag{2.3.5}$$

2.4 Application of concentrated sunlight

Concentrated photovoltaics can be defined into two categories: low concentration photovoltaics (LCPV) and high concentration photovoltaics (HCPV), whose concentration value is 2~50 and above 300 respectively. It should be noted that the numbers given above represent an average value and, in reality, the concentration actually reach 2000 in the center of the device and 200 on the edge for example (*i.e.* there is an un-uniform concentrating effect. Therefore, cooling system are required in HCPV due to significant heat generation. In the CPV market, the three largest power plants in the world were built by Suncore in Golmun China with 50MW output, AMONIX in Colorado USA with 30MW output, and Soitec Solar in South Africa with 22MW output.

The wide application of concentrator PV stems from the fact that it can significantly increase solar cell efficiency. Mainly this is because the current increases almost linearly with the concentrator number, which would leave the efficiency unaffected if voltage remained unaltered. However, as the concentrator number increases, the voltage value also increases, thus contributing to a higher efficiency. This is due to a larger separation of the quasi-fermi levels (Voc), while under concentration, because more e-h pairs are generated, resulting in quasi-fermi level for electron closer to conduction band and the quasi-fermi level for holes moves closer to valence band. Ideally, the efficiency would continuously increase as the concentration factor increases, but due to non-negligible contact resistance which lead to dramatic heat loss as a function of the current squared, this is not the case.

Fig. 2.8 shows that for tandem, in case $E_{g1}<E_{g2}$, the efficiency (current) of the device is zero, because the bottom sub-cell cannot absorb any photons of sufficient energy, which leads to zero current. Also, the external potential which is the chemical potential (the difference between two quasi Fermi level of electrons' and holes) cannot be larger than the corresponding bandgaps of the sub-cells.

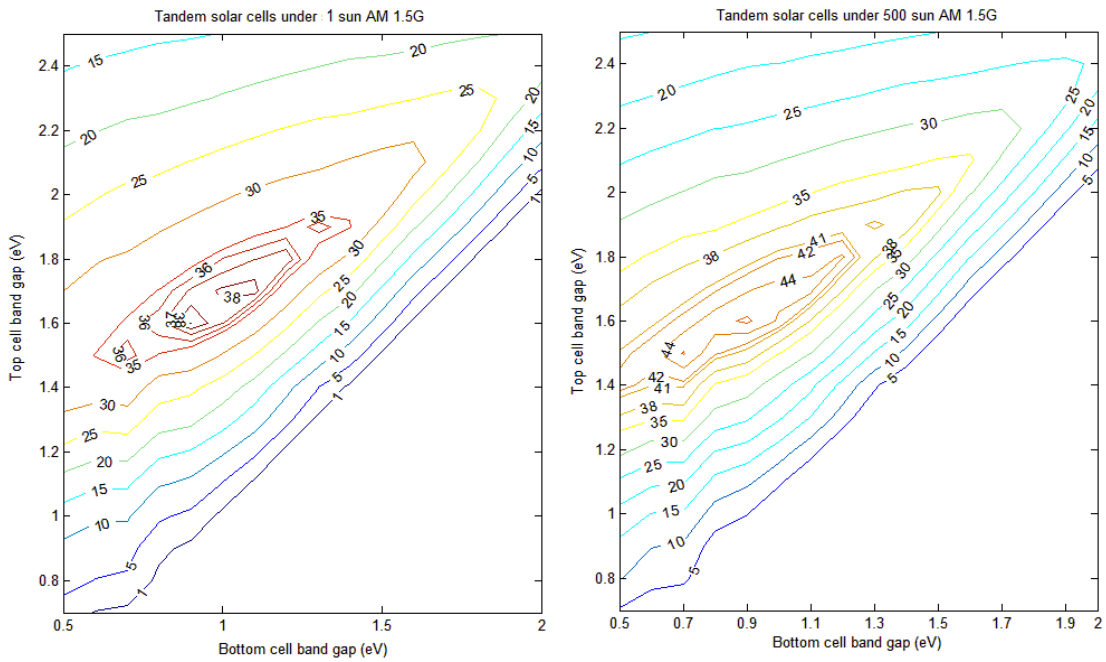

Fig. 2.8 Bandgap optimization and efficiency calculation of tandem under AM 1.5 G spectrums with 1 sun and 500 sun concentration

In 3-junction or multi-junction cells, whose bandgaps are $Eg_1>Eg_2>Eg_3$ from top to bottom, the top cell would utilize the photons with energy above Eg_1, the middle cell would utilize the photons with energy between Eg_1 and Eg_2, and the bottom cell would utilize the photons with energy between Eg_2 and Eg_3. Since sub-cells are connected in series, only the lowest current generating sub-cell would be the limiting total current (while the extra current in the other cells would be lost in the form of heat), and the voltages of all the sub-cells will be added to give the total voltage of the cell. Optimization for each bandgap of different solar cell models, the efficiency limit, and devices' final current are presented in Table 2.1.

Table 2.1 Optimized bandgap and efficiency limit for single/double/triple junction devices under various concentration factor regimes

Concentration		Single-junction	Double-junctions	Triple-junction	Triple junctions Ge bottom cell
1 sun	Bandgap(*eV*)	1.35	1.6, 0.9	2.0,1.4,0.9	1.9, 1.2
	Efficiency (%)	29.3	39.0	44.75	39.7
	Current (mA/cm^2)	32.9	25.2	171.9	19.7
500 sun	Bandgap(*eV*)	1.15	1.6, 0.9	2.0,1.4,0.9	1.9, 1.2
	Efficiency (%)	35.1	46.4	52.1	48.1
	Current (mA/cm^2)	20761	12649	8649	9828
46200 sun	Bandgap(*eV*)	1.15	1.5, 0.7	2.0,1.4,0.9	1.9, 1.2
	Efficiency (%)	39.4	51.8	57.5	54.2
	Current (mA/cm^2)	$1.938*10^6$	$1.340*10^6$	$7.974*10^5$	$9.066*10^5$

Hence the maximum efficiency for single-junction devices under one sun is 29.3% (1.35 *eV*); the maximum efficiency for double junctions devices, under one sun, is 39.02% (1.6 *eV*, 0.9 *eV*); the maximum efficiency for triple junctions devices with Ge (0.67 *eV*) fixed for bottom sub-cell, under one sun, is 39.68% (1.9 *eV*, 1.2 *eV*, 0.67 *eV*). Consequently, the greater the number of junctions there are, the higher ideal maximum efficiency can be achieved. Under 46200 sun, the maximum concentration, the maximum efficiency for single-junction devices is 49.37% (1.15 *eV*); the maximum efficiency for double junctions devices is 51.81% (1.5 *eV*, 0.7 *eV*); the maximum efficiency for triple junctions devices with Ge (0.67 *eV*) bottom cell is 54.23% (1.9 *eV*, 1.2 *eV*, 0.67 *eV*). Consequently, the larger the sun concentration, the higher the maximum efficiency achieved. Hence, concentration is an effective approach to enhance a solar cell's efficiency; however, concentration comes with a wide range of incident angle coupling in the device as a challenge. Fig. 2.9 gives an example of a lattice matched (LM) multi-junction with a traditional duo-layer antireflection coating working under concentration.

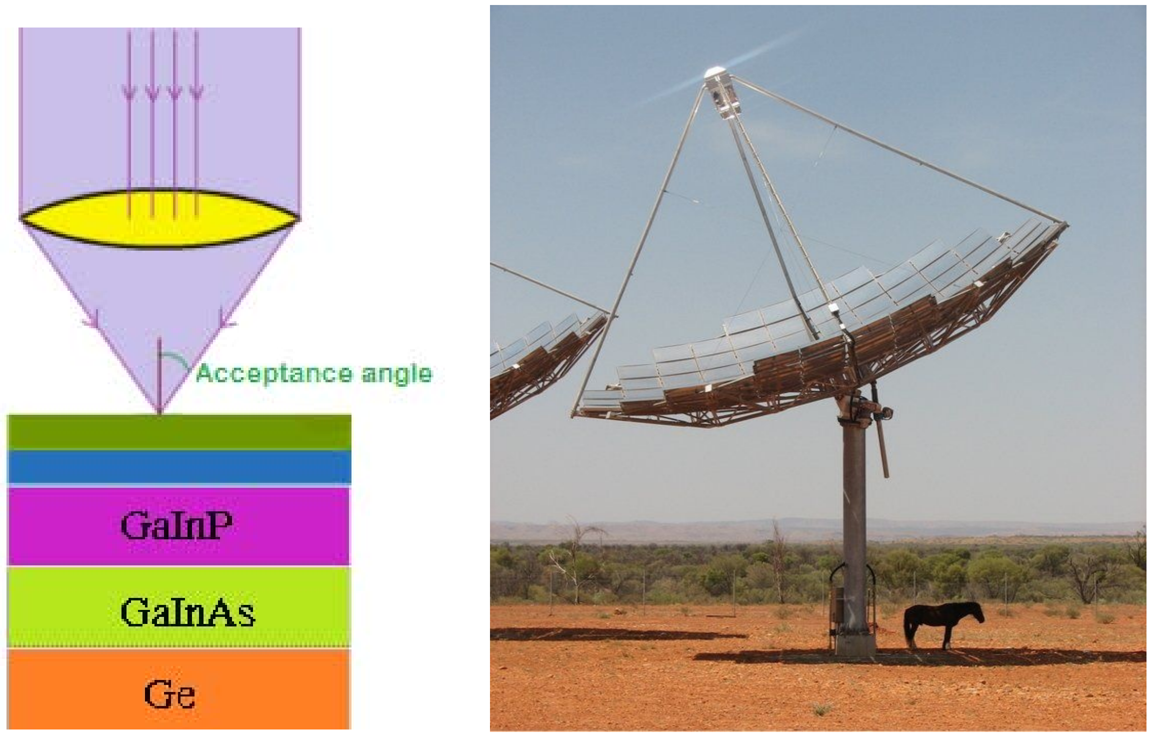

Fig. 2.9 An example of LM multi-junction device operated under concentrator and an example of concentrated photovoltaic (CPV) system

2.5 New concept – Quantum well

A quantum well is a nano-structure imbedded in the i-region that can broaden the absorption spectrum of a device without adding an extra junction which may cause lattice mismatch and/or tunnel junction problems that would degrade overall device performance. Hence, it's a relatively new concept to boost efficiency. Here, dilute N (in terms of GaInAsN) is to be taken as an example since it's perfectly lattice matched with GaAs, the bandgap can be tuned by adjusting the N concentration to serve as a bottom sub-cell, and it's an ideal material for quantum engineering considering that both the electron and hole quantum confinement energy level can be aligned to encourage thermal assistant resonant tunneling.

According to the confinement energy schemes of electrons and holes, two different semiconductors (*i.e*, for a material A embedded in B, where $E_{g\_A}<E_{g\_B}$ -- for example, GaInAs / dilute N GaInAsN embedded in GaAs-- the lower band gap material A is known as the well while the higher band gap material B is known as the barrier) which form a periodic structure, whose thicknesses are both of the order of nanometers, can allow carriers to transmit through the well/barrier structure. Based on the barrier's thickness, either multi-quantum wells or a superlattice structure will be formed. In the case of barriers thick enough to prevent a carrier from tunneling from one well to another, a quantum well structure is formed without a mini-band. On the other hand, with barriers thin enough to let a carrier see the coming layers as a periodic potential (which it can tunnel through), a superlattice is formed with a miniband.

Optics absorption property and effective band gap depend on the materials of the well and barrier, their individual thickness, and the number of periods.

Due to the difference in the density of states between the quantum well structure and that of the bulk material, it also gives a different absorption coefficient from that of bulk materials, which is studied by Fermi-Golden rule and $k*p$ method [10].

It can be seen that the density of state does not depend on temperature, yet the probability of a state being occupied depends on the temperature and the number of electrons.

Taking the number of photons transferred from any two states whose energy difference is E (absorb energy during transition) and subtracting the number of photons transferred from any two states whose energy difference is –E (emit energy during transition), which is the net absorption, indicates the absorption coefficient at energy E. Assume state b has higher energy than state a this net transition rate per unit volume can be expressed in the following equations.

$$R = R_{abs} - R_{ems} = R_{a \to b} - R_{b \to a} \tag{2.5.1}$$

$$= \frac{2}{\Omega} \Sigma_{k_a} \Sigma_{k_b} W_{abs} f_{E_a} \left(1 - f_{E_b}\right) - \frac{2}{\Omega} \Sigma_{k_a} \Sigma_{k_b} W_{ems} f_{E_b} \left(1 - f_{E_a}\right) \tag{2.5.2}$$

where f_{Ex} is the occupation probability at energy Ex, following Fermi-Dirac distribution;

W_{abs} is the transition rate of a photon transiting from state a to higher energy state b;

W_{ems} is the transition rate of a photon transiting from state b to lower energy state a.

$$\alpha(E) = \frac{\#\ of\ photons\ absorb/sec/}{R_p/E} = \frac{R}{R_p/E} \tag{2.5.3}$$

$$\alpha(E) = \frac{2\pi e^2 \hbar}{n_r c \varepsilon_0 m_0^{\,2} E \Omega} \Sigma_{k_a} \Sigma_{k_b} \left| \varepsilon \cdot P_{ba} \right|^2 \delta(E_b - E_a - E)\left(f_{E_a} - f_{E_b}\right) \tag{2.5.4}$$

Absorption in QW is a total effect of absorption from bulk materials, excitons, and quantum wells [11,12,13], which give broader absorption regions.

$$\alpha_{bulk}(E) = \frac{4\pi^{3/2} e^2 \mu^{3/2} \left| \varepsilon \cdot P_{ba} \right|^2}{n_r c \varepsilon_0 m_0^{\,2} E \Omega} \left(\frac{E - E_g}{\hbar} \right)^{1/2} \tag{2.5.5}$$

$$\alpha_{QW}(E) = \frac{4\pi^3 e^2 \mu \left| \varepsilon \cdot P_{ba} \right|^2}{n_r c \varepsilon_0 m_0^{\,2} E \Omega} \Sigma_k \Theta \left(E - E_g - \frac{k \hbar^2}{8 \mu L^2} \right) \tag{2.5.6}$$

$$\alpha_{exciton}(E) = \frac{2\pi^2 e^2 \hbar |e \cdot p_{cv}|^2}{n_r c \varepsilon_0 m_0^{\,2} E \Omega} \sum_n \alpha_n \, \delta(E - E_g) \tag{2.5.7}$$

Where μ is the permeability, n_r is the refractive index of the material, ε_0 is the permittivity of the vacuum, h is the Plank constant.

2.6 Light management

Light management includes manipulating the light behavior at the device front surface (which corresponds to textured antireflective gratings, plasmonics & wave guide) and back surface (which corresponds to coherent and incoherent textured mirror to increase light path).

2.6.1 Front surface light management

Industry wise, SiN single layer is generally used as antireflective (AR) layer for Si solar cells. In terms of research, the bi-layer coating is used to further reduce reflection loss on III-V devices. Other than the traditional plain layer AR, textured AR is also studied to bend the maximum amount of light into devices under broader spectrum; meanwhile, it has better angular tolerance to off normal incident angle, which is especially useful to multi-junction photovoltaic under concentrators. This is going to be explained in detail in chapter 3.

2.6.2 Back surface light management

Incoherent back reflector or coherent back reflector can efficiently increase (at least double) the light path of a device of a given thickness, which is mainly used on the bottom cell. The highest efficiency GaAs single cell, approaching the detailed balance limit, uses a coherent-back-mirror technique to achieve full absorption with a thinner device thickness for which the thickness is less than the diffusion length for minority carrier to recombine.

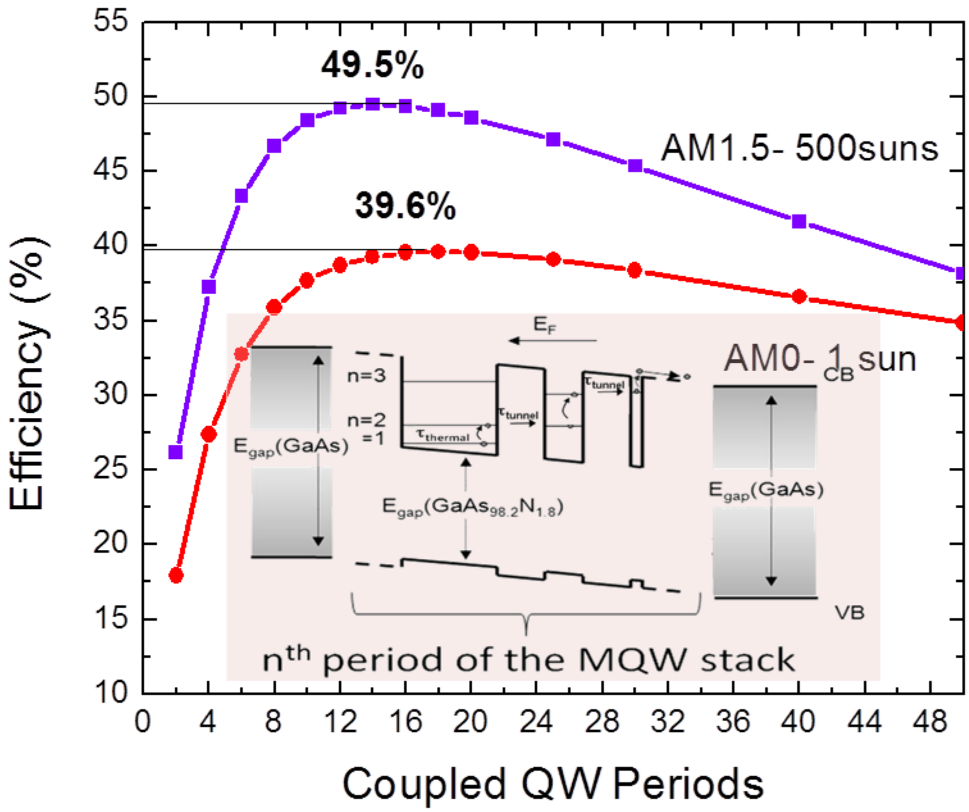

Fig. 2.10 The number of coupled quantum well versus efficiency relation for 1 sun and under concentrator (originally from A. Alemu [14] and G. Vijaya [15])

Obviously, the application which requires ultra- thin or ultra-lightweight field, such as space cells, asks for outstanding absorption property in limited thickness. With the advantages given in sub-chapter 2.5, dilute N is of great interest as a future PV material. And the calculated efficiency of dilute N 3-junction device can reach 39% and 49% under concentrator by assuming ideal carrier extraction by drift-diffusion model, which requires 16 coupled QW periods (48 wells) to reach this efficiency as shown in Fig. 2.10. However, carrier extraction in QW is not 100%, resulting in exponentially decreasing total extraction efficiency as the number of well increases. Consequently, a light management technique is needed to reach similar absorption with fewer wells. On the other hand, dilute N has short diffusion length, around 40 *nm*, which also requires light coupling technique to sufficiently reduce its thickness to avoid minority carrier recombination. Even though the examples given here are mainly III-V solar cells, light management is also important for other material system which needs improve absorption.

2.7 State of the art

Both laser interference lithography and wet etching are not something invented in this work. Laser interference lithography (LIL) was well studied for the misalignment of Lloyd's-Mirror, duty-cycle (the ratio between the photoresist remaining lines versus the pattern period) to exposure time, incident angle and post-bake temperature relations [16].

Most of the work took the advantage of fast and mask-less from LIL, but using a slow and small scale etching technique like reactive ion etching (RIE). Comparing to the previous work in literature, this work takes into account of GaAs's etching property, and make the full process scalable and rapidly, which is beneficial for obtaining the light trapping effect in module scale.

2.8 Summary

This chapter mainly talked about several aspects people have tried in III-V compound semiconductor solar cell field and successfully proved, to improve solar cell efficiency. Still, there are some other techniques under research and development, which haven't overtaken the current existing science and engineering, such as III-V on silicon substrate which confronts 4% lattice constant difference, and thermal expansion coefficient difference, nanowire solar cells which have the potential to get rid of those two aforementioned challenges. However they haven't shown better performance.

Some laboratories also tried wafer bounding technique by growing two junctions individually and bounding them together as a four-junction device [17,18], which leads to 44.7% and 46.5% efficiency for 4J devices under 297 and 324 concentrator respectively. This technique is focused on reducing the growth complexity and potential defect recombination centers. The bounding process is carefully done by plasma-cleaning the two surfaces and pressing them together, so the two pieces can stick together by van der Waals' force. For the 5J wafer bonding technique, 35.5% efficiency is demonstrated under AM1.5G and 41% is found under concentrator. The most complicated structure of 6J IMM devices has been made by emcore [19] with 33.7% efficiency under AM0 spectrum, yet this is a lower efficiency compared with the 4J devices. So there is still a long way to go and many aspects to optimize for multi-junction device to reach high efficiency.

Chapter 3 Theoretical Preparation

This chapter begins with a literature survey regarding common experimental approaches which have been studied to achieve sub-wavelength textures, while pointing out the available patterns achievable through various approaches. Within the framework of basic Fresnel equation and three mainstreams of simulation models (rigorous coupled-wave analysis (RCWA), finite difference time domain (FDTD), and effective medium approach- also known as transfer matrix method (TMM)) which are generally used to study the properties of designed light management structures, we will evaluate these simulation models. Based on the pros and cons of those 3 models, an effective medium approach is chosen for the sub-wavelength texture that attempts to improve the antireflective (AR) property. Four examples of 1D binary with rectangular/triangular grating and 2D hemispherical/pyramidal gratings are calculated and compared, and which demonstrate that 2D pyramid have the best AR performance in a broad spectrum for a single junction PV device. (It needs to be mentioned that these four examples represents four types of index profile, which cover larger number of morphology types.) The 2D pyramid grating, therefore, was chosen and applied to multi-junction concentrated photovoltaic devices, taking into account the current matching limit that reduces the current loss to one third of that from conventional bi-layer antireflective coating (ARC) design. In the end, the ray optics used for a back reflector is also introduced for the theoretical preparation of the next chapter's fabrication guidelines.

3.1 Literature research on enhancing light trapping from textured ARC

With a general overview about continuous grading of the refractive indices, in order to reduce reflectivity, the next step is the fabrication of front surface textured solar cells.

These could be an approach to achieve continuous variation of the refractive index. Various approaches have been employed to fabricate subwavelength gratings or nano-structures, such as nano-imprinting lithography [20,21], electron beam (e-beam) and laser interference lithography [22], self-assemble lithography [23,24], and so on. All these methods to obtain texture can generally be grouped into two categories, bottom-up or top-down. The bottom-up approach involves the growth of a coat or texture starting from the substrate upwards; while the top-down approach consists of the fabrication of AR materials by selectively etching from the original planar material, which is based on non-uniform etching rate between different materials or crystallographic orientations. A few basic principle and examples used in the fabrication of textured ARCs are discussed below.

Si wet etching

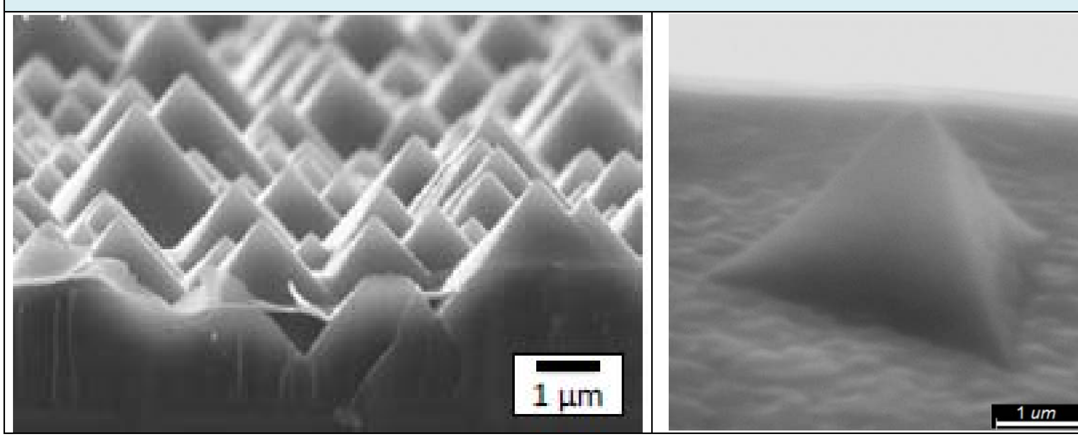

Fig. 3.1 SEM of crystalline Si (100) anisotropic etching in KOH (a) side view, (b) magnified structure

Reactive ion etching

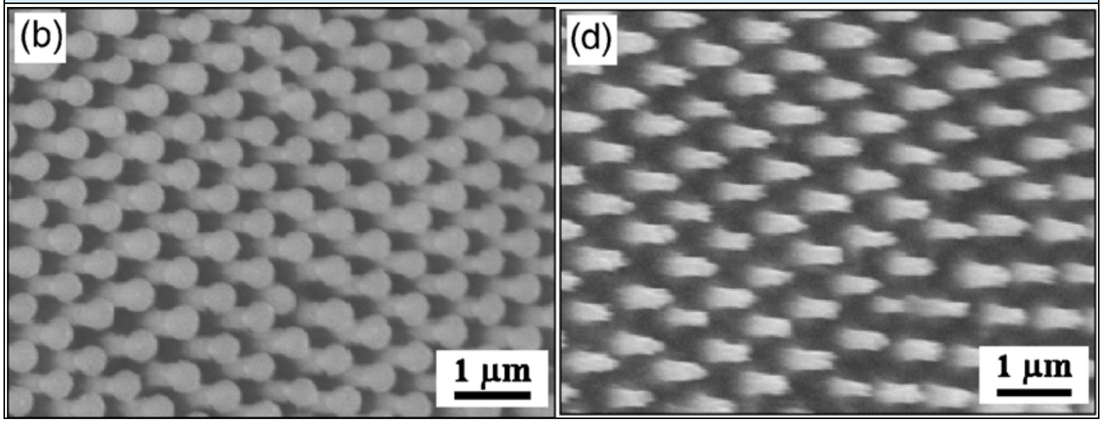

Fig. 3.2 SEM images of textured Si (b) tilted (20^{o}) image showing templating silica array and underneath silicon etched by SF_6 RIE for 9 min. (d) silicon arrays after 9 min HF etch. (by C.H. Sun *et al.*)

Self –assemble lithography (Thermally de-wetted nano-template)

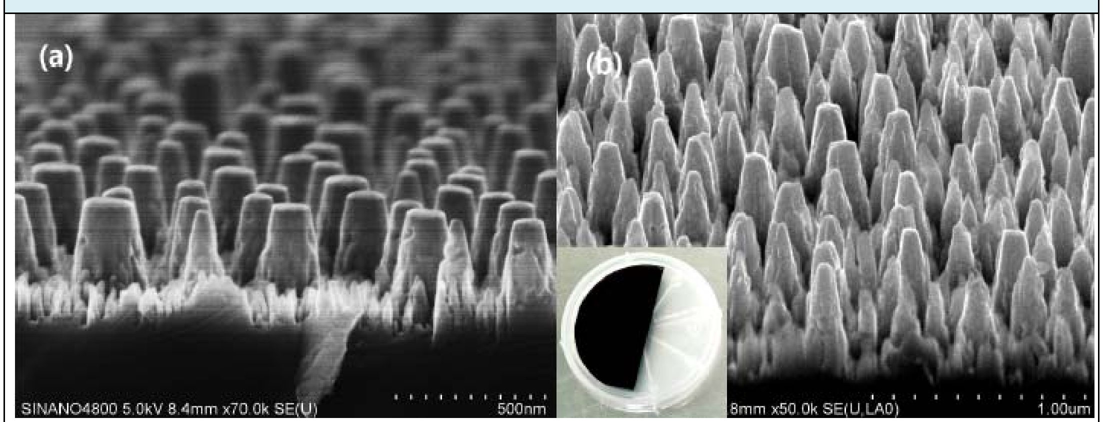

Fig. 3.3 Al(Ga)InP sub-wavelength structure profile etched through the optimized recipe, but different time (a) t = 3 min; (b) t = 5 min. (ref [25] by R. Y. Zhang *et al.*)

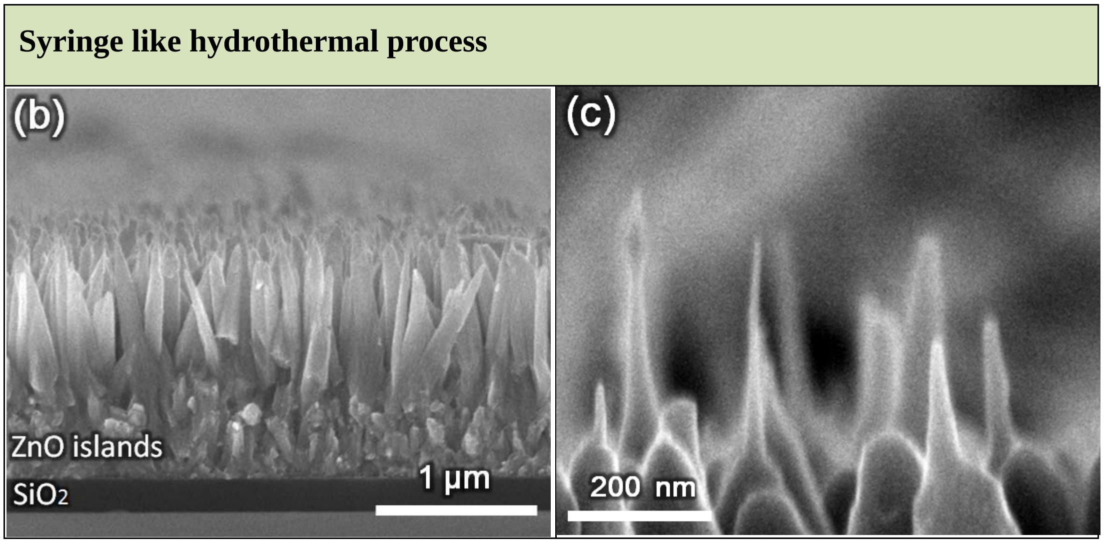

Fig. 3.4 (b) Cross-sectional SEM images of the syringe-like ZnO NRAs. (c) The high-magnification image showing the ultra-small tips on the ZnO NRAs. (ref [26] by L.K. Yeh *et al.*)

Si anisotropic etching and reactive ion etching will be explained in detail in section 3.1.1 and 3.1.2 respectively. Self-assemble lithography, as shown in Fig. 3.3, similarly uses masks to create textures. A 50 *nm* film of SiN is deposited on Al(Ga)InP to fabricate a low-surface-energy layer, so that the 10 *nm* Au film on SiN can agglomerate into nano-spheres during the high temperature heating process (500 ^oC, 100 *sec*, in N_2 environment), which is the etching mask. In the end, Au and SiN residue masks are removed by a wet etchant. All in all, the key trick for the top-down methods involves using various techniques to manufacture masks by either internal intrinsic property or external materials.

Other top-down approaches have obtained nano-structures that mostly contain undesired surface defects, which are unavoidable during the etching process [27]. The induced surface defects act as recombination centers, which result in a large carrier losses in solar cells. Hence, most of the reported efficiency enhancements, achieved with the adoption of AR nano-structures, were fabricated through bottom-up approaches [28,29]. Syringe-like ZnO NRAs, shown in Fig. 3.4, were synthesized using one-step hydrothermal process. Before synthesis, a 200 *nm* SiO_2 passivation layer was deposited on the device by e-beam evaporation to prevent the potential shortage caused by the conductive ZnO. Subsequently, a ZnO seed layer was deposited by e-beam evaporation on SiO_2 for the subsequent growth of ZnO NRAs. The samples with ZnO seed layers were then placed upside-down, positioned at the bottom of the beaker, and heated to 95 *℃* for 3.5 hours in the aqueous solution containing zinc nitrate hexahydrate (10 *mM*) and ammonia. Finally, the syringe-like NRAs thus obtained were cleaned with ethanol and dried in air.

3.1.1 Anisotropic wet etching

The concept of light trapping has been widely utilized in solar cell fabrication, especially for very high efficiency devices. Surfaces textured with upward and 'inverted' pyramids, and with V-shaped grooves have been used both to reduce reflection and to trap light internally within the cell. Surface texturing technique on Si has been popular since the mid-1970s [30] and the most common way is wet chemical etching using KOH[31], which contributes to the formation of micro pyramids due to the large difference in etching rate along various orientations. Taking Si as an example, the (110) plane is the fastest etching primary surface. The ideal (110) surface has a more corrugated atomic structure than the (100) and (111) primary surfaces. The (111) plane is an extremely slow etching plane that is tightly packed, has a single dangling-bond per atom, and is overall atomically flat [32]. The strongly stepped and vicinal surfaces to the primary planes are typically fast etching surfaces. The effective parameters which impact etching rate includes solution concentration, temperature and etching time. Multi-crystalline silicon wafers can undergo anisotropic etching too, but random orientation of crystalline planes reduces the effectiveness of anisotropic etching. Multi-crystalline silicon is often etched in acidic solutions or through mechanical means like laser texturing or reactive ion etching (RIE) [33].

For (100) silicon wafers with thermally grown oxide or nitride layer (around 200 - 300 *nm*), Bachman[34] *et al.* (Anisotropic silicon etch using KOH, INRF application note Process name: KOH01 1999) have reported a way to etch them using KOH. It is found that KOH wet-etch attacks silicon preferentially in the (100) plane, producing a characteristic anisotropic V-etch, with sidewalls that form a 54.7^{o} angle with the surface (35.3^{o} from the normal). This etching process is independent of the doping concentration for As, P and SC.

3.1.2 RIE dry etching for moth eye texture

Surfaces coated with a moth-eye structure of sub-wavelength roughness are known to show superior AR properties. Such a surface was first discovered on the cornea of night-flying moths by Bernhard in 1967 [35]. The eyes of this insect are covered with a regular array of conical protuberances with a spacing ranging from 180 to 240 *nm* and height varying between 0 and 230 *nm*. The reflectance of their cornea was investigated in the wavelength range from 300 to 700 *nm*. Stavenga [36] *et al.* investigated 19 butterfly species and showed that the nipple shape plays a rather significant role in the reduction of reflectance. They also probed that the nipple width plays a more secondary role, whereas the feature height has the more crucial primary role. Reflectance is reduced as the height increases. The first artificial moth-eye structure/film was produced by recording the interference patterns of low coherent laser beams on a photoresist. Currently, structures with a surface area of 0.5 m^2 can be produced by a complex holographic optical process or plasma treatment.

Sun *et al.* reported a bioinspired templating technique for fabrication of broadband moth-eye ARCs on SC silicon substrates. The resulting sub-wavelength-structured ARCs exhibit superior broadband antireflective performance than commercial SiN_x coatings. The schematic illustration of the templating procedures for making wafer-scale silicon arrays is shown in

Fig. 3.2. In summary, monolayer silica colloidal crystals with non-close-packed (ncp) structures are created by spin-coating. The ncp silica particles can be used as the etching mask during a SF_6 reactive ion etching (RIE) process. By exposure to SF_6, arrays of nipple like structures are directly formed on silicon wafer (note, the etching selectivity between silicon and silica can be adjusted to more than 10:1). At last, removal of the silica nano-particles from the silicon substrate is accomplished with HF.

3.1.3 Self-assemble lithography

A thin film of metal (*i.e.* 10-40 *nm Ag*) will crack and shrink into spheres under a rapid thermal annealing (RTA) process, as if they are self-assembling into nano-particles. This phenomenon is from the effect of surface tension [37], during which nano-particles help to reach the lowest surface energy under a certain temperature. For example10 *nm* Ag film sputtered by e-beam will mostly form 30 *nm*-100 *nm* particles with 10 *nm*-80 *nm* distances under 400 ^{o}C annealing in a N_2 environment for 3 *min* [38]. The self-assembled Ag particles can further behave as an etching mask in the following reactive-ion etching (RIE) process. The nano-particles' agglomerated pattern depends on the thickness of the film, the annealing temperature, time, pressure, metal material as well as the base material under the metal, which could together vary the particles' size and density.

The induced nano-particles may act as growing or etching seeds for the following process, adopted as bottom-up or top-down technique respectively. When top-down approach is used, the nano-particles need to be stable enough to survive during the etching process. Depending on the material to be etched, a different type of gas is chosen. For example, when Ag is used for the self-assembled mask, a CHF_3/CF_6 mixture is used in RIE process for silica etching [39], and Ar gas is used for SiNx layer etching. Other materials are also used for their self-assembly property, such as Au [40], Pt [41], alumina [42], and CsCl [43].

3.1.4 State-of-the-Art

The structure made by a thermally de-wetted nano-template is shown in Fig. 3.3. The measured reflection performance between 300-1500/2000 *nm* based on the optimized structure, *i.e.* the measured reflectivity at 8^{o} and at 45^{o} off-normal angle, are compared by the RCWA simulation. The reflectivity of less than 5% over 200-1800 *nm* and a wide view (up to 45^{o}) has been achieved in the optimized sub-wavelength structure (SWS).

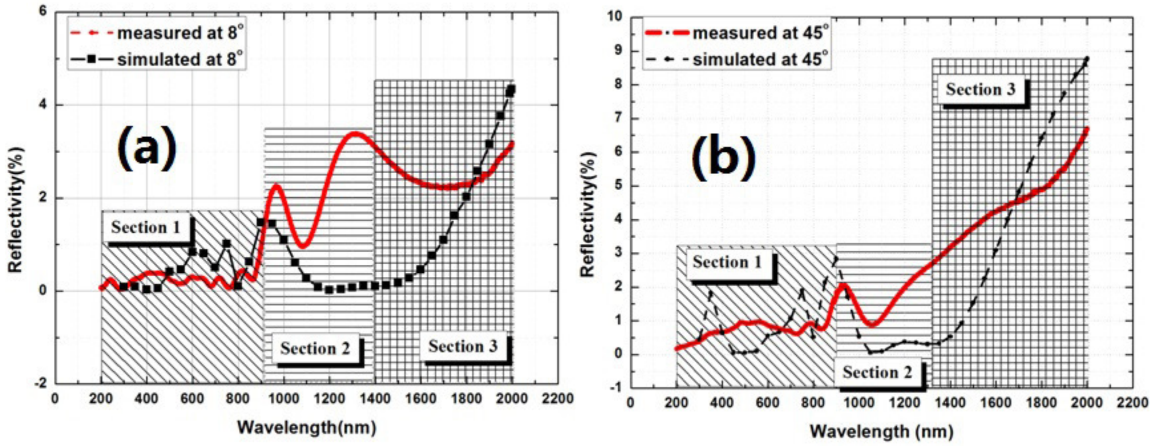

Fig. 3.5 The measured and simulated reflection spectra comparison for Al(Ga)InP SWS as shown in Fig. 3.2 (b); (a) incident angle is 8°, (b) incident angle is 45°.

ARC must be carefully optimized to get the minimum photon loss regardless of the technique used. There are several simulation methods for planar films, such as the use of series Fresnel Equations, which describes interface between two media, or multi-reflections between parallel-medium boundaries. Another technique is to use the transfer matrix method to deal with thin films, which explains how the electro-magnetic field transforms from the air to the substrate. For more complex structures with non-uniform morphologies, such as grating and texturing, the previous two methods cannot precisely predict the light behavior, which requires a more advanced approach. Rigorous coupled wave analysis (RCWA) is the rigorous way to discuss scattering and diffraction behavior between gratings, which could be used to find reflectivity. RCWA is a very-advanced method, but demands a large amount of calculation. Most of the work based on RCWA is either confirming experimental results [44] or analyzing textures [45] with fixed parameters. Very little work is done that treats all parameters as variables and optimizes the proper texturing morphology or grating geometric parameters. Because this method to some extent is relatively hard to do self-coding, some companies have written commercial software for RCWA, *e.g.*, 'RSOFT'. But due to their high price (roughly $10,000), it is not implementable for every laboratory. In sub-chapter 3.2.4, it will show that the TMM could reach results similar to RCWA calculations in sub-wavelength scale simulation. The principle and equations of these three methods will be explained in detail in the next sub-chapter.

As the efficiency of a solar cell is more dependent on the number of photons with energy above the bandgap, this work focuses on the fraction of integrated reflected photons instead of on the reflectivity. The conventional dual-layer ARC, (usually MgF_2-ZnS), can have good antireflection properties for normal light, but it is not implementable for wide acceptance angle concentrators' application as shown in Fig. 3.30. To this end, there were a few options, such as SiO_2 and metallic [46] nanoparticle plasmonic scattering, micro texturing, and sub-wavelength dielectric gratings. Sub-wavelength dielectric gratings demonstrated better suitable characters in III-V direct bandgap solar cells compared with the other two approaches, whose application is mainly in thin film solar cell devices. Their objective is to reduce the physical thickness of the photovoltaic absorber layers, and keep the optical thickness constant. Although silicon nano-tips and syringe-like Si nano-wire could get the reflectivity down to as low as 1% (as the structure in Fig. 3.4

Fig. 3.4, it is hindered for III-V multi-junction solar cells. Firstly, because the large area at the front surface would increase the recombination velocity, which would in turn increase surface recombination; secondly, due to wavelength-scale base of the structure, the scattering effect would enlarge the light path length, which leads to a challenge in optimizing the thickness of sub-cells; thirdly, because the micro-scale height of the texturing would increase absorption. Hence, this work concentrates on the properties of antireflection and angular tolerance for sub-wavelength dielectric grating on concentrated photovoltaic systems.

3.2 Simulation methodology for calculating AR properties

By knowing the possible structures made through different experimental approaches in literature, we are going to simulate these various structures and find out which type has better AR properties in a one-junction application. Next, I will then apply this structure to a multi-junction device under concentrated insolation. With respect to the application to a planar film calculation, all methods could lead to exactly the same solution. Here, I will go into detail of how they work, and give a brief comparison of these methods by concluding their pros and cons.

3.2.1 Simulation using Fresnel equation

Fresnel's equation governs the electric field relation at any planar interface boundary. If it is applied to a single-layer, *i.e.*, a sandwich structure of three media and two interfaces, the action of light at each interface must be analyzed. Since the light will never stop propagating backward and forward in the central medium, the final reflection coefficient is a sum of a geometric series with infinite number of terms from beams that are reflected backward.

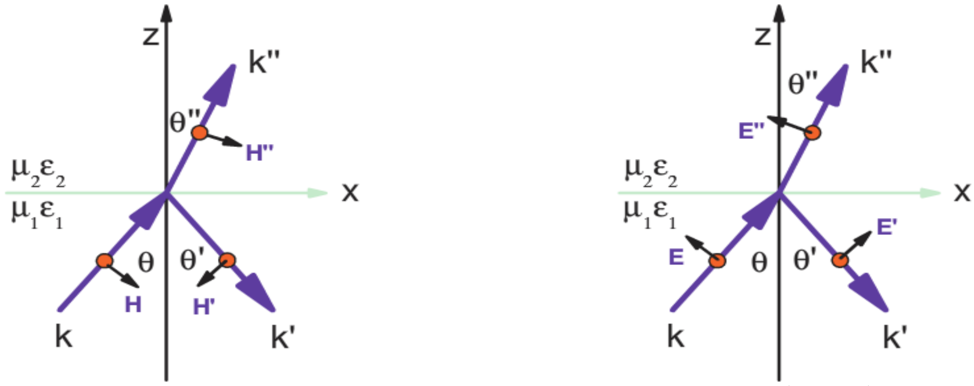

$$\frac{E'}{E}=\frac{\sqrt{\varepsilon_1}\cos\theta-\sqrt{\varepsilon_2}\cos\theta''}{\sqrt{\varepsilon_1}\cos\theta+\sqrt{\varepsilon_2}\cos\theta''}=-\frac{\sin(\theta-\theta'')}{\sin(\theta+\theta'')}$$

S mode

$$\frac{E'}{E}=\frac{\tan(\theta-\theta'')}{\tan(\theta+\theta'')}$$

P mode

Fig. 3.6 Fresnel relation of reflected *vs.* incoming electric field for S mode and P mode

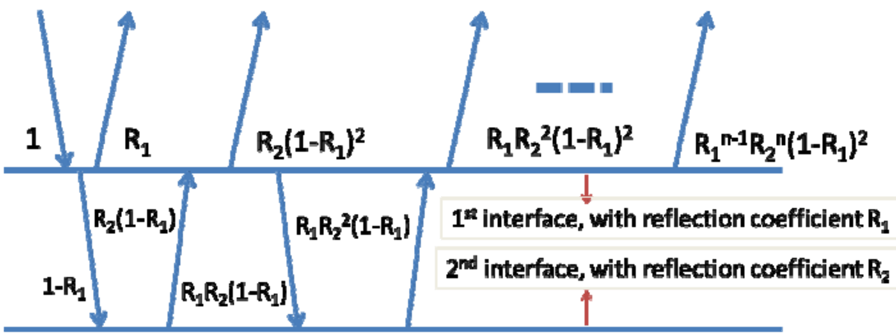

Fig. 3.7 An example of Fresnel equation applied on 3-material system with thick middle layer

Fig. 3.7 gives an example of magnitude from each reflection, for when the thickness of middle material is in large scale compared with wavelength so that the light coupling effect from interference can be ignored. The magnitude from multiple reflection and transmission finally returning to the light generating medium is, therefore, a geometric series. If the reflection coefficient between the 1st and 2nd medium is R_1, and the reflection coefficient between the 2nd and 3rd medium is R_2, the total reflection from the two interfaces is $R_1+R_2(1-R_1)^2/(1-R_1R_2) = (R_1+R_2^2-R_1R_2)/(1-R_1R_2)$. In case $R_1=R_2$, such as when light goes from air into a thick cover glass and then back into air again, the reflection is $R_1/(1+R_1)$.

3.2.2 Rigorous coupled wave analysis - RCWA

I am starting my analysis from the original RCWA formulation, explaining how it is related to reflectivity calculation.

We define the space in three regions, region 1 ($z<0$), region 2 ($0<z<d$), region 3 ($z>d$), with average relative permittivity ε_1, ε_2, and ε_3 respectively. It is assumed that each of the three regions has the permeability of free space. The diffraction of an obliquely incident plane wave is on a loss-less (relative permittivity is a real number) sinusoidal grating, with the incident wave polarized perpendicular to the plane of incidence (s mode). Hence the electric field has only a y component. The divided region and angle notation are shown in Fig. 3.8, where θ is the incident angle in region 1, and d is the thickness of region 2 along z axis.

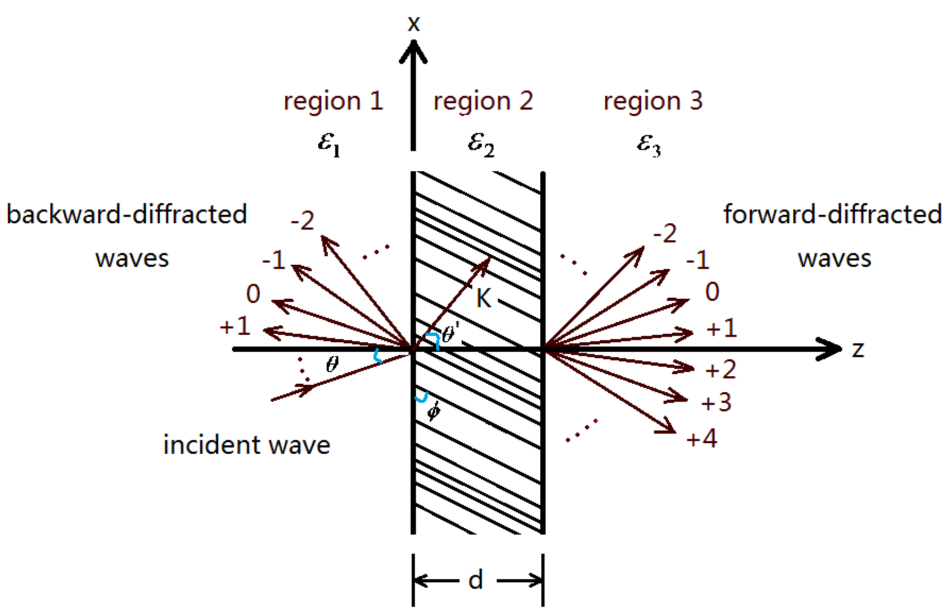

Fig. 3.8 Geometry for planar-grating diffraction

The relative permittivity in modulated region 2 ($0<z<d$) is

$$\varepsilon(x,z) = \varepsilon_2 + \Delta\varepsilon \cos[K(x\sin\phi + z\cos\phi)] \tag{3.1}$$

where, ε_2 is the average dielectric constant in region 2;

$\Delta\varepsilon$ is the amplitude of the sinusoidal relative permittivity;

$K = \frac{2\pi}{\Lambda}$, Λ is the grating period;

ϕ is the grating slant angle.

The general approach for finding electromagnetic solution is to solve the wave equation in each region and then matching electric and magnetic fields as well as their tangent at the boundary ($z=0$, and $z=d$). The electric field in the three regions (all oscillating in y direction) may be expressed as

$$E_1 = \exp[-i(\beta_0 x + \xi_{10} z)] + \sum_h R_h \exp[-i(\beta_h x - \xi_{1h} z)] \tag{3.2}$$

$$E_2 = \sum_h S_h(z)\exp[-i(\beta_h x + \xi_{2h} z)] \tag{3.3}$$

$$E_3 = \sum_h T_h \exp\{-i[\beta_h x + \xi_{3h}(z-d)]\} \tag{3.4}$$

where, $\beta_h = k_1 \sin\theta - hK\sin\phi$ for any integer h (the wave index);

$\xi_{lh}{}^2 = k_l{}^2 - \beta_h{}^2$ for l = 1,3 (the region index);

$k_l = 2\pi\sqrt{\varepsilon}\lambda$ for l = 1,2,3; λ is the free space wavelength;

$i = \sqrt{-1}$;

R_h is the normalized amplitude of the h^{th} reflected wave;

T_h is the normalized amplitude of the h^{th} transmitted wave;

R_h and T_h are to be determined from the matching of the electric and magnetic fields. Substituting (3.1) and (3.4) into the Helmholtz equation in the grating region, $\nabla^2 E_2 + k_2 E_2 = 0$, results in an infinite set of coupled wave equations:

$$\frac{\Delta\varepsilon}{8\varepsilon_2}\frac{d^2 S_h(u)}{du^2} = (\cos\theta' - hu\cos\phi)\frac{dS_h(u)}{du} - \rho h(h-B)S_h(u) + S_{h+1}(u) + S_{h-1}(u) \qquad (3.5)$$

where, $S_h(u) = S_h(z)$;

$u = i\kappa z$; $\kappa = {\pi\Delta\varepsilon}/{2\lambda\sqrt{\varepsilon_2}}$;

$\rho = {2\mu^2\varepsilon_2}/{\Delta\varepsilon}$;

$B = {2\cos(\phi - \theta')}/{\mu}$;

$\mu = {\lambda}/{\Lambda\sqrt{\varepsilon_2}}$.

If S and S' are defined as state variables, (3.5) can be written in matrix form# as

$$\begin{bmatrix} S' \\ S'' \end{bmatrix} = [b_{rs}]\begin{bmatrix} S \\ S' \end{bmatrix} \qquad (3.6)$$

where, S, S', and S'' are the column vectors of S_h, dS_h/du, and d^2S_h/du^2 respectively. $[b]$ is the coefficient matrix determined from (3.5), whose dimension is fourth the size of S, because both column and row are twice the size of S.

Up to this point, this system of coupled-wave equations is derived without assumptions and approximations. If n waves are retained in the analysis for example, the boundary condition provides *4n* linear equations, due to the continuity for electric field, the

---

As is shown in the Appendix A: the state equation

continuity for magnetic field, the continuity for tangential electric field, and the continuity for tangential magnetic field.

Judging from linear algebra algorithms, the solution of (3.6) can be expressed in terms of the eigenvalues and eigenvectors of the coefficient matrix [b]. Assuming q_m is the m^{th} eigenvalue and w_{hm} is the m^{th} element of row, corresponding to the i^{th} eigenvalue, in matrix *[w]* composed of the eigenvectors, we have the relation:

$$S_h(u) = \sum_{m}^{2n} C_m w_{im} \exp(q_m u) \tag{3.7}$$

Matrix [b] in (3.6) is *2n*2n* matrix, with *2n* eigenvalues. Consequently, the specific solution is a linear combination of *2n* general solutions, with *2n* unknown coefficients C_m. Furthermore, R_h and T_h are other *2n* unknown values to be determined. Therefore, the number of equations available, *4n*, is exactly equal to the number of unknowns, so that each R_h and T_h can be calculated.

The criteria for the number of orders to retain is determined by two requirements,

1) Energy conservation:

$$\sum_h (DE_{1h} + DE_{3h}) = 1 \,, DE_{1h} = \mathrm{Re}\left(\xi_{1h} / \xi_{10} \right) R_h R_h^{*} ,\; DE_{3h} = \mathrm{Re}\left(\xi_{3h} / \xi_{10} \right) T_h T_h^{*} ,$$

2) Convergence to the proper solution with an increasing number of field harmonics for all the grating and the incident-wave parameters.

DE_{1h} and DE_{3h} are the diffraction efficiencies in region 1 and 3 individually. The quantity $\mathrm{Re}\left(\xi_{lh} / \xi_{10} \right) = \cos\theta_{lh} / \cos\theta_{l0}$, where θ_{lh} is the diffraction angle for the h^{th} order wave in the l^{th} medium.

As ϕ approaches but does not equal zero[*], all the reflected wave vectors in region 1 approach an identical direction and $\theta_{1h} \to \theta_{10}$, so the resulting reflected intensity of the composite wave is $\sum_h |R_h|^2$. Likewise, all the transmitted wave vectors in region 3 approach a single direction; and the resulting transmitted intensity of this composite waves is $\sum_h |T_h|^2$. So RCWA is later applied for calculating the reflection coefficient. In the case where $\phi \to 0$, and the amplitude of the sinusoidal relative permittivity $\Delta\varepsilon = 0$, it is reduced to a single-layer problem.

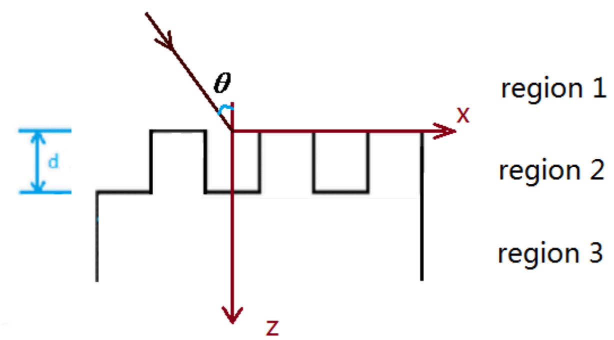

Fig. 3.9 Geometry for binary rectangular-groove grating

For further analysis, we can discover that $K = \dfrac{2\pi}{\Lambda}$ is the period in k-space, so the electric field as shown in (3.2)-(3.4) is expressed in Fourier series. From this idea, RCWA is applied to textured interface as in Fig. 3.9.

---

[*] This is because the above analysis is derived from Floquet theorem, which is valid for infinite periodic structures. However when the slant angle is exactly zero (pure reflection grating), the modulation is no longer periodic since it has a finite number of cycles.

From discrete Fourier transform the relative permittivity can be expanded in the form of

$$\varepsilon(x) = \sum_p \varepsilon_p \exp\left(i \frac{2\pi px}{\Lambda} \right) = \sum_p \varepsilon_p \exp(ipKx) \tag{3.8}$$

Following the previous analysis about *TE* mode where incident light is in *x-z* plane with incident angle θ, the incident normalized electric field that is normal to the plane of incidence is given by

$$E_{inc,y} = \exp[-ik_0 n_1 (x \cdot \sin\theta + z \cdot \cos\theta)] \tag{3.9}$$

$$E_{1,y} = E_{inc,y} + \sum_h R_h \exp\left[-i\left(k_{xh}x - k_{1,zh}z\right)\right] \tag{3.10}$$

$$E_{3,y} = \sum_h T_h \exp\left\{-i\left[k_{xh}x + k_{3,zh}(z-d)\right]\right\} \tag{3.11}$$

where, k_{xh} is determined from the Floquet condition, $k_{xh} = k_1 \sin\theta - hK$.

$$k_{l,zh} = \begin{cases} +k_0\left[n_l^{\,2} - \left(k_{xh}/k_0\right)^2\right]^{1/2} & k_0 n_l > k_{xh} \\ -ik_0\left[\left(k_{xh}/k_0\right)^2 - n_l^{\,2}\right]^{1/2} & k_{xh} > k_0 n_l \end{cases} \qquad l = 1,3$$

In region 2, the electric field in *y* component and the magnetic field in *x* component may be expressed as a Fourier expansion in terms of space-harmonic fields,

$$E_{2,y} = \sum_h S_{yh}(z)\exp(-ik_{xh}x) \tag{3.12}$$

$$H_{2,x} = -i\left(\frac{\varepsilon_0}{\mu_0}\right)^{1/2} \sum_h U_{xh}(z)\exp(-ik_{xh}x) \tag{3.13}$$

Inserting (3.12) into Maxwell's Equation $\nabla \times E_2 = -i\omega\mu_0 H_2$, and (3.13) into Maxwell's Equation $\nabla \times H_2 = i\omega\varepsilon_0\varepsilon(x)E_2$, we could obtain two differential equations,

$$\frac{\partial E_{2y}}{\partial z} = i\omega\mu_0 H_{2x} \tag{3.14}$$

$$\frac{\partial H_{2x}}{\partial z} = i\omega\varepsilon_0\varepsilon(x)E_{2y} + \frac{\partial H_{2z}}{\partial x} \tag{3.15}$$

Substituting (3.12), (3.13), and (3.8) into (3.14) and (3.15), and eliminating H_{2z}, we could obtain the coupled-wave equations in each order h, expressed in terms of permittivity Fourier expansion.

$$\begin{aligned} \frac{\partial S_{yh}}{\partial z} &= k_0 H_{xh} \\ \frac{\partial U_{xh}}{\partial z} &= \left(\frac{k_{xh}{}^2}{k_0}\right) S_{yh} - k_0 \sum_p \varepsilon_{(h-p)} S_{yp} \end{aligned} \tag{3.16}$$

Similar to the analysis for a planar grating, the solution process comes down to a *4n* linear equations' problem. However, in this case, the relative permittivity in the form of Fourier transform is also in every order. So various textures, including shape, period, and depth, resulting in various Fourier transforms on permittivity, will contribute to different solutions.

Note that if we take the second order derivative equation instead of two first order derivative equation, the matrix reduces from *2n*2n* to *n*n*, which takes 1/8 of the previous overall computational time of the eigenvalue problem.

3.2.3 Finite difference time domain – FDTD

FDTD algorithm was first proposed by Yee in 1966, employing second-order central differences. This is a method for approximating wave propagation in isotropic media in one or more dimensions, which originated in electromagnetic field and was later adapted to acoustics. The FDTD method employs finite differences as approximations to both the spatial and temporal derivatives that appear in Maxwell's equations. Consider the Taylor series expansions of the function $f(x)$ expanded about the point x_0 with an offset of $\pm\delta/2$:

$$f(x_0 + \delta/2) = f(x_0) + \delta/2\, f'(x_0) + 1/2!\, (\delta/2)^2 f''(x_0) + 1/3!\, (\delta/2)^3 f'''(x_0) + \ldots \quad (3.17)$$

$$f(x_0 - \delta/2) = f(x_0) - \delta/2\, f'(x_0) + 1/2!\, (\delta/2)^2 f''(x_0) - 1/3!\, (\delta/2)^3 f'''(x_0) + \ldots \quad (3.18)$$

where, the primes indicate differentiation. Subtracting the second equation from the first and dividing by δ yields

$$[f(x_0 + \delta/2) - f(x_0 - \delta/2)]/\delta = f'(x_0) + 1/3!\, (\delta/2^2)^2 f'''(x_0) + \ldots \quad (3.19)$$

Which can be rewritten as

$$f'(x_0) = [f(x_0 + \delta/2) - f(x_0 - \delta/2)]/\delta + O(\delta^2) \quad (3.20)$$

The $O(\delta^2)$ term represents all the hidden terms that are at higher order of δ . In case δ is sufficiently small, neglecting $O(\delta^2)$ can give a reasonable approximation to the derivative can be obtained.

FDTD implementation on 1D Maxwell's equation

Consider a 1D electric-magnetic field [47] that electric field has only z component, thus magnetic field has only non-zero component in y direction. The two-vector Maxwell's equation would be reduced to two scalar equations, written as

$$\mu \frac{\partial H_y}{\partial t} = \frac{\partial E_z}{\partial x} \quad (3.21)$$

$$\epsilon \frac{\partial E_z}{\partial t} = \frac{\partial H_y}{\partial x} \quad (3.22)$$

These two equations therefore give the temporal derivation in terms of spatial derivation, which can be used to advance a field by the other, known as a leap-frog method. If we define Δx as the spatial step size between sample points, and Δt as the temporal step size and index m refers to the number of spatial step, while index q the temporal step, the location in space (x) and time (t) can be replaced by $m\Delta x$, and $q\Delta t$, sampling the space and time dependent field as $E_z(m,q)$ and $H_y(m,q)$. The two scalar equations from Maxwell's equation can be rewrote as

$$\mu \frac{H_y\left(m+\frac{1}{2},q+\frac{1}{2}\right)-H_y\left(m+\frac{1}{2},q-\frac{1}{2}\right)}{\Delta t} = \frac{E_z(m+1,q)-E_z(m,q)}{\Delta x} \tag{3.23}$$

$$\epsilon \frac{E_z(m,q+1)-E_z(m,q)}{\Delta t} = \frac{H_y\left(m+\frac{1}{2},q+\frac{1}{2}\right)-H_y\left(m-\frac{1}{2},q+\frac{1}{2}\right)}{\Delta x} \tag{3.24}$$

Solving these for $H_y\left(m+\frac{1}{2},q+\frac{1}{2}\right)$ and $E_z(m,q+1)$ yield,

$$H_y\left(m+\frac{1}{2},q+\frac{1}{2}\right) = H_y\left(m+\frac{1}{2},q-\frac{1}{2}\right) + \frac{\Delta t}{\mu\Delta x}\left[E_z(m+1,q) - E_z(m,q)\right] \tag{3.25}$$

$$E_z(m,q+1) = E_z(m,q) + \frac{\Delta t}{\epsilon\Delta x}\left[H_y\left(m+\frac{1}{2},q+\frac{1}{2}\right) - H_y\left(m-\frac{1}{2},q+\frac{1}{2}\right)\right] \tag{3.26}$$

The indices in these two equations are generic, therefore they hold for every E_z and H_y node. These two relations indicate that the future value of H_y only depends on its previous value and the neighboring electric fields; similarly, E_z only relies on its past value and the neighboring magnetic fields value.

Similar concept can be adapted for 3D condition, with four extra relations. It can be concluded that FDTD is solving the whole space *E-B* field as it propagating through various medium. Taking into account of boundary condition, the reflectivity would be derived by dividing the reflected electric field over the incoming field and multiplying its complex conjugate value.

3.2.4 Effective medium approach – transfer matrix method

Similar to the derivation of Fresnel Equations in Appendix B, the transfer matrix method is also derived from Maxwell's Equations [48]. Assume the plane of incidence to be the *y-z* plane, *z* being the direction of stratification. Let's take *TE* polarization as an example, where the electric fields in the *y* and *z* directions are all zero, and the magnetic field in the *x* direction is zero. So the Maxwell's vector equations reduce to six scalar equations, shown as follows:

$$\begin{aligned} &\frac{\partial H_z}{\partial y}-\frac{\partial H_y}{\partial z}+\frac{i\varepsilon\omega}{c}E_x=0 \\ &\frac{\partial H_x}{\partial z}-\frac{\partial H_z}{\partial x}=0 \\ &\frac{\partial H_y}{\partial x}-\frac{\partial H_x}{\partial y}=0 \end{aligned} \qquad (3.27)$$

$$\begin{aligned} &\frac{i\omega\mu}{c}H_x=0 \\ &\frac{\partial E_x}{\partial z}-\frac{i\omega\mu}{c}H_y=0 \\ &\frac{\partial E_x}{\partial y}+\frac{i\omega\mu}{c}H_z=0 \end{aligned} \qquad (3.28)$$

These equations show that H_y, H_z and E_x are only depend on *y* and *z*. Eliminating H_y, H_z by taking the x-component of the wave equation, it follows that

$$\frac{\partial^2 E_x}{\partial y^2}+\frac{\partial^2 E_x}{\partial z^2}+n^2 k_0{}^2 E_x=\frac{d(\ln\mu)}{dz}\frac{\partial E_x}{\partial z} \qquad (3.29)$$

where,

$$n^2=\varepsilon\mu, k_0=\frac{\omega}{c}=\frac{2\pi}{\lambda_0} \qquad (3.30)$$

To solve equation (3.29), a trial solution can be taken, which is a product of two functions, one involving *y* only and the other involving *z* only:

$$E_x(y,z)=Y(y)U(z). \qquad (3.31)$$

Eq. (3.29) comes to be

$$\frac{1}{Y}\frac{d^2Y}{dy^2} = -\frac{1}{U}\frac{d^2U}{dz^2} - n^2k_0^2 + \frac{d(\ln\mu)}{dz}\frac{1}{U}\frac{dU}{dz} \tag{3.32}$$

Now the terms on the left only depend on y, whilst the terms on the right only depend on z. Hence (3.32) cannot hold unless both sides are equal to a constant (denoted as $-K^2$):

$$\frac{1}{Y}\frac{d^2Y}{dy^2} = -K^2 \tag{3.33}$$

$$\frac{d^2U}{dz^2} + n^2k_0^2U - \frac{d(\ln\mu)}{dz}\frac{dU}{dz} = K^2U \tag{3.34}$$

For the sake of convenience, set

$$K^2 = k_0^2\alpha^2 \tag{3.35}$$

Then (3.33) contributes to $Y = [const]e^{ik_0\alpha y}$, and consequently E_x is in the form of

$$E_x = U(z)e^{i(k_0\alpha y - \omega t)} \tag{3.36}$$

where, $U(z)$ is a (possibly complex) function of z. Equation (3.28) analogously indicates that H_y, and H_z are given by expressions of the same form:

$$H_y = V(z)e^{i(k_0\alpha y - \omega t)} \tag{3.37}$$

$$H_z = W(z)e^{i(k_0\alpha y - \omega t)} \tag{3.38}$$

According to equations (3.27) and (3.28), the amplitude functions, U, V and W are related to each other by the following three relations:

$$\begin{aligned} V' &= ik_0(\alpha W + \varepsilon U) \\ U' &= ik_0\mu V \\ \alpha U + \mu W &= 0 \end{aligned} \tag{3.39}$$

The superscript prime symbol denotes differentiation with respect to z. Substituting W from $\alpha U + \mu W = 0$ into $V' = ik_0(\alpha W + \varepsilon U)$, and together with $U' = ik_0 \mu V$, two simultaneous first-order differential equations for U and V can be found:

$$\left.\begin{aligned} U' &= ik_0 \mu V \\ V' &= ik_0\left(\varepsilon - \frac{\alpha^2}{\mu}\right)U \end{aligned}\right\} \tag{3.40}$$

Taking derivation to z so as to reach two equations involving U and V separately, finally (3.30) gives the following second-order linear differential equations:

$$\frac{d^2U}{dz^2} - \frac{d(\ln \mu)}{dz}\frac{dU}{dz} + k_0^2\left(n^2 - \alpha^2\right)U = 0 \tag{3.41}$$

$$\frac{d^2V}{dz^2} - \frac{d\left[\ln\left(\varepsilon - \frac{\alpha^2}{\mu}\right)\right]}{dz}\frac{dV}{dz} + k_0^2\left(n^2 - \alpha^2\right)V = 0 \tag{3.42}$$

On account of the substitution rule, which is a consequence of the symmetry of Maxwell's Equations, it immediately follows that for the *TM* wave ($H_y = H_z = 0$), the non-vanishing components of the field vectors are of the form:

$$H_x = U(z)e^{i(k_0\alpha y - \omega t)} \tag{3.43}$$

$$E_y = -V(z)e^{i(k_0\alpha y - \omega t)} \tag{3.44}$$

$$E_z = -W(z)e^{i(k_0\alpha y - \omega t)} \tag{3.45}$$

where,

$$\left.\begin{aligned} U' &= ik_0 \mu V \\ V' &= ik_0\left(\varepsilon - \frac{\alpha^2}{\mu}\right)U \end{aligned}\right\} \tag{3.46}$$

and W is related to U by means of the equation

$$\alpha U + \mu W = 0 \tag{3.47}$$

U and V now satisfy the second-order linear differential equations:

$$\frac{d^2U}{dz^2} - \frac{d(\ln \varepsilon)}{dz}\frac{dU}{dz} + k_0^2\left(n^2 - \alpha^2\right)U = 0 \tag{3.48}$$

$$\frac{d^2V}{dz^2} - \frac{d\left[\ln\left(\mu - \dfrac{\alpha^2}{\varepsilon}\right)\right]}{dz}\frac{dV}{dz} + k_0^2\left(n^2 - \alpha^2\right)V = 0 \tag{3.49}$$

Since the function *U(z)* and *V(z)* each satisfy a second-order linear differential equations (3.41) and (3.42), U and V can each be expressed as a linear combination of two particular solutions, say U_1, U_2 and V_1, V_2. These particular solutions cannot be arbitrary; they may be coupled by the first-order differential equation.

$$\left.\begin{aligned} U_1' &= ik_0\mu V_1 \\ V_1' &= ik_0\left(\varepsilon - \frac{\alpha^2}{\mu}\right)U_1 \end{aligned}\right\} \quad (3.50) \qquad \left.\begin{aligned} U_2' &= ik_0\mu V_2 \\ V_2' &= ik_0\left(\varepsilon - \frac{\alpha^2}{\mu}\right)U_2 \end{aligned}\right\} \tag{3.51}$$

From these relations it obeys $V_1U_2' - U_1'V_2 = 0$, $U_1V_2' - V_1'U_2 = 0$, hence, $\frac{d}{dz}\left(V_1U_2 - U_1V_2\right) = 0$

which implies that determinant D is a constant, associated with any two arbitrary solution of (3.40) , *i.e.* D is an invariant of this system of equations.

$$D = \begin{vmatrix} U_1 & V_1 \\ U_2 & V_2 \end{vmatrix} \tag{3.52}$$

For our purpose, the most convenient choice of the particular solution is

$$\left.\begin{aligned} U_1 &= f(z), \quad U_2 = F(z) \\ V_1 &= g(z), \quad V_2 = G(z) \end{aligned}\right\} \tag{3.53}$$

Such that

$$f(0) = G(0) = 0 \quad \text{and} \quad g(0) = F(0) = 1 \tag{3.54}$$

Then the solution with

$$U(0) = U_0, \quad V(0) = V_0 \tag{3.55}$$

may be expressed in the form of $\left.\begin{aligned} U &= FU_0 + fV_0 \\ V &= GU_0 + gV_0 \end{aligned}\right\}$, or in matrix notation,

$$Q = NQ_0 \tag{3.56}$$

where, $Q = \begin{pmatrix} U(z) \\ V(z) \end{pmatrix}, Q_0 = \begin{pmatrix} U_0 \\ V_0 \end{pmatrix}, N = \begin{pmatrix} F(z) & f(z) \\ G(z) & g(z) \end{pmatrix}$ (3.57)

On account of the relation *D=constant*, the determinant of the square matrix *N* is a constant. The value of this constant may immediately be found by taking *z=0*, giving $|N| = Fg - fG = 1$.

It is usually more convenient to express U_0 and V_0 as functions of *U(z)* and *V(z)*. Solving for U_0 and V_0, we obtain,

$$Q_0 = MQ \tag{3.58}$$

where,

$$M = \begin{pmatrix} g(z) & -f(z) \\ -G(z) & F(z) \end{pmatrix} \tag{3.59}$$

This matrix is also uni-modular, $|M| = 1$ (3.60)

The significance of *M* is clear: it relates the *x*- and *y*-components of the electric (or magnetic) vectors in the plane *z=0* to the components in an arbitrary plane *z* = *constant*. Now, we saw that knowledge of *U* and *V* is sufficient for the complete specification of the field. Hence for the purposes of determining the propagation of a plane monochromatic wave through a stratified medium, the medium only need be specified by an appropriate two by two uni-modular matrix *M*. For this reason we shall call *M* the characteristic matrix of the stratified medium. The constancy of the determinant *M* may be shown to imply the conservation of energy.

We shall now consider the form of the characteristic matrix for cases of particular interest. In case of light propagating in homogeneous dielectric film, ε, μ and $n = \sqrt{\varepsilon\mu}$ are constants. If θ denotes the angle normal to the wave makes with the z-axis, we have by (3.50) $\alpha = n\sin\theta$.

For a TE wave, we have according to (3.41) and (3.42),

$$\left.\begin{aligned} \frac{d^2U}{dz^2} + \left(k_0^2 n^2 \cos^2\theta\right)U = 0 \\ \frac{d^2V}{dz^2} + \left(k_0^2 n^2 \cos^2\theta\right)V = 0 \end{aligned}\right\} \tag{3.61}$$

The solutions of these equations, subject to the relations (3.40), are easily seen to be

$$\left.\begin{aligned} &U(z) = A\cos(k_0 nz\cos\theta) + B\sin(k_0 nz\cos\theta), \\ &V(z) = \frac{1}{i}\sqrt{\frac{\varepsilon}{\mu}}\cos\left[B\cos(k_0 nz\cos\theta) - A\sin(k_0 nz\cos\theta)\right]. \end{aligned}\right\} \tag{3.62}$$

Hence the particular solutions (3.53) which satisfy the boundary conditions (3.54) are

$$\left.\begin{aligned} &U_1 = f(z) = \frac{i}{\cos\theta}\sqrt{\frac{\mu}{\varepsilon}}\sin(k_0 nz\cos\theta), \\ &V_1 = g(z) = \cos(k_0 nz\cos\theta), \\ &U_2 = F(z) = \cos(k_0 nz\cos\theta), \\ &V_2 = G(z) = \frac{i}{\cos\theta}\sqrt{\frac{\varepsilon}{\mu}}\cos\theta\sin(k_0 nz\cos\theta). \end{aligned}\right\} \tag{3.63}$$

If we set

$$p = \sqrt{\frac{\varepsilon}{\mu}} \cos\theta \tag{3.64}$$

The characteristic matrix can be simplified as

$$M = \begin{pmatrix} \cos(k_0 nz\cos\theta) & -\frac{i}{p}\sin(k_0 nz\cos\theta) \\ -ip\sin(k_0 nz\cos\theta) & \cos(k_0 nz\cos\theta) \end{pmatrix} \tag{3.65}$$

For a *TM* wave, the same equations hold, with p replaced by

$$q = \sqrt{\frac{\mu}{\varepsilon}} \cos\theta \tag{3.66}$$

The reflectivity and transmission coefficients from transfer matrix method

Let A, R, and T denote, as before, the amplitudes (possibly complex) of the electric vectors of the incident, reflected, and transmitted waves respectively. Further, let ε_1, μ_1 and ε_l, μ_l be the dielectric constant and the magnetic permeability of the first and the last medium, and let θ_1 and θ_l be off-normal (direction of stratification) angles of the incident and transmitted waves.

The characteristic matrix for a pile of homogeneous films is expressed

$$M(z_N) = M_1(z_1)M_2(z_2 - z_1)\ldots M_N(z_N - z_{N-1}) = \begin{pmatrix} m_{11} & m_{12} \\ m_{21} & m_{22} \end{pmatrix} \tag{3.67}$$

The boundary conditions demand that the tangential components of E and H shall be continuous across each of the two boundaries of the stratified medium. This gives, if the relation $\vec{H} = \sqrt{\frac{\varepsilon}{\mu}} \vec{s} \times \vec{E}$ is also used, the following relations for a *TE* wave

$$\left.\begin{aligned} U_0 &= A + R, & U(z_1) &= T \\ V_0 &= p_1(A - R), & V(z_1) &= p_l T \end{aligned}\right\} \tag{3.68}$$

$$\text{where, } p_j = \sqrt{\frac{\varepsilon_j}{\mu_j}} \cos\theta_j \ , \tag{3.69}$$

The four quantities U_0, V_0, U, and V given by (3.68) are connected by the basic relation (3.58); hence,

$$\left.\begin{aligned} A + R &= (m_{11} + m_{12} p_l)T, \\ p_1(A - R) &= (m_{21} + m_{22} p_l)T, \end{aligned}\right\} \tag{3.70}$$

m_{ij} being the elements of the characteristic matrix of the medium, evaluated for $z = z_1$.

From (3.70) we obtain the reflection and transmission coefficients of the film:

$$r = \frac{R}{A} = \frac{(m_{11} + m_{12} p_l)p_1 - (m_{21} + m_{22} p_l)}{(m_{11} + m_{12} p_l)p_1 + (m_{21} + m_{22} p_l)} \tag{3.71}$$

$$t = \frac{T}{A} = \frac{2p_1}{(m_{11} + m_{12} p_l)p_1 + (m_{21} + m_{22} p_l)} \tag{3.72}$$

where, r and t are then the ratios of the amplitudes of the magnetic and not the electric vectors.

3.2.5 Pros and cons of different methods

Pros and cons of Fresnel Equation method

Fresnel Equation method is the most straightforward method to know light's action at a planar boundary, which can quickly give a prediction of how much energy will be lost. Especially for the condition when the phase-change can be ignored, such as a thick layer invalidating light's coherence. Even for a planar system with several kinds of materials, the reflection can be calculated based on geometric series without writing any program.

However, to get the exact solution for thin multi-layer would be much more tedious, due to complicated actions going forward and backward with phase changing and half-wave loss. Nevertheless, a rough estimation can be quickly obtained because the amplitude shrinks fast as the order increases.

Pros and cons of the RCWA method

RCWA uses a Fourier expansion to represent the transition in permittivity and the field in each region, which leads to higher order linear equations. The limitations of RCWA include the difficulty of convergence – a large number of spatial harmonics (orders) must be retained in the analysis to obtain accurate results. The more terms we keep, the more accurate are the results we can obtain, but the heavier the calculation load. At the same time, having insufficient number of terms contributes to a non-conserved energy, and hence a significant error. For instance, there are four extreme examples that need a large number of orders and points to be evaluated; first, a conducting grating illuminated with a transverse-magnetic-(*TM*-) polarized wave; second, a pulse-width-modulated grating [49,50,51], whose period is usually much larger than the wavelength and each grating period is composed of grooves with sub-wavelength size features; third, crossed-grating structures, in which a few orders are retained along each direction; and fourth, the two-dimensional (2D) mesh of spatial harmonics[Y]. Besides the large amount of calculation of the physical properties, there are also some factors from mathematics. To find all the

---

[Y] As the Fourier transform of permittivity is shown among each order's equations, the 1D texture is transformed as $\varepsilon(x)=\sum_{h}^{H}\varepsilon_h \exp(ihKx)$, assume retain H terms, then the 2D texture is transformed as $\varepsilon(x,y)=\sum_{h}^{H}\sum_{h}^{T}\varepsilon_{ht}\exp(ihK_x x)\exp(ihK_y y)$ should retain $H*T$ terms.

eigenvalues and eigenvectors of an $n*n$ matrix, it requires the computation time roughly to the order of n^3, and it is practically very important to reduce computation time in those applications requiring accurate computation.

Nevertheless, RCWA is an advanced method that can deal with anisotropic media, and it can solve both reflection and diffraction, however it requires higher ordered terms in the analysis to get an accurate result.

Pros and cons of the FDTD method

Finite-difference time-domain is a 3D simulation, able to accurately tackle a wide range of problems. However, as all numerical methods, it has its share of artifacts and the accuracy is contingent upon the implementation. It can solve complicated problems, but it is generally computationally expensive. Solutions may require a large amount of memory and computation time. From the introduction of FDTD in chapter 3.2.2, it can be seen that this method is solving the E-B field in the whole space by grids. Because it is neglecting 2nd order and higher order of step size, the accuracy depends on how small the step size is chosen. Comparing with thin film method and RCWA, which are dealing the interfaces, FDTD calculates more superfluous data for the purpose of the reflectivity calculation.

Pros and cons of the transfer-matrix method

TMM treats the grating region as many uniform thin films, with an effective permittivity as a single value instead of a Fourier expansion. The physical origin of the transfer matrix method is also from Maxwell's Equations, but it handles the electric field in each layer as a 2*2 characteristic matrix, and the electric field in the deepest region can be transmitted from the incident field by the transformation of the elements in the characteristic matrix. Since the composition of the vectors of forward and backward electric waves determines the final electric field, the multiple reflections in every layer are automatically taken into account. We should notice that the transfer-matrix method requires the medium to be a homogeneous dielectric film, or a stratified medium that can be treated as a series of homogeneous dielectric films. So, strictly speaking, it cannot solve non-planar morphology or an anisotropic medium, unless the non-planar medium could be approximated as multi-layer structure and each layer has an effective dielectric characteristic. Nevertheless, this approximation leads to another problem that the shape and period of texture would not influence the effective permittivity. Some previous work reported that when the structure is in sub-wavelength scale, the transfer-matrix method based on the effective medium approach gives almost identical result to FDTD and RCWA, as demonstrated in Fig. 3.10 due to no scattering between the trenches and all generated from Maxwell's equation.

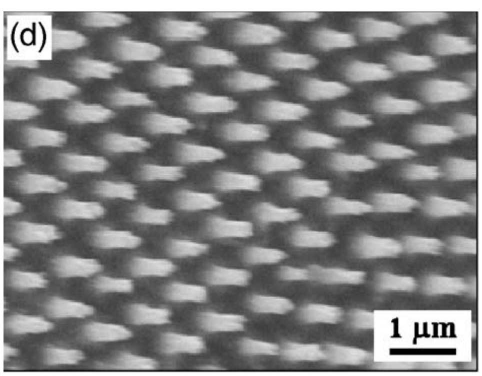

(a)

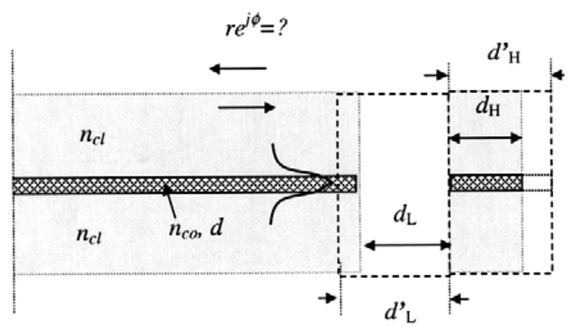

(c)

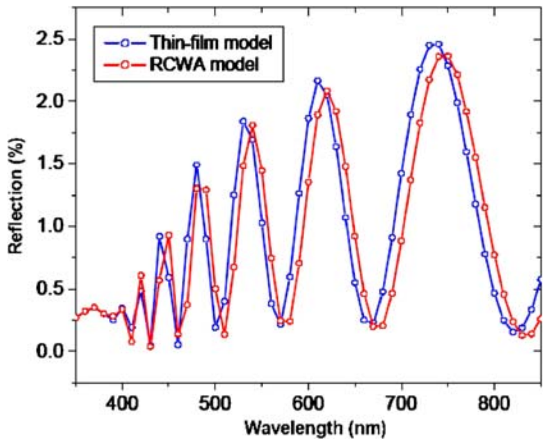

(b)

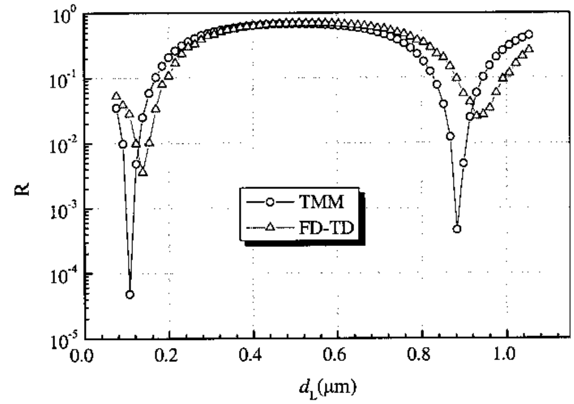

(d)

Fig. 3.10 Simulation results comparison for sub-wavelength scale texture (a) Silicon nano arrays, (b) TMM vs. RCWA simulation result for reflection as a function of wavelength on texture shown in (a) when the cone has 210 *nm* base radius and 800 *nm* height[52], (c) the structure used for TMM vs. FDTD simulation (d) TMM vs. FDTD simulation result for reflection (R in unit of %) as a function of trench width d_L on texture shown in (c) when d_H = 274 *nm* and H = 3.0 *μm* [53]

3.3 Simulation results for optimized AR morphology and materials

Until now, we have looked into the experimental approaches and what the general textures are that are possible to be fabricated. Also we studied some common applied methodology people used to simulate the behavior of various AR designs, among which thin film method based on effective medium approach is chosen for this simulation work. With the goal of minimizing the integrated photon loss over a broad spectrum (380 *nm* - 2000 *nm*) which means single-junction application, geometric parameters were optimized individually for four typical structures. And the simulating results are going to be reported below. Though only four types of structure are given here as examples, larger numbers of variety are actually covered, because different kinds of texture are indicating their certain effective refractive index distribution. For the textures appear to be different in morphology but sharing the same refractive index profile, they therefore have identical antireflective property, with simple geometric conversion for optimized morphology parameters.

3.3.1 1D binary grating with rectangular cross Section (2D pillar grating)

The simplest case of textured surface is 1D rectangular binary grating, which is shown in Fig. 3.11. (And this type of 1D grating mathematically has the same behavior as 2D pillar grating, whose refractive index is distributed as two individual values.) For single-layer and grating, there is only one material above the substrates. However, it plays a role of two layers, with four degrees of freedom to control, d_1, d_2, T, and f, which refer to the thickness of groove, the thickness of flat layer, the grating period, and the ratio of ridge, respectively, as shown in Fig. 3.11. To calculate the refractive index in grating we assume that the index is a linear average of the two mediums. The refractive index for the grating area is shown in equation (3.73); showing that the period of the binary grating will not affect the final result. So the binary grating model is a three-dimensional problem.

$$n_g = n_{ambient} \cdot (1-f) + n_{AR} \cdot f \tag{3.73}$$

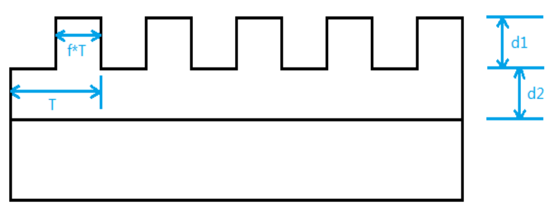

Fig. 3.11 Binary rectangular-groove grating used for ARC with parameter notation

Choosing the grating material to be ZnS on c-Si (100), and $f = 0.5$, the minimum integrated reflectivity (reflection) occurs at *height-grating = 80 nm*, *layer-thickness = 54 nm*, with the *reflection = 5.40 %.* Meanwhile, for $f = 1$, (single-layer dielectric) the minimum average of TE and TM polarization occurs at *height-grating + layer-thickness = 56 nm*, with the *reflection* equal to *11.94 %.*

Comparing f=*0.5* and f=*1*, Fig. 3.12 illustrates that the case of f=*0.5* has lower minimum reflection. The refractive index is more continuous in $f=0.5$ than $f=1$. So it can be concluded that with the continuity of refractive index increasing from the ambient to the substrate, the reflection will highly reduce.

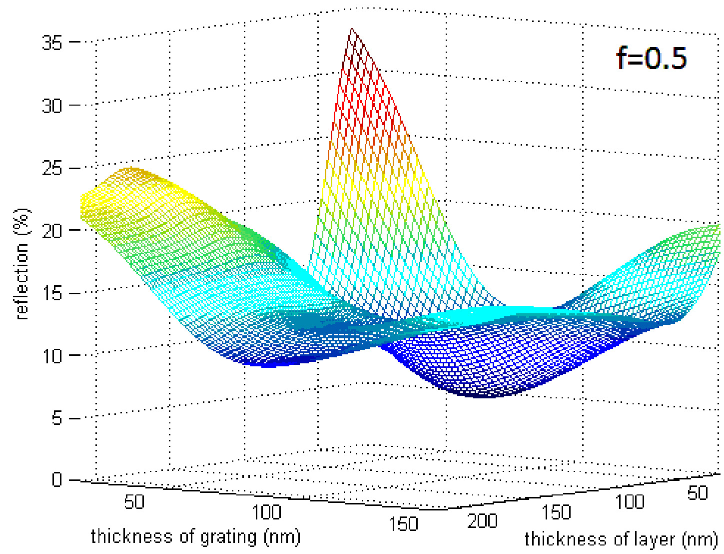

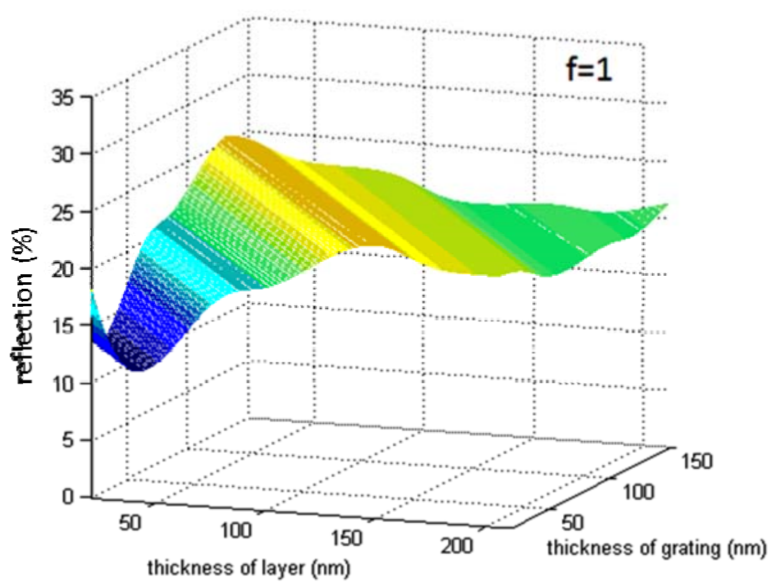

Fig. 3.12 Reflection coefficient versus thickness comparison for double and single-layer

How will the reflection change with f? Assume f varies from 0.1 to 0.9 and increases every 0.1, thicknesses for both grating and layer varies from 10 to 150 *nm* and increases every 5 *nm*, thus Fig. 3.14 (a) can be obtained. Numbers in bracket near each point represent the corresponding thicknesses for grating and flat layer respectively. These thicknesses are optimized for minimum total reflectivity, which represents the integral of reflectivity over the black body spectrum from 380 *nm* to 1100 *nm*. It also shows that with increasing f, the minimum reflection decreases until $f = 0.3$; and as f continuously increases, the minimum reflection increases.

We can see from Fig. 3.14 (b) that there is an prominent trough on each reflectivity versus wavelength curve. Furthermore, as the incident angle increases, the reflection coefficient trough is increasing while the corresponding wavelength is decreasing.

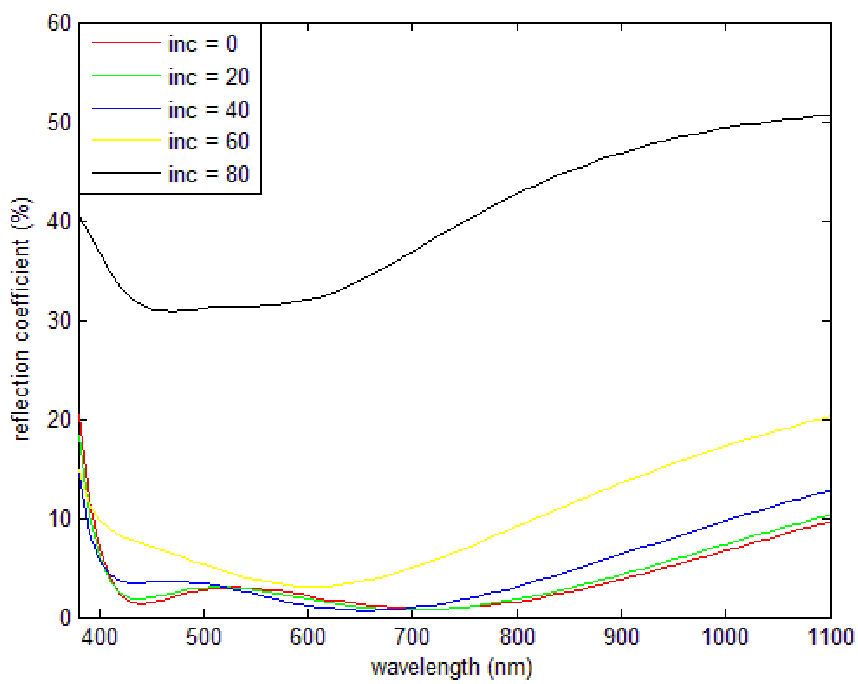

Fig. 3.13 Angular dependence of incident angle for MgF_2-ZnS double-layer on c-Si(100) at AM 1 optimized thickness [100 *nm*, 54 *nm*]

Reflectivity on c-Si(100) for binary rectangular-groove grating for ZnS is presented in Fig. 3.14 (c). As the Fig. 3.14 (c) shows, the optimal parameters are the thickness of grating equal to 100 *nm*, and the thickness of layer equal to 55 *nm*. The angular and the wavelength dependence for reflectivity at these settings are also shown in Fig. 3.14 (c). At the optimized thickness, the angular dependence for the binary grating structure is better than single-layer AR coating, with a wider window to reach low reflectivity. However, no significant improvement compared with double-layer ARC is seen, as shown in Fig. 3.13. First, they all have a wide wavelength window for low reflectivity, from 440 *nm* to 700 *nm*. Second, the minimum reflection coefficients of the structure are nearly the same, because the effective result of the grating region is similar to that of MgF_2 in a double-layer. But the binary grating uses just one coating material, and can adjust the refractive index by ridge ratio, which can solve the problem of the availability to materials with the right indices.

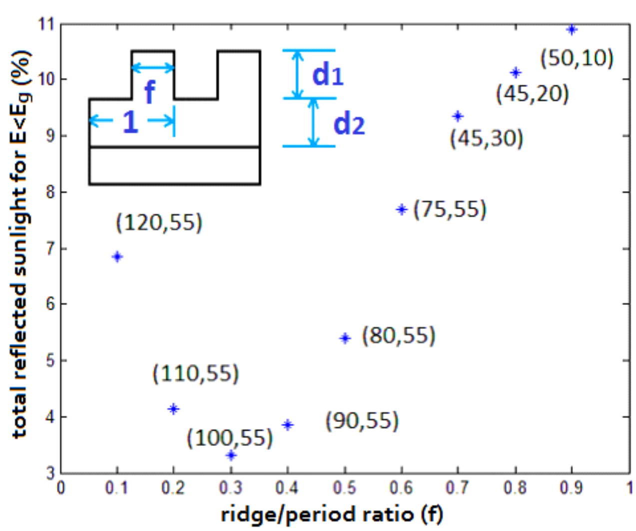

(a)

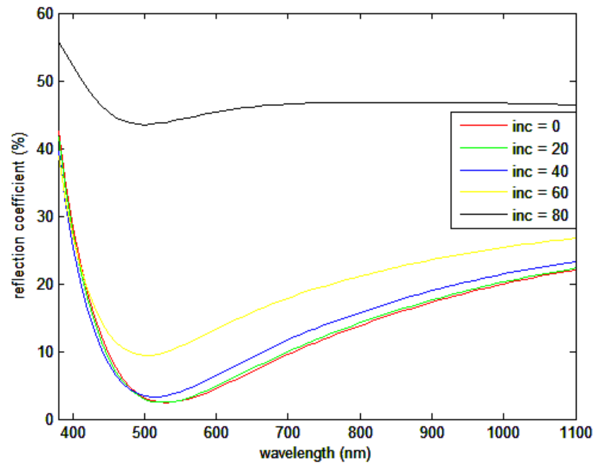

(b)

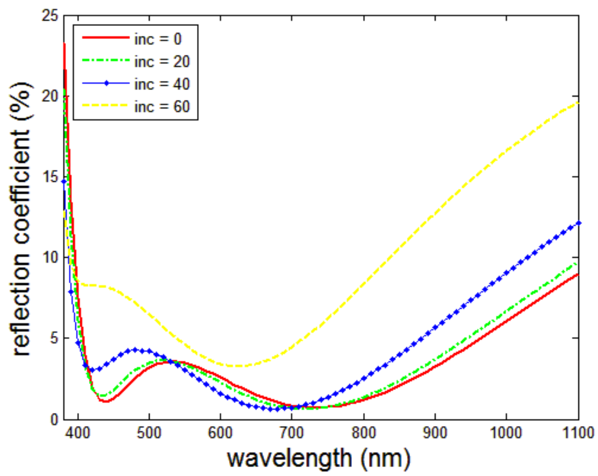

(c)

Fig. 3.14 Variation of reflectivity with various optimized parameters for ZnS binary grating structure.

(a) Minimum optimized total reflectivity vs. groove ratio for binary grating structure. Numbers in bracket near each point represent the corresponding thicknesses for grating d_1 and flat layer d_2.

(b) Angular dependence for single-layer ZnS on c-Si (100) at optimized thickness 56 *nm*

(c) Angular dependence for ZnS binary grating with optimized parameters

The average reflectivity of 5% still did not satisfy our expectations, so we will continue to look for more complicated structures. From the analysis studied in binary grating, the continuity of refractive index plays a significant role in reducing reflection coefficient. Hence, dielectric textured materials with a continuous grating of refractive index should be studied.

3.3.2 1D binary grating with a triangular cross section

From the analysis of binary grating, we find that if the refractive index of antireflection structure increases its continuity from ambient to substrate, the reflection coefficient would decrease. So why not make the structure even more continuous? Hence 1D grating with triangle cross section is studied, as shown in Fig. 3.15. If the triangle structure, whose height is *H,* is sliced into *M* layers, then the thickness for each layer is expressed as equation (3.74), and the distance from the center of the m^{th} layer to the top is expressed as equation (3.75). The refractive index for the m^{th} layer can be written as equation (3.76), where f_m is the ratio of dielectric material occupied within the m^{th} layer.

$$d = \frac{H}{M} \tag{3.74}$$

$$h_m = (m - \frac{1}{2})d \tag{3.75}$$

$$n_m = n_{ambient} \cdot (1 - f_m) + n_s \cdot f_m \tag{3.76}$$

$$f_m = \frac{h_m}{H} \cdot \frac{a}{T} = \frac{a}{MT}\left(m - \frac{1}{2}\right) \tag{3.77}$$

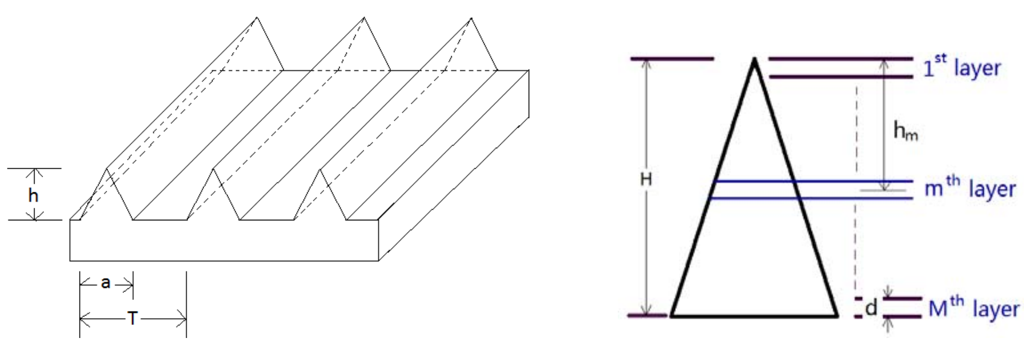

Fig. 3.15 Schematic of 1D grating with triangular cross section

To minimize the refractive index variance, one can make the AR material to be made out of the substrate itself; and set the texturing to continuously grade till the planar part. 1D grating with triangular cross section (Fig. 3.15) may act close to an ideal ARC; since the effective refractive index smoothly varies from the air to the substrate; which helps in minimization of reflection [3]. The next process is to figure out how the height would influence the integrated reflectivity. Take a Si solar cell as an example; when the occupation ratio *a/T* equals to 1, the refractive index can reach the most continuous condition. As Fig. 3.16 shows, as the height increases, the smaller the reflectivity gets, because larger height increases the continuity of refractive index.

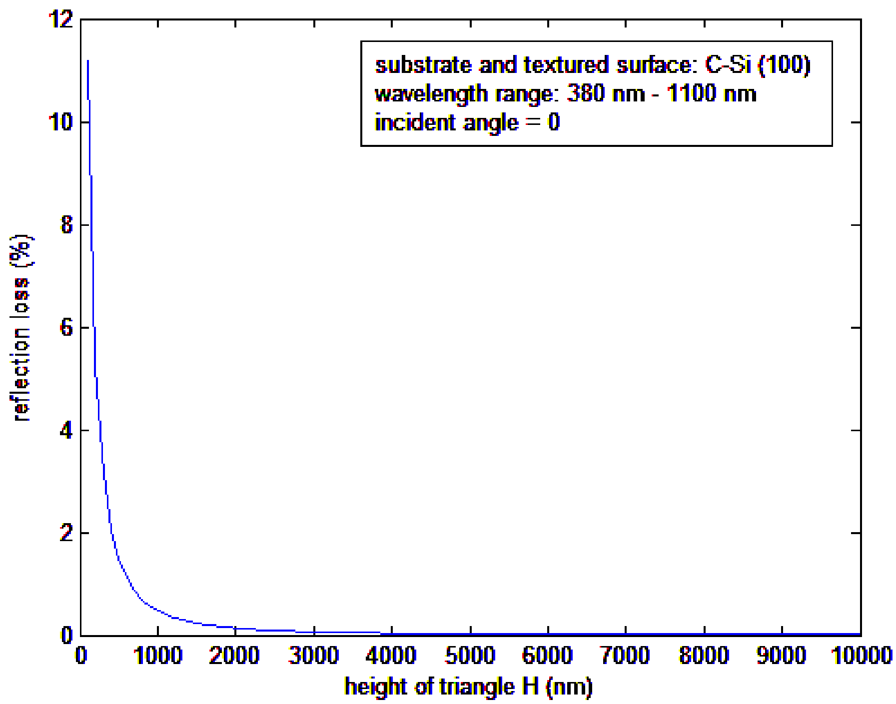

Fig. 3.16 Reflectivity of 1D grating with triangle cross section versus the height of ridge

---

[3] Here it is necessary to emphasize that transfer-matrix method is only suitable for dielectric material. For instance for metal produced with Fig. 3.15's structure, the average refractive index could vary continuously from air to bulk metal; but metal cannot transmit light, hence can't be used as a AR material.

This 1D grating with a triangle cross section is nearly ideal AR texture. It can make the reflectivity shrink to much lower than 1%, even for a whole spectrum from 380 *nm* to 1100 *nm*; when the height of triangle is above 800 *nm*, which indicates that over a large range of height, we can always get a low reflectivity. Next, the angular tolerance property of this structure is looked into. Setting the height to be 6 μm and analyzing the angular dependence of this 1D triangle grating, we can define the wavelength dependence and angular dependence for both TE and TM mode in Fig. 3.17.

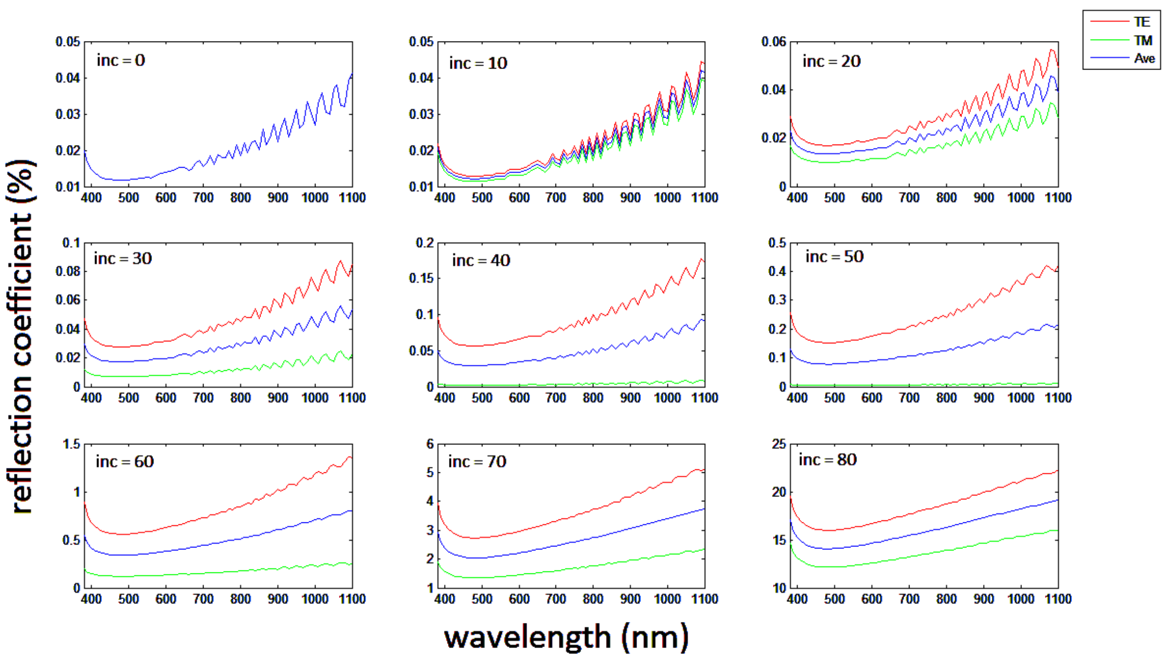

Fig. 3.17 Angular and wavelength dependence for reflectivity at H = 6000 *nm*

Three main indications can be concluded from Fig. 3.17. First, as incident angle increases, the reflection coefficient increases sharply; however, even at incident angle of 80^{o}, the reflectivity is still below 20%. For binary grating or double-layer structure, its average over all wavelengths, as shown is Fig. 3.14, reflection is around 40%. Second, the TM polarization, at any incident angle (despite normal light) and at any wavelength, produces lower reflectivity than TE polarization. Third, as the incident angle increases, the reflectivity for TE polarization keeps on increasing, but TM polarization is not. Comparing inc = 20^o with inc = 30^o and inc = 40^o, we find at inc = 20^o TM polarization has a larger reflectivity than the other two cases.

For a specific case with the height of the grating h=6μm, we could find the integrated energy loss dependence on incident angle in Fig. 3.18. The energy loss is below 0.5% even at 60^o incident angle. However, this application is not implementable for III-V solar cell. Firstly, the large area at the front surface increases the recombination velocity. Secondly, due to wavelength scale base for the structure, the scattering effect varies the light path length, leading to a challenge in optimizing the thicknesses of sub-cells. Thirdly, the micro-scale height of the texturing increases absorption.

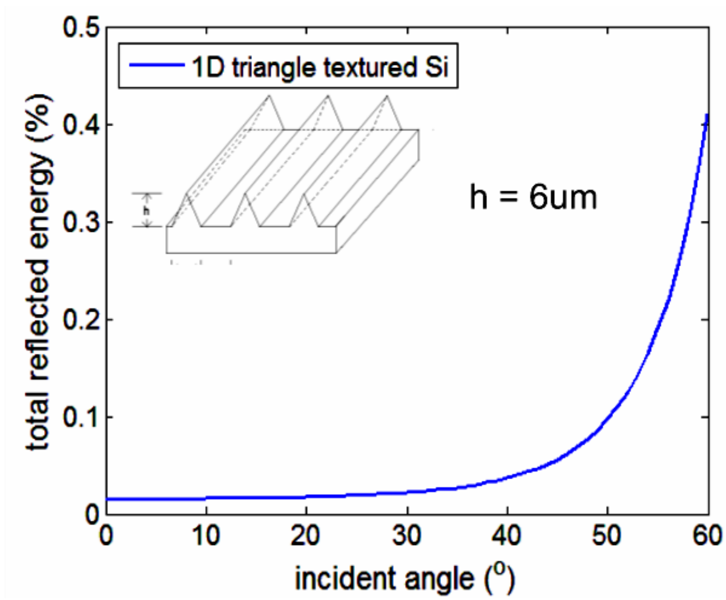

Fig. 3.18 Reflection of 1D grating with triangle cross section

From the Fig. 3.17, it can be seen that as the height of the triangle increases, (resulting in a smaller gradient in the refractive index), the integrated reflectivity decreases. Compared with 2D pyramid or needle-like texture, the gradient is larger if they are of the same height as 1D triangle grating. Consequently, to get the same antireflection result, the height of the 2D structure ought to be larger. This approach, then, is more applicable for Si solar cell, with low absorption coefficient, instead of III-V solar cells.

In the literature, it is shown that silicon nanotips [54] and syringe-like Si nano-wire [55] experimentally could get the reflectivity as low as 1%; but only when the height of structure is in the micron scale, which matches with this simulation prediction. The optimized parameter exceeds low profile limit, not fitting in the thin-film method modeling requirements. So the thin-film method cannot give a precise evaluation, only a rough estimate. The micro scale direct texturing is hindered in III-V multi-junction solar cells. All these facts demand antireflection dielectric structure on III-V solar cells. Later, we will discuss its application to specific solar materials; with focus on wavelength and angular dependence.

3.3.3 2D hemisphere grating (2D moth eye grating)

After studying two types of 1D gratings, which neither outperform the traditional bi-layer approach nor are applicable to thin film III-V materials, we are going to look for other structures, starting from 2D hemisphere grating and the month eye grating inspired from butterfly species. As the Fig. 3.19 shows, the hemisphere with radius R is sliced into M layers. If the number of layers is large enough, so that the m^{th} layer in the middle can be approximated as a cylinder, whose radius is given by equation (3.78), and thickness is given by equation (3.79), then the distance from the center of cylinder to the bottom is shown as equation (3.80). The ratio occupied by the dielectric material with each period can be written as equation (3.81). The refractive index for the grating area is shown as equation (3.82), indicating that the period of the binary grating will not affect the final result.

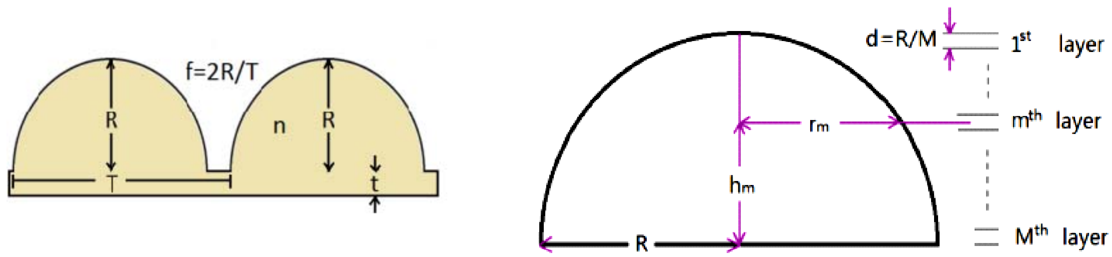

Fig. 3.19 Structure and parameter notation for 2D hemisphere grating

$$r_m = \sqrt{R^2 - {h_m}^2} \tag{3.78}$$

$$d = R/M \tag{3.79}$$

$$h_m = \left(M - m + \frac{1}{2} \right) d \tag{3.80}$$

$$f = \frac{\pi {r_m}^2}{\pi R^2} = \left(\frac{r_m}{R} \right)^2 \tag{3.81}$$

$$n_g = \left({n_{ambinent}}^2 \cdot (1-f) + {n_{AR}}^2 \cdot f \right)^{1/2} \tag{3.82}$$

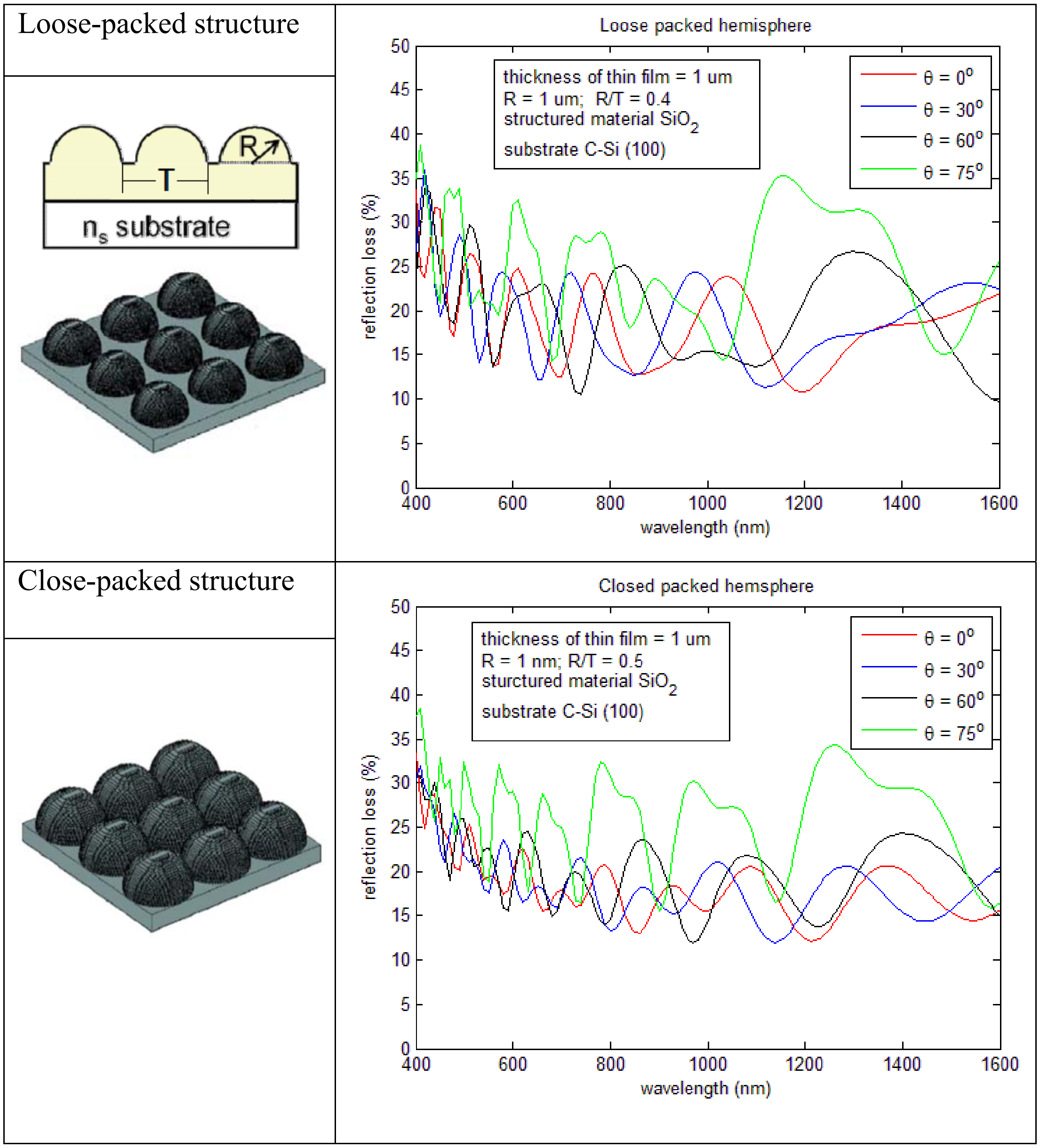

Fig. 3.20 2D hemisphere textured surface reflectivity versus wavelength

Comparing the transfer matrix result with RCWA simulation [56], beside the periodic property and divergence between incident angle as discussed in pyramid texturing, we found there is another discrepancy. We can see from RCWA's result, the reflectivity with incident angle = 30^o is even smaller than that of incident angle = 0^o, which is not quite convincing. Again, transfer matrix still can get a good approximation at micro scale for hemisphere structure, which gives us confidence in transfer matrix to optimize 2D AR textures.

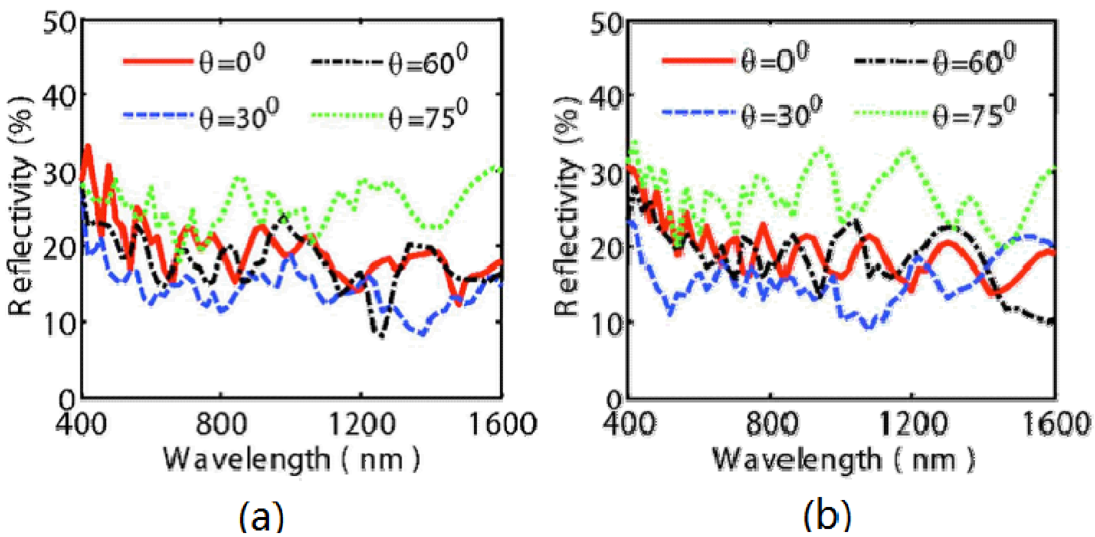

Fig. 3.21 Reflectivity simulation of hemisphere grating from the literature: (a) loose-packed structure, (b) close-packed structure [ref. 56]

In a typical triple junction solar cell, GaInP, GaAs and Ge are used for each junction from top to bottom. Generally, 15-20 *nm* Al-rich AlInGaP or Al-rich AlGaAs are used as low surface recombination velocity window layers. Because the refractive indices for AlGaInP and AlGaAs are close to each other; here $Al_{0.8}Ga_{0.2}As$ is considered as the top semiconductor layer beneath the antireflective structure. The variables for hemisphere structure include the radius R, ratio of ridge f, and the coating material's refractive index n_{AR}. By optimizing the texturing, we found that when the ideal refractive index of antireflection material is 2.4, the ideal ratio of groove f is 0.6. The minimum fraction of the reflected photons from 380 *nm* to 2000 *nm* would occur, in materials like TiO_2 and ZnS.

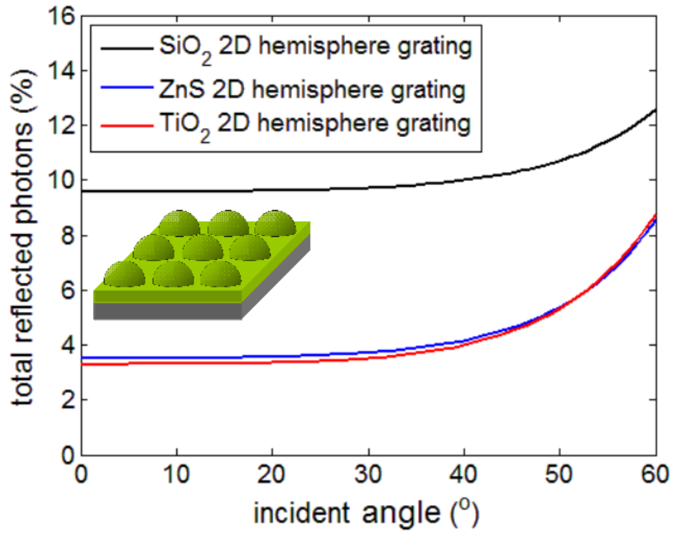

Fig. 3.22 Angular dependent photon losses for 2D hemisphere grating made with various materials for an AM1.5G incident spectrum over the 0.38-2 micron range

Further analysis of the parameters allowed us to optimize each material for normal light. Although refractive index of ZnS and TiO_2 are not quite the same [57], they can lead to similar angular and wavelength dependence as shown in Fig. 3.22. The reflectivity is tolerant of incident angle, around 3.3% when it is less than 30^o. As the angle increases to 60^o, the reflectivity reaches up to 8.8%. Since SiO_2 is widely used as ARC (and plasmonic) materials, it has also been included in our simulations; yet as shown here, SiO_2 performs poorly in comparison with materials having higher indices of refraction.

3.3.4 2D pyramid grating (2D cone grating)

With the study of 2D moth-eye structure, we would like to know if it is possible to further reduce reflection loss. So we will now look into the AR properties of a 2D pyramid grating, with the same process of optimizing the material and optimizing the geometric parameters.

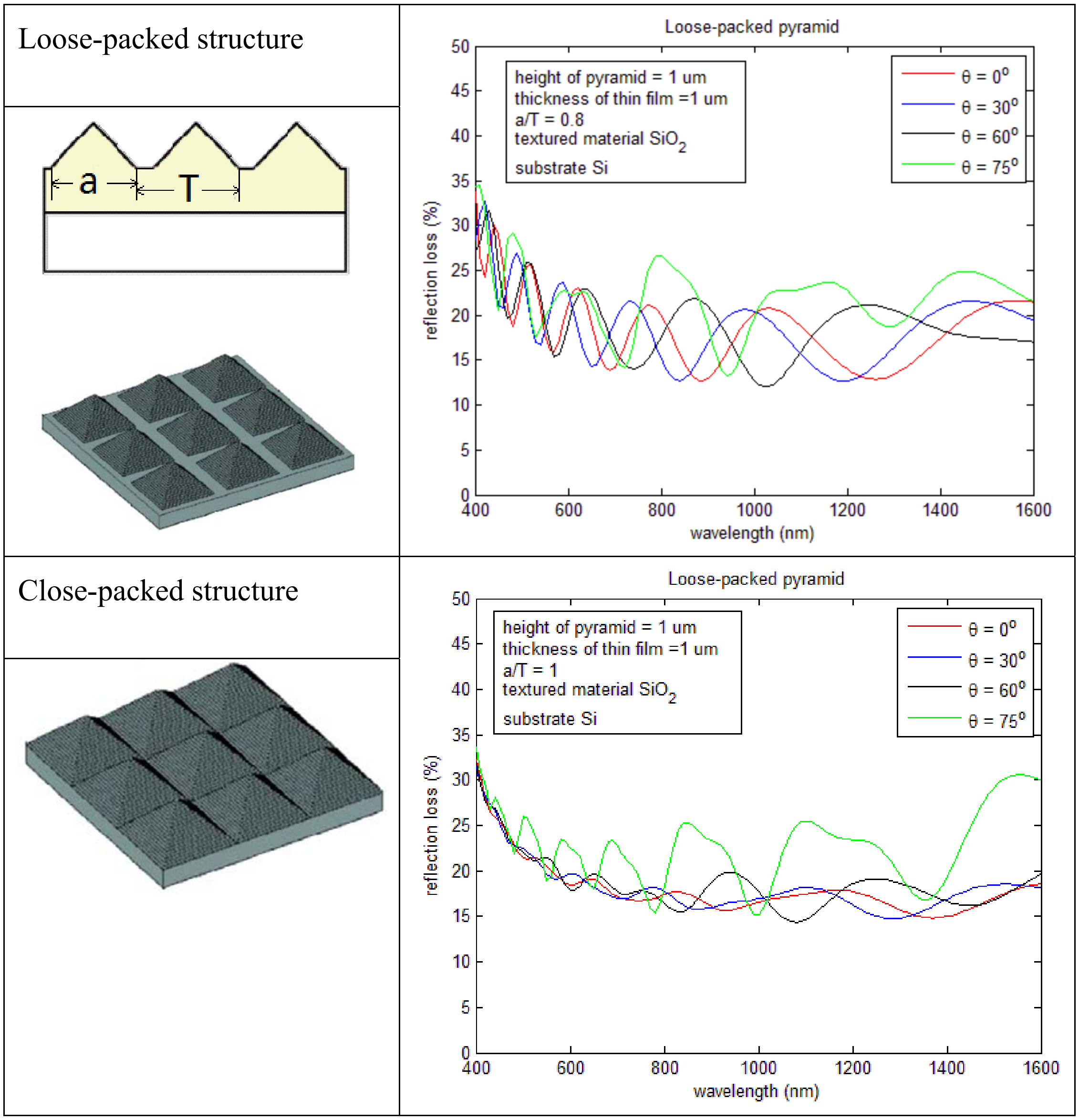

Fig. 3.23 2D pyramid textured surface reflectivity versus wavelength with angular dependence

Similar to the analysis in 1D grating with triangular cross section, the ratio for 2D pyramid is just the square of the right side of equation (4.5). To compare with simulation in literature, all the parameters are set to be the same, (and for better comparison, the linear average of electric permittivity [58] is taken; as the model of RCWA suggests, instead of the linear average of refractive index), results are shown in Fig. 3.23.

Comparing with the result from RCWA in the literature [59], above results are roughly in the same reflectivity region, oscillating among identical values. It also obeys the general law that as incident angle increases, reflectivity increases. However, this result from the transfer matrix has more explicit periodic property; and the difference from different incident angle is not as obvious as that from RCWA, as shown in Fig. 3.23.

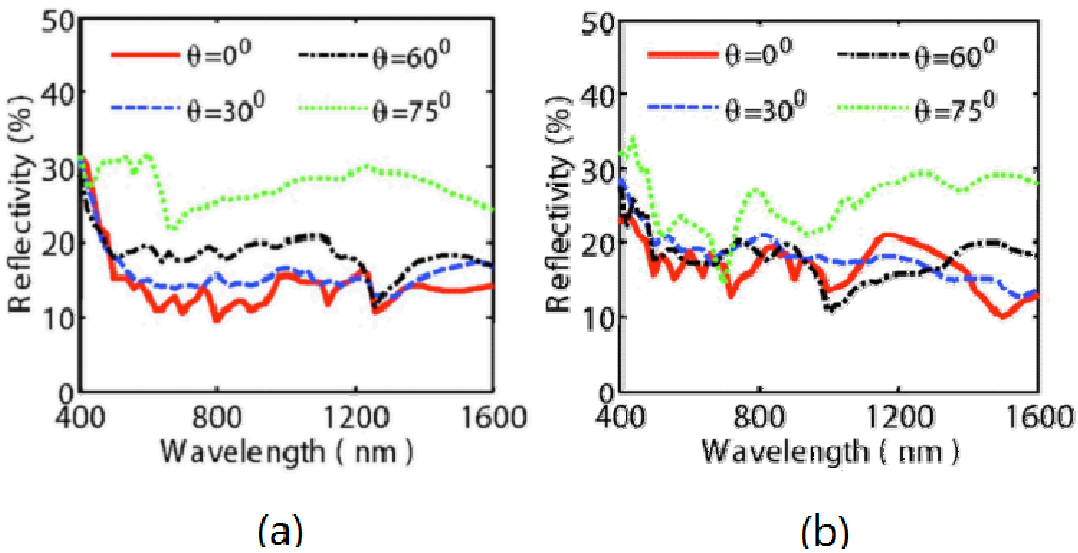

Fig. 3.24 Reflectivity simulation of pyramid grating from the literature: (a) loose-packed structure, (b) close-packed structure [ref. 56]

The main reason could be the limitation of the transfer matrix that is dealing each layer as independent and uniform dielectric material, which requires periodic textured surface to be in order of sub-wavelength range. However, the parameters used in literature are at micro scale, which is out of the transfer matrix's application. However, RCWA is based on Fourier transform; which takes into account multi-reflections between periodic textures. Despite ignoring multi-reflections between periodic textured surfaces, transfer matrix can still create a good approximation even for micro scale pyramid structure. This is due to the fact that effect of multi-reflections is relatively small.

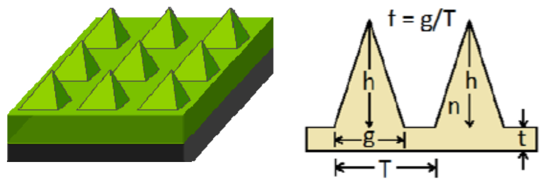

Fig. 3.25 Structure of 2D pyramid grating with parameter notation

Similar to the optimization in the hemispherical array structure, the minimum photon-loss occurs when the ridge ratio is equal to 0.8, and the AR's refractive index is equal to 2.6. The closest materials to this index are SiC and ZnS. A more optimal matching of *h, t* and *f* can be made with ZnS dispersion data. We find that for efficiently coupling the light in a wide spectral range (380-2000 *nm*), the optimal pyramid AR structure for normal light, with an integrated photon loss of 1.83%, occurs when its pyramid height is 375 *nm*, the thickness of planar film is 65 *nm*, and the ratio of ridge is 0.8.

Along with a set of accurate geometric parameters for the optimized structure, we also want to know how tolerant this 2D pyramid grating is to fabrication errors, since it is challenging to make the structures exactly the same as a simulation. So we are now going to check the fabrication tolerance of this 2D pyramid texture. Effect on reflectivity with variation of the base/period ratio, the pyramid height and the thickness of planar film is shown in Fig. 3.26. It is shown that the pyramid grating has fabrication tolerance, which is around 100 *nm* in height and 15 *nm* in thickness. The *f* ratio of the pyramid base versus the pitch is set at 0.8.

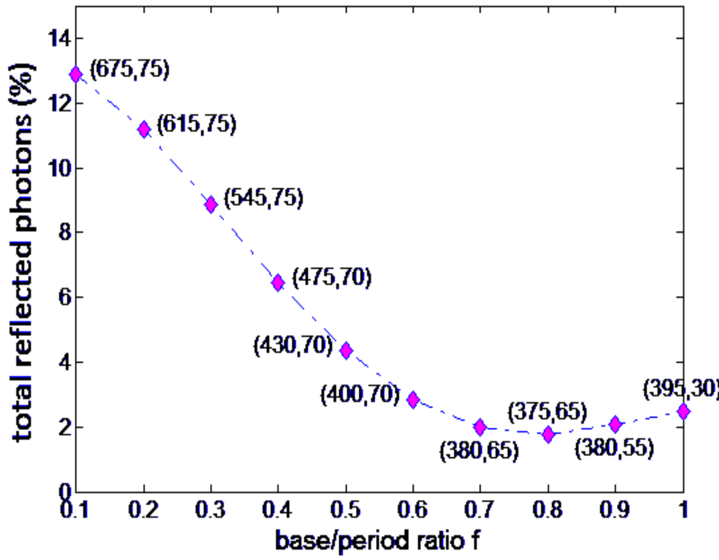

(a)

Reflected photon loss (%)

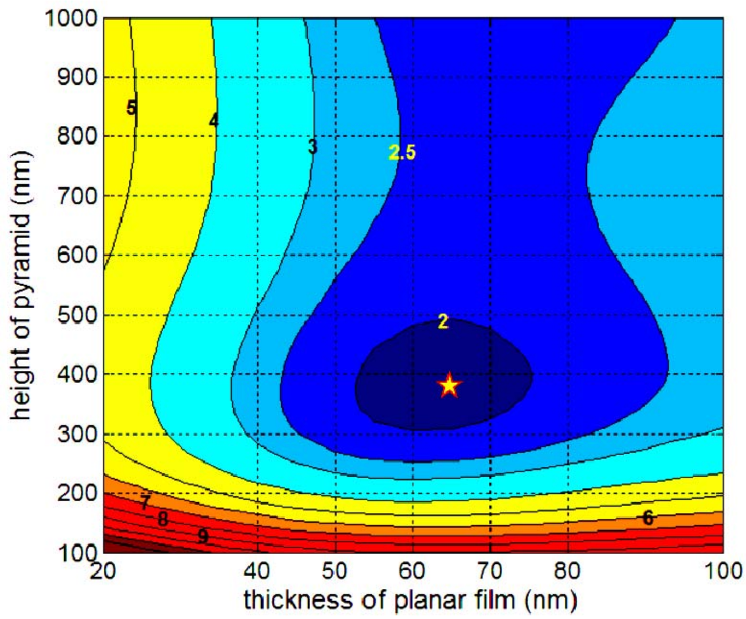

(b)

Fig. 3.26 Optimization of ZnS 2D pyramid grating from 380 *nm* to 2000 *nm* (incident AM1.5G)

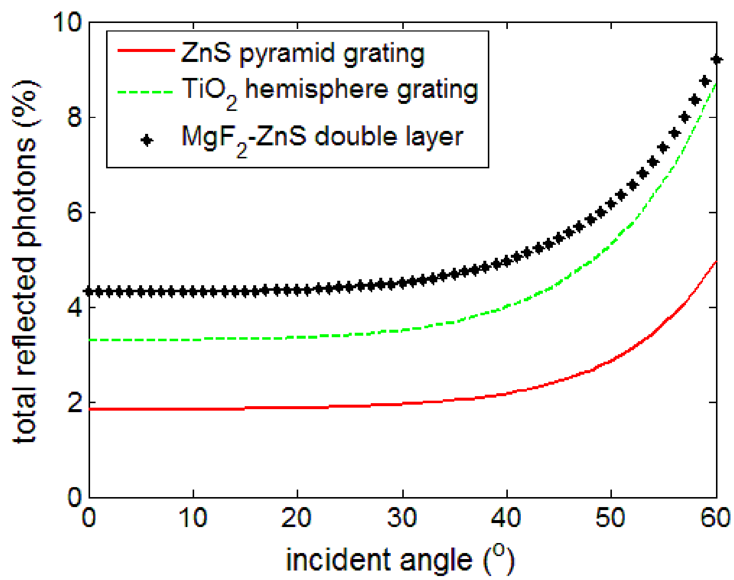

Fig. 3.27 Photon loss comparison for proposed structures with conventional double-layer ARC

From this geometric property, we can get the angular dependence of the ZnS pyramid antireflection texture; as shown in Fig. 3.27. Hence, we can see that the optimized pyramid texture performs better, both over the spectrum range and over wider incidence angles. When the incident angle is less than 30^o, the photon loss is nearly independent of incident angle, (~1.8%), however, as the angle increases beyond 40^o, the photon loss increases sharply. As the angle increase to 60^o, the photon loss reaches nearly 5%. When compared with conventional double-layer ARC, and 2D hemisphere grating, 2D pyramid grating exhibits better antireflection and angular tolerance properties.

3.4 Angle of incidence/concentrator aperture tolerance results for MJ CPV application

Until now, all the optimizations have been presented by minimizing the total photon-loss in a 1-junction application, and it has been found that 2D pyramid texture has the best AR property. In this subchapter, we will first take into account the integrated photon loss in each sub-cell of a multi-junction device, which is essential for maintaining current matching for the multi-junction solar cell. Then, we will take into account the concentrator aperture to this multi-junction application by integrating the photon reflection over the incident angle. The importance of using concentrators for higher conversion efficiency was introduced earlier in chapter 2.4.

As demonstrated in the Fig. 3.28, by multiplying the reflectivity vs. wavelength over the number of photons vs. wavelength relation, the area under the integrated curve gives the number of photon loss, which indicates the current loss. The number of photon loss for single junction device such as Si solar cell can be directly determined by the area. And the number of photon loss for multi-junction devices is determined by the largest area among all the sections. That is to say, we need to minimize the maximum number of photon loss in all the sub-cells.

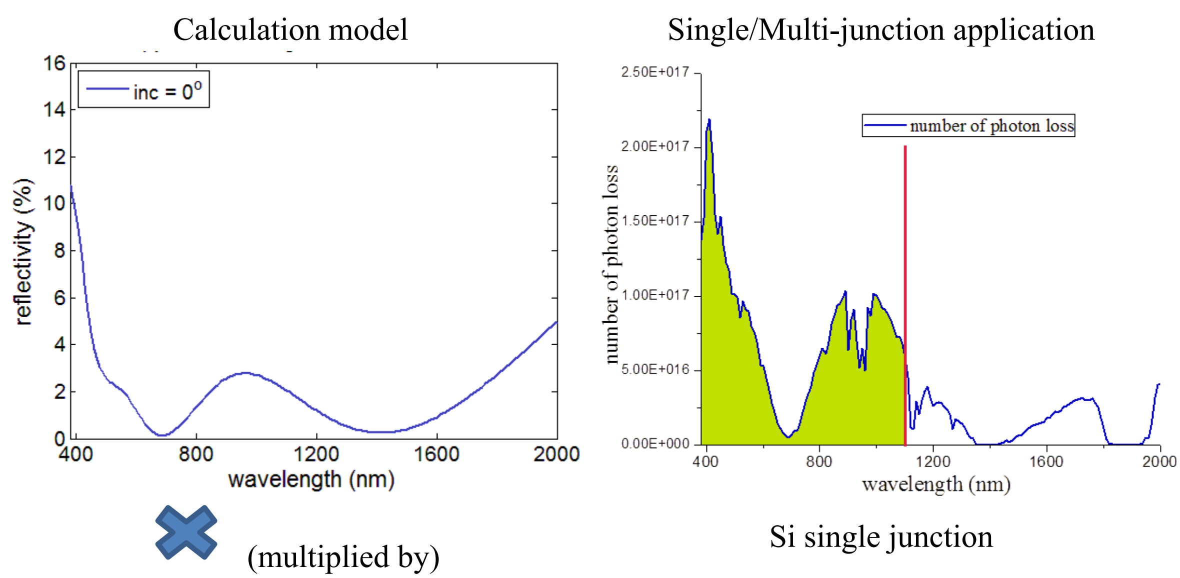

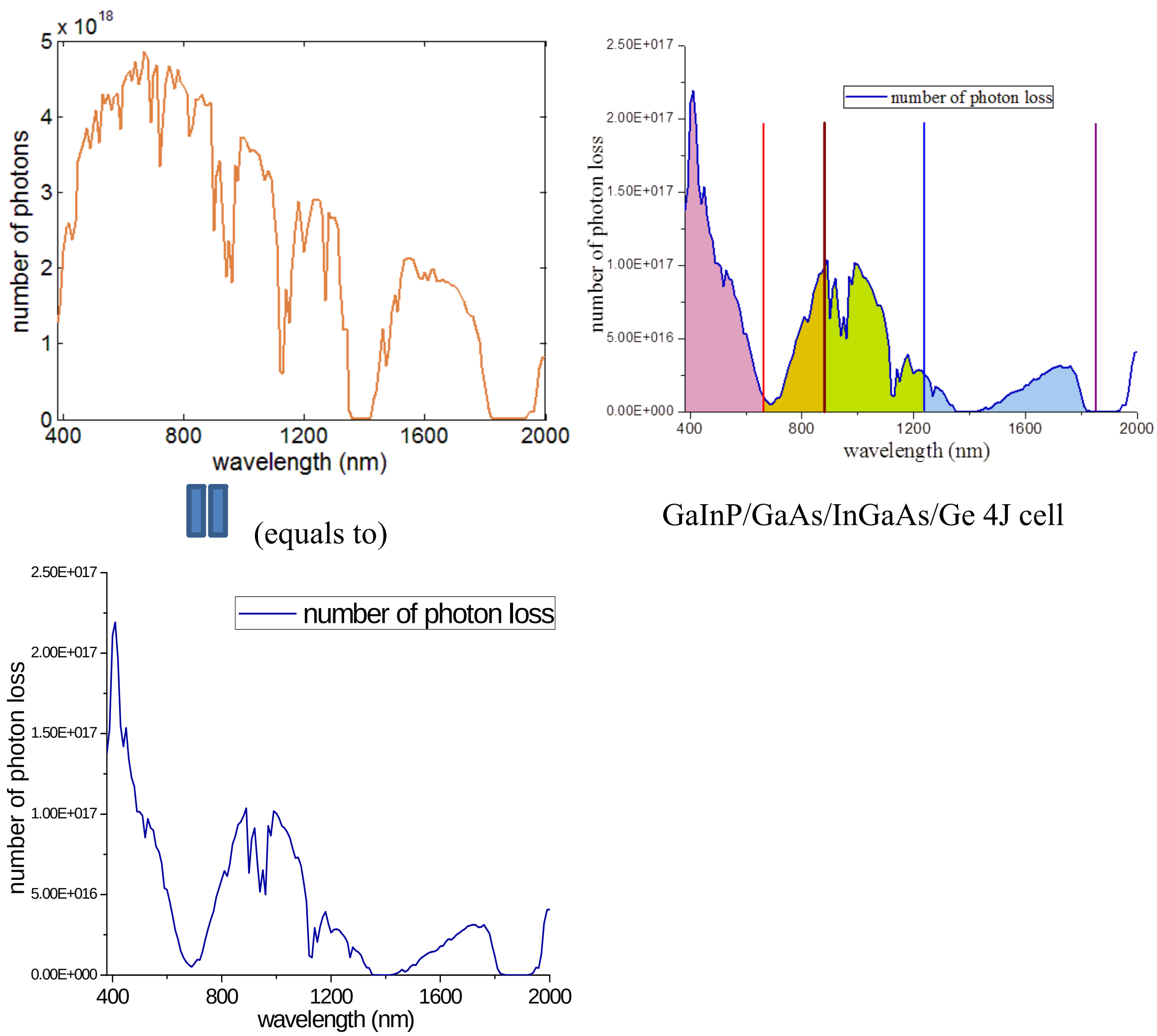

Fig. 3.28 Examples of calculating photon-loss in single and multi-junction solar cell devices

As shown in Fig. 3.29, under normal sunlight incidence, for a GaInP/ GaAs/ Ge multi-junction solar cell, the main current loss caused by AR grating is associated to the GaInP sub-cell (these devices being inherently current rich for Ge sub-cell). In this case the minimum current loss happens when the base/period ratio is 0.8, the height of pyramid is 330 *nm*, and the thickness of planar film is 65 *nm*. Similar optimization can be done for operation under concentration, by integrating photon loss over the entire incidence cone. Hence, the geometric parameters for the gratings can be different from those under normal light. Gratings need to be specifically designed for various concentrators and solar cell devices. The current loss in each subcell resulting from AR structure is shown in equation (3.83).

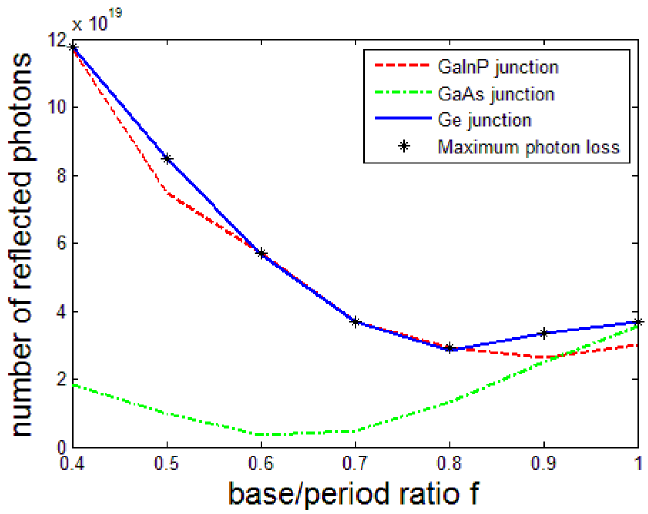

Fig. 3.29 AR grating causing photon loss in each junction for a GaInP/GaAs/Ge multi-junction solar cell under AM1.5G illumination

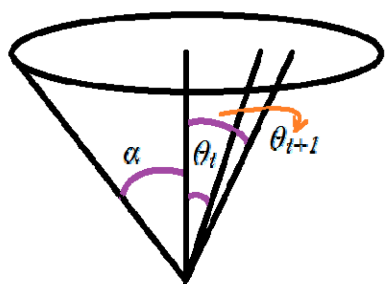

Fig. 3.30 Notations of concentrator's light cone

As HCPV (high concentration photovoltaic) are usually used in III-V material systems, there exist different types of concentrators which reach high concentration value. For example, concave mirrors, convex lens, and Fresnel lens. Despite various installation methods, the concentrator-solar cell device relation can be simplified as Fig. 3.30, which shows the schematic of a concentrator with the acceptance angle of α, and the notations used in eqn. (3.83). As shown in eqn. (3.83), the concentration factor has no effect on the total current loss.

$$I_u = q\frac{\sum_{i=1}^{m-1}\pi\left(\tan^2\theta_{i+1}-\tan^2\theta_i\right)\left(N_{u,i}+N_{u,i+1}\right)/2}{\pi\tan^2\alpha} \tag{3.83}$$

where, u is the index or subcell (varying from 1 to the number of junction in multi-junction devices),

q is the electron charge,

i is the order of annulus from the center to the outer edge of concentrator.

Assume the concentrator was divided into m annuli, $\theta_m = \alpha$ is concentrator's acceptance angle. $N_{u,i}$ is the integrated photon loss at i^{th} annulus over the u^{th} subcell's working spectrum.

Compared with parameters like the base planar thickness and the occupation ratio; it demonstrated that the height of pyramid is more sensitive to the light cone's acceptance angle. Fig. 3.31 illustrates the results for 2 common triple-junction (3J) devices and a 4-junction device. When operating in conjunction with imaging concentrators (*i.e.*, Fresnel or parabolic), at high acceptance angle (~60^o), for an optimal dielectric sub-wavelength texturing, enables current losses for these devices (optimized for minimum photon loss conditions), to be less than 2.2%, 3J-LM GaInP(1.87 *eV*) / GaAs(1.42 *eV*) / Ge(0.67 *eV*), 2.7% for MM GaInP / GaAs / InGaAs(1.0 *eV*), and 3.8% for 4J hypothetical GaInP/ GaAs / InGaAs / Ge solar cell.

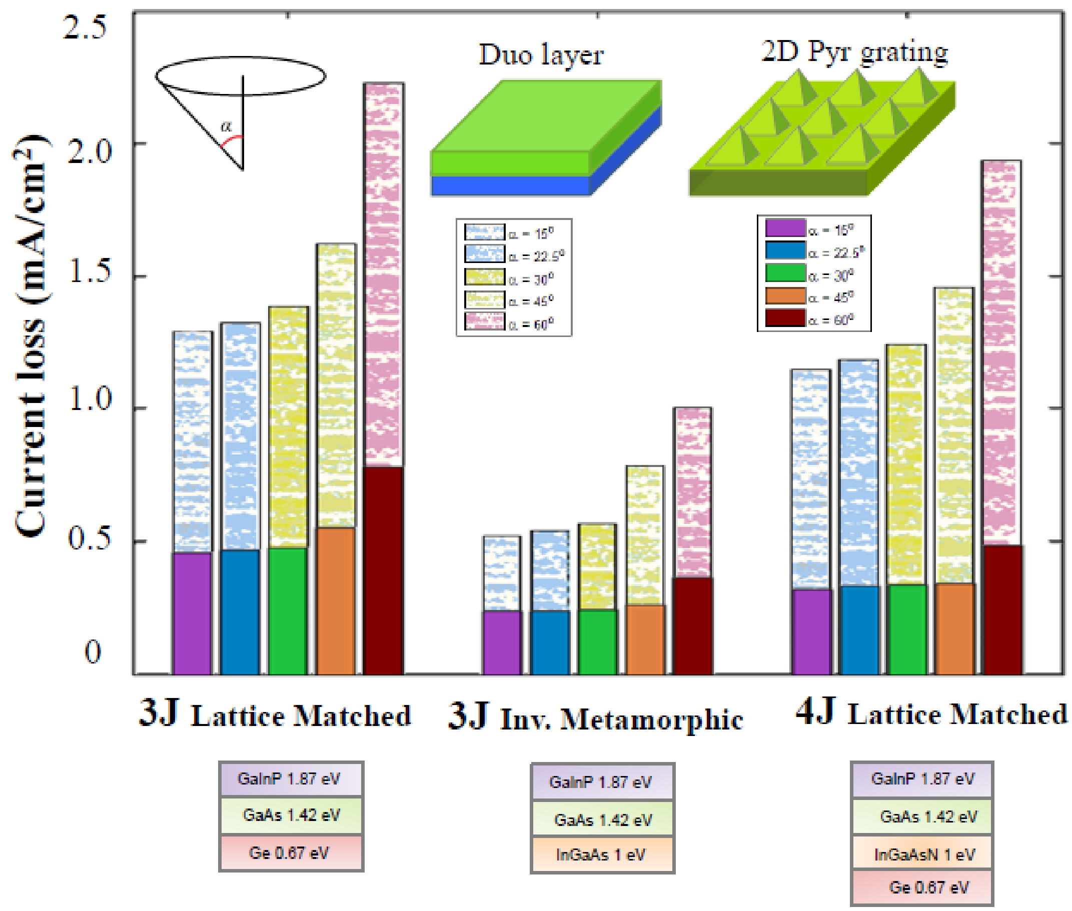

Fig. 3.31 Comparison of current loss (between duo layer (crayon) and 2D pyramid grating (solid color) on multi-junction devices), as a function of angle of focusing cone, for various multi-junction devices

3.5 Ray optics for back reflector

After studying the front surface anti-reflection property, we are now going to look into the optical behavior at the back surface in order to see how the texture affects the light path, further increasing absorption within the device. In this application, the texture is no longer subwavelength in scale for the purpose of gradually changing the index profile; however, it is in wavelength scale in order to create diffused and scattered rays. And ray optics is generally used for analyzing such micrometer size gratings.

Ray is an idealized assumption of light that uses approximate solutions to Maxwell's equations, not describing interference or diffraction phenomena, which requires the objects propagated through or around have much greater dimension that of the light's wavelength. And this approach can be used geometrically for back reflector.

3.5.1 Lambertian surface

If the back reflector can be considered as Lambertian surface [60], which follows Lambert's emission law that radiant intensity observed from an ideal diffusely reflecting surface radiator is proportional to the cosine of the angle between the direction of the incident light and the surface normal, the effective light path can be calculated [61] taking into account of multiple refection within medium and total internal reflection beyond its critical angle. However, this type of surface only exists in hypothesis. Commercially, Lambertian surface is used in integral sphere integrated reflectivity measurement, yet only within certain wavelength region. Because the ideal totally random-textured surface doesn't exist, and the ideal reflector doesn't exist for the whole spectrum, integrated sphere would be specifically labelled which spectrum they are suitable to work with. So blazed grating will be discussed next since they are more achievable in experiments.

3.5.2 Blazed grating

A blazed grating [62] is a special diffraction grating that is optimized to achieve maximum grating efficiency in a given diffraction order, generally not the zeroth order, so that the maximum optical power is concentrated in the desired diffraction order with the residual power in the other orders minimized. But the challenge is that this condition can only exactly be achieved for single wavelength, and specific diffraction order, while the goal of this work is to achieve long light path for a wide spectrum and all the orders generating internal total reflection. And if the long effective light path for the broad spectrum cannot be achieved, the increase of light path close to QWs' band-gap would be preferred. Hence the grating texture would be studied from a single wavelength at QW's band-gap.

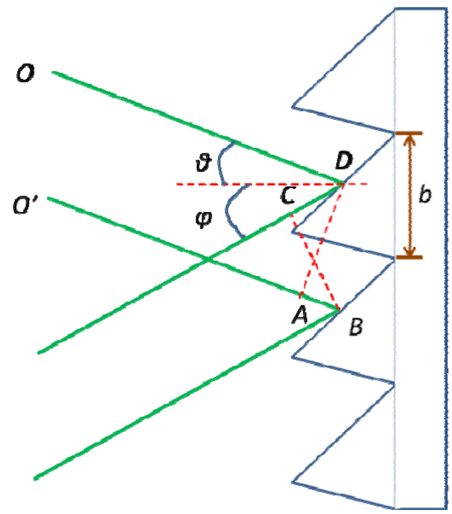

Fig. 3.32 Scheme of blazed grating

To describe blazed grating, two types of efficiency are usually used to represent how well it can diffract light. Absolute efficiency is the ratio of the energy of the diffracted light to the energy of the incident light, and the relative efficiency is the ratio of the energy of the diffracted light to the energy from the light reflected from a polished (mirror-like) surface. The diffracted light intensity can be derived and expressed in the following equations. The light path difference between beam *O* and *O'* is CD–AB, expressed in form of incident angle θ, diffracted angle φ and grating period b, CD-AB = $b(\sin\varphi-\sin\theta)$. If define half-phase difference between successive waves, $\alpha = kb(\sin\varphi-\sin\theta)/2$, the sum of reflected electric field from N facets is

$$\Sigma E = E_0e^{2i\alpha} + E_0e^{4i\alpha} + E_0e^{6i\alpha} + \ldots + E_0e^{2Ni\alpha}$$
$$= E_0e^{2i\alpha}\frac{1-e^{2Ni\alpha}}{1-e^{2i\alpha}} \tag{3.84}$$

Intensity $I = |\Sigma E|^2 = \Sigma E \bullet \Sigma E^*$

$$= E_0e^{2i\alpha}\frac{1-e^{2Ni\alpha}}{1-e^{2i\alpha}}E_0e^{-2i\alpha}\frac{1-e^{-2Ni\alpha}}{1-e^{-2i\alpha}}$$

$$= E_0{}^2\frac{1-e^{2Ni\alpha}-e^{-2Ni\alpha}+1}{1-e^{2i\alpha}-e^{-2i\alpha}+1}$$

$$= E_0{}^2\frac{2-2\cos N\alpha}{2-2\cos\alpha} = E_0{}^2\frac{\sin^2 N\alpha}{\sin^2\alpha} \tag{3.85}$$

where k is the wave-vector in semiconductor, which can be simply converted by multiplying refractive index n to the wave-vector k_o in vacuum, since in this case the wavelength in semiconductor λ is a portion of that in vacuum λ_o following the relation $\lambda = \lambda_o/n$

Because in the application of increasing the light path in QWs region, rather than maximum diffraction intensity at certain order with specific wavelength, we need to maximum all the diffraction intensity whose diffraction are larger than the critical angle so that the largest amount of light won't escape from the semiconductor-air interface. Therefore, the integrated relative efficiency at 1200 *nm* over the diffraction angle 15^o to 90^o is chosen as the optimization parameter. A MATLAB program based on equation (3.85) is used to calculate and optimize integrated relative efficiency with several geometric parameters in optimization loops. Fig. 3.33 gives a simple example of a 1D blazed grating simulation of integrated relative efficiency from 15^o to 90^o with fixed geometric parameters, such as 2 μm grating feature (as ‘b’ in the program defined in Fig. 3.32) and 400 μm beam size.

Here, the key implicit assumption that I made is that the reflection from a flat (mirror-like) surface is equal to the sum of the all the diffraction order’s intensity, which is valid if the surface doesn’t transmit or absorb any light energy.

```
clear;clc
% when N is large, approaching to a constant value
% sum(I) should always be smaller than sum(I_n)

inc = 0; inc = inc/180*pi;
Out = 15:1:89; Out = Out./180.*pi;
b = 2; % um grating size
N = 400/b;
wavelength = 1.2; % um
n = 3.5;
k = 2*pi./wavelength*n;

for m = 1:length(Out)
    out = Out(m);
    a = k*b/2*(sin(out)-sin(inc));
    I(m) = sin(N*a)/sin(a); I(m) = I(m)^2;
end

Out_n = 1:1:89; Out_n = Out_n./180.*pi;
for m = 1:length(Out_n)
    out = Out_n(m);
    a = k*b/2*(sin(out)-sin(inc));
    I_n(m) = sin(N*a)/sin(a); I_n(m) = I_n(m)^2;
end

sum(I)/sum(I_n)
plot(Out_n./pi*180,I_n./sum(I_n))
```

Fig. 3.33 A MATLAB program example of blazed grating to calculate relative efficiency with fixed parameters (without optimization loop)

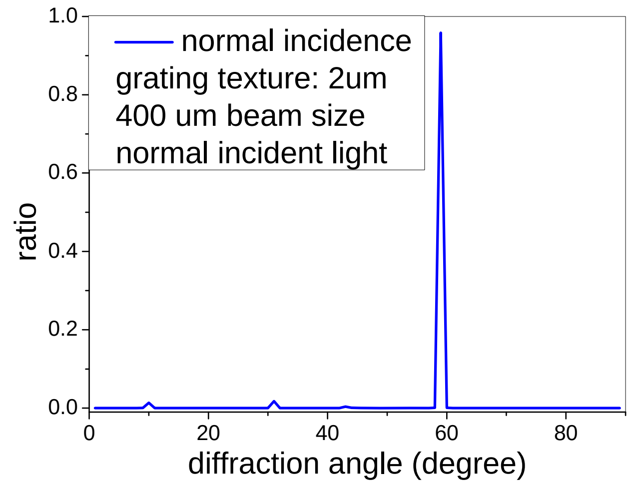

Fig. 3.34 Simulation result of relative efficiency corresponding to the program and parameters in Fig. 3.33

As presented in Fig. 3.34 that the main diffraction happens at 58°-59° diffraction angle when the grating has 2 μm profiles size and beam size is 400 μm. And 98.5% of the light is diffracted relative efficiency of diffraction angle larger than 15° which indicates a near perfect light trapping. And based on this grating design, we also interest in how the other wavelengths respond to the grating. It can be predicted that the diffraction pattern will be independent of the beam size when the beam size (or the grating size, whichever is smaller) reach certain large scale compared with grating's texture feature. And in this code, it indeed confirmed that at 2 μm texture size, when the beam size varies from 0.25 μm to any larger value, the dominating diffraction angle stays at 58°-59°, and as the beam size reduces, diffraction angle at 10°, 20 °, and 31° starts to play an important role.

When the incidence is set to equal to outgoing angle, simulation shows error due to zero dominator created singularity. Consider blazed grating has the property of low diffraction at the 0th order; outgoing angle is set from 1° to 90°.

3.6 Conclusion

This chapter examined three main simulation methods for calculated textured surface, describing their working principles. By comparing their pros and cons, we showed the suitability of the thin film method to model sub-wavelength texture's anti-reflection property and we implemented this method to evaluate optimal textures for single and multi-junction III-V devices, operating under high concentration. We showed that a carefully designed 2D sub-wavelength grating significantly reduces the photon losses and improves current matching issues, over those commonly encountered for planar double-layer ARCs. As the thin film method is based on dividing the complex structure into multi-layers, and treating each layer to be uniform, the choosing number of the slices is a critical factor for a more

Naturally, the more layers to be sliced, the more precise the result should be. We have found that when the thickness of the layer is equal to one tenth of the minimum wavelength is the critical point. Next, we are going to apply the technique to guide the experimental results in chapter 5. But first in chapter 4 we will present the implementation/optimization of the laser interference lithography for development of 2D gratings.

Chapter 4 Implementation of Laser Interference Lithography for Sub-wavelength Texturing

In this chapter, following a brief survey of prior art, we will discuss experimental setup and process optimization for the practical realization of sub-wavelength textured structure.

4.1 Introduction

As previously stated, antireflective coating (ARC) and texturing are widely studied to reduce the reflection loss, including the optimization of material and geometric morphology. Grated surface with continuously changing refractive index has been demonstrated to let the light gradually bend into substrates (*i.e.* solar cell devices), with reduced reflection loss, achieving greater harvesting absorption. Back reflectors have been developed from perfect mirror to a variety of textured mirror, to further increase the light path. This strategies can improve the efficiency and allow the development of much thinner devices; especially devices made of materials with poor minority carrier properties (*i.e.*, dilute nitride, and III-V/Si *etc.*), or devices that incorporate weak absorbers like multi-quantum wells (MQW) where thickening the absorber thickness may detrimentally affect the Voc [63]. Within the context of MQW-enhanced devices recently Inoue and collaborators[64] have demonstrated that using backside grooves with a dielectric interface could result in an effective optical path that is 5 times the actual thickness of the MQW layers, reaching over 50% EQE in the MQWs region.

Lambertian surface, which is known to have the most random texture, can theoretically raise the light path to $4n^2$ times that of the general plain mirror (~40x for a common III-V semiconductor). Even though Lambertian surface can be assumed in analysis for formulating purpose [65,66], it's a challenge, however, to fabricate ideal Lambertian texture, especially in a fast and low cost way.

In this work we have developed a method to overcome this challenge. The method uses laser interference lithography (LIL) combined with a stepper motor and sample rotation capability (0-90^o) to create 2D photoresist (PR) patterns (gratings pitch and shape) with a sub-wavelength resolution (here 55 *nm*) without the need for any masks. Subsequently we use a selective wet etchant to create a desired texture depth on GaAs-based substrates/solar cells. In this work we have limited our investigations to substrate dimensions of 3" (7.5 *cm*). However in principle the approach can easily be readily expanded to process 6 inch or even 12 inch wafers by controlling beam expander's size or adopting a step motor. This is a fast and low cost technique, which exposure and etching time together takes 5 *min*.

4.2 Literature research on enhancing light trapping from textured back side interface

Before going into details of experimental set-up and procedure, we are going to look into the impact of back side interface on solar cell performance. Scientists have studied both coherent and incoherent mirror to increase effective light path for higher absorption in ultra-thin solar cells for overcoming the weak sub-bandgap absorption of devices incorporating quantum dots (QDs) or quantum wells (QWs). Several publications experimentally demonstrated convincing results to validate the effect of both coherent and incoherent mirrors, which can respectively reach around 4 times and 10 times effective light path comparing with single light path in III-V quantum well working spectrum (1.0 *eV* ~1.4 *eV*). Theoretical simulation regarding the electric field within the QWs region is also analyzed by drift-diffusion model for further understand of how coherent mirror assists light coupling for harvested photon absorption, as seen in Fig. 4.1[67], the photon flux relative to the incident photon flux (with no ARC), as a function of depth in the solar cell is presented for 500 *nm*, 650 *nm*, and 800 *nm* for the 3 conditions of no back reflector, incoherent reflector as well as coherent reflector.

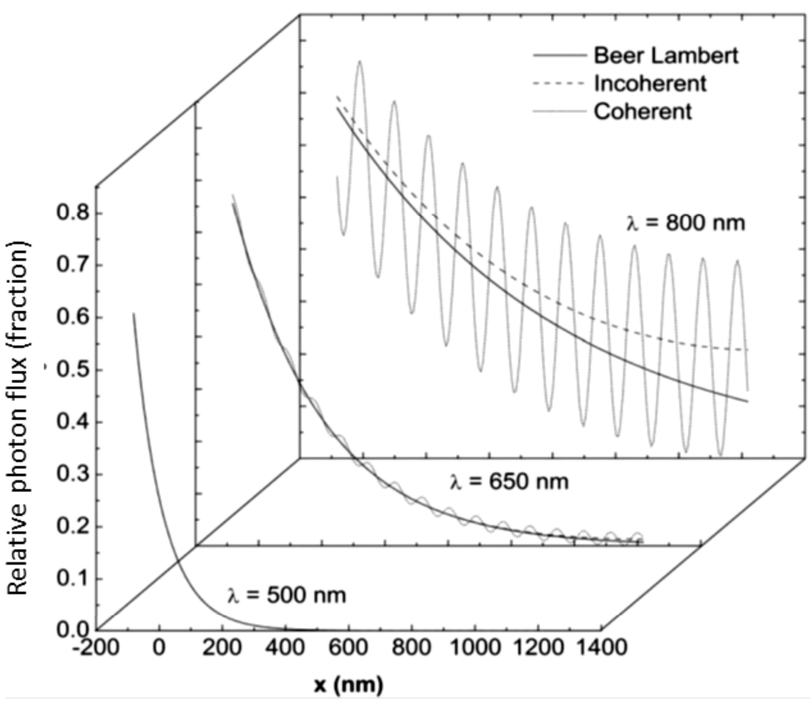

Fig. 4.1Relative photon flux in the solar cell for 800 *nm* wavelength light for the case of no back reflector, incoherent and coherent back reflections

As demonstrated in Fig. 4.2, both coherent and incoherent reflectors turn out to improve photon absorption comparing with no reflector situation resulting in similar 5-6% Jsc enhancement, and coherent reflector perform clearly visible fringes in external quantum efficiency (EQE) at long wavelength, due to interference between forward and reflected backward propagating fields.

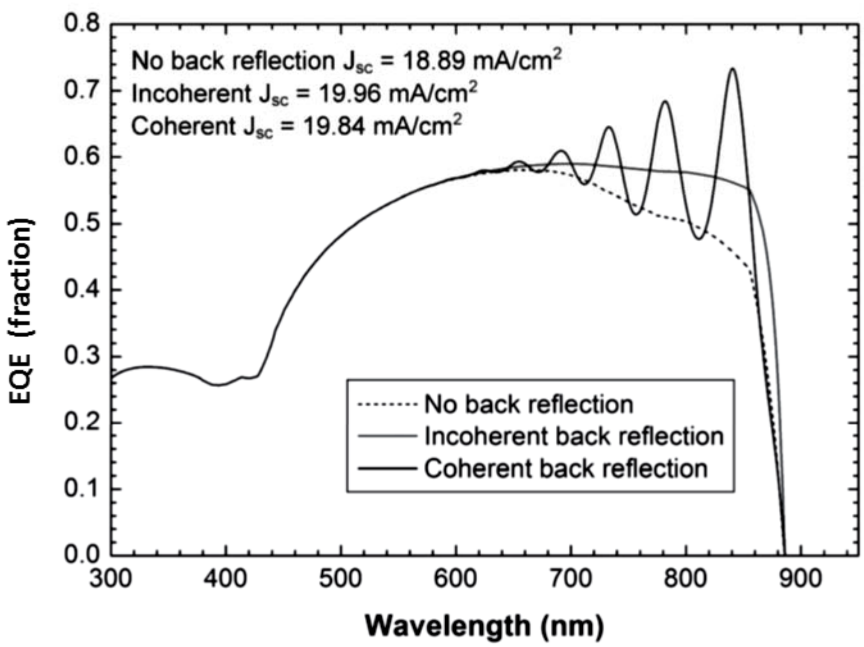

Fig. 4.2 External quantum efficiency calculated for the GaAs solar cell with no back reflector, incoherent reflection from an Au mirror and coherent reflection

Giving the complicacy of post growth processing of ultra-thin devices, it is not easy to texture both the front and back surfaces for near ideal transparency and Lambertian random grading. So the coming question is whether we can find a way to locate the QW at the spot of constructive interference to assist photon absorption without a textured reflector. Drift-diffusion model certainly is a powerful tool to optimize the design of solar cell devices, with all the practical parameters, however it demands heavy calculation which makes it hard to use for optimization purpose. Thin film methods, a simple and fast approach, designed to analyze optical behavior is perfect in this condition to find out where constructive interference happens. But from simulation, it shows that the overall absorption enhancement by optimizing the QWs position from coherent reflector is not as significant as experimental results have been published, which is going to be demonstrated and discussed in chapter 5. We now are going to focus on the fabrication process for controllable 2D texturing.

4.3 Laser Interference Lithography (LIL)

Among various pattern fabrication techniques, such as photo lithography, nano-imprinting lithography [68], e-beam lithography [69], and nano-sphere lithography [70], focused ion beam lithography [71,72], which have their unique advantages and certain application fields, laser interference lithography is used in this specific application due to its mask-less, fast, and scalable characteristic, and the availability in our laboratory. Interference lithography also known as holographic lithography is a patterning technique for regular fine arrays using two or more coherent light waves. Two-beam interference can generate 1D fringes with minimal and maximal intensity; three-beam interference can generate hexagonal symmetric arrays; and four-beam interference can generate rectangular symmetric arrays. This work is using double exposure two-beam laser interference lithography to create 2D periodic pattern [73]. Laser source ensures coherent light without using monochromator or filter to meet coherence requirement; and a concave mirror ensures a uniform wavefront, prior to beam splitting at sample stage (as shown in Fig. 4.4),

Laser's power determines exposure time for photoresist mask, and etchant concentration determines etching duration. The fabrication scale depends on both beam expansion area and laser power. The whole procedure is within minutes, which meets the need for solar cell industry of speedy fabrication. Also, there are a few advantages for this technique, such as its tunable profile, and atmosphere environment. Applying this texture as front

AR grading or back reflector can significant improve absorption, extremely helpful in MQW devices, so that less number of QW can reach the same absorption however not trade off V_{oc} or carrier extraction efficiency.

4.3.1 Laser interference lithography operation principle

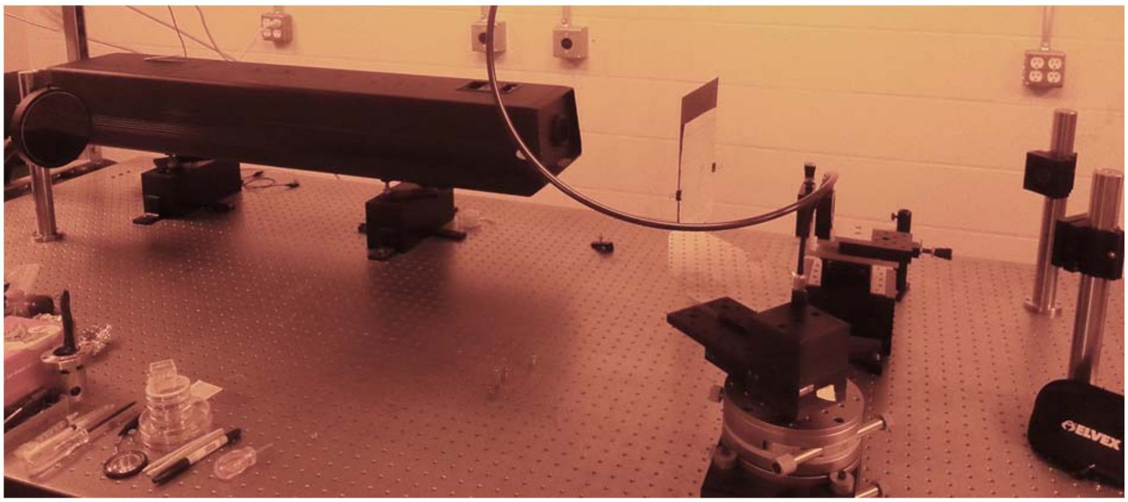

Fig. 4.3 Picture of laser interference lithography set up

Before going into details regarding the fabrication procedure, we will discuss the operation principle of laser interference lithography is going to be explained first. As shown in a simplified schematic, here the laser is expanded by the first order of Newton Ring, which emerges as a divergent beam. Making use of a concave mirror's property of focusing light, a parallel low-divergence light beam -of 75 mm in diameter- can be directed forward the sample stage. A timer-controlled shutter is placed anywhere before beam expansion to control exposure time. A portion of the light beam is reflected by an inclined mirror and onto the sample stage. The difference in light path between the direct beam and the beam reflected from the mirror creates the interference pattern.

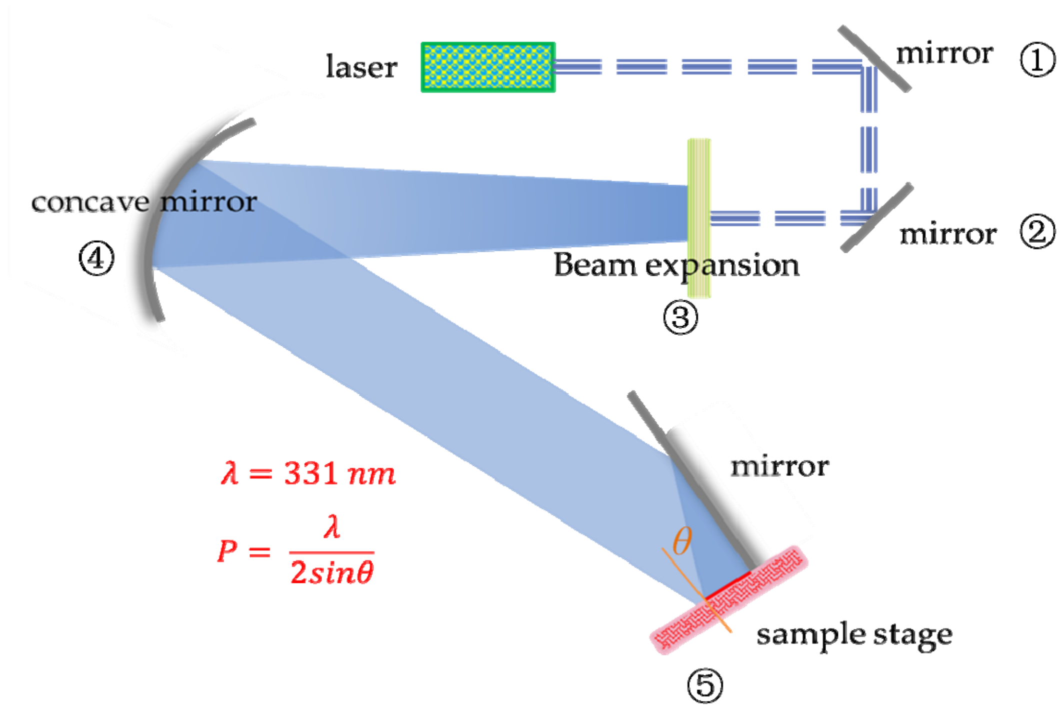

Fig. 4.4 Schematic of laser interference lithography

As the symbols defined in Fig. 4.5, the period of interference pattern follows the equation in Fig. 4.4, where the period is proportional to the laser wavelength (331 *nm*), and decreases as incident angle increases. This relation is derived below:

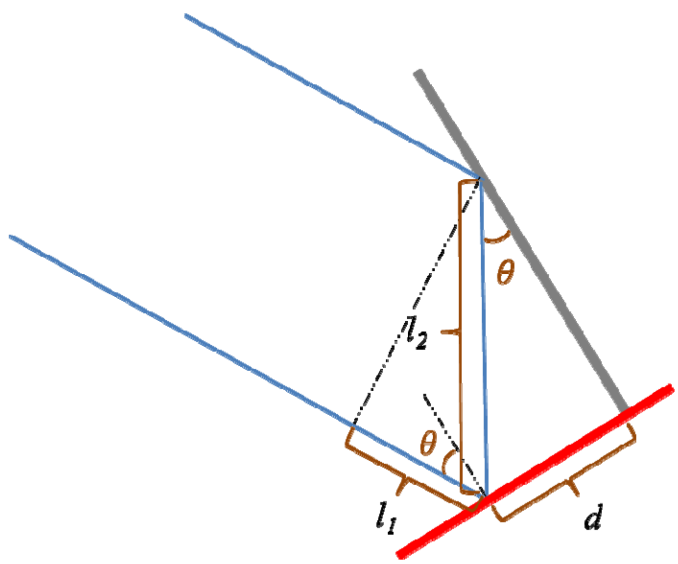

Fig. 4.5 Schematic for laser interference lithography period derivation

$$l_{1n} - l_{2n} = l_{1n}sin^2\theta = n\lambda \Rightarrow l_{1n} = {}^{n\lambda}/_{sin^2\theta} \tag{4.1}$$

$$l_{1n-1} - l_{2n-1} = l_{1n-1}sin^2\theta = (n-1)\lambda \Rightarrow l_{1n-1} = {}^{(n-1)\lambda}/_{sin^2\theta} \tag{4.2}$$

$$d_n = l_{1n}sin\theta \tag{4.3}$$

$$d_{n-1} = l_{1n-1}sin\theta \tag{4.4}$$

$$P = d_n - d_{n-1} = (l_n - l_{n-1})sin\theta = \left[\frac{n\lambda}{2sin^2\theta} - \frac{(n-1)\lambda}{2sin^2\theta}\right]sin\theta = \frac{\lambda}{2sin\theta} \tag{4.5}$$

The light path difference for any position on the sample stage can be geometrically written as l_1-l_2, and when it's integral number of 2λ, the interference constructive happens, so the distance between nearby constructive interference is period. For example between n^{th} order and n-1^{th} order of constructive interference, the distance is $P = \lambda/(2\sin\theta)$, proportional to wavelength. Therefore shorter wavelength laser has smaller feature limit $\lambda/2$, when incident angle equals to $\pi/2$. To obtain smaller profile, extreme ultraviolet lithography (known as EUV or EUVL), multiple patterning (as used in Intel's 14 *nm* integrated circuits) are used.

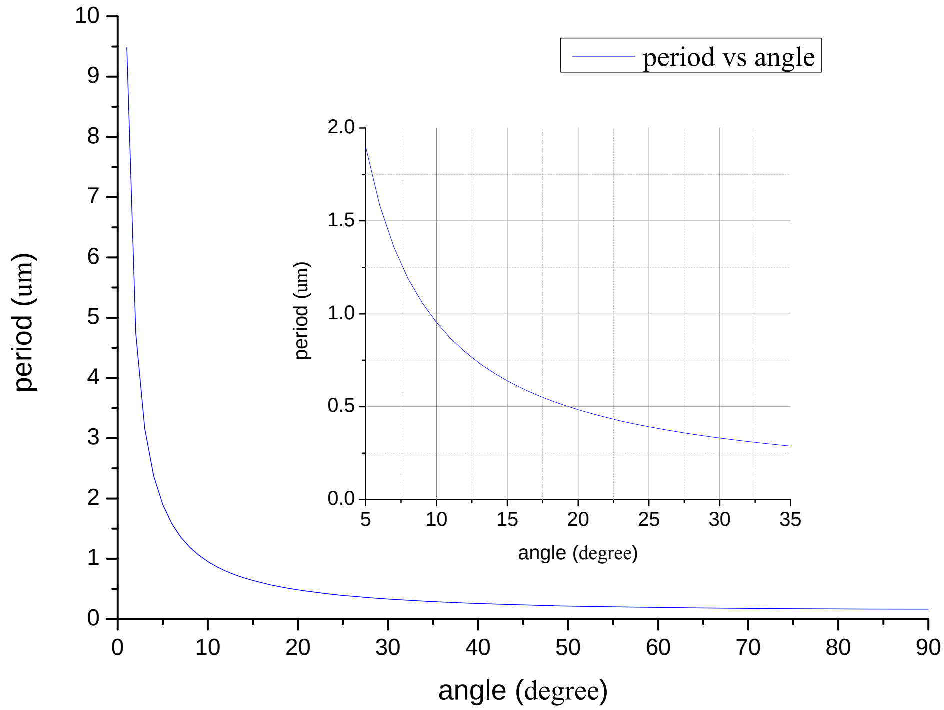

Fig. 4.6 Profile period vs incident angle relation in laser interference lithography set up

As Fig. 4.6 shows, the period significantly reduces as the incident angle increases when the incident angle is under 20^o, yet, it keeps a mild reduction as the incident angle further increases till it reach fabrication limit. When the incident angle is less than 5^o, the fabrication error is relatively high; and when it's larger than 30^o, there is not much effect on changing the pattern's period. For the sake of stabilization in fabrication, 5° – 30° is hence used for profile size 2 μm-330 nm.

4.3.2 Optical Alignment

Now let us focus on the set-up and alignment conditions used in here. In this work, the laser has a 331 *nm* wavelength, which requires cooling water and a water pump to assure sufficient water flow for more efficient cooling effect. Similar to a typical shoes-socks relation, people always put on socks first then shoes, and take off shoes first then socks.

In this condition, cooling water is similar to the role of socks, and water pump is similar to that of shoes. Consequently before turning the laser on, start the cooling water (socks) first then the water pump (shoes), and after turning the laser off, let water run for 20 *min* to completely cool down laser system, then turn off the water pump (shoes) first, and then cooling water (socks). Meanwhile, the laser has self-protection interlock, once the cooling water flow doesn't have enough flow speed, the interlock as shown on the right of Fig. 4.7 will automatically shut down the laser, with an indicator 'flow' light on. Since 331*nm* light is in UV region, which cannot be recognized by human's eyes, an extra blue light beam is blended with the UV light to help with alignment and tracing the light projecting direction. During alignment process, the power should be set lower than operating value in order to protect eyes. For example the working power is 80 *mW*, 20 *mW* is used in alignment.

Laser part:

To make full use of laser power generated, there is a controller for laser alignment, which ensures maximum power output, avoiding any beam bouncing inside the cavity resonator and losing its power. Once laser beam is centered, the green light will stay in the center of cross as shown in Fig. 4.7. Otherwise, slowly and delicately adjust fine knob at the back of laser source to make it stay in the center. During the initial warming up period, the power and alignment may fluctuate, it's consequently suggested to adjust the alignment once the laser is stable other than adjusting it from time to time.

Fig. 4.7 The picture of alignment controller

Optics part:

Beside a laser source involved as a light source, there is a shutter to control exposure time, two dielectric mirrors to redirect laser's direction, a beam expander to convert a laser beam into a divergent beam, a concave mirror to collimate the divergent beam into a parallel beam, and a sample stage with Lloyd's mirror set-up to mount samples and create interference.

Alignment of mirrors:

The first two steps of the alignment are to confirm that laser can reach mirror ①, mirror ② and beam expander ③. (Note: these two mirrors do not appear to be mirror-like for human's eyes, because they are UV reflectors coated by dielectric materials which do not have high reflection in visible spectrum; and general metal (*i.e.* Al, Au, and Ag) reflectors have good reflection in visible and infrared region, yet high transmission in UV spectrum.) Consider in this set-up, mirror ①, ② and ④ cannot move forward/backward or left/right, their initial position needs to be geometrically designed for easier adjustment later on, which obeys the following principles:

- the axis along the laser beam exiting to the reflecting mirror ① is parallel with the center of reflecting mirror ② to the center of the concave mirror ④,
- the axis between reflecting mirror ① and ② is perpendicular to the axis between the center of reflecting mirror ② and the center of the concave mirror ④,
- the beam expander stage ③ is along the axis between the center of the reflecting mirror ② and the center of the concave mirror ④.

These can be achieved according to the screw holes on the optics table. Then adjust the height and facing direction of mirror ① and ②, to let the laser beam almost reach the center of them. But very likely, even when the laser beam is reaching the expander ③, there is not any light coming out on the other side, which indicates the light doesn't go through the center of the expander. Carefully rotate the direction of mirror ② till the strongest light shows behind the expander. (The alignment can be done in this way only if the beam expander is roughly at the right position. If in case the light path is totally disturbed, remove the expander ③, adjust the direction of mirror ② to let the beam reach the center of concave mirror ④, then carefully mount stage ③ at such a place that light can come out from the other side (y-axis alignment), and parallel beam got reflected from mirror ④ (x-axis alignment).)

Alignment of beam expander:

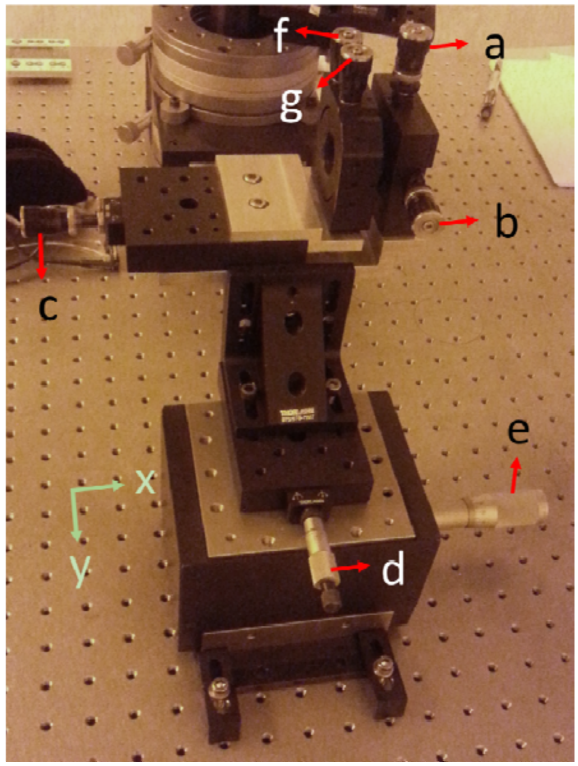

Fig. 4.8 The beam expander controller stage

The two mirrors in set up are only for changing laser's direction. The critical optics alignment process starts from beam expansion. There are a few ways to expand beams, such as multiple-prism beam expander [74], extra-cavity beam shaping, and telescope theory. Some optics companies like Newport [75], Thorlabs [76], and Eo Edumund [77] all have commercial laser beam expander products by telescope principle and have fixed magnification. This home-made beam expander is using the 1st order of Newton Ring. Newton ring is equal thickness interference, which is ensemble by a flat glass and a plano-convex lens. Adjusting the distance at the four corners of the flat glass, the symmetry of expanded beam can be achieved. (The curve of sphere optics determines the expansion magnitude) The concave mirror needs to be placed almost at the focus length from the beam expansion, in order to make parallel reflected light. The parallelization can be checked by moving a centric circle paper screen. Perfect parallelization will lead the same size blue beam at any position between ④ and ⑤, as shown in Fig. 4.10 (b).

This beam expander stage ③ is the most critical alignment part for this alignment, as it can be seen in Fig. 4.8, there are 7 knobs to adjust outcome beam intensity and uniformity as well. Rotate knobs a & b, to make the beam into circle shape as much as possible. Repeat mirror ② as well as a, b knobs adjustment several times for maximum intensity and the roundest beam, which may end with what shows in Fig. 4.9 (a). Put the centric circles screen in front of concave mirror ④, adjust knob d, which is moving the full beam expander set-up along y-axis to let the expanded beam roughly reach the center of screen. Then move the screen in front of sample stage ⑤, it may show un-uniform light beam as demonstrated in Fig. 4.9 (b). Further adjust knob d to let the brightest area locate in the center (in sense of left and right).

Knob c and e together control the expanded area by putting the effective cone light source at the concave mirror's focus length. Put screen at ④ and adjust c to make the bright area as small as possible hence reaching higher power, and then adjust knob g to make the beam as bright as possible. Move the screen to ⑤; further adjust knob e to let the brightest area move up and down to the center.

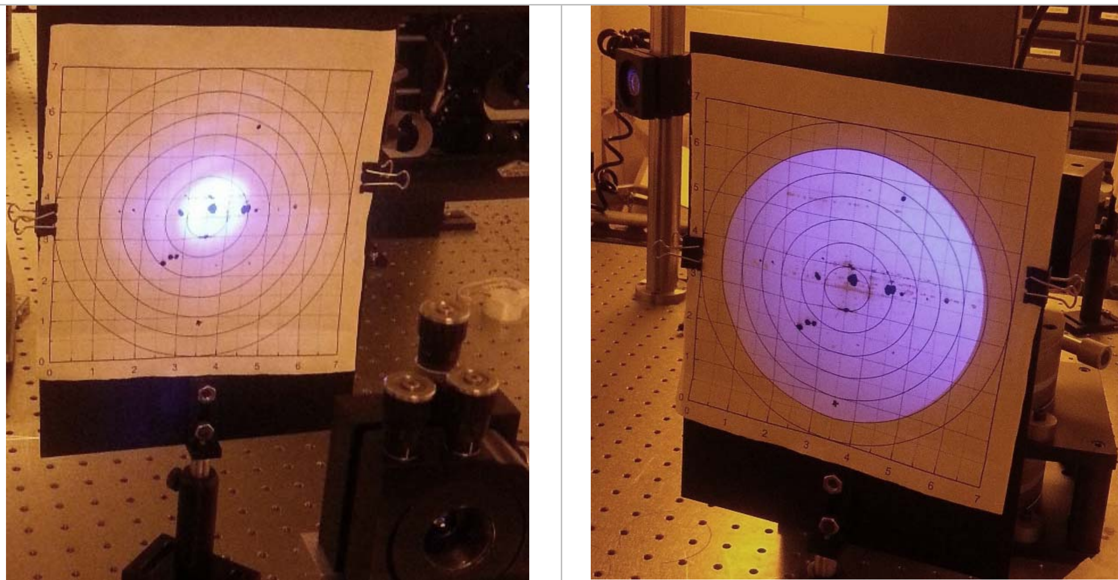

(a)	(b)

Fig. 4.9 Examples of centric circles screen during optics alignment (a) projected output from beam expander; (b) projected in front of sample stage

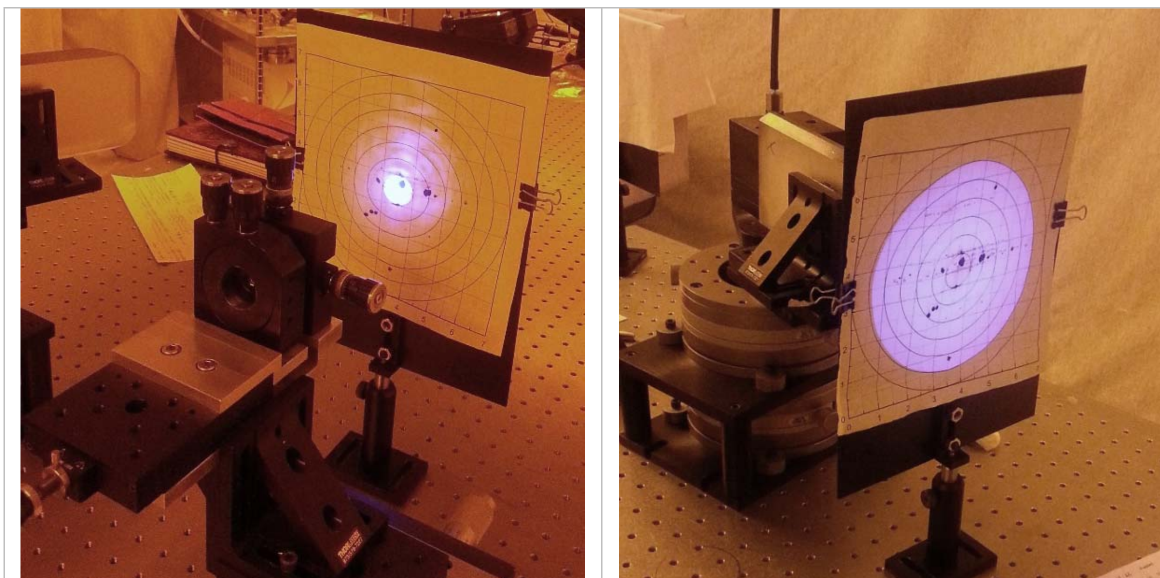

(a)	(b)

Fig. 4.10 Examples of centric circles screen after optics alignment (a) projected output from beam expander; (b) projected in front of sample stage (Lloyd's mirror set-up)

Knob f and g are fine alignment to make Newton ring has better symmetry. Even though, only the center beam (the 1st order of Newton ring) is used in this experiment, making the

2nd, 3rd order rings symmetric can make sure the intensity's uniformity in the 1st order. Since the higher order rings has much lower intensity, it's relevantly easier to see if the expansion is symmetric from them, otherwise intensity would quickly fade in some direction. Once the alignment is completed, images in Fig. 4.10 should be able to be seen after the beam expander and before the sample stage, with symmetry in polar coordinate.

Alignment of sample stage:

The final alignment is the sample stage position and facing direction, which acts as both sample mounting stage and beam splitter.

Start with mounting the sample stage slightly off the center, as demonstrated in Fig. 4.11. Since light reflected by mirror will lose some power, and expanded beam has higher intensity in the center, the sample stage is therefore mounted more to the right, in order to let the beam directly coming from concave mirror and reflected from mirror on sample stage has similar intensity.

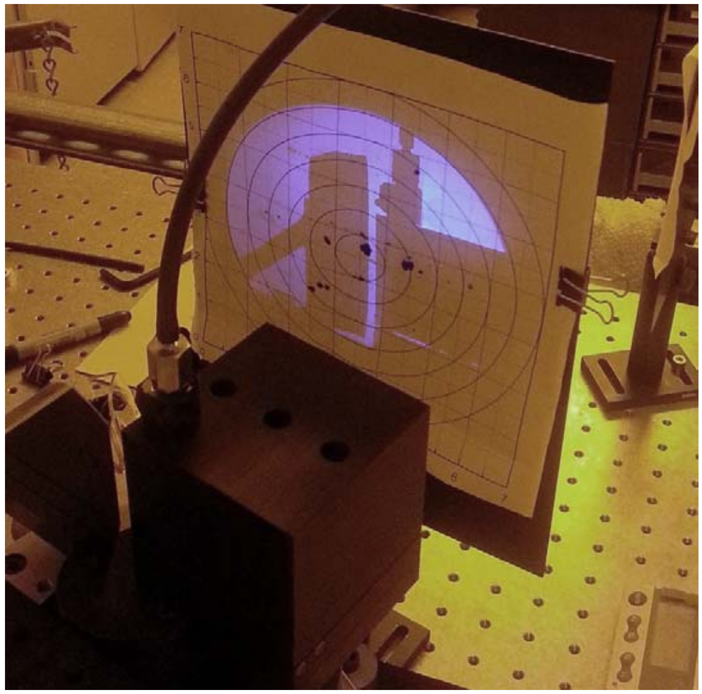

Fig. 4.11 Demonstration for sample stage mounting position

The next step is looking for 0° off normal angle to mirror. If it reaches desired position, the light from laser and reflected from mirror on sample stage will exactly fuse together as one beam. Coarse adjust by checking a semitransparent paper (transparent plastic file folder turns out to be a perfect candidate during alignment process) in the region between the concave mirror and sample stage. Then move the semitransparent paper backward, between the concave mirror and the beam expander for fine alignment. Because the mirror only reflects part of light from source beam, the reflected beam is smaller and dimmer than the original one. In order to exactly center the two beams, put a semitransparent screen close to beam expander, where the source beam hasn't been expanded widely. In this case, it's much easier to find the aligned position. Once it's fully aligned, the 2 dots will merge into 1. Mark down the angle A1 of the stage mirror's position for further use. Similarly, the sample stage side can be aligned in the same way by mounting a mirror. The same reason of low intensity from partially reflected beam, the mirror mounted needs to be big and reflective. Mark down the aligned sample stage position A2. By knowing at angle A1, the sample stage mirror is normal to the incoming light, the angle of parallel to light can be easily found out as A1-90°. Since the system doesn't automatically fix stage and mirror's relative angle, their position need to be individually changed once there is a need to adjust incident angles. A1-90° and A2 value are hence important. Generally once the optics is well aligned; there is no need to re-align before each patterning process, due to screw-fixed position for all the optics parts.

Even though in this work, polarization is not critical for final profile due to the mirror beam splitter generating no phase change nor polarization, 3-beam or 4-beam interference requires more control of polarization, which determines the intensity profile of the interference pattern[78,79]. The polarization of different beams is controlled by beam splitters. A kind of common beam splitters (called pellicle mirror[80]) is generally half-reflecting and half-transmitting when light is incident at 45°, which is achieved by thin metal (or dichroic) coated mirror. The thickness of the coating is controlled in order to meet the needs. Polka dot beam splitter[81] achieves this property by creating small metal dots with roughly half of the beam splitter's area covered. Cubes[82] made from two triangular glass prisms with controlled thickness adhesives glue together can also obtain the half-half property for a certain wavelength by adjusting resin layer's thickness. To control phase shift at beam splitter, high reflective index reflective dielectric is coated to give a phase shift of 0 or π, since phase shift happens only from low refractive index to high refractive index. So if a high index dielectric material is coated on the front surface, the transmitted beam will have zero phase-shift, but the reflected beam will be phase-shifted by π. However, if a high index material is coated on the back surface, neither reflected nor transmitted beam will have phase change.

Fig. 4.12 gives an example of how beam splitters work for a 4-beam interference lithography. This work[83] also simulated that for a two-beam configuration, the maximum intensity contrast is obtained when the two beams are TE polarized, independently of the angle of incidence of the beams. Yet for a four-beam configuration, the polarization affects not only the interference contrast but also the pattern itself. The maximum contrast happens when two opposite beams are TE polarized and the other two beams are TM polarized for any angle of incidence. Any other polarization configuration will contribute to different patterns with less contrast.

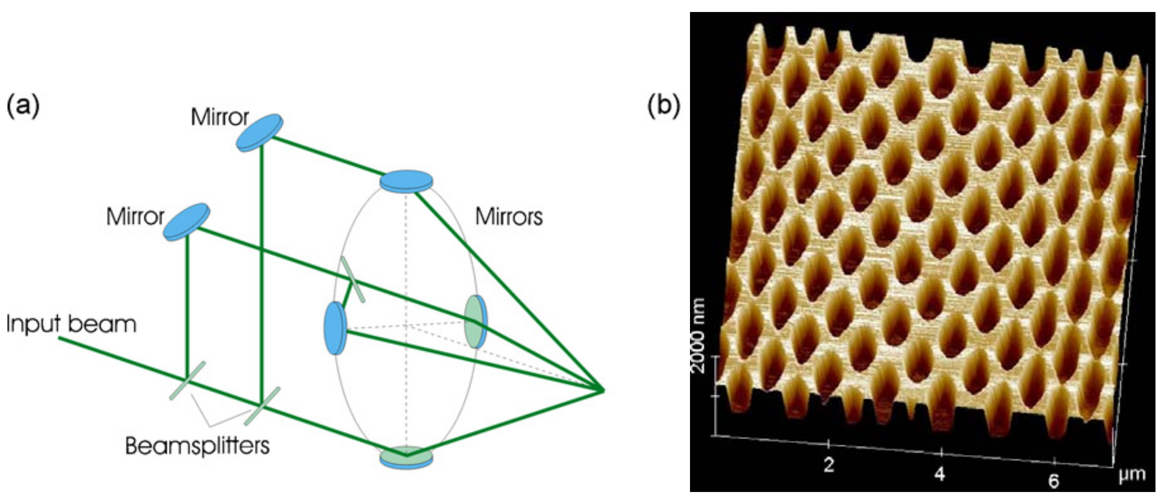

Fig. 4.12 An example of 4-beam interference lithography (a) Schematic of beam splitters and mirrors for coherent beams from single input; (b) AFM image of developed photoresist after exposure

4.3.3 Experimental procedure

With well aligned LIL set-up, we will look into the experimental procedure to achieve the textured rear reflectors, which mainly include the fabrication of a photoresist mask by

LIL, etching of the desired features using selective etchants, and subsequent.The evolution of the surface morphology in each step is illustrated in Fig. 4.13.

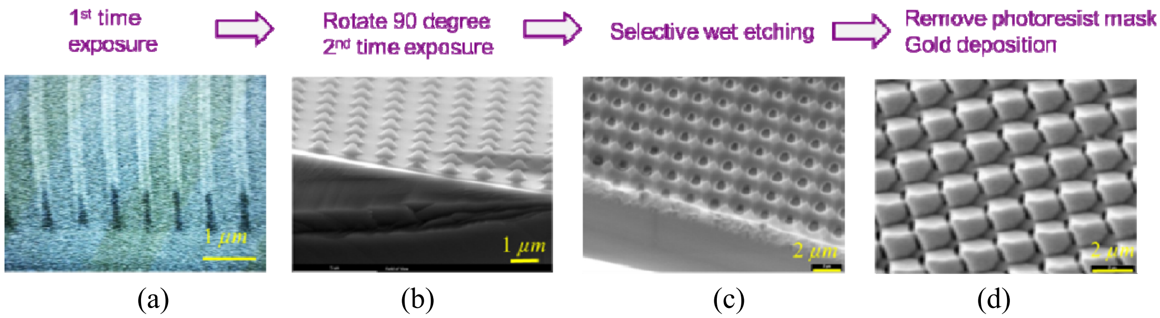

Fig. 4.13 SEM image of GaAs solar cell during back-surface interference lithography texturing process (a) 1D textured photoresist after single exposure; (b) 2D textured photoresist on GaAs; (c) textured photo-resist (PR) and GaAs after wet etching before removing PR; (d) textured GaAs after removing photoresist with Au coating as textured back reflector

The sample is first coated with an S1818 Shipley photo-resist at speed 1500 *rpm* for 50 *sec* and 4000 *rpm* for 35 *sec* (leading to ~ 2 *μm* thickness), followed by a soft bake at 115°C for 60 *sec*. The sample is then mounted on the LIL exposure stage. The process uses: an 80 *mW* 331 *nm* UV laser beam (which is expanded to ~ 7.5 *cm* radius), an initial exposure time of 95 *sec*, a 2nd exposure, a hard bake (at 115°C for 60 *sec*), an immersion in MF319 resist-developer solution, a post bake at 115°C; and finally a wet etch at a rate of 10 *nm/sec* for 200 *sec* in H_3PO_4:H_2O_2:H_2O (volume rate 3:2:20) solution. This step also etches the photo-resist mask, yet at a much lower etching rate; hence adding an additional degree of freedom in shaping the depth of the grooves. In the end, we fabricated a textured semiconductor upon which we will deposit a dielectric layer (*i.e.* 15 *nm* ZnS) and then a layer (*i.e.* 200 *nm*) of Au for reflection purposes.

Spin coating technique:

To reach uniformly coated photoresist, gradually increased spin speed is applied in this work. Final spin speed is also required to fall into maximum coating uniformity spin range supplied by datasheet from the photoresist company. (Maximum coating uniformity is typically attained between the spin speeds of 3500-5500 *rpm*.[84])

Profile size control technique:

The beauty of laser interference lithography resides in its scalability potential and applicability for any pattern size above the laser limit, which is half of laser's wavelength ~150 *nm*. To confirm that the two light beams reaching sample have the same incident angle and intensity, the mirror and sample stage is kept at 90° all the time, and the rotation axis (which is usually the joint of mirror and sample stage) is located at one of laser beam diameter. From the derivation in equation (4.1)-(4.5), it is shown that larger off-normal angle results in a smaller period, so does textured profile. Consider positive photoresist property, longer exposure time gives rise to smaller occupation ratio (size of remaining photo-resist base/groove period) of remaining mask, which directly affects the future device morphology.

Exposure technique:

It's always a challenge to make the laser beam, emanating from beam expansion to be ideally uniform. Two approaches are applied to reduce non-uniformity. First, a concave mirror focuses the light right after beam expansion. Second, the sample stage is located almost at the center of expanded laser beam, slightly away from the mirror. Because light intensity drops slightly after reflected by mirror, this ensures that the two beams from concave mirror and mirror have the same intensity. In case of various incident angles, the effective light intensity reaching the photoresist is different. More explicitly, a larger incident angle θ leads to lower intensity, requiring longer exposure time to maintain the same dose, as shown in equation (4.6). (*e.g.*, with area A of light beam from laser light, if the incident angle is 90 degree, all the light reaches sample. Also with area A, if the incident angle is 60 degree, the same area A of light beam from laser light, will reach sample, with area A/cos60 got lighted up, which equivalent to intensity on the sample reduced to half for energy conservation.)

4.4 Experimental results for micro and sub-micro textures

As mentioned earlier, the texturing includes the photoresist-mask development, etching process, and followed subsequently a standard coating of the surface using vacuum evaporation of dielectric (passivation) and metal (reflector/contact) materials. Therefore experimental procedure and recipe for the fabrication of photoresist etching mask and anisotropic will be described.

4.4.1 Effects of changing recipe to surface texture

Should be noted that every parameter in the recipe plays an important role for the final morphology. Photoresist thickness and exposure dose are directly related, while generally thicker photoresist requires higher exposure dose. Here exposure dose is the product of exposure power and time; exposure time is discussed in the later part to simplify study by assuming the power is a fixed value.

Incident angle

As shown in Fig. 4.15, larger incident angle leads to smaller grading period, smaller pitch, and at the same time lower effective dose, resulting in longer exposure time required as exposure time and incident angle relation demonstrated in Equation (4.6).

$$Exposure \quad time \propto \frac{1}{Power \cdot \cos\theta} \tag{4.6}$$

Table 4.1 incident angle v.s. effective power and exposure time to keep dose at 38.5J/cm^2

Incident angle θ (°)	Calculated Period (*nm*)	Effective power (mV)	cos θ	Exposure time (sec)
5	1899	79.70	0.996	90
10	953	78.78	0.985	91
15	639	77.27	0.966	93
20	484	75.16	0.940	95
25	392	72.50	0.906	99
30	331	69.28	0.866	104

Exposure time

Exposure time not only determines whether the photoresist can be removed after developing, but also determines the feature size versus period size, offer called as occupation ratio. If two samples are exposed under the same incident angle and power, the one with longer exposure time will have smaller feature size in the end, if the exposure time is tuned around the reference recipe. Once the exposure time is played far from the given reference, for example much shorter, what may happen is that only the place where has been exposure twice got enough dose to be removed under developer, while the place been exposed or exposed only once does not have enough dose to be removed, which leads to photoresist grid with pyramid tips at the grid cross. Hence the substrate has photoresist holes rather than photoresist pyramids, as shown in Fig. 4.15 (c).

Similar effect can be seen if thicker photoresist appears under reference recipe, such as the edge of substrate due to non-perfect uniformity in spin coating.

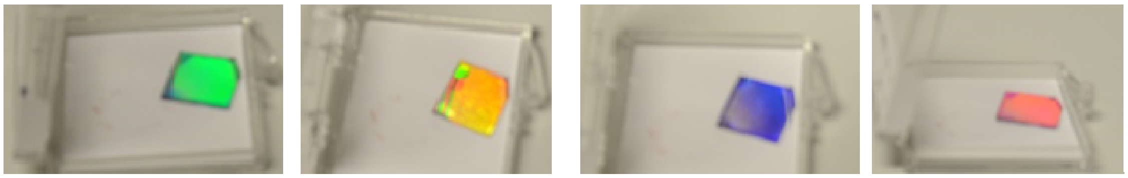

Fig. 4.14 Visual appearance of the sample at different view angles

Due to 2 μm period and 1 μm pyramid size, visible light can be scattered between these gratings, resulting in different sample colors when viewed from different angles as in Fig. 4.14, which demonstrates the scattering effect. According to the region where optical light path need to enlarge, the profile of PR mask can be controlled through LIL set up in such a way to meet the need.

Fig. 4.15 presents a few examples of photoresist pattern with different texture sizes, varying from 400 *nm* to 1500 *nm* pitch size, and 200 *nm* to 800 *nm* feature size, due to adjustable recipe, which is going to act as etching mask for the following procedure explained in the following session.

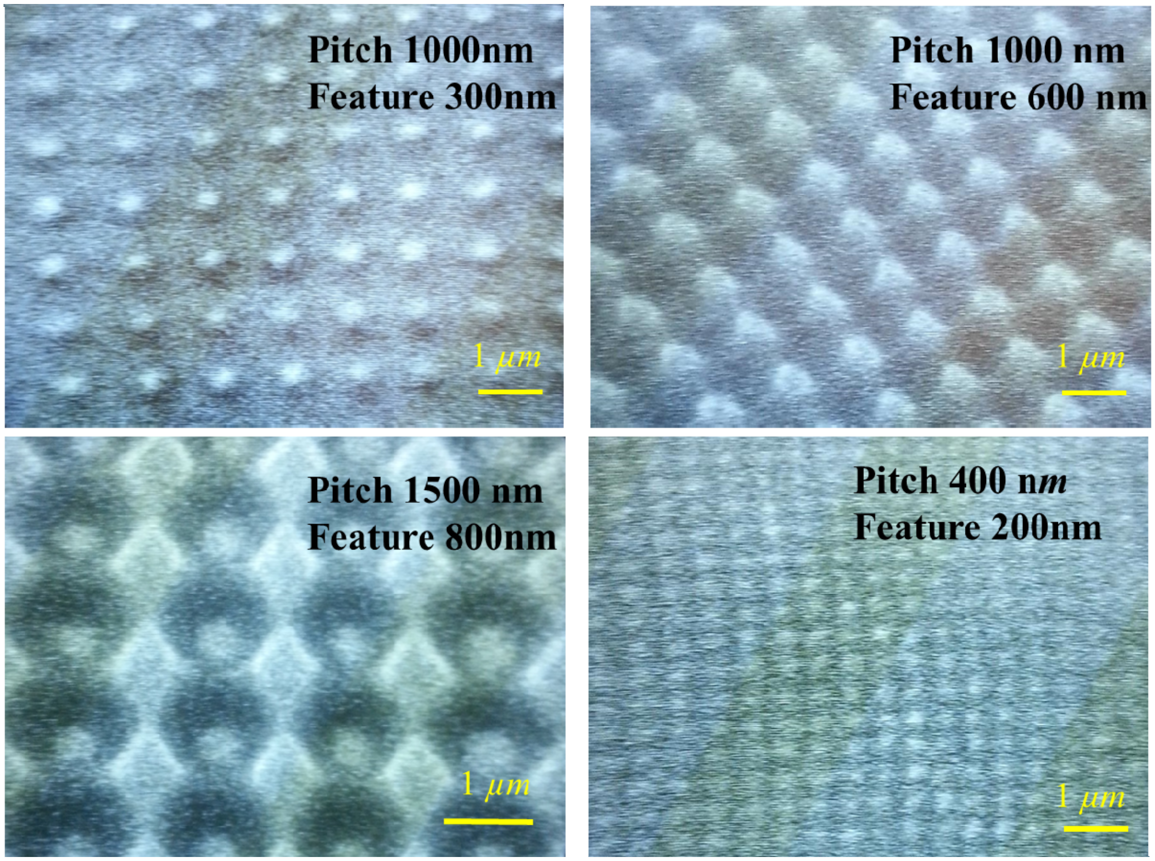

Fig. 4.15 SEM of four lithography samples with different experiment set up or fabrication recipe

4.5 Selective wet etching

Once the photoresist etching mask is formed, in this work, the etching process is implemented by the immersion of the sample in H_3PO_4:H_2O_2:H_2O (volume rate 3:2:20), a standard GaAs mesa etching solution in our lab with calibrated etching rate of 10*nm/sec*. We also evaluated the impact of changing the composition of the etching solution, *i.e.* to achieve higher etching rate or a modulation of the etch profile/anisotropy. For example, H_3PO_4:H_2O_2:H_2O (volume rate 3:2:5) was formed to etch at 35 *nm/sec*. For the semiconductor for compound semiconductors used here, *i.e* GaAs or InGaAs, (100)-

oriented epi-layers, the texture may present slight asymmetry, due to non-uniform etching rate for different crystallographic facets along {011} axis.

Selective etching as its name justified, no matter liquid-phase ('wet') or plasma-phase ('dry') etching technique, is based on the etching selectivity between masks and substrates or between etching layers and stopping layers, which during this work has been applied for creating 2D pattern, thinning devices by removing substrate from the back, and epitaxial lifting off devices from substrates by etching the only active layer (AlAs) between substrates and grown structure. In the 2D pyramid pattern fabrication, mesa etching solution is a good candidate for meeting the need, which is exactly etching III-V semiconductor layers but not the positive photoresist. So the solution would vary depending on substrates' material system; *i.e.* GaInP/GaAs/InP system can use oxidizer H_2O_2 as well as one of the more common acid such as H_3PO_4, HNO_3, H_2SO_4, HCl, $C_6H_8O_7$, and CH_3COOH, which is a combination of oxidizer and oxide-dissolver mixture.

Many etchants have been reported for GaAs, however very few of them are isotropic, which is due to different surface activity of the Ga and As, as Fig. 4.13 (d) shows in this work that the GaAs pyramids do not have perfect symmetry after wet etching. The arsenic face has two unsatisfied bonds per atom. Consequently, although some reconstruction occurs in the surface layer, it is still more reactive than the Ga face, and thus etches at a faster rate. As a result, most etches give a polished surface on the As face. (The Ga face is etched much slower, due to no unsatisfied bonds, tending to show up surface features and crystallographic defects.) [85]

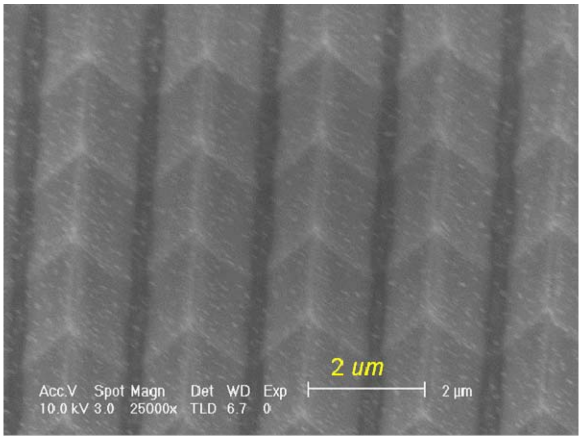

(a)

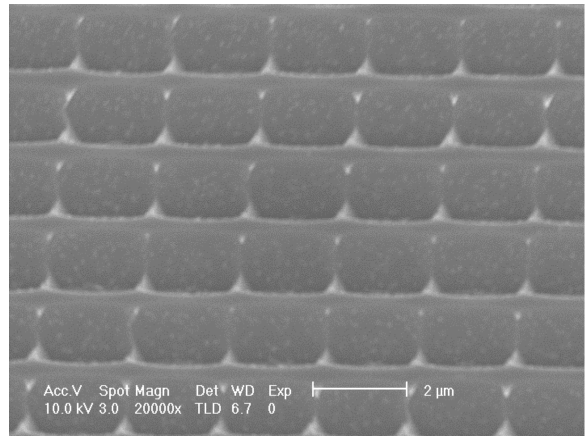

(b)

Fig. 4.16 SEM images of textured GaAs without photoresist (a) vertical direction refers to (010) orientation (b) horizontal direction refers to (010) orientation

Fig. 4.13 (c) presents the morphology of etched GaAs substrate with photoresist remaining mask. To complete the incoherent mirror and for better quality of image, Au is coated on top of GaAs pyramid grading as shown in Fig. 4.13 (d). Fig. 4.16 also demonstrates the different etching rate between two crystal orientation, where (a) and (b) are representing the same sample on the same spot, just viewing from different angle. In Fig. 4.16 (a), the vertical direction in the image is (010) orientation, which is obviously etched; yet in Fig. 4.16 (b), the vertical direction in the image is (110) orientation, which indicates much lower etching rate than (010) leading to small pyramid tips and not fully separate individual pyramids.

Subwavelength photoresist grading usually has difficulty in wet etching compared with wavelength-scale grading, for several reasons. 1st, it might be due to less uniformity photoresist mask when falling into low profile, so 1um period photoresist 2D pattern can work well in certain area which has correct cone height and base ratio. This judgment is based on the fact that area close to sample edge got etched but the center wasn't, and these two regions have the same profile period size, with thicker photoresist on the edge during spin coating. 2nd reason, it may because 2D photoresist pattern is acting not only as etching mask, but also etching center/seed, and only if the seed is big enough. This guess is based on the phenomenon that 400 *nm* period 2D photoresist pattern survived after etching process, but the GaAs substrate is not etched at all.

4.6 Summary

This chapter presented a rapid and scalable fabrication technique for surface texturing, that combines laser interference lithography with a selective wet etching technique, And we have shown that the texture pattern is controllable from the period sizes (of 400 *nm* - 2 *μm*) , occupation ratio (0.2-0.6) by tuning the process recipe.

Next chapter, we will evaluate the optical characteristic of fabricated samples and compare the results with simulations[4].

[4] Thanks to Professor Peichen Yu and her students from National Chiao Tung University, Taiwan for this cooperation work

Chapter 5 Characterization of the Structure to Evaluate Reflection Properties of Fabricated Structure and Application for Enhancing the Performance of Quantum Engineered Solar Cells

This chapter is first going to present the simulation result by commercial software (*i.e.* RSoft) to evaluate textured back mirror, then it will move on to the implementation of the structures to quantum engineered solar cells. In the simulation, the circumstance of light, coming from air and reflected to air is different from practical light behavior, coming from semiconductor and reflected into semiconductor, but since it is a possible way to fit with reflectance measurement in order to know whether the simulation is valid, consider simulation always gives some results, either correct or wrong. So this work designed an angular dependence reflection measurement set-up with fixed incoming light and outgoing light direction. By comparing the fabrication process of solar cell devices with incoherent and coherent mirrors, the ones with coherent mirrors would be relatively easier produce. So we innovated the ideal of positioning the quantum wells at the coherent constructive position, and splitting the quantum wells into two parts which locate at optimized positions individually. However, the simulation results said even by locating QWs at optimized positions, the absorption is not significantly improved, which leaded us to implement the incoherent mirrors into quantum engineered solar cells. In the end, with the framework of quantum well solar cells the experimental designs of devices post –growth process are demonstrated.

5.1 Characterization of the Structure to Evaluate Reflection Properties of Fabricated Structure

This work is mainly focused on increasing the effective light path within the QW working spectrum (*i.e.*, 870 *nm* to 1200 *nm*). Furthermore due to high reflectivity in infra-red region among common metals, a 200 *nm* Au layer is used as the mirror material; meanwhile Au has perfect alignment in work function with GaAs. A thin layer of dielectric material (*e.g.*, 15 *nm* ZnS) is deposited between the textured substrate and the Au mirror layer for passivation purposes. (Note: the structure is suitable for increasing the effective light path for the full spectrum if proper mirror material is deposited.)

The profile and feature of the textured gold back reflector apparently affects its diffraction behavior; therefore which morphology to choose for longer effective light path, similar question as in chapter 3 for larger amount of bended light, is raised up. However, consider Au is no longer dielectric material, and texture is no longer in sub-wavelength region, effective medium approach in this case is not a valid approximation due to plasmonic and scattering effect. Consequently a more powerful model is needed to calculate more accurate light performance. As shown in Fig. 5.1 by the structure in Fig. 5.2, a beam of parallel incident light coming from single direction, reaching GaAs substrate with 2D pyramid textured photoresist of 2 μm periods, 1 μm height and 1 μm base length, is splitted into several orders among various solid angles. (The picture in Fig. 5.1 is taken by collecting the diffraction on a paper screen, which indicates that if people look at the samples from different angles, diverse color can be seen at various positions.)

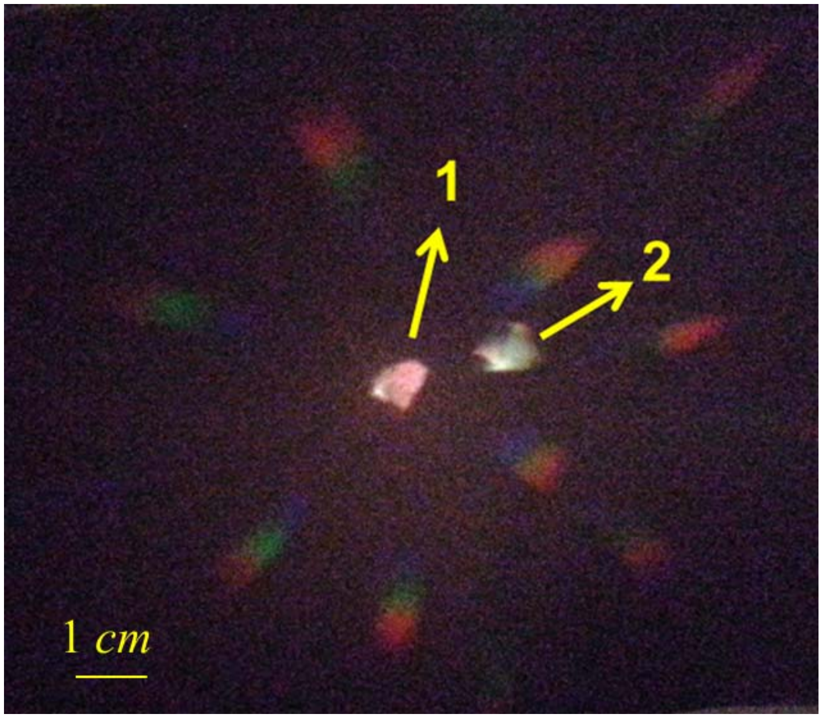

Fig. 5.1 An actual picture of scattering pattern projected on screen

It can be seen that within the same diffraction order, diffracted color is varying from blue to red in visible spectrum as polar angles increase, which indicates from short wavelength to long wavelength. (Here, there are two white color spots in the center of the diffraction pattern. The one marked as '1' is the 0^{th} order of diffraction (specular reflection) following reflection theorem/Snell law, and the one marked as '2' is the reflection from another planar sample without any texture pattern.)

Consider the goal of creating this type of reflector is to increase light path for higher absorption, and to find out how the effective light path depends on the morphology. It is hence critical to build up a model to calculate the effective light path in order to further optimize it.

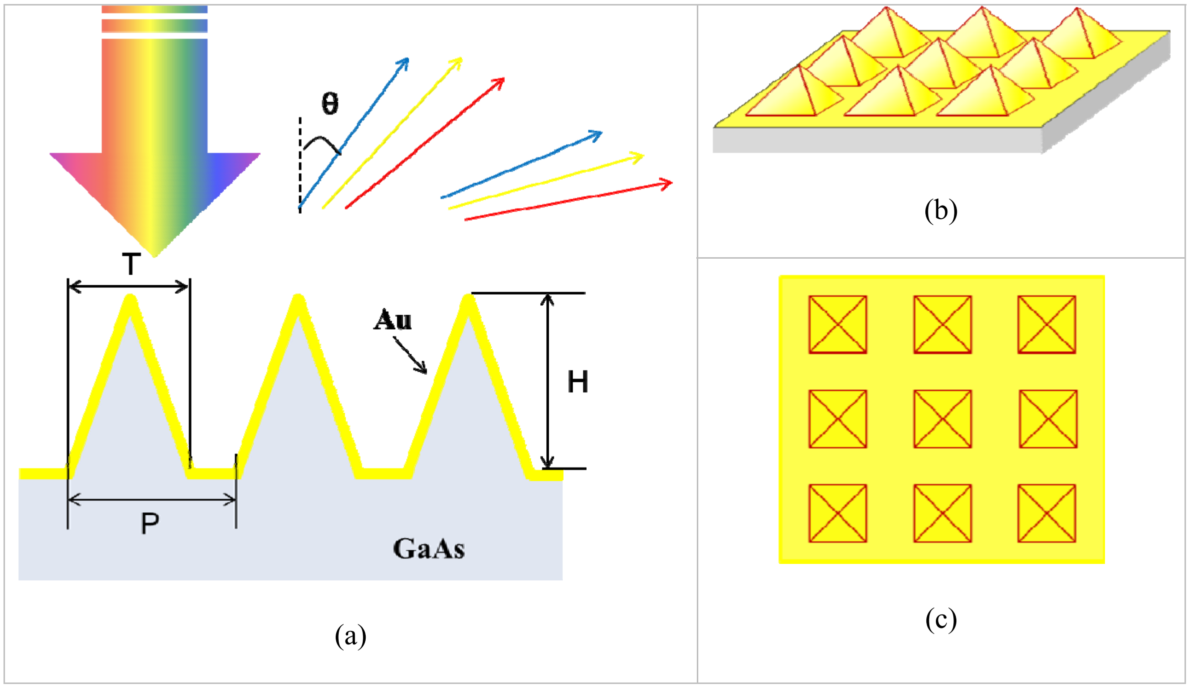

Fig. 5.2 Schematic of light diffraction on textured Au surface.

(a) cross-view of textured Au reflector with normal incident light and diffracted light at different orders; (b) side-view of textured Au reflector; (c) top-view of textured Au reflector

There are several significant parameters determining effective light path. For example, from the aspect of light, there are intensity of each diffracted order, wavelength dependence of diffraction solid angle that includes two independent angles (colatitude & longitude or called azimuthal angle & polar angle), which are finalized by texturing morphology, such as gold thickness (due to non-perfect reflector), pyramids' occupation ratio, base size, height, as well as period. It is challenging to present all their relations in 2D or 3D figures, hence it's important to omit some variable to simplify this question.

As indicated in Fig. 5.2 that larger polar angle θ contributes to longer effective light path. The azimuth angle φ, similarly discrete value as θ, doesn’t affect effective light path, which consequently should be simplified by integration. Therefore, the model for effective light path (ELP) can be expressed in equation (5.1) if d is the thickness of absorber[5]. $S_{\theta,\varphi}(\lambda)$ is the weight of diffracted light at solid angle (θ,φ), which is defined as the intensity at solid angle (θ,φ) divided by the incoming light intensity $I(\lambda)$ at specific wavelength λ.

$$ELP(\lambda) = \int_0^{\pi/2} \oint_0^{2\pi} S_{\theta,\varphi}(\lambda) * d/\cos\theta(\lambda) \mathrm{d}\varphi \, d\theta \tag{5.1}$$

The effective light path within certain spectrum region, such as within a sub-cell whose working region is λ_1 *to* λ_2, can be integrated over the light source as expressed in equation (5.2), usually sun light AM1.5G with distribution explained in Chapter 2.

$$ELP\_region(\lambda_1, \lambda_2) = \int_{\lambda_1}^{\lambda_2} ELP(\lambda) \cdot I(\lambda) \, d\lambda \tag{5.2}$$

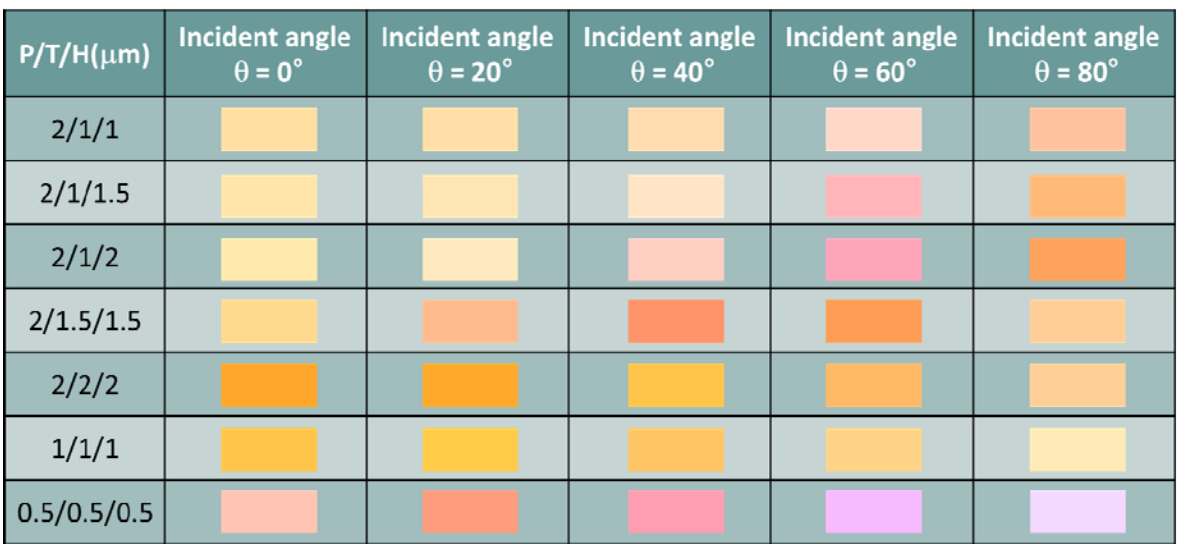

Fig. 5.3 Color viewed by eyes at specular reflection direction when sunlight comes from different off-normal angles

[5] For single-junction application, absorber thickness is simply the device thickness. Yet for multifunction, *d* is the thickness of the junction which would actually absorb that wavelength. For example, the InGaAs QWs grown in GaAs cell's i-region, *d* is the combined thickness of InGaAs, regardless of GaAs portion.

RCWA from Rsoft software can further give what color this type of samples would appear to human's eyes if observer is looking along the direction where reflected angle equals to incident angle, as incident sunlight comes from different directions. As it is shown in Fig. 5.3 the color that is a combination effect of different wavelength with certain weight differs as any single parameter changes, which matches with what we practically see from the samples made in lab, generally gold to pink color.

The condition of light coming from air and reflected to air is different from practical condition that light comes from semiconductor and reflected into semiconductor, but since it is a possible way to fit with reflectance measurement in order to know whether the simulation is valid, consider simulation always gives some results, either correct or wrong. Here it shows the simulation results first, and will later be compared with experimental results.

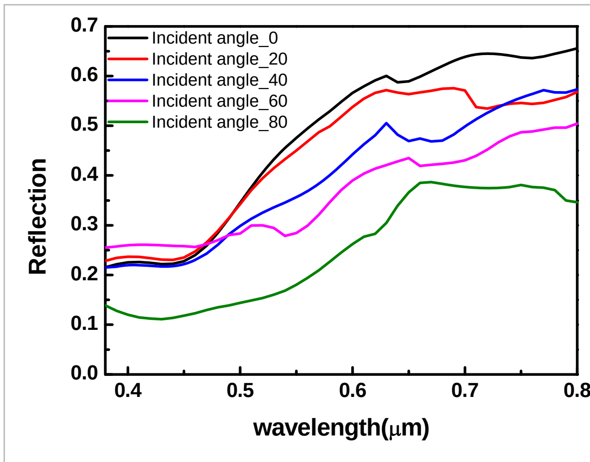

(a)

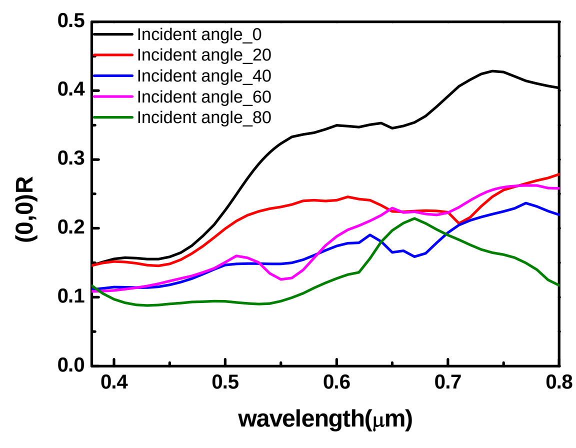

(b)

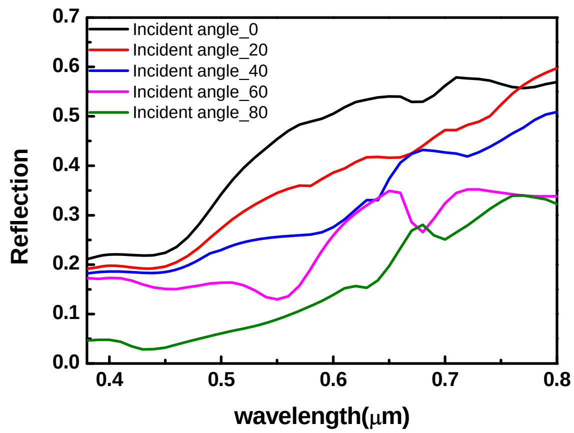
Incident angle_0
Incident angle_20
Incident angle_40
Incident angle_60
Incident angle_80
Reflection
wavelength(μm)

(c)

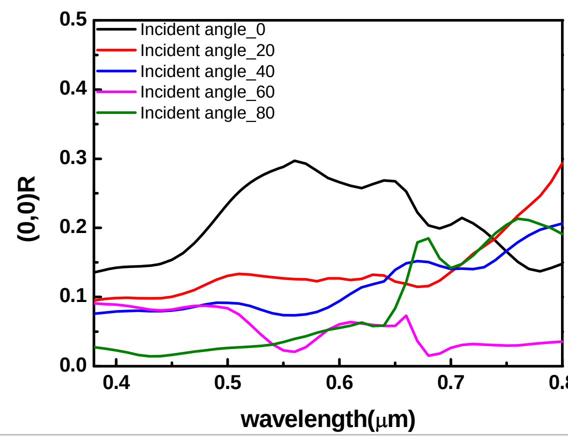
Incident angle_0
Incident angle_20
Incident angle_40
Incident angle_60
Incident angle_80
(0,0)R
wavelength(μm)

(d)

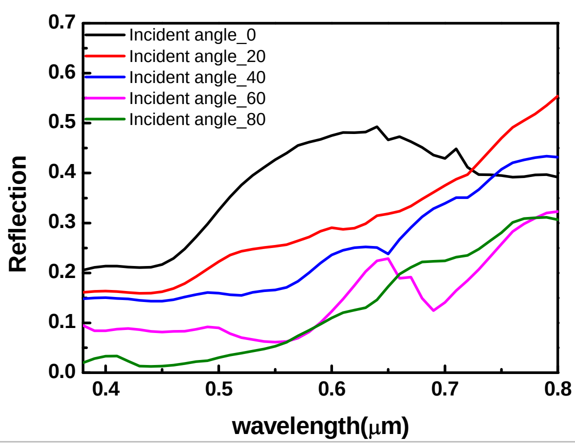
Incident angle_0
Incident angle_20
Incident angle_40
Incident angle_60
Incident angle_80
Reflection
wavelength(μm)

(e)

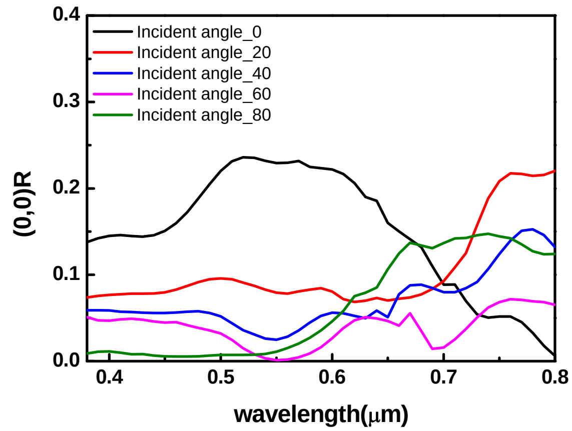
Incident angle_0
Incident angle_20
Incident angle_40
Incident angle_60
Incident angle_80
(0,0)R
wavelength(μm)

(f)

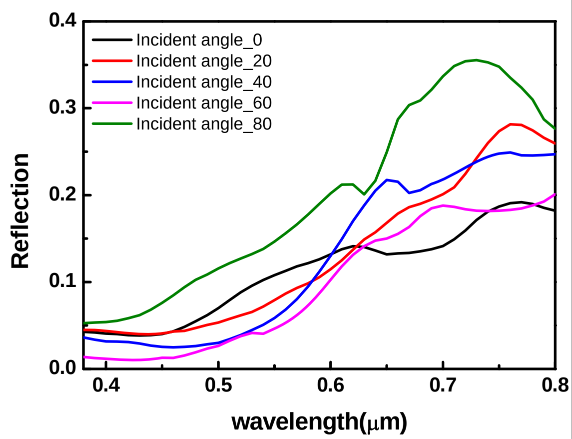
Incident angle_0
Incident angle_20
Incident angle_40
Incident angle_60
Incident angle_80
Reflection
wavelength(μm)

(g)

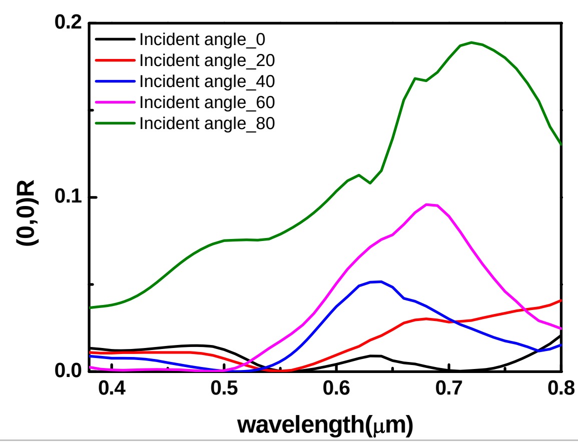
Incident angle_0
Incident angle_20
Incident angle_40
Incident angle_60
Incident angle_80
(0,0)R
wavelength(μm)

(h)

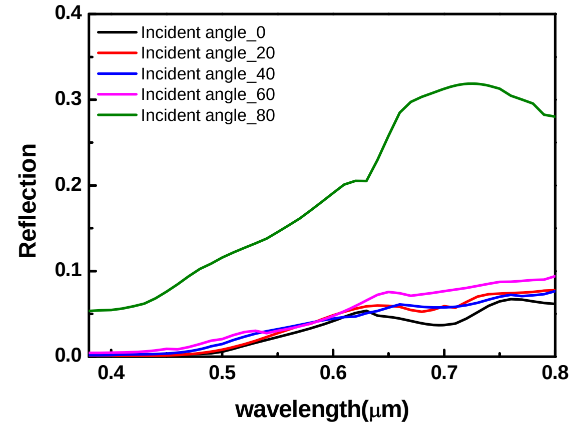

(i)

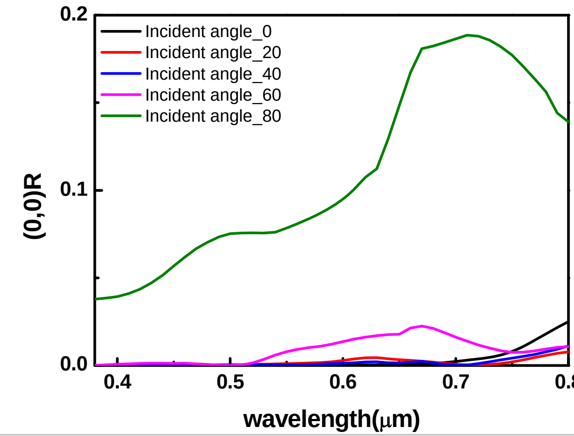

(j)

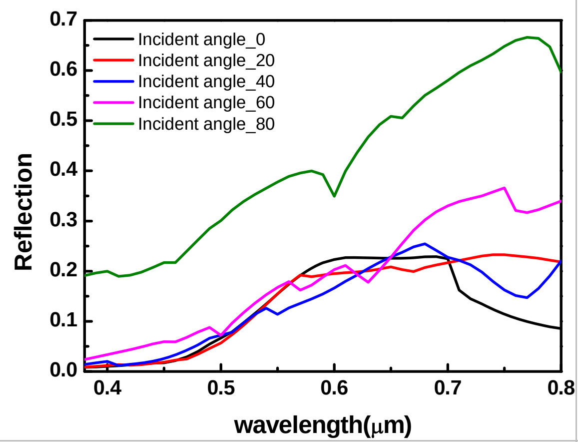

(k)

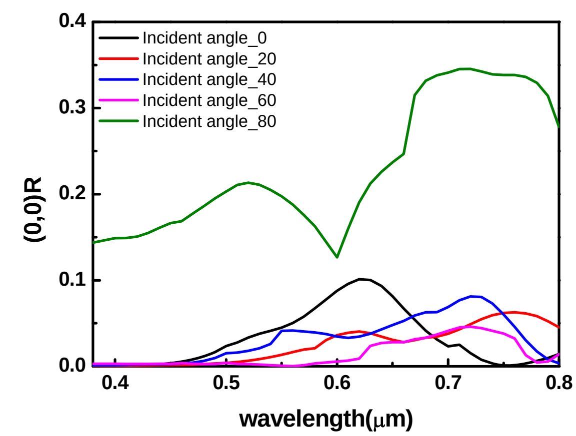

(l)

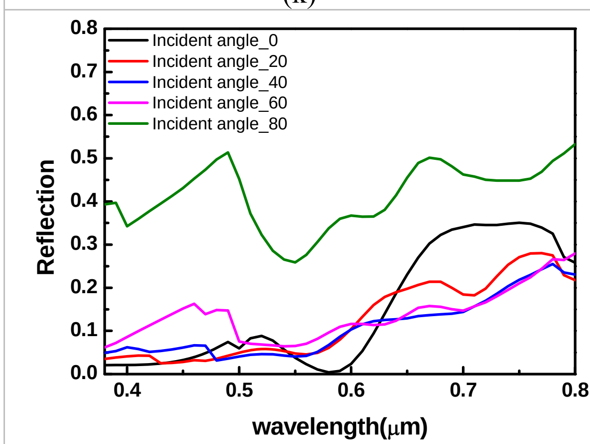

(m)

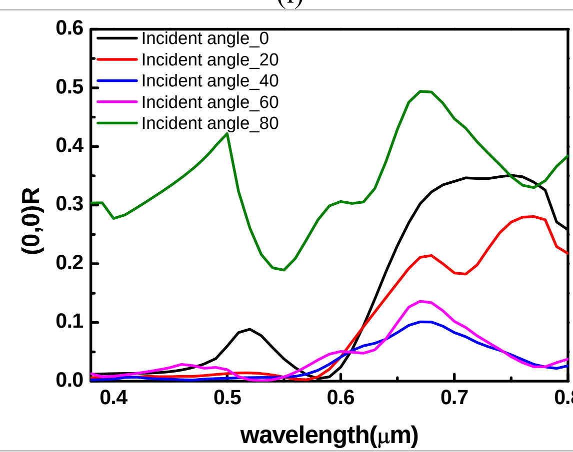

(n)

Fig. 5.4 Integrated diffracted light and specular reflection (ratio) —(0,0)R (ratio) according to different incident angle: (a&b) period P = 2 μm, pyramid base length T = 1 μm, pyramid height H = 1 μm; (c&d) period P = 2 μm, pyramid base length T = 1 μm, pyramid height H = 1.5 μm; (e&f) period P = 2 μm, pyramid base length T = 1 μm, pyramid height H = 2 μm; (g&h) period P = 2 μm, pyramid base length T = 1.5 μm, pyramid height H = 1.5 μm; (i&j) period P = 2 μm, pyramid base length T = 2 μm, pyramid height H = 2 μm; (k&l) period P = 1 μm, pyramid base length T = 1 μm, pyramid height H = 1 μm; (m&n) period P = 0.5 μm, pyramid base length T = 0.5 μm, pyramid height H = 0. 5μm

From Fig. 5.4, it can be concluded that

1. Smaller incident angle indicates higher reflection (comparing (a) (c) and (e)), since more order of diffraction would occur.

2. Structures with full occupation (P/T/H all equal to 2, or 1, or 0.5 micron as shown in (i) (k) and (m)) have obviously higher reflection at 80^o incident angle, because the pyramids have 63^o base angle < incident angle, therefore 0^{th} order diffraction ray would go upward rather than downward compared with base angle > incident angle condition, consequently giving stronger reflection.

3. 2 μm size has lower reflection than 1 μm profile (i) vs. (k), due to more rays got trapped between pyramids. Based on that theory (which can fit (a) vs. (c) vs. (e) as well as (a) vs. (g), lower reflection with taller pyramid), 0.5 μm feature is expected to have even higher reflection, but it's actually showing lower reflection (m) than that from 1 μm.

Experimental set up and measurement for specular reflection:

This work also designed an angular dependence specular reflection measurement by adding two Au mirror into conventional reflectivity measurement, without changing light source or monochromator’s position (since the lens system cannot move simultaneously with them). The experiment set-up is shown below. (Incident angle can theoretically vary from 0^o to 90^o, actually value limited by table size.)

(a)

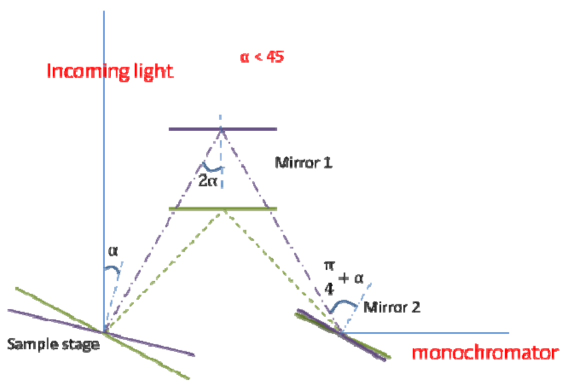

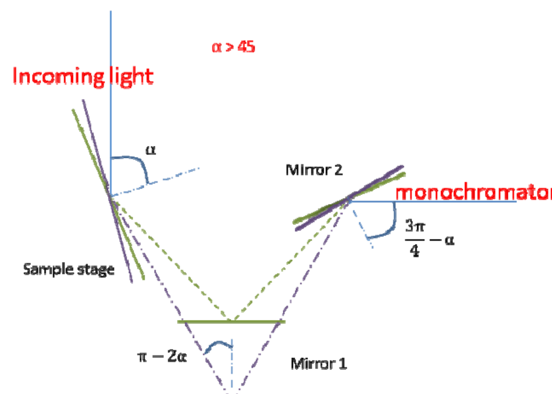

(b) (c)

Fig. 5.5 Angular dependence reflection measurement (a) experimental set-up, (b) schematic of incident angle <45°, (c) schematic of incident angle >45°

There are many possible combinations for 2-mirrors' position and direction to forward light into monochromator's entrance slit, but it is preferred to make the adjustment simple and easy to analyze from time to time when the incident angle changes. As shown in Fig.

5.5 (b), for the incident less than 45^{o}, when the incident angle decreases, mirror 1 is only moving further from sample without changing direction, and mirror 2 is only changing facing direction more towards monochromator without changing position. Similarly, for the incident angle larger than 45^{o} as shown in Fig. 5.5 (c), when the incident angle increases, mirror 1 is only moving further from sample without changing direction, and mirror 2 is only changing facing direction more towards monochromator without changing position. The incident angles to sample and towards two mirrors are presented in the respective schematic as well.

Due to the intrinsic working principle of this system that monochromator separates light by grating, telling computer certain grating position refers to corresponding center-wavelength, and detector measures intensity without knowing wavelength property, computer connects them into a wavelength-intensity curve. Generally narrower slit should be preferred for better wavelength resolution. At the same time, as the slits get narrower, the radiation power reaching the detector would decrease which imposes limitations on the accuracy of measurement [86]. On the other hand, wider exit slit leads to a spectrum band rather than single wavelength coming out to detector, similar to integration, contributing to possibly different spectrum curve compared with that from narrow slits depending on dispersion. To optimize throughput, it is suggested to use the widest slits, while maintaining other system requirements [87]. It is also important to keep slits width the same during experiment for comparison purpose.

In this experiment, the monochromator is Triax 320 Jobin Yvon Horiba [88], which has 2 entrance ports, and 2 exit ports, with focal length 320 *mm*, F number F4.1, dispersion

2.64 *nm/mm*, and triple grating turret with 2 gratings. The grating used during experiment is 1200 @ 900 *nm*. Here the focal length is the distance from the exit-imaging mirror to the focal plane, with longer focal length giving better resolution. F number (f/#) is the input aperture of the monochromator, describing the light gathering power that increases as the inverse square of the f/#. The 1st order (n = 1) of dispersion (*nm/mm*) is calculated by $d/n/F = (1/1200)mm*10^6(nm/mm)/1/320mm = 2.604bnm/mm,$ where d is the period of grating.

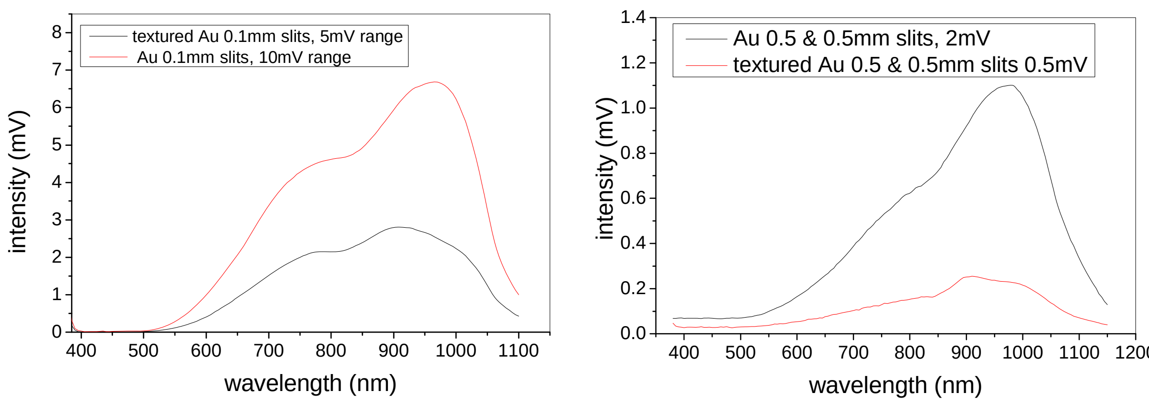

(a) (b)

Fig. 5.6 An example of light spectrum reflected by Au mirror and textured Au mirror at the same from different slits width (a) 0.1 *mm* for both entrance and exit slits at 16.5^o incident angle, (b) 0.5 *mm* for both entrance and exit slits at 60^o incident angle

The intensity versus wavelength curves shown in Fig. 5.6 don't represent the light property reflected from the sample, even with reflected angle equal to incident angle, mainly due to two reasons. First, the intensity is detected by Si detector, which has its non-uniform spectrum response, as shown in Fig. 5.7. Second, the light after reflected by sample has been reflected twice by Au mirror, not perfect mirror for the whole wavelength, as shown in Fig. 5.8, a comparison between reflection spectrum given online and calculation from thin film method by using metal's complex refractive index [89,90,91].

Therefore data need analysis to transform into useful information, which is reflectivity we want to compare with simulation result. In experiment, the conventional Au mirror and textured Au mirror both have been deposited 200 *nm* Au, and simulation work above was using 100 *nm* Au. Thin film method calculation shows this two thicknesses Au gives the same reflectivity for conventional Au mirror, which can be assumed true for textured Au.

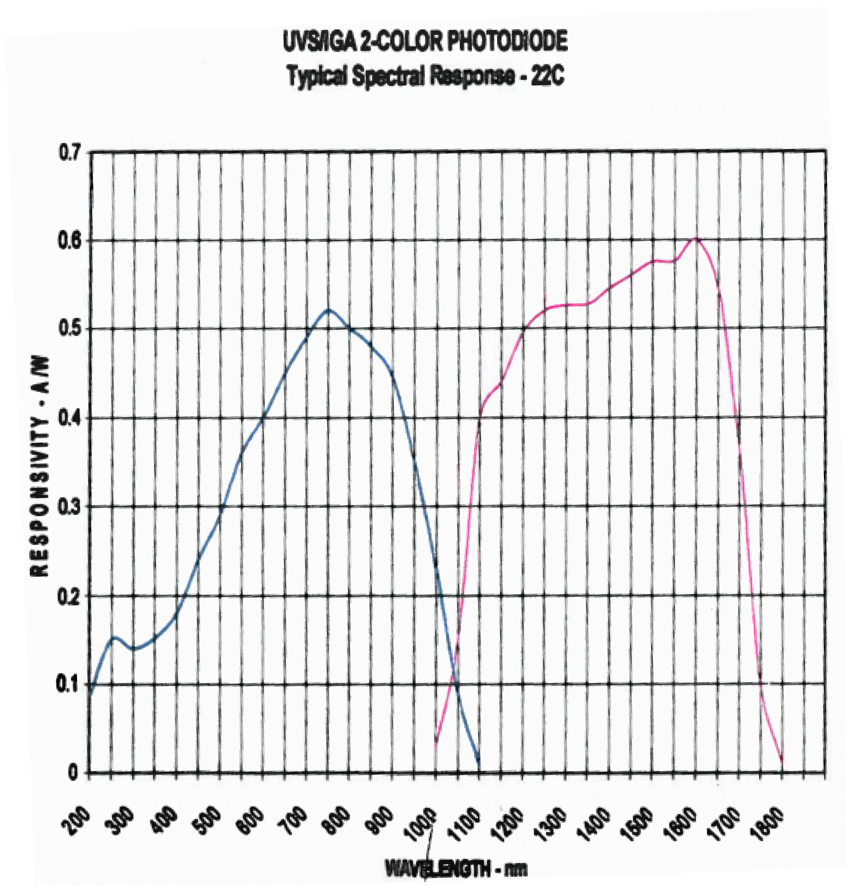

Fig. 5.7 UVS/IGA 2-color photodiode typical spectral response at -22^{o}C

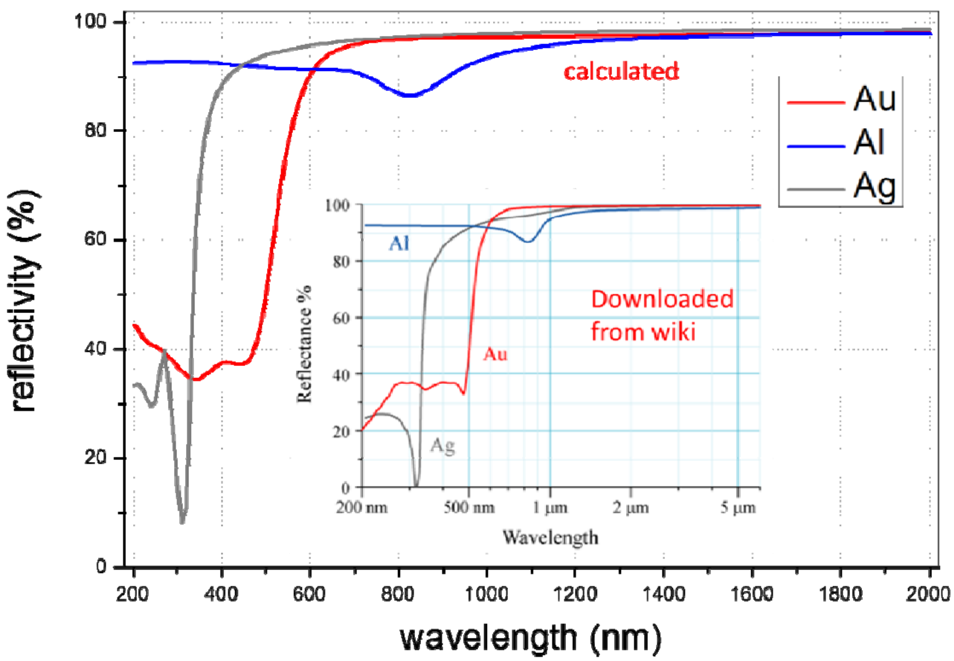

Fig. 5.8 Calculated reflectivity from self-coding software for three common mirror material (Au/Al/Ag) comparing with that from wiki

After normalizing the measured data to a reference plane-Au mirror's reflectivity at certain incident angles, it turns out that the textured mirror is acting like a 2D blazed grating, whose goal is to minimize the specular reflection and maximize higher orders reflection. Given the refractive index of a semiconductor sample and the law of refraction ($n_1 sin\theta_1 = n_2 sin\theta_2$), light bent into to III-V photovoltaic device has less than 15^o incident angle, which is very close to the behavior of normal-incident light, this work is going to analyze normal-incident light as an example. Higher order of diffraction indicates larger diffraction angle leading to internal total reflection, contributing to longer light path, which is the main approach to improve absorption. Consequently, a larger amount of non-specular reflection is more efficient to increase the integrated light path than that from plain mirror only with specular reflection. The behavior of light inside a semiconductor is challenging to measure since total internal reflection would occur at the interface between air and solar cell devices. The light behavior in the air is, therefore, measured and later used to infer its behavior in the semiconductor.

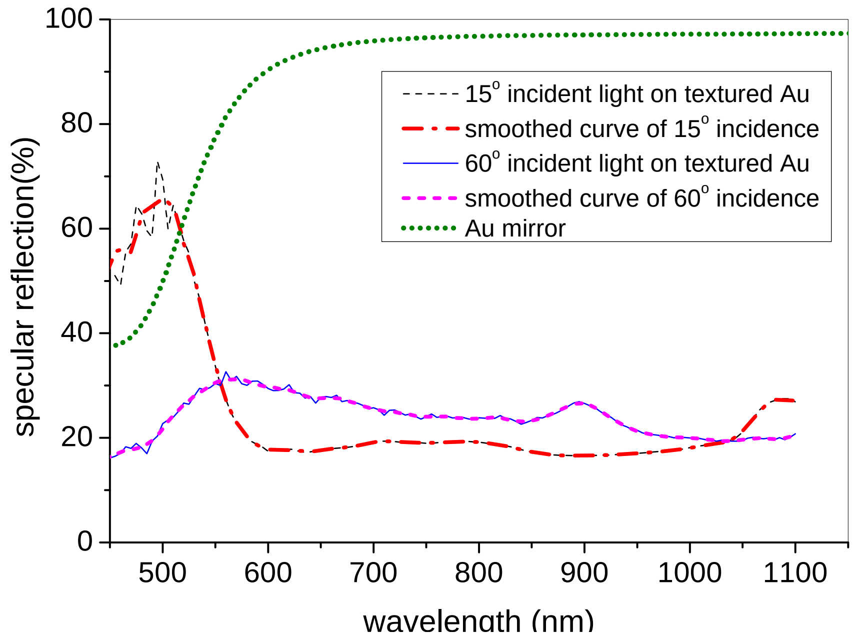

Fig. 5.9 Normalized specular reflectivity of textured Au mirror vs plain Au mirror

As seen in Fig. 5.9 comparing with plain Au mirror, textured Au mirror with 2 micro meters feature and pitch size reveals an almost 70% reduction in specular reflection for both 15^{o} and 60^{o} incident angle; which, consequently, contributes to higher order diffraction and increasing effective light path.

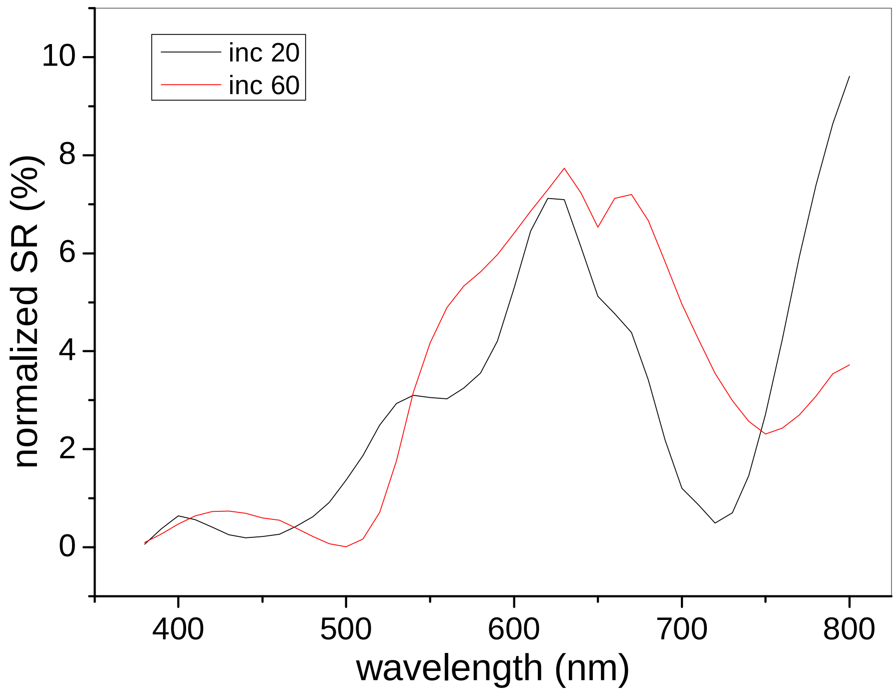

Fig. 5.10 Normalized specular reflection of simulation data from RSoft with assuming conserved integrated reflection as plain mirror

By comparing experimental specular reflection shown in Fig. 5.10 and its relevant theoretical simulation by RSoft program, it is found that the experimental data of specular reflection didn’t have good match with simulation result by RSoft, which might because the normalization is assuming integrated diffraction from every order is conserved with plain mirror. However this assumption is only valid when the light beam has not been reflected many times between the gratings and the Au coating on grating behaves almost as perfect mirror. (Diffused metal mirror practically has only 50-60% reflection.)

The calculation shown above represents how light behaves out of the device with textured Au reflector. Yet to know the improvement for device performance, a slight change need to be modified, rather than light coming from air and reaching Au texture on top of semiconductor, light comes from semiconductor and reaches Au texture whose back is air, meaning travelling in semiconductor, as shown in Fig. 5.11. Even though the physical model changed, the mathematical model for calculating effective light path follows the same idea as shown in equation (5.2). Consider the light behavior in air (demonstrated in Fig. 5.9) and the diffraction equation including refractive index (n) of semiconductor, the maximum order of diffraction light inside semiconductor would have ~3 times of that in air, since the equivalent wavelength in semiconductor is 1/n of that in air. This indicates the portion of light diffracted to high order is very likely to be even higher than 70% as demonstrated in air.

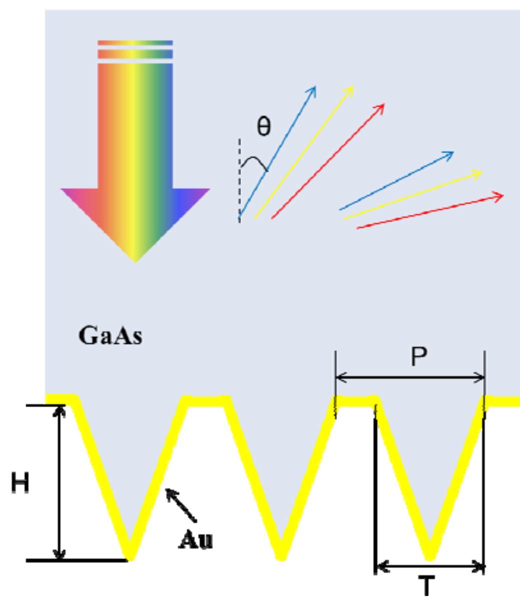

Fig. 5.11 Schematic of modified model for light path in solar cell devices

Between coherent reflectors and incoherent reflectors, there is a question of which one works better for devices. This chapter presents the simulation of a coherent reflector applied to a device incorporating QWs to investigate details such as locating the wells at the position of constructive interference and splitting the wells by thin film method. This will allow us to see if it is possible to significantly improve the device's absorption while avoiding the tedious post-growth processes associated with using an incoherent reflector. The model is verified by fitting with experimental EQE/IQE on a lift-off quantum well device implemented with Au back mirror, which resulted in a good fit. However, the calculation of optimizing the QW position reveals that the incoherent reflector is required for promising photon recycling. Next, this chapter will give the post-growth procedure for lift-off devices which use either conventional upright growth or inverted growth techniques while adopting a back textured reflector.

5.2 Conclusion for the characterization of rear mirror

Reflectivity which is defined as the ratio of reflected light intensity over incoming light intensity is the main parameter to compare with simulation. But practically incoming light intensity is not measured in experiment and only a portion of the reflected light goes into monochromator and measured. Special data analysis approach is required to obtain reflectivity. It is found that the experimental data of specular reflection didn't have good match with simulation result by RSoft, which might because the normalization is assuming integrated diffraction from every order is conserved with plain mirror. However this assumption is only valid when the light beam has not been reflected many times between the gratings and the Au coating on grating behaves almost as perfect mirror. (Diffused metal mirror practically has only 50-60% reflection.)

Based on our 2D grating giving 2D diffraction, with diffracted beam intensity depending on wavelength, texture structure, incident angle, and the order of diffraction (solid angle), it is challenging to find out the effective path over a wavelength region by integrating over solid angle. If we can find out exactly how light get diffracted inside semiconductor, we can theoretically calculate effective light path, which is derived by equation in this chapter, but that's not a usual approach for this problem; since diffraction light is existing not only at certain solid angle, but also continuously over the full space. To simplify the output parameters in calculation, and still get the desired results, absorption rather than diffraction is calculated, which is the total incoming light from atmosphere subtract total integrated reflection from every solid angle into air. Based on absorption length, absorption coefficient (*i.e.*, quantum well absorption coefficient in this case), and absorption rate relation (1-integrated R), the effective light path can be calculated in a much simpler way.

5.3 QW positioning for light coupling

The fabrication process of solar cell devices with incoherent would be relatively easier to produce than the ones with incoherent mirrors. So we wondered whether positioning the quantum wells at the coherent constructive position, or splitting the quantum wells into two parts which locate at optimized positions individually can improve absorption. To find out the answer, we did simulation for these two conditions, with program validation compared with experimental quantum efficiency data from thin film lift-off devices.

For thin film device, such as lift-off cells, the light coupling created by back reflector leads to coherence emphasis and coherence destruction at different locations. The positioning of quantum wells (QWs) is, therefore, important to make coherence emphasis happen at the QW location. The use of QWs and resonant tunneling effects are studied for harvesting absorbed photons[92]. Given the lattice mismatch between GaAs and InGaAs, once the accumulated InGaAs thickness goes beyond 75 *nm*, the strain starts to relax which reduces current exportation. Therefore, effective QW design is critical to reach high efficiency. This work analyzes the necessity of rigorously devising a device structure (blueprint) by demonstrating the disparity between well designed and poorly designed devices using transfer matrix thin film method. This work also adapts this simulation method with the drift diffusion model to obtain external quantum efficiency (EQE); approaching to that from experimental data in both GaAs junction and InGaAs QWs spectrum through a circumspective change of parameters, where quantum well absorption coefficient used have been fitted from both simulated through 8 band k*p model and back calculated through experimental absorption data.

The drift-diffusion model [93] is considered as the most precise and advanced model to predict device performance and optimize structure, taking into account of all parameters including finite absorption and limited carrier lift time. Work from Lumb *et.al.* demonstrated the light coupling effect in thin devices [94], which is calculating the electric field at every point within devices. This work, on the other hand, found similar results by utilizing a different and much faster method. Namely, by the thin-film method in the form of transfer-matrix method [95]; this is a much faster approach, and would be an easier simulation method to explain the fringes in quantum efficiency. To validate this approach, simulation results were compared with experimental data based on EQE/IQE behavior from single junction GaAs with InGaAs QWs lift-off cells. Much work has been done to improve light coupling in QW region for the purpose of photon recycling, such as light trapping with nanostructure for antireflection purpose [96], and textured reflector to enlarge effective light path [97,98]. But from the post-process explained in chapter 5.2.2, it can be seen that texturing the back surface for incoherent reflector is not an easy process. This work, therefore, built another model based on the EQE fringes phenomenon to find out whether the location of QW will affect the final device performance. For example, locating the well's position at the constructive interference spot, where there is maximum intensity to absorb, or separating the QWs into two (or even more) parts to let them individually sit at the 'sweet spots' to further make use of light coupling.

5.3.1 EQE/IQE measurement on a lift-off QW device

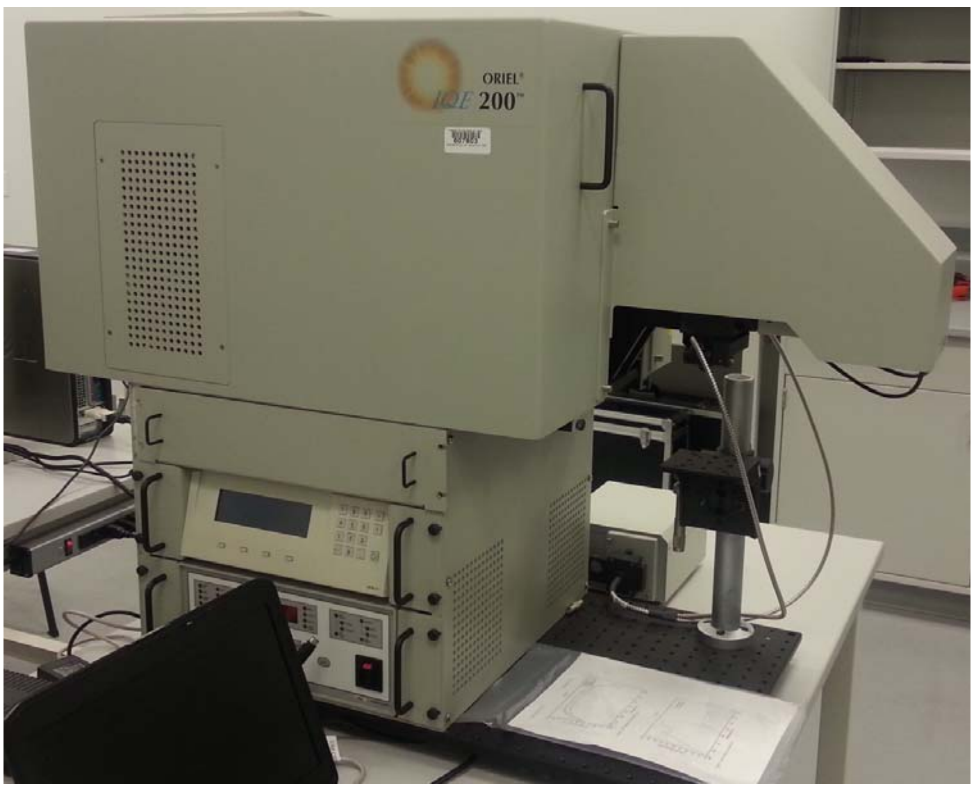

Fig. 5.12 ORIEL IQE 200 for EQE/IQE measurement set-up

EQE/IQE measurement is done on ORIEL IQE 200, whose working principle is splitting a white light beam into individual wavelength which are parallel and shine onto the solar cell device; measuring the corresponding I-V by two-probe and the reflectivity is measured to obtain the reflection response as a function of wavelength of incident light. Thus, we can obtain the EQE and IQE versus wavelength relation. In other words, this equipment is integrating the spectrum response with reflectivity measurement to get quantum efficiency. Using this equipment, the sample stage should be adjusted in order to position the sample at the focal point of the light beam, with the smallest beam area and sharpest beam edge. The size of the light beam is around 0.5 X 2 *mm* while the solar cells made in our lab are 2 X 3 *mm* with a relatively large isosceles triangle front contact in the center, as shown in Fig. 5.12, which definitely needs to be avoided in measurement due to reduced exposure area. Consequently, for comparable results, the light beam position always needs to be placed in a similar spot on different samples (e.g. always on the right side of the sample without any portion reaching the center triangle or falling out of the device's working area). Due to the fact that the light port is right on top of the sample, around 10-15 *cm* distance, it is hard to mount an amplifier to check contact. It is, therefore, necessary to check the connection via a multi-meter in order to make sure that all the probes are well contacted before scanning the spectrum; which may take a few minutes. For example, when one probe is delicately touching the front contact, it should create voltage difference (V_{oc}) while the other probe is either touching the metal stage (for traditional devices) or the handle (for lift-off devices where it acts as back contact) while under illumination.

This work compares IQE and EQE performance for 3 cell configurations: a thinned device with Au back reflector, a thinned device without the back reflector, and a lift-off cell with an Au reflector. And these 3 configurations are processed on cells which have the same structure and were fabricated in the same growth. The device MBE 216 is an upright grown solar cell with MQW embedded, as demonstrated in Fig. 5.20. As can also be seen in Fig. 5.20, the final device is quite complex and is simply sitting on Au-coated handle without any adhesive material which makes it difficult to remove the contact layer. If we tried to remove the contact layer, the small piece of device would simply peel off from the handle as it is immersed in the etchant or rinsed by water. Therefore, the contact layer is left for lift-off cells. Therefore, to maintain comparability, we did not remove the contact layer from the thinned cell.

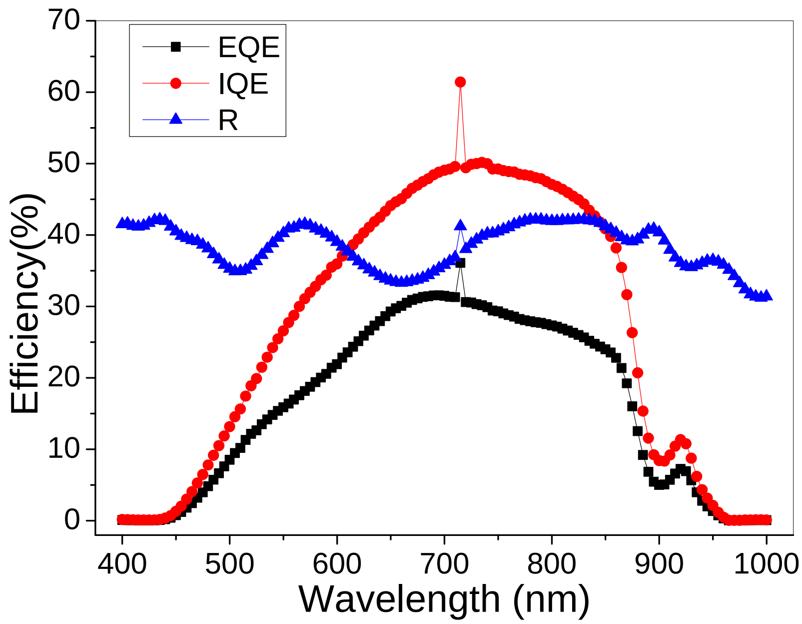

Fig. 5.13 QE measurement of MBE 216 thinned device without Au

As seen in Fig. 5.13, there is a peak around 720 *nm* for sample MBE 216. This is because of a change of filters through the wide band scan. Non-zero EQE/IQE above 870 *nm* is obviously shown in Fig. 5.13, which is the response from the AlGaAs quantum wells (QWs) and indicates an effective QW growth. The device has almost no response for the spectrum under 450 *nm* and the IQE is no more than 55%; this is due to the remaining contact layer (high doped GaAs) absorbing photons. Meanwhile, there is no AR design, which makes the reflection loss fluctuate around 40%.

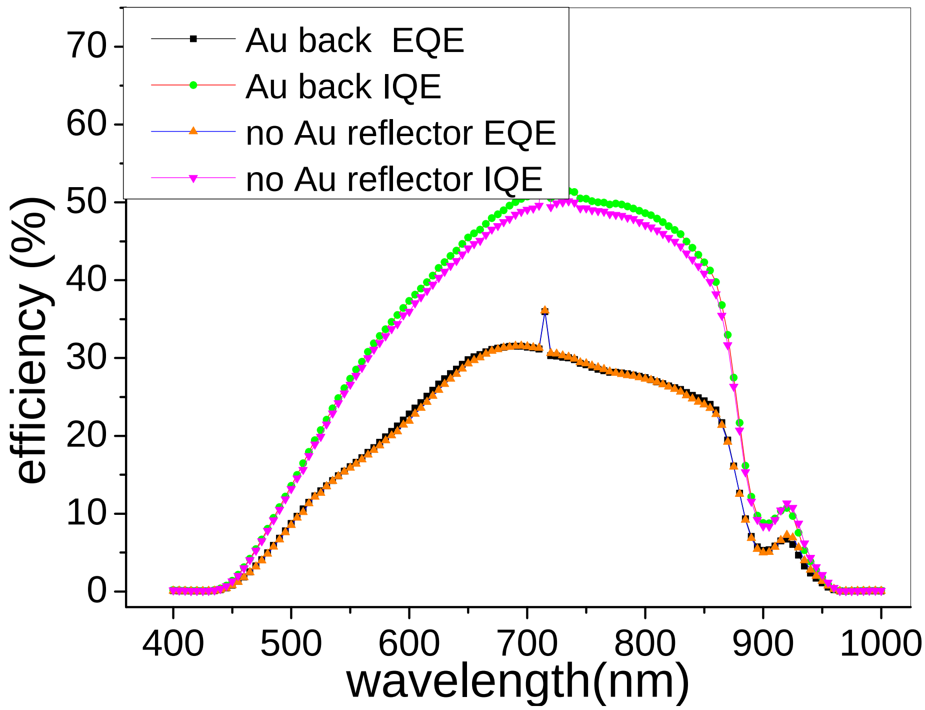

Fig. 5.14 Comparison of EQE and IQE for MBE 216 thinned device with/without Au reflector

By comparing the IQE and EQE for the thinned device MBE 216 (Fig. 5.14) with and without Au back reflector condition, the sample with Au reflector has slightly higher IQE- up to absolute 2% higher in GaAs working spectrum- corresponding to 4% improvement. This improvement results from the Au back reflector causing a longer light path within the devices, leading to higher absorption. The EQE improvement, however, is not as significant due to substantial reflection losses. However, it should be noted that the quantum efficiency in the QW spectrum is very close under these two conditions. This may be because of an intrinsically low value in QE; consequently 4% of 10% improvement is not quite detectable.

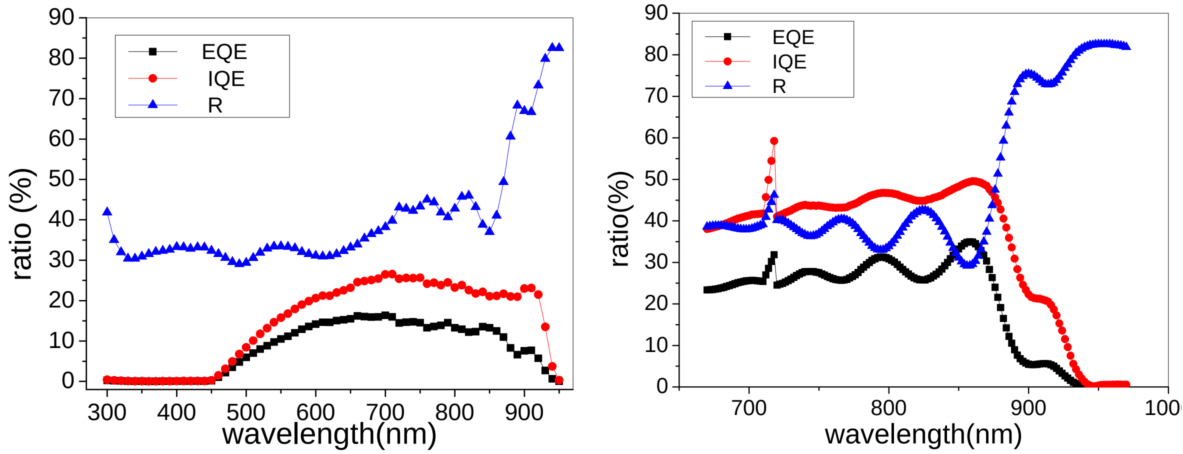

(a) (b)

Fig. 5.15 EQE/IQE and reflectivity measurement of MBE 216 lift-off cell: (a) rough scan; (b) precise scan

The reflection loss below GaAs bandgap becomes exceedingly high, approaching 85%, which is abnormal for common semiconductor-air interface. Since common semiconductor-air interface reflection calculations are assuming infinite thickness of semiconductor and result in 30-40% reflection; this doesn't fit lift-off device situation whose thickness is around 2 μm. Consider energy conservation, light was absorbed slightly above 872 *nm,* contributing to IQE. Au has almost ideal reflection behavior in the infrared region; thus, the remaining light which reaches the lift-off film and Au interface is reflected back to air as final reflection shown in the blue curve of Fig. 5.15. Therefore, the reflection loss is high because of low absorption. From the precise scan displayed in Fig. 5.15 (b), there are obvious fringes in the deep red spectrum region, just as calculated in Fig.4.2 from literature. This phenomenon is from a light-coupling effect for different wavelengths. Because the incoming light from the air-semiconductor interface and outgoing light from Au-semiconductor interface don't have the same magnitude, the intensity of destructive interference would not reduce to zero. The ratio between (a) and

(b) is possibly because light beam reaches different positions. It can be seen that during rough scan in (a) there is larger reflection loss, which might come from the center isosceles triangle.

The fringes effect can be calculated by self-coding thin film method program, taking into account: the layer thickness, refractive index, as well as absorption coefficient, which will be demonstrated in the next sub-chapter.

Usually thin-film devices are presented to have higher performance in V_{oc} and efficiency, which is based on a different design for thin film devices with a higher doping level, where the diffusion length is not required to be as high. Higher doping levels lead to wider separation of quasi-fermi level and consequently higher V_{oc}. But these samples are from the same growth (therefore, exactly the same structure), hence the IQE from the lift-off thin-film device has a lower value. However, comparing Fig. 5.14 with Fig. 5.15, the lift-off cell demonstrated significantly higher IQE above the GaAs bandgap spectrum, which is possibly because of easier for e-h to escape in lift-off device, and no free carrier recombination in substrate.

5.3.2 Experimental data fitting with theory

The absorption coefficient in quantum well spectrum is required in order to predict the quantum well location effect for the device performance, in which case there are two approaches to get the absorption coefficient value -- experimentally measuring the grown samples' EQE and back engineering the absorption based on the structure, and theoretically calculating the value based on the design, as the quantum wells' behavior is different as that of bulk material due to quantum effect. The simulation data, as given in

Fig. 5.16, can be used directly, yet the EQE measurement data generally has a random unit which needs to be normalized.

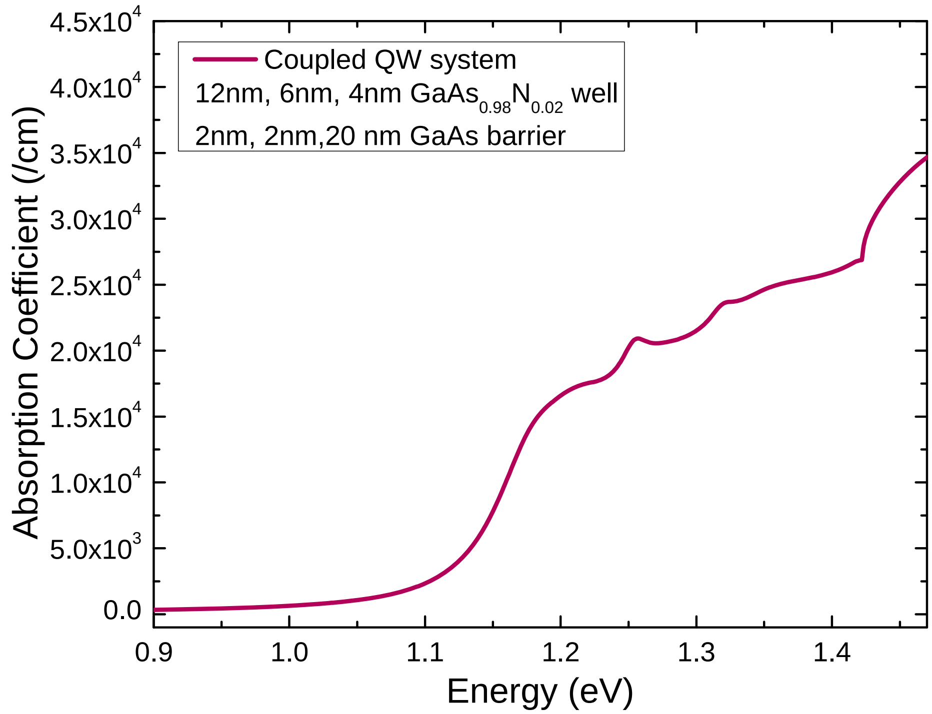

Fig. 5.16 Calculated QW absorption coefficient by 8 band k*p model

Considering that a well-designed GaAs device has nearly perfect IQE at its bandgap energy, the normalization is done by assuming there is only reflection loss (~32.5%) at the energy corresponding to the highest EQE, leading to 67.5% EQE. So the EQE at other energies is deduced by multiplying the ration of 67.5% divided by measured EQE with maximum value, as given in Fig. 5.17. By knowing the EQE and the total thickness (90 *nm*) of the wells, the absorption coefficient can be calculated by equation (5.3) with an assumption of 100% carrier extraction efficiency.

$$EQE(\lambda) = (1 - R(\lambda))(1 - e^{-\alpha(\lambda) \cdot l})$$

$$\alpha(\lambda) = -\frac{\ln\left(1 - \frac{EQE(\lambda)}{1 - R(\lambda)}\right)}{l} \tag{5. 3}$$

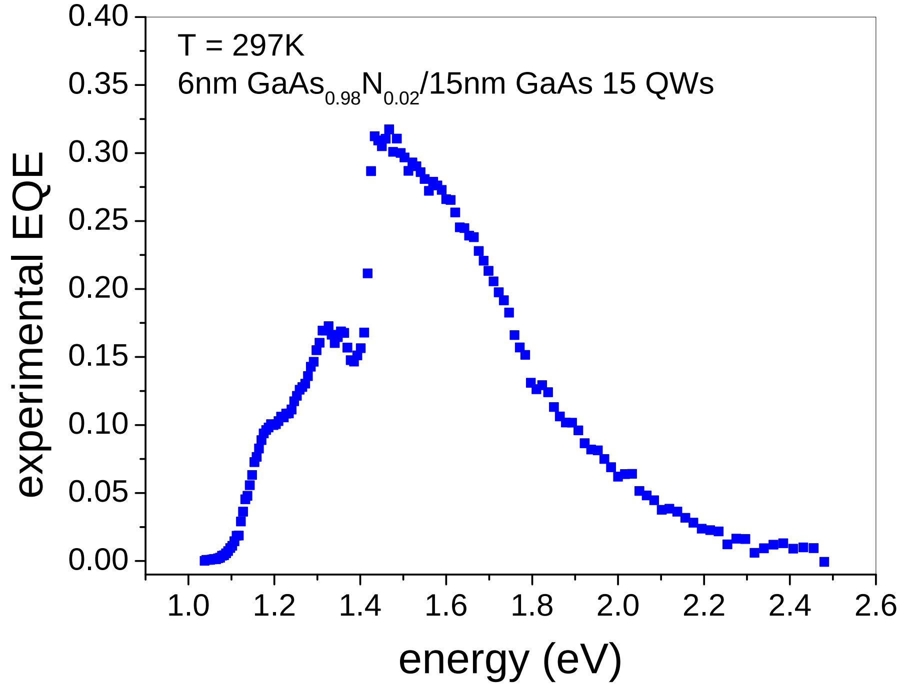

Fig. 5.17 Experimental data of dilute N QW EQE with no ARC

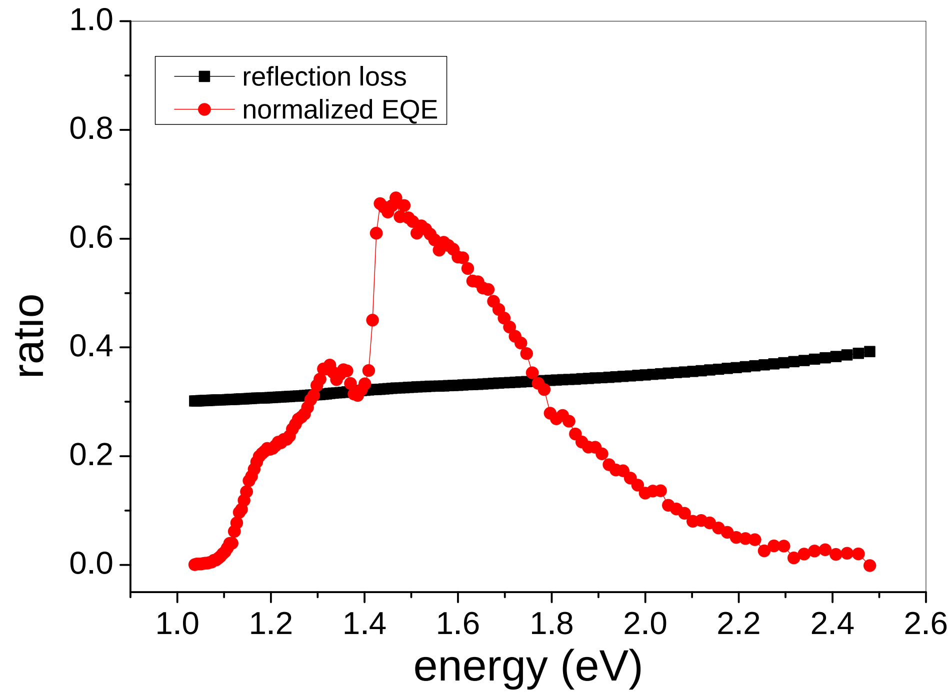

Fig. 5.18 Calculated reflection loss of GaAs substrate with no AR and normalized EQE from experimental measurement of $GaAs_{0.98}N_{0.02}$ QWs in GaAs device with back mirror

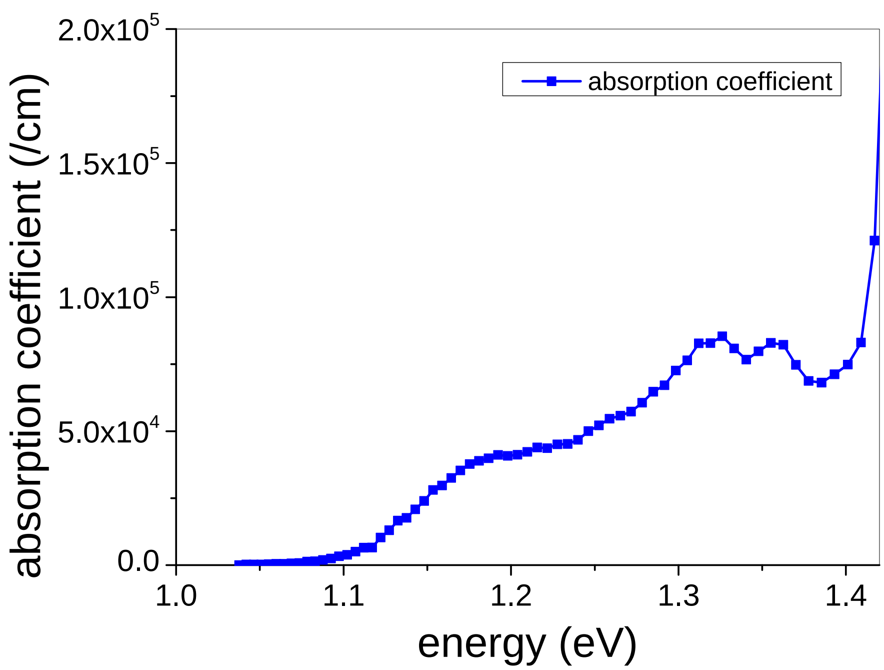

Fig. 5.19 Back calculated absorption coefficient of dilute N QWs from experimental EQE measurement in case of no back mirror

If there is a back mirror, and assuming the mirror is an ideal mirror with 100% reflection, the light path is doubled from the initial thickness, equivalently the absorption coefficient is cut into half in order to maintain the same amount of absorption as presented in equation (5.3). And if we consider the mirror as a diffused mirror, with around 55% reflection for example, the light path is increased to 1+55% of the original thickness; consequently the absorption is 1/(1+55%) of the value calculated from no mirror assumption.

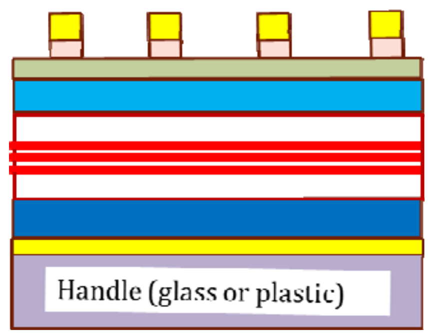

Fig. 5.20 Scheme of lift-off MBE216 GaAs 1J device with InGaAs MQW

During the simulation, the variable is tuned around the fabricated device's parameters. For example, the total thickness is fixed as 1.5 μm, with 15 QWs in the i-region (thickness of InGaAs wells being 6 nm, thickness of GaAs barriers being 15 nm), and emitter thickness varies from 0.20 to 0.35 μm. Note: the distance from back mirror to QW position can vary by adding integral wavelength for similar optics behavior, yet it requires the distance to be short in order to lose coherence; otherwise the model would loses its validity. Similarly, as the protection glass on solar cell modules, in micro-meter range, it is treated as a medium rather than an AR coating; since the light reflected from solar cell-glass interface is no longer coherent with incoming light from glass-air interface.

The simulation work was done by using thin-film method based on transfer matrix which changes the parameters of base thickness, well thickness, and back reflector's refractive index (leading to different reflection coefficient). Considering the MBE system doesn't directly give the growth thickness, which is controlled by growth temperature and time, the actual growth thickness simulated from thin film method is back engineering to calibrate the system. The growth plan consisted of a 1300 *nm* base and a 3 *nm* well thickness. Note, this GaAs with InGaAs quantum well lift-off cell is measured without ARC or window layer removed.

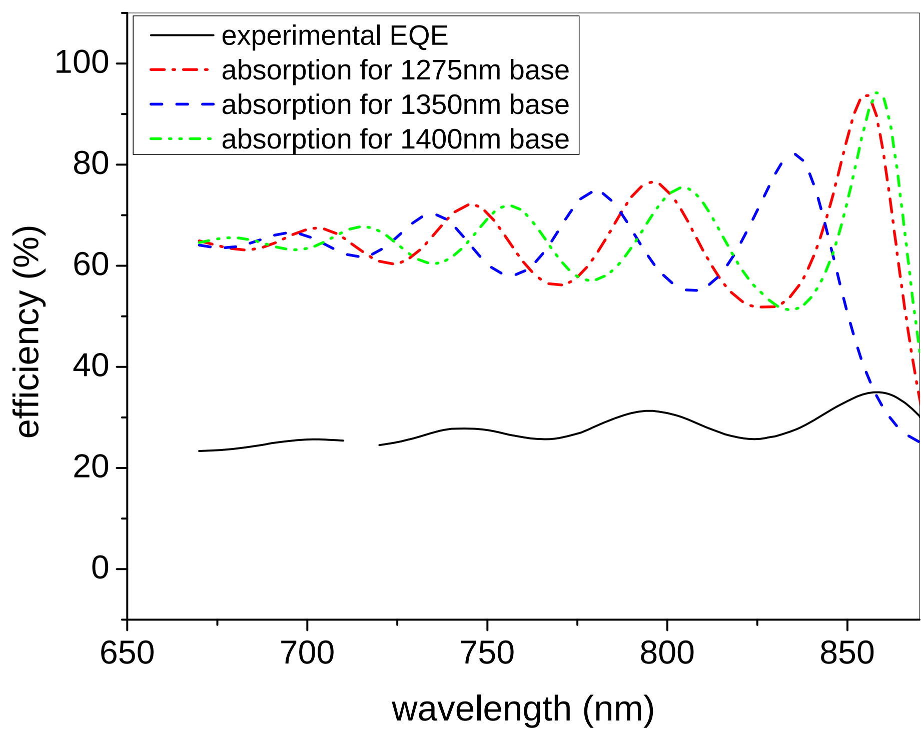

(a)

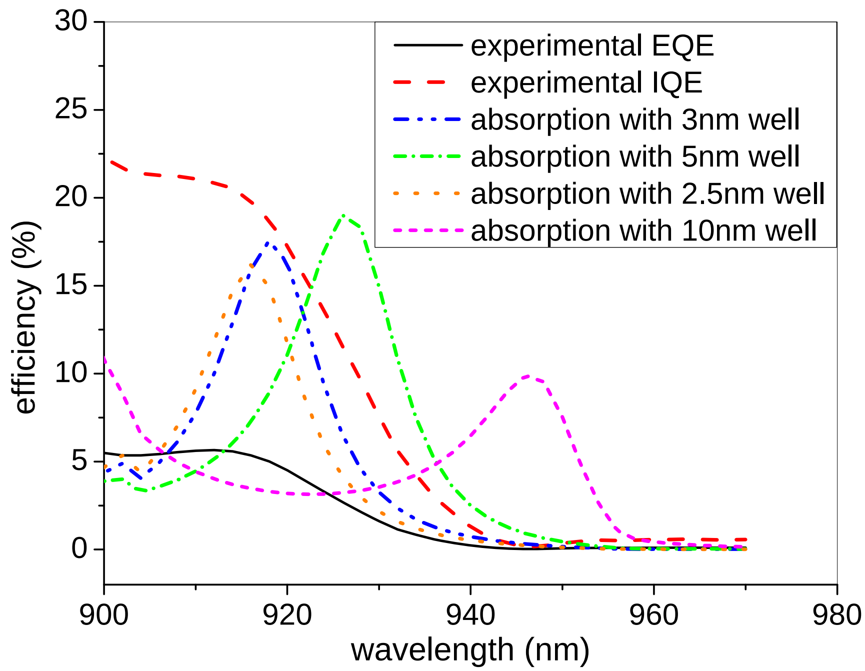

(b)

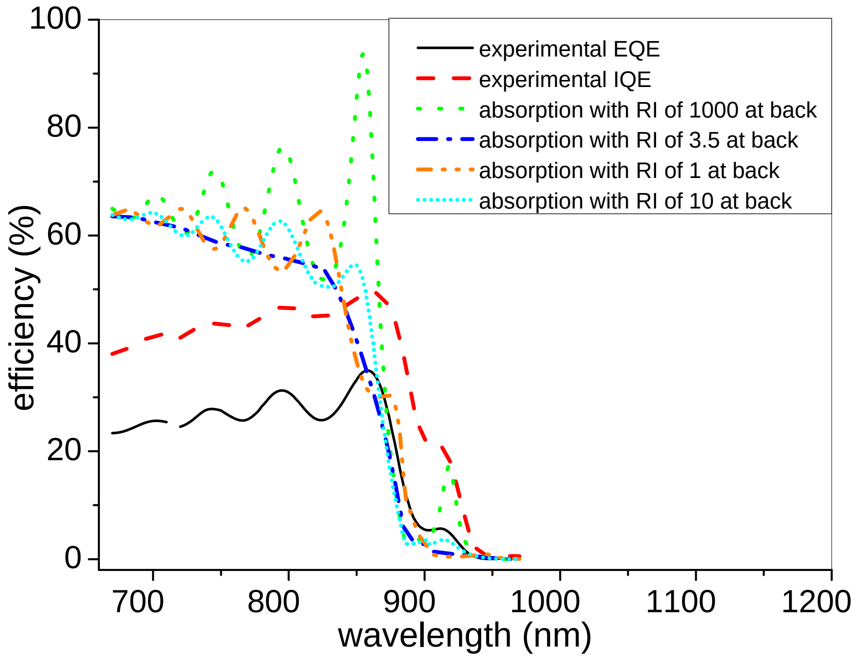

(c)

Fig. 5.21 Experimental EQE compared with simulated absorption coefficient (a) according to various base thicknesses; (b) according to various quantum well thicknesses based on fixed bandgap; (c) according to various reflections on back surface.

From Fig. 5.21, it can be seen that the base thickness affects the EQE peek position as well as the oscillation period versus wavelength. If the back reflector has 98.6% reflection, 1275 *nm* gives the best fit in GaAs working region. To better compare experimental EQE and simulated absorption, EQE was multiplied by 2 in (b) and (c) to oscillate in the same region. From Fig. 5.21 (b), it can be seen that the well thickness determines where the peak absorption happens in the quantum well working spectrum. A thicker well leads to a peak at longer wavelength. The bandgap of the quantum well is measured from PL, indicating 1.32 *eV*. From Fig. 5.21 (c), it can be seen that the material behind solar cell device determines the oscillation amplitude due to light coupling. Peak/valley ratio determines reflection on the back surface. Both air at back or material with refractive index of 10 gives 28% reflection, yet there is a pi phase difference in the GaAs region. Considering Au is highly reflective material, it is very likely that there is an air gap between Au handle & lift off cell. This was confirmed in SEM image, as seen in Fig. 5.28 (c).

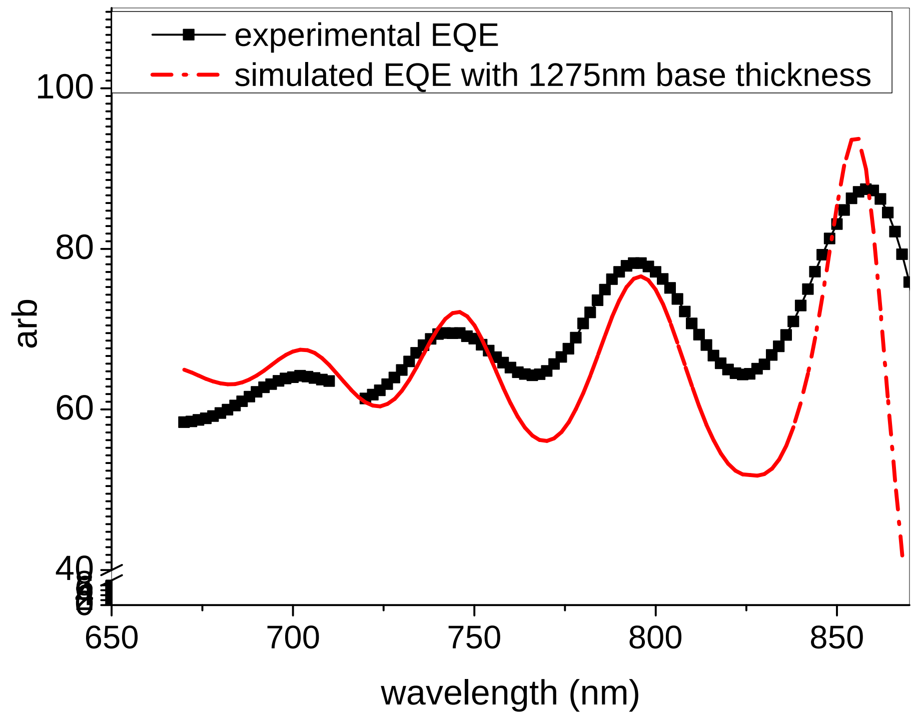

Fig. 5.22 Comparison of simulated EQE with experimental EQE measurement

5.3.3 Simulation of QW positioning effect

As seen in Fig. 5.23, the reflectivity losses and absorption amount are indeed affected by the placement of the quantum wells at different depths. The best and worst positions are defined by optimizing the integrated reflectivity over AM 1.5G spectrum. Furthermore, it can be seen that the best location obviously has lower reflectivity around 1.32 *eV* compared with the worst location, which means more photons are harvested around this energy. It can be applied to QWs whose first confined energy is around 1.32 *eV* since, normally, the absorption close to bandgap is reduced dramatically and requires the most improvement. However, its overall reflection loss is not significantly lower than that at the worst position. The reflectivity for both the worst and the best position is almost 100%, which is due to the zero absorption coefficients from 1.0-1.1*eV,* as shown in Fig. 5.18 and Fig. 5.19.

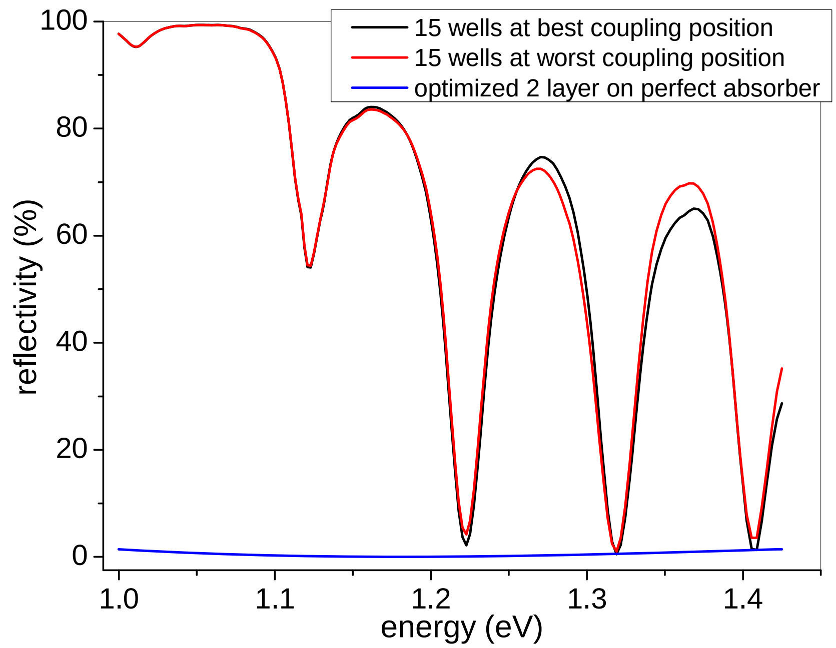

Fig. 5.23 Comparison of calculated reflection loss in case of 15 wells located at optimal best coupling and worst position

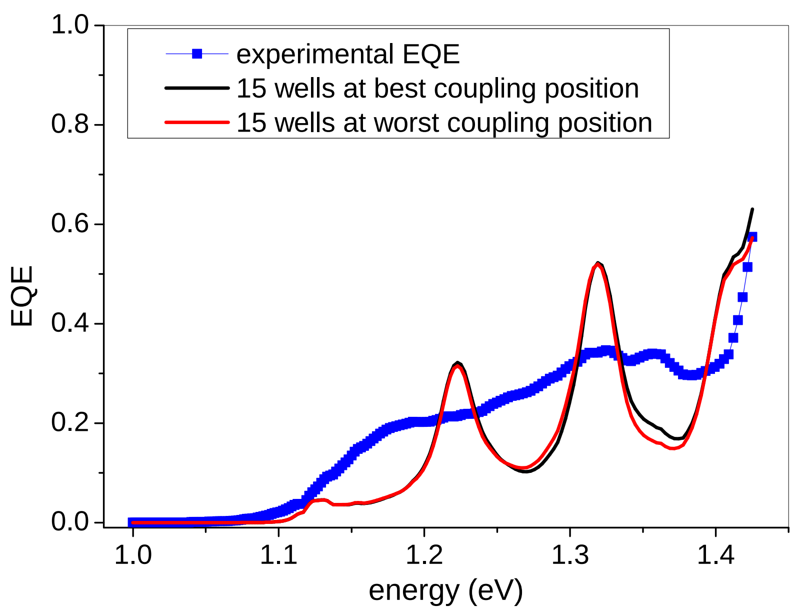

Fig. 5.24 Comparison of calculated EQE with back mirror and without AR in case of 15 wells located at optimal best coupling and worst position

Fig. 5.23 demonstrates how the continuous 15 QWs' position difference affect the device's reflectivity. As is shown by the red and black curve, there are obvious absorption peaks at 1.22 *eV,* 1.32 *eV,* and 1.41 *eV*, which are at the optimal light coupling positions. However, photons at other energy band are highly reflected. Therefore the reflectivity curve shows fringes. By comparing the black and red curves, the best coupling position has lower reflection around 1.27 *eV*, yet with higher reflection around 1.36 *eV*. The red curve indicates overall slightly better performance mainly due to non-uninform spectrum, lower intensity at higher energy. Fig. 5.24 shows what the EQE would be in these two conditions and compares it with the experimental value shown in the blue curve. It can be seen that, the blue data doesn't actually match with simulated work, following the main trend. It might be because a perfectly smooth mirror is assumed in simulation; however, a practical back mirror is actually a diffused mirror, without a sharp interface with the semiconductor. The practical mirror hence doesn't create as significant standing wave for light coupling as an ideal mirror would. A comparison simulation results of 15 QWs located at the optimized best coupling position and worst coupling position, as well as 15 QWs splitted into 7 wells and 8 wells located both at optimized constructive or both at destructive interference positions are shown in Fig. 5.25. The difference between these four conditions is not tremendous, due to the thicknesses requirement of quantum well and barrier in order to let minority carrier tunnel through barriers. The total region of a few coupled wells and barriers would occupy both constructive and destructive coupling area, leaving little margin to optimize the overall coupling impact.

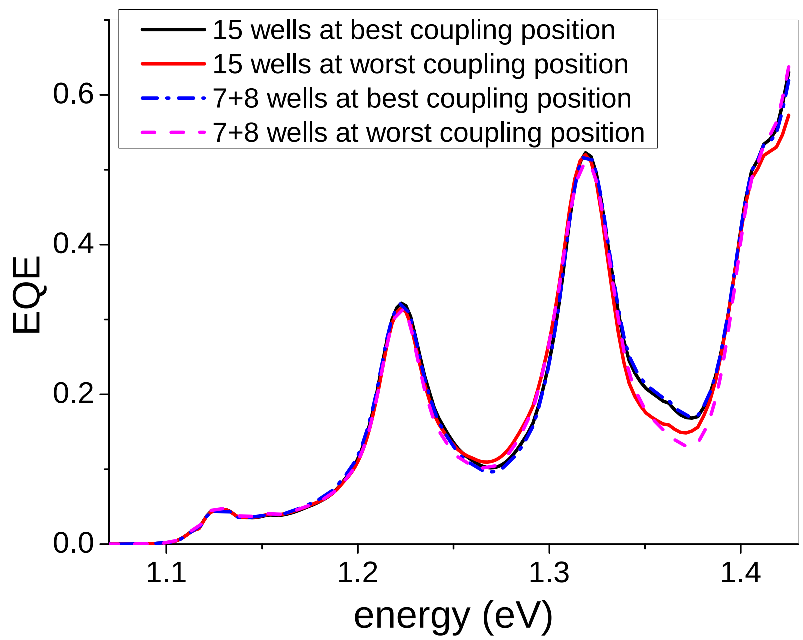

(a)

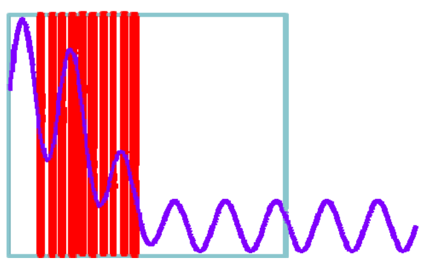

(b)

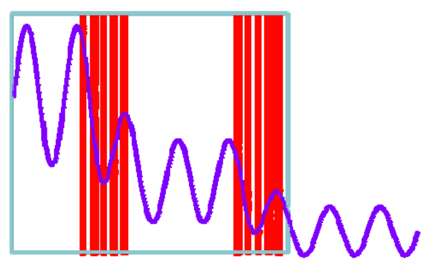

(c)

Fig. 5.25 (a) Calculated reflectivity comparison in case of continuous 15 wells located at optimal best and worst position and splitting QWs into 7 continuous plus 8 continuous wells for their best and worst position; (b) a demonstration of energy got absorbed as wave passing one set of continuous wells; (c) an example of energy got absorbed as wave passing 2 sets of continuous wells

By adapting this simulation method with the drift diffusion model to obtain IQE/EQE for 2J devices, including QWs in the bottom cell, with thin-film-method to calculate how devices would behave based on their individual cell's bandgap, emitter and base thickness, defects level, diffusion length, and reflection loss at each wavelength. Fig. 5.26 demonstrates EQE and IQE from a GaInP/GaAs 2 junction device without QWs, whose emitter thicknesses are 30 *nm* and 150 *nm*, and whose base thicknesses are 1000 *nm* and

3000 *nm* for top cell and bottom cell respectively. The optimized ARC bi-layer used in this simulation is 102 *nm* MgF_2 on top of 74 *nm* ZnS for AM1.5G spectrum. First, it can be seen that IQE is around 5% lower than GaInP sub-cell, and 3% lower in GaAs sub-cell who is the current limiting cell. So it also shows that the ARC was designed to lower the reflection loss in GaAs sub-cell.

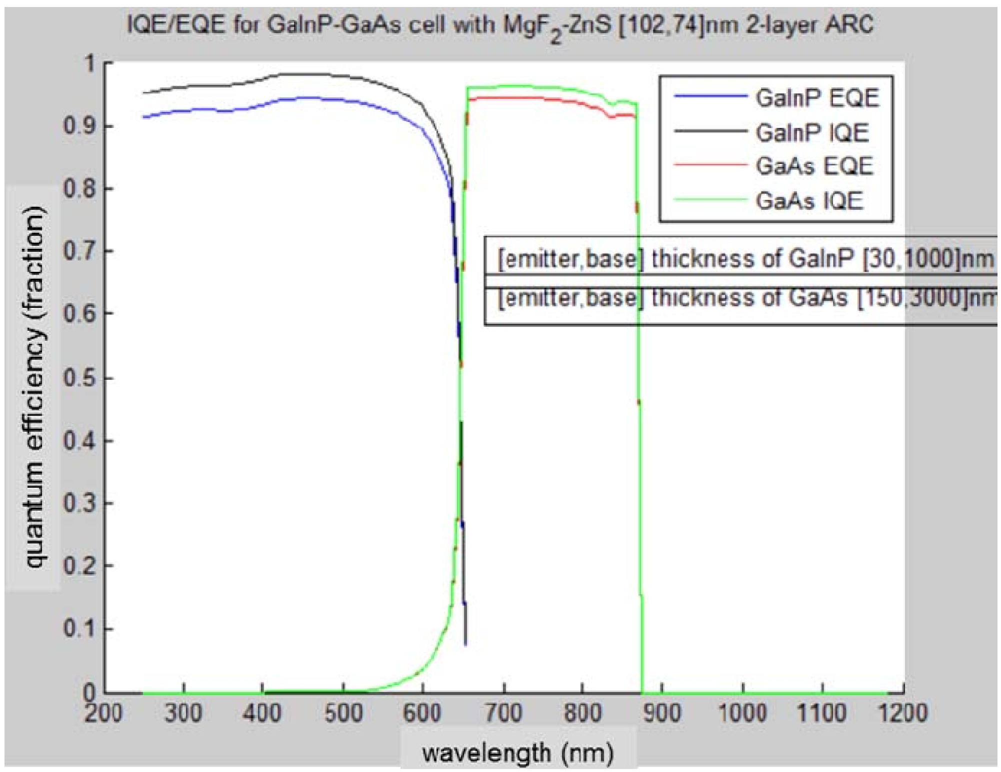

Fig. 5.26 EQE/IQE simulation on 2J GaInP-GaAs device with optimal bi-layer ARC from drift diffusion model and thin film method

5.4 Experimental designs for light management process

The difference of using coherent mirror and designing the QW's location as the four conditions discussed in chapter 5.3.3 is not tremendous, which leads us to the implementation of incoherent reflectors to quantum engineered solar cell devices for high absorption.

5.4.1 QW SC's structure

Quantum well solar cells aim to broaden the usable spectrum for increasing current, but this will also, potentially, result in a trade-off of decreasing the V_{oc}. The primary advantage of these QW solar cells that they avoid many of the challenges associated with adding extra junctions (*e.g.*, defects, tunnel junctions, and current-match issue which degrade performance).

5.4.2 Process procedure

Epitaxial lift-off provides a viable and strategic solution towards cost reduction in III-V devices through the recycling and reuse of the substrate. A complete growth and post growth process using this technique has been developed during this work. It consists of the growth of a thin AlAs etching layer (15 *nm*) underneath the conventional epi-grown p-n junction layers. This layer can be removed in HF solution, thus allowing GaAs substrates to be recycled. Post growth processes need to be carefully designed based on the growth methods used, *i.e.* conventional upright or inverted. Both upright and inverted growth approaches, followed by post growth process metallization on lift-off ultra-thin devices have been studied. Extreme care is required during processing and general handling of these devices because their thickness (2 μm) makes them fragile. A quick sketch of this process is as follows: the inverted structure was processed through front side metallization, lift-off, and bound with Au coated handle in the end; whereas the upright structure was processed by back side metallization, bound with handle, lift off, and front side metallization in the end.

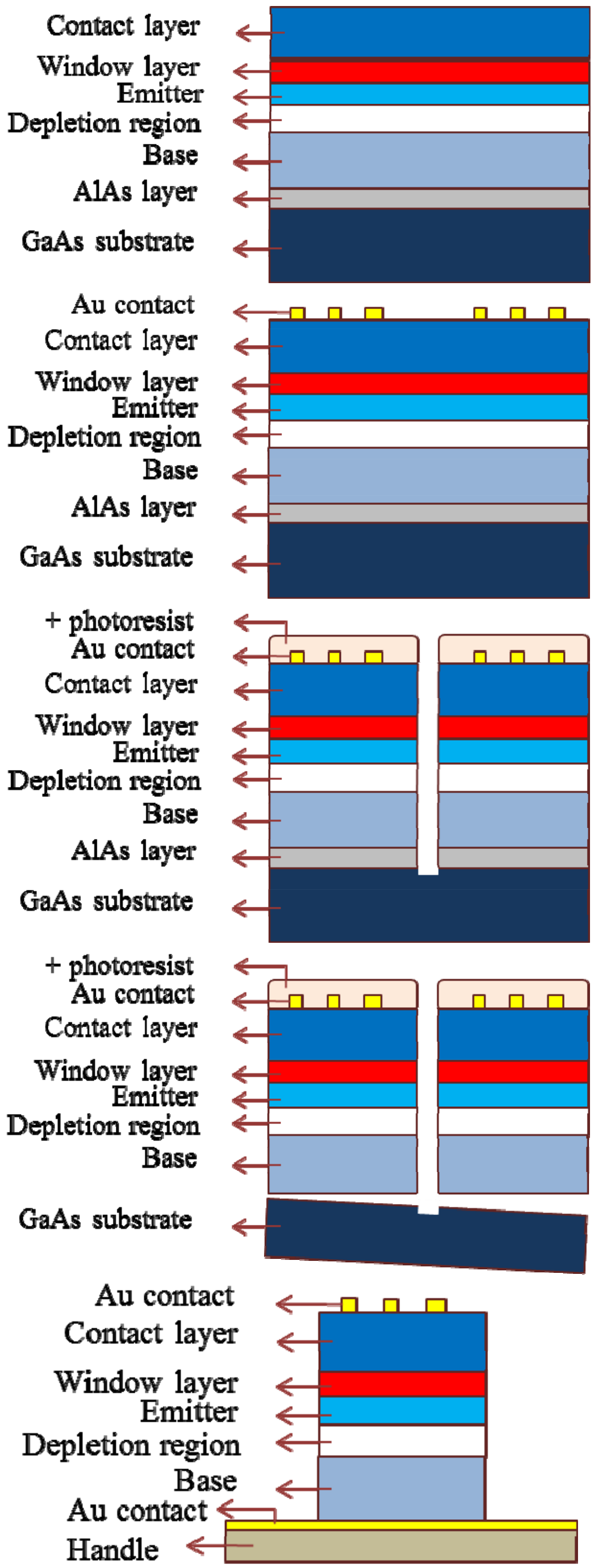

Start with conventional upright grown sample with AlAs etching layer between substrate and device structure

Front side negative PR pattern for metallization

Au deposition

Remove PR residue and extra Au on top of PR

Positive PR mesa etching pattern

Non-selective mesa etching (keep positive PR on†) by 3:2:20 H_3PO_4:H_2O_2:H_2O

Cut wafer into smaller pieces for later lift off

HF solution lift off device film into individual cells
Cells would sink under HF

Transfer individual cells into H_2O

Use Au coated handle to lift up cells from H_2O‡

(a)

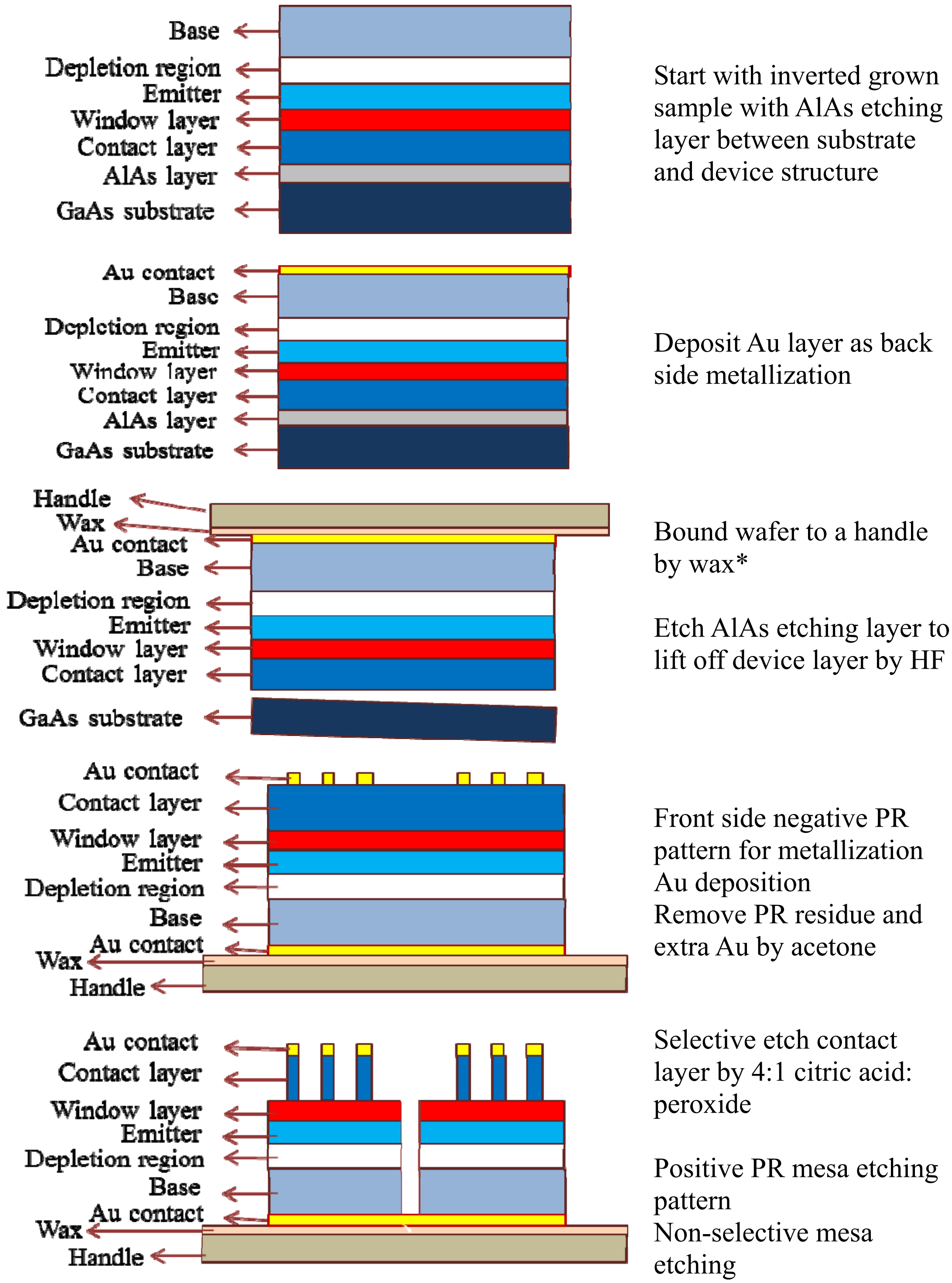

(b)

Fig. 5.27 The flow chart of post-growth processing for (a) conventional upright grown structure and (b) inverted grown devices

† During this work, I initially removed the PR and kept on the lift off etching step. However, the significant strain in the i-region forces the thin film to roll into several layers' cylinder which cannot be flattened. So I kept the PR on while performing the AlAs etching to see if it would help to keep the thin film flat. And it works!

‡ This is a very tricky and time-consuming process since the lift-off cells would either sink to the bottom of the beaker or float on the water surface. If it has sunk, one must first carefully lift it to water surface. Then, once it's floating, both handle and tweezer will push the tiny piece of sample away where it may stick to the inner wall of the beaker. After lifting the individual cells from the water, it was very likely that either there is bad contact (due simply to it sitting on the handle) or the device is shorted (because of the edge touching the handle). In the end, the positive PR was removed by acetone and low temp hot plate was used to dry the samples. Since there is no adhesive material between handle and thin film, acetone is first carefully dropped onto the thin film, being sure to not let the film move off of its handle. Nitrogen gas was not used to dry the samples because it tended to blow away the ultra-thin devices.

* During the various attempts in this work, I have tried both wax and photoresist as an adhesive medium. They both had advantages and disadvantages for the process. For example, the wax would re-melt four times during the photoresist patterning process necessary for front metallization and mesa etching. This causes the mechanically pressed flat (i.e. uniform thickness) layer of wax to become non-uniform, resulting in a warped surface. This warped surface may lead to misalignment between front contact pattern and mesa etching pattern. On the other hand, wax is stable under acetone, keeping the lift-off thin film devices adhered to the handles. Photoresist is coated uniformly by the spinner, not having a melt-challenge during baking processes. However, it contains small amounts

of water, which will form water vapor and crack the thin film during the four baking processes.

Fig. 5.27 (a) demonstrates the flow chart of post growth process based on conventional upright and inverted grown devices, converting a fully grown wafer into operating solar cells. Fig. 5.28 demonstrates the appearance of MQW devices after complete process.

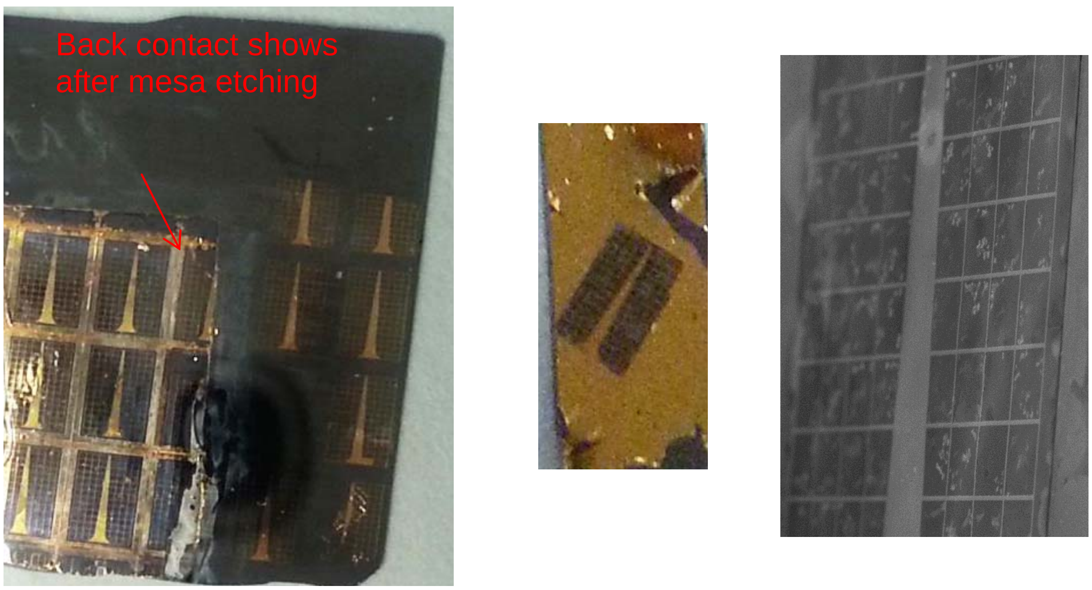

(a) (b) (c)

Fig. 5.28 The appearance of epitaxial lift-off MQW devices after post-growth processing with (a) inverted grown structure under optical microscope (OM), (b) traditional upright grown structure on Au coated handle, (c) traditional upright grown structure under SEM

The detailed growth procedures for conventional upright GaAs single junction devices includes: growing a GaAs buffer layer on the GaAs substrate, followed by growing 15 *nm* AlAs etching layer, then solar cell device, (take p-i-n device as an example, which contains n++ layer, n+ layer, depletion region, may contain QW structure, p+ layer, p++ layer, window layer and contact layer.) The respective post growth procedure with the goal of protecting ultra-thin film from exposure to multiple chemical and physical processes includes: front contact pattern (photoresist coating, soft baking, UV exposure, hard baking, developing), Au coating, Au lift off, mesa etching (photoresist coating, soft baking, UV exposure, hard baking, developing, acid etchant etching), wax bounding to a handle, HF etching to lift off substrate, warm T, boiling M, cold A to remove the glass handle, removal from solution and placed onto an Au coated handle where it is air dried and annealed. It should be noted that air dry is an inescapable step; skipping it or not allowing sufficient time to dry will cause water vapor to break the ultra-thin films during annealing.

The detailed growth procedure for inverted GaAs single junction devices includes: growing a GaAs buffer layer on the GaAs substrate, followed by growing 15 *nm* AlAs etching layer, the same as conventional upright structure growth until now. But, the coming solar cell devices need to be grown upside down.

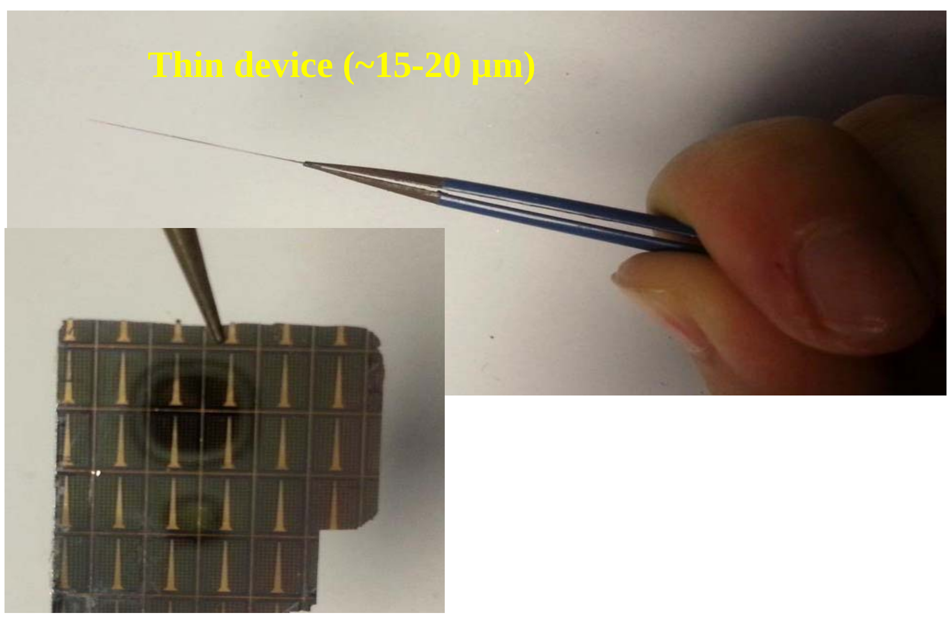

Fig. 5.29 Top view and side view of a thinned sample by etching substrate

Ultra-thin devices obviously require more tedious processing procedures, no matter which technique is used to tailor the thickness dimension. From the flow chart given in Fig. 5.27, it can be seen that it is quite challenging to apply back a textured mirror onto lift-off devices due to the low margin for fabrication. So in order to apply this incoherent reflector, there are two methods. One method is to grow a thicker layer of GaAs on top of AlAs etching layer than the conventional upright growth; so after lifting off the film, the back side has sufficient thickness for texturing. On the other hand, for inverted growth devices, a thick layer of GaAs should be grown at the end of growth- as the top layer. The other method is to fabricate on thinned devices, as presented in Fig. 5.29. In this approach, the device is going through upright growth, front side metallization, and mesa etching. Then it is mounted on a wax-coated handle, in which case the wax is melted by the heat of gliding the handle on a hot surface. So the wax won't be uniformly coated as a thin layer. Instead it will merely match the size and shape of the sample. Consequently, after putting the sample down from one edge- while it is held on the other end and pressed tight to the handle (still on the hotplate to keep the wax melted) - it is necessary to remove the extra wax. Otherwise the remaining wax on the edge will make the back side of the thinned sample into a 2D W shape, thicker on the edge due to protection from wax, also thicker in the center due to slower etching. Through various attempts, I found out that warm trichloroethylene solution is the best candidates to remove extra wax. Warm, but not boiling hot, trichloroethylene can dissolve wax without removing the samples from their handles, as in the degreasing process. Following this process, the etching can reach relatively good uniformity, slight thinner on the edge as demonstrated in Fig. 5.29.

The sample surface is divided into 4 regions under low interference angle, as shown in

Fig. 5.30, and the area of region I would increase as the interference angle increases. Since the dimension of region I's side is limited by L*tanθ, where L is the length of mirror and θ is the incident angle in experimental set-up as designed in Fig.4.4. If the pattern is well made, it should be visible by naked eye from the light diffraction effect, even though the pattern is micrometers in size. For example, region I will show changing color as the substrate is tilted in two directions along the edge. Region II's color only changes as the sample is tilted along the horizontal axis shown in Fig. 5.30 (a). Similarly, region III's color only change as the sample is tilted along the vertical axis. In this way, we can quickly and convincingly check the quality of samples without using SEM or microscope.

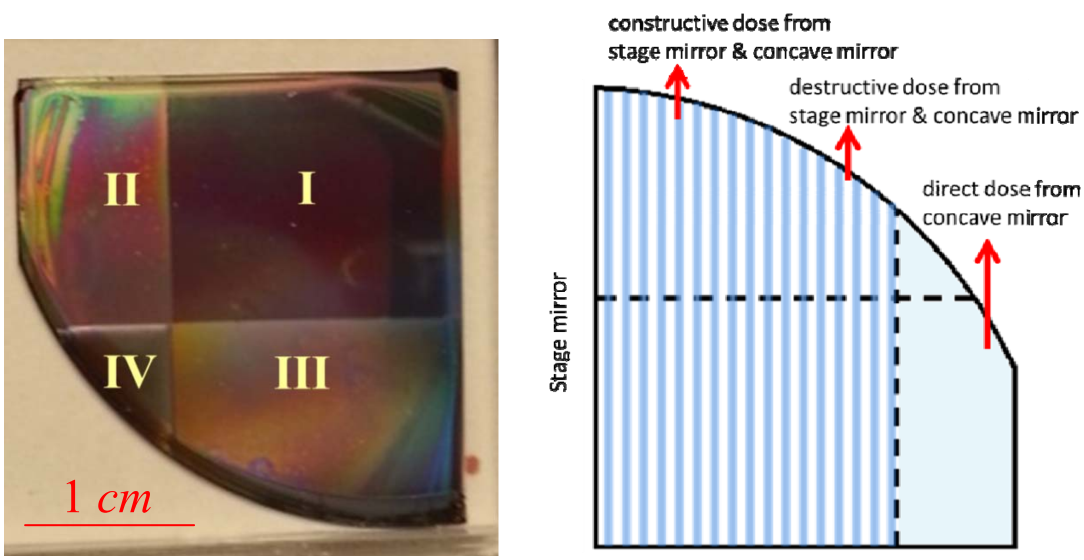

(a) (b)

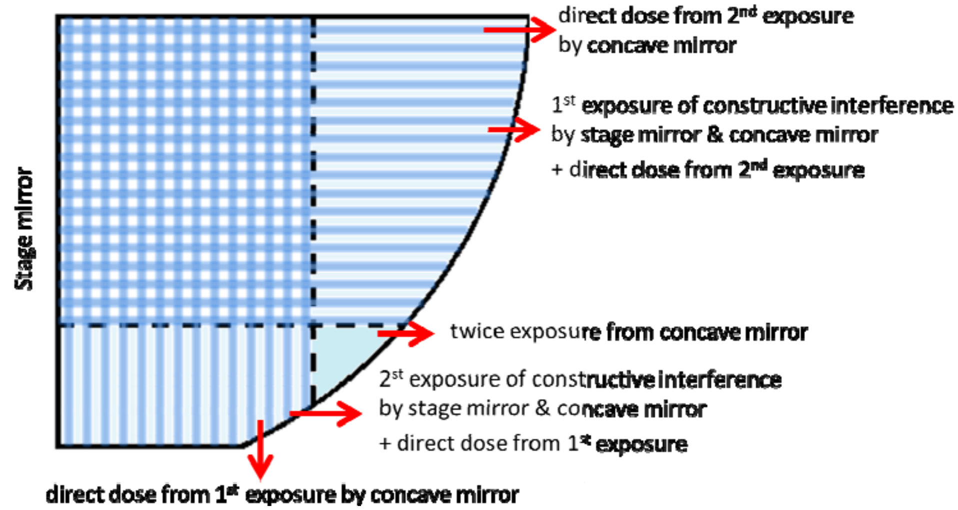

(c)

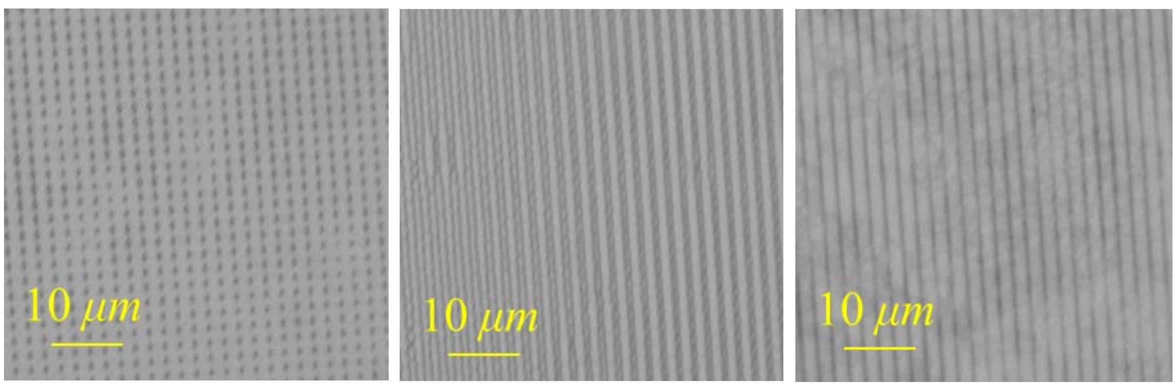

(d) (e) (f)

Fig. 5.30 MBE 220 (a) after interference lithography with PR pattern; (b) scheme and explanation of exposure amount with single time exposure; (c) scheme and explanation of exposure amount with two-time exposure; (d) after 200 *sec* wet etching in area I without PR residue under microscope, (e) after 200 *sec* wet etching in area II & III without PR residue under microscope, (f) after 200 *sec* wet etching in area II & III without PR residue on the edge of sample under microscope

Due to the laser interference lithography having limited exposure area under low incident angle, because of finite scale of stage mirror, the surface is divided into 4 regions as presented in Fig. 5.30 (a), corresponding to double interference exposure, single interference + direct uniform exposure, single interference + direct uniform exposure, and double uniform exposure from I to IV as labeled in picture respectively. Fig. 5.30 (d) shows the microscope image of 2D texture made from area I; (f) is showing the microscope image of 1D texture made from area II & III; (e) is showing the microscope image between 1D and 2D texture at area II & III after wet etching due to different exposure dose; (f) is showing the microscope image of 1D texture on the edge of area II & III where there is thicker PR, where the laser dose is not high enough to create 2D or even semi 2D PR pattern. And area IV doesn't have any pattern, since plain light beam was shinned on this area without any interference.

5.5 Summary

In this chapter I first tried to discuss whether locating QWs at the optimized coherent constructive position would increase absorption so that the post-growth process may be simplified. However from simulation and discussion, it shows that textured reflector is still needed for increasing effective light path. Second I applied light trapping techniques on solar cell devices and showed their effect on the I-V characteristic, efficiency, and EQE/IQE. Third I explained how the post-growth process should be incorporated with device structure depending on their growth technique.

Experimental lift-off cells with Au reflector have obvious EQE/IQE fringes in the infrared region, which matches with thin film method simulation. This phenomenon has been studied by drift-diffusion method in literature and is a very complicated model with heavier calculation requirements. The agreement between my results, which are based on the thin-film method, and those based on the drift-diffusion method proves that thin-film-method is an effective approach for optics related behavior. Based on experimental absorption coefficient data, this model is applied on QW positioning calculations, trying to study whether locating the QWs at the coupled constructive position would improve absorption. If it can significantly improve absorption by placing the QWs at the optimized position from coherent mirror, the post growth process of solar cells can be much easier. However, the period of constructive coupling is around 1000 *nm*/3.5/2 = 142 *nm* which is much smaller than the MQW thickness. Furthermore, the QW is absorbing a spectrum band rather than a single wavelength. This means that the QW position doesn't have as dramatic an effect on the absorption as originally expected. Textured back reflector is still needed to enhance light harvesting.

Consequently, this work designed complete growth and post growth process for both conventional upright epi-grown p-n junction and inverted devices, considering that extreme care is required during processing and general handling of their thickness (2 μm). Due to processing, special layers are need during growth (*e.g.* around 15 *nm* AlAs layer is used as etching layer for lift-off cells and InGaAs is used as the stopping layer for thinning cell), therefore, before growth the structure needs to be designed according to their eventual post growth processing.

This work specifically looked into the solar cells' behavior within the spectrum of QW region located as the bottom cell since this is the new technology to further boost efficiency with well-developed technique in top and middle cells. Also, the angular dependence reflection loss is presented by a solar cell I-V characteristic under solar simulator, which is a more convincing way to demonstrate AR effect than reflectivity measurements. Devices with ARC show 30% more current than without ARC, as well as a slightly improved V_{oc}, due to surface passivation. The details of angular dependent I-V set-up will be explained in Appendix C.

Appendix A: Galveston Project -- Optical Properties and Prospect of Solar Panels

This part is to simulate and compare theoretical output under direct sunlight for Solar World static panels, which is undertaken in five main steps.

1. Model the actual sun's position, which determines the incident angle of sunlight to solar panel, to get the intensity of radiation from blue sky.

As the earth rotating around the sun, the sun rise and sun set time varies during the year. Again, according the definition of our local time, the 12:00 AM usually is not the actual solar noon during throughout the year. So, there is way to correct the time error between local time and solar time, which is depending on the longitude, time region, the day of the year, and local time. Also, there is a difference of time region between summer and winter, in order to keep the calculation simple and straight, winter time can be used for general correction, and add 1 hour for summer time. Take March 17 as an example, which is the 76^{th} day (d = 76) from the beginning of the year 2013. So when it's 10:00 AM in local time, the local solar time can be corrected as the following, which is 9:29 AM.

Local time (**LT**): 10:00

Time difference with Greenwich Mean Time: **T_GMT** = -6

Local time maridian (**LSTM**) = 15*T_GMT=-90

Equator of time (**EoT**) = 9.87*sin(2B)-7.53*cos(B)-1.5*sin(B)=-9.0638, where, B = 360/365*(d-81)=-4.9315

Time correction factor (**TC**) = 4*(longitude - LSTM)+EoT=-30.5962

Local solar time (**LST**) = LT+TC/60=9.4901

Based on this time correction approach, any time during the year, the local solar time can be known.

2. Choose a sunny day from relatively dry season (*i.e.*, later autumn, winter and early spring), which doesn't have significant scattering due to humidity, nor clouds absorption.

Because the panel set up with emphases after 13:00, in accordance with the dry season, and sunny day requirement, March 27 is chosen to be analyzed. From the model build in part 1, the radiation intensity on March 27 is shown in Fig. A.1. the elevation angle versus hours on March 27 is shown in Fig.A.1. In consideration of modules facing south and tilt angle equal to 17.22 degree, and the panel is facing east to south 17 degree, the incident angle versus hours on March 27 is shown in Fig. A.3.

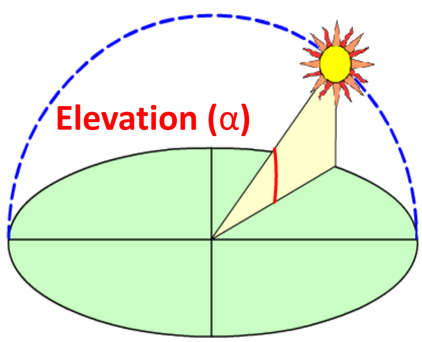

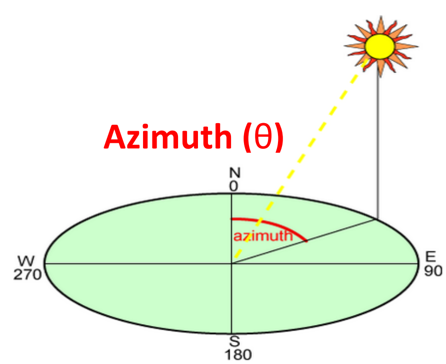

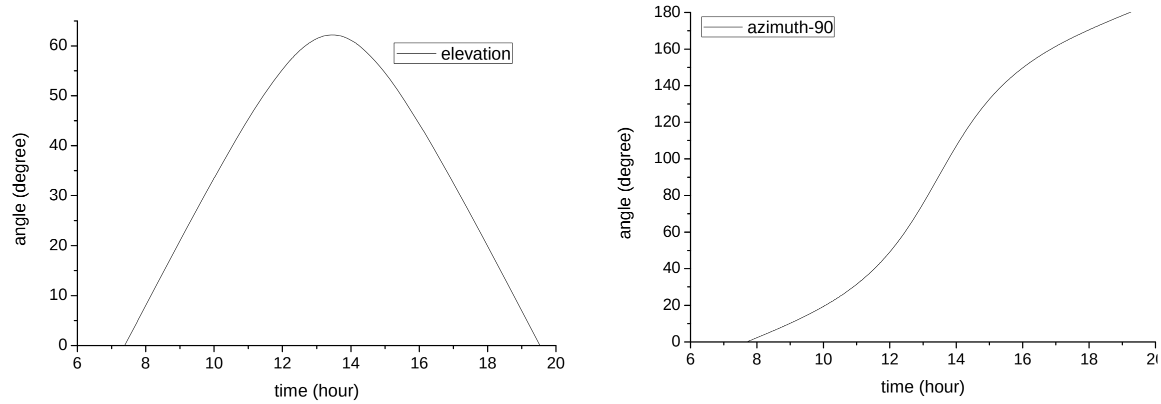

Fig. A. 1 Sunlight elevation angle and azimuth angle versus time on March 27 2013 in port of Galveston

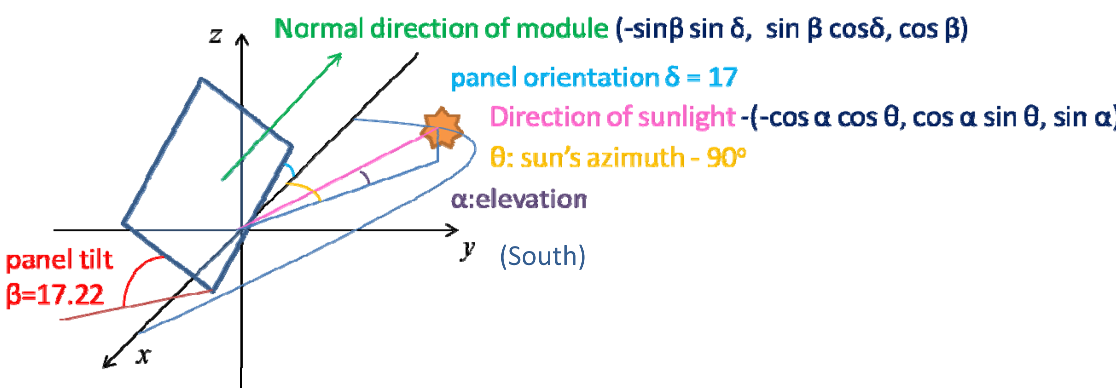

Fig. A. 2 Schematic of module installation and sunlight direction

The angle between two vectors, which are the normal direction of module and direction of sunlight, indicates that incident angle equals to acos(cos α sin β sin(θ +δ)+cos β sin α)

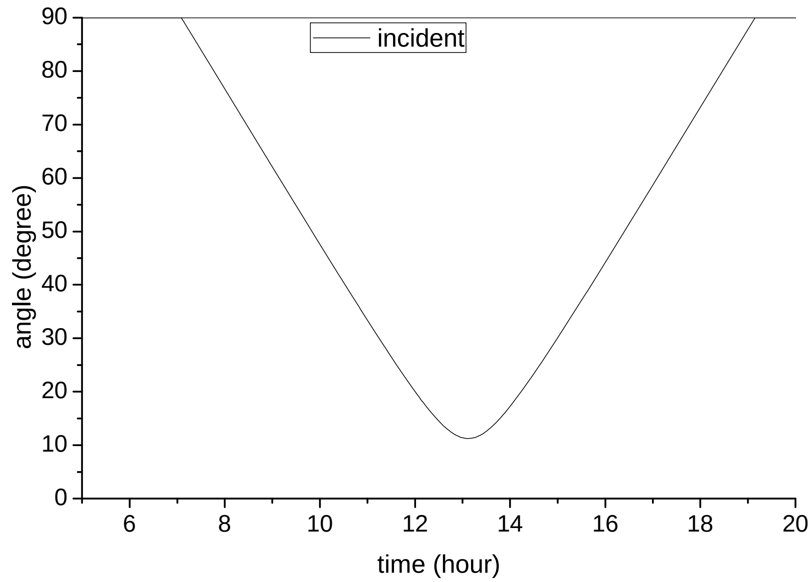

Fig. A. 3 Sunlight incident angle towards solar panel versus time on March 27 2013 in port of Galveston

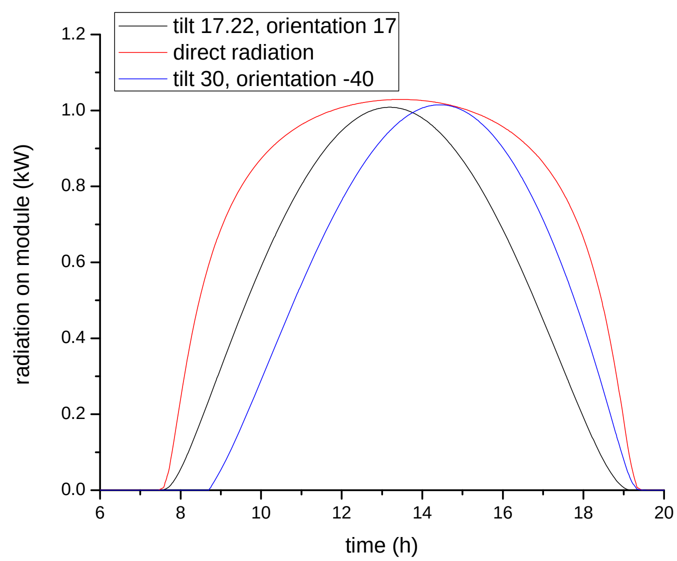

Fig. A. 4 direction radiation power compare with power reaching panel with two examples of mounting direction

3. Considering the SW using SiN ARC, calculate its the reflection loss versus hours according to specific day, which is shown in Fig. A.5 with other two AR designs.

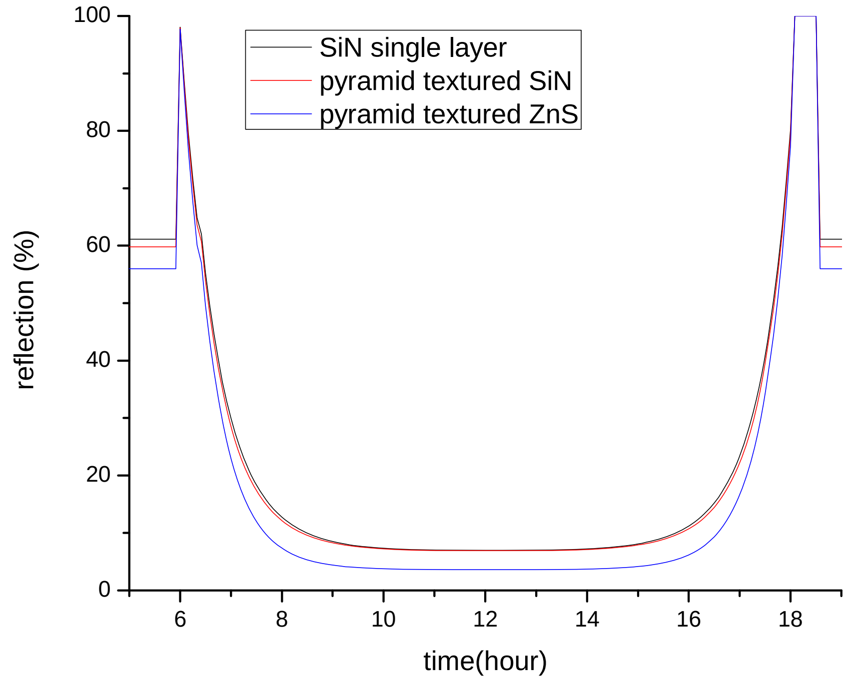

Fig. A. 5 SW 250's reflection loss versus time on March 27 2013 in port of Galveston, over 380~1120 *nm*

4.From part 2 and 3, calculate the theoretical power output and compare with measured power.

Measured output power = Incoming light intensity*area

*0.8124 (Portion of energy above 1.1ev)

*(1-reflection (incident angle, wavelength))

*cos (incident angle)

*(1-X (shadow))

*cover glass transmission ratio

*contact loss = **coe**

*IQE

*other unknown factors

Theoretical output power = incoming light intensity *area*Efficiency

The precise prediction of output power would be an integral of generated power at each wavelength over wavelength, since each wavelength contributes to different reflectivity and spectrum response. But too many unknown factors, like cover glass transmission, shadow loss, internal quantum efficiency (IQE), contact loss and so on, makes precise prediction to be impossible. So for an approximation, output power can be approached as a product of a series of integrals from each individual factor over wavelength. By treating all the unknown factors together as a new coefficient (noted as coe), the unknown parameters can be known in group. Applying this new defined coefficient back into calculation, with the reflection loss substituted by various AR design, the hypothetical panel's output power can be predicted.

Prediction of output power:

$Power_{SiNlayer}$=part*(1-$R_{SiNlayer}$)*cos(incident angle)*power*area*coe-Emit;

5. Optimize geometric parameters of pyramid SiN / ZnS grading, and simulate their reflection loss during the day. It says that SiN with 0.3 pyramid base / period ratio, 130 *nm* pyramid height, and 76 *nm* planar film underneath pyramid, the reflection loss reaches minimum, 6.9% in 380~1120 *nm* region, which is crystalline silicon solar cell working area. And similarly, ZnS with 0.7 pyramid base / period ratio, 145 *nm* pyramid height, and 58 *nm* planar film underneath pyramid, the reflection loss reaches minimum, 3.6% in 380~1120 *nm* region, which is crystalline silicon solar cell working area. Comparing the textured AR (antireflective) design with conventional single layer ARC (antireflective coating), it shows that same material texturing made from SiN presenting

almost identical reflection property. Yet higher index material made from ZnS presents obvious AR property. Their reflection properties are shown in chapter 3.

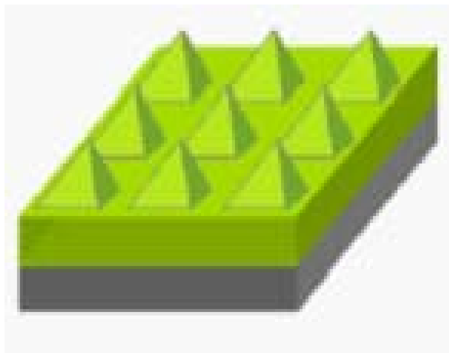

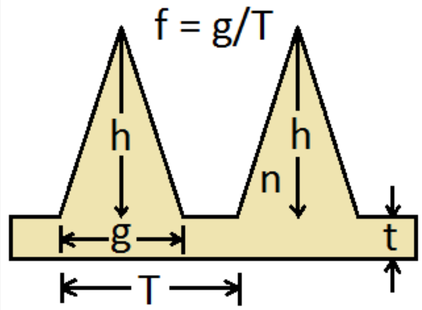

From part 2 and part 5, calculate the theoretical power output if SiN ARC is replaced by SiN pyramid grading or ZnS pyramid grading.

power_SiN = part*(1-R_SiN)* cos (incident angle)*power*area*coe-Emit;

power_ZnS = part*(1-R_ZnS)* cos (incident angle)*power*area*coe-Emit;

From the value of DC voltage and DC current, it indicates that 60 (156mm*156mm) individual cells are series connected. So the thermal emition can be calculated from the temperature measured, as shown in Fig. A.5, which is ignorable comparing with output power.

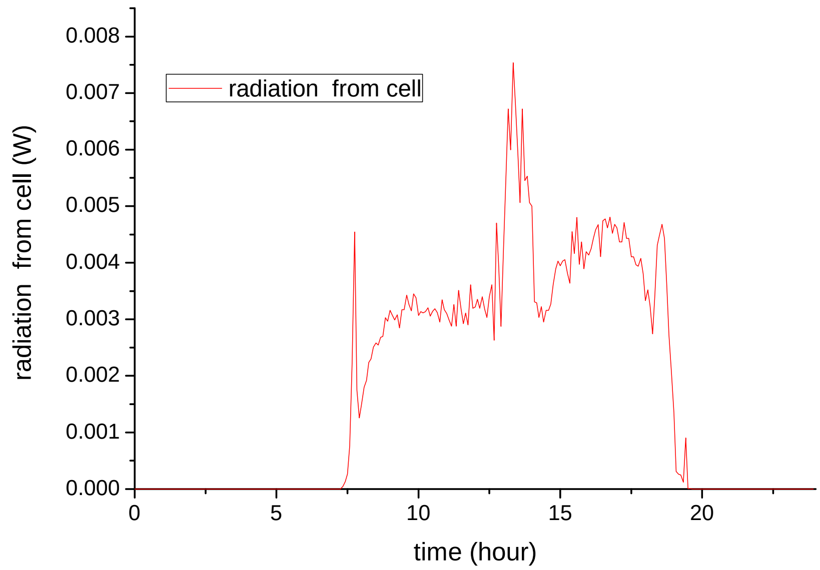

Fig. A. 6 Thermal radiation of SW250 on Mar. 27, 2013

All in all, the theoretical power output for Solar World static panel with SiN sinlge layer, SiN pyramid grading, ZnS pyramid grading AR design is shown in Fig. A.7. Compare with non- tracking panel, the tracking Solar World as shown in red curve, which is exactly the same model and tile angle, give significantly higher power output in the morning and afternoon time, when it presents higher incident angle. However, it shows power oscillation at peak output, which is probably due to mechanically non-ideal tracking performance. Also its output cuts at 225 W, so do non-tracking Solar World and Yingli panels, which may be due to limited ability of energy conversion from Enphase. Graded AR designs demonstrate promising power output improvement comparing with traditional planar ARC. However, incident angle is still a shortcoming for them comparing with tracking panel, which is not avoidable, because only the component of radiation perpendicular to modules can absorbed.

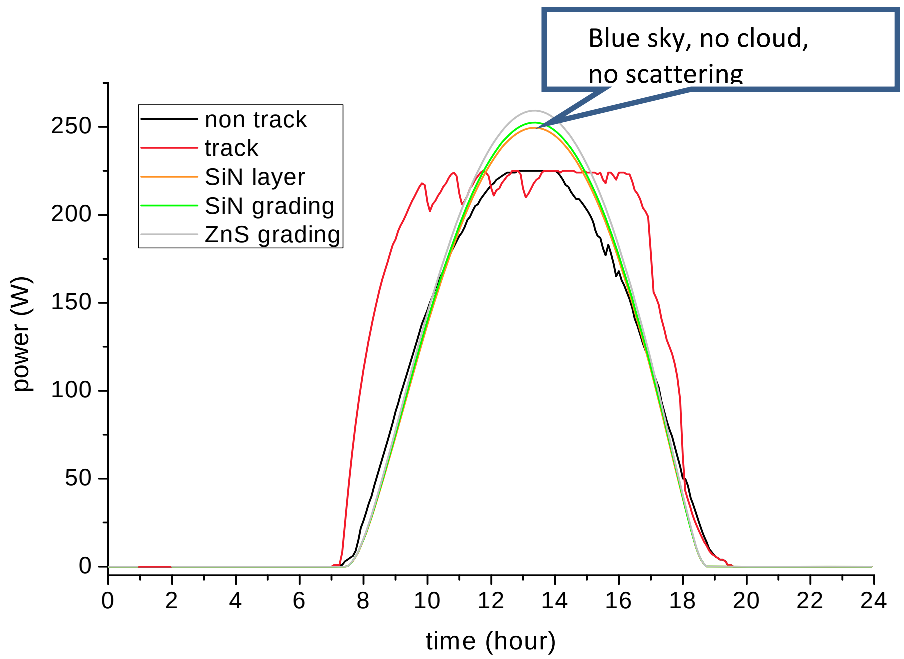

Fig. A. 7 Output power prediction of Solar World 250 mono crystalline panel's if it fabricated with well-designed AR grading, and a comparison with measured output power in both static and tracking condition

6. Generally, the goal for solar panel is to produce as much energy as possible. However in accordance with practical electricity needs, various energy consumption happens. When the tilt angle equals to 39 degree, and panel's orientation angle equals to 51 degree, the energy generated between 9:00 and 14:00 reaches maximum value on the day of March 27, which is 4.66 kWh. Similarly, if there is more demand before 13:00, the installation of panel can also be adjusted. When the tilt angle equals to 55 degree, and panel's orientation angle equals to 69 degree, the energy generated reaches maximum value on the day of March 27, which is 5.16 kWh. Also, if there is more demand after 13:00, when the tilt angle equals to 35 degree, and panel's orientation angle equals to -42 degree, (where the minus sign means panel facing to west, and south to west 42 degree) the energy generated reaches maximum value on the day of March 27, which is 3.52 kWh.

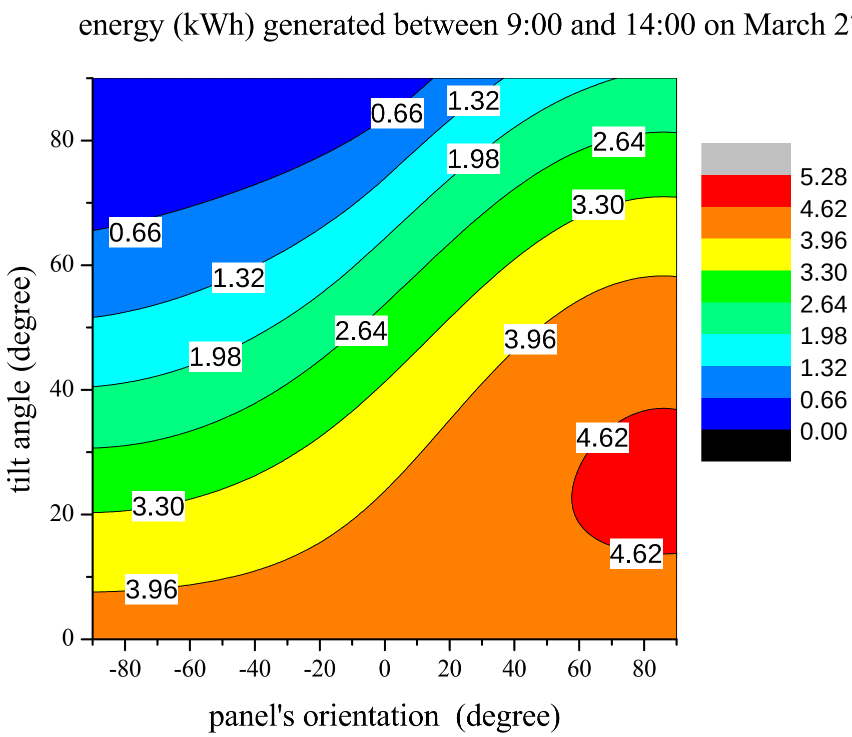
energy (kWh) generated between 9:00 and 14:00 on March 27
tilt angle (degree)
panel's orientation (degree)
0.66
1.32
1.98
2.64
3.30
3.96
4.62
5.28
0.00
-80
-60
-40
-20
0
20
40
60
80

(a)

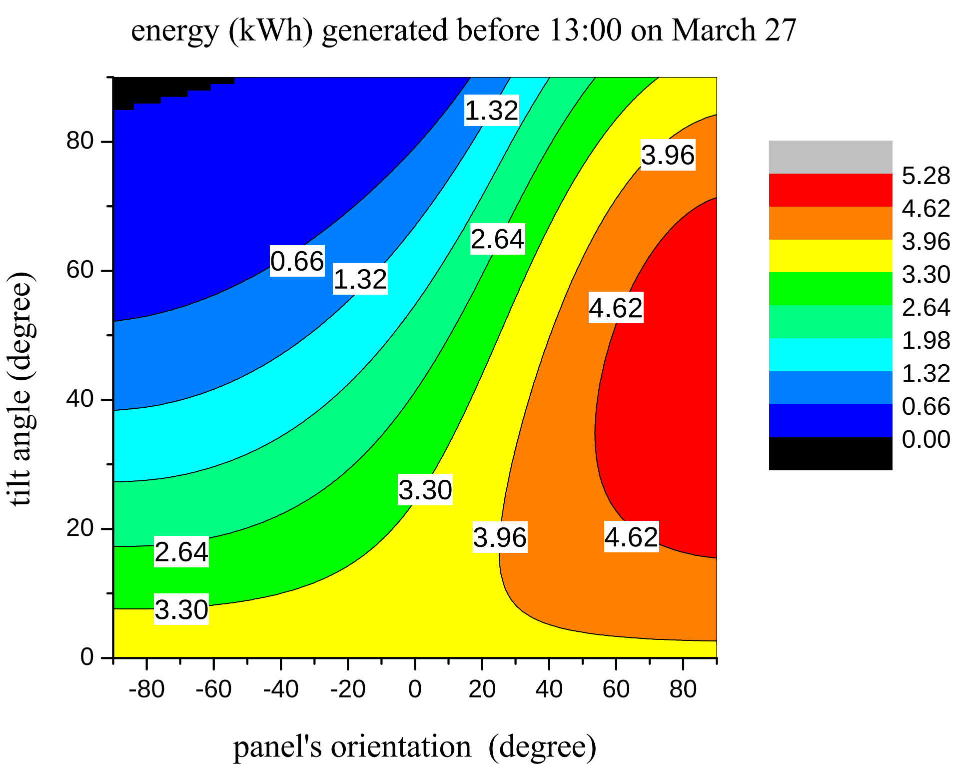
energy (kWh) generated before 13:00 on March 27
tilt angle (degree)
panel's orientation (degree)
0.66
1.32
1.98
2.64
3.30
3.96
4.62
5.28
0.00
-80
-60
-40
-20
0
20
40
60
80

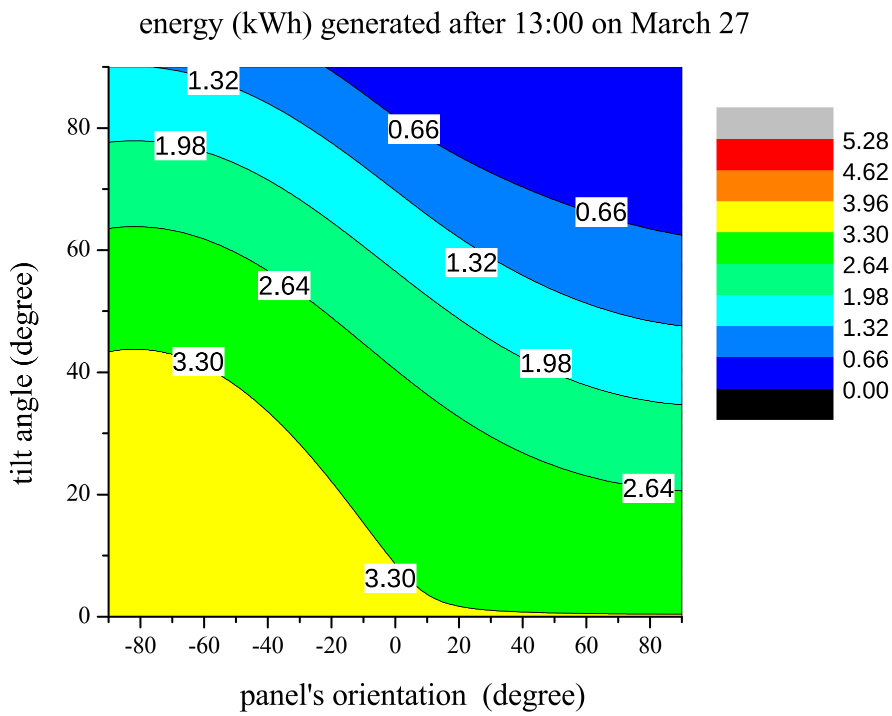

Fig. A. 8 optimization of solar panel's tilt and orientation angle to get maximum energy (kWh) for specific time demand (a) between 9:00~14:00 solar time (b) before 13:00 solar time (c) after 13:00 solar time

Rainy/hazy day, humid weather, Oct. 20

On an ideal hazy day, when diffusion scattering causes the radiation from all the direction is equal

$$\text{Measured power} = \text{incident light intensity} * \text{effciency} * \text{area}$$

$$\text{incident light intensity} = \int I_i(inc_i)\, \mathrm{d}inc$$

$$= \int I0*(1-R(inc_i))*\cos(inc_i)\, \mathrm{d}inc$$

Appendix B: Refractive index profile of textured surface

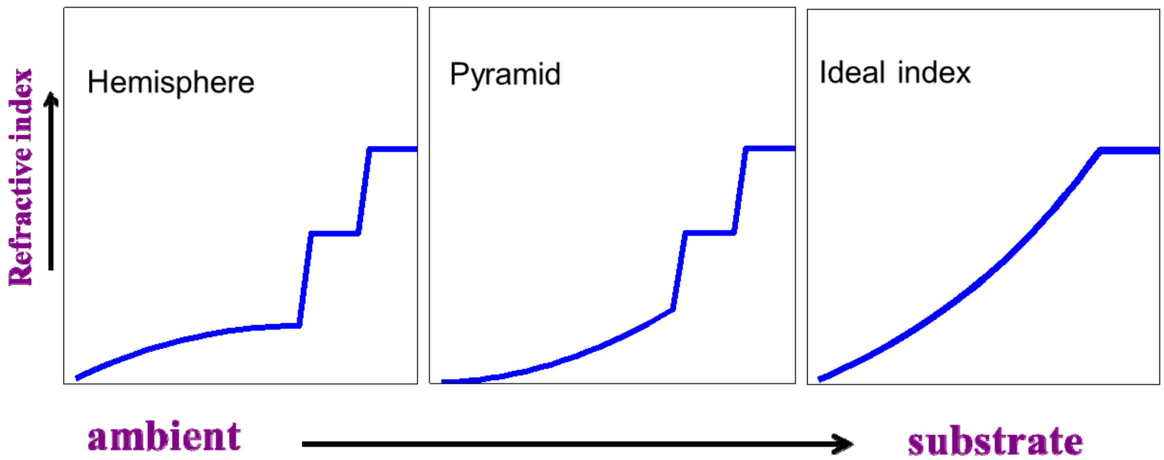

Fig. B.1 refractive index profile from air to substrate

As Fig. B.1 shows that the effective refractive index of 2D hemisphere and pyramid slowly changes from 1 to a greater value which is between the refractive index of air and the textured dielectric material. Due to non-full occupied structures, there is a step which corresponds to the bottom of texture to a planar dielectric AR film. Then there is another step coming from dielectric high index material to semiconductor interface. Compared with the ideal index profile, pyramid structures share the common feature of positive 2nd derivative, while hemisphere structures possess negative 2nd derivative, which makes 2D pyramid grating has better anti-reflective property. Because the refractive index of the dielectric material is smaller than that of the semiconductor, rather than fully occupied sub-wavelength structures, partially occupied grating helps to compensate the discontinuous index.

Appendix C: ARC system

ARC system has been maintained and upgraded in convenience and security. For example a jack was installed to lift up the glass jar, which was initially lifted by a weight hanged on a fixed pulley. The plastic cement around strand wire got torn from long-term frication by non-suitable size between pulley and rotation axis, which created much difficulty to pull-down or lift-up the weight in order to open or close the chamber. So the new installed jack makes the open and close chamber much easier, with better alignment when put the glass jar back to the stage.

Relays for mechanical pump and diffusion pump were installed for security purposes, which control the flow of high value current by low current switches. As the original design was directly plugging and unplugging the power-supply cord every time before and after growth, electricity sparkle often happens.

The diffusion pump and mechanical pump were totally opened and cleaned up part by part in March 2012, with clean oil (250 *ml* for diffusion pump).

	
Diffusion pump got opened and cleaned	

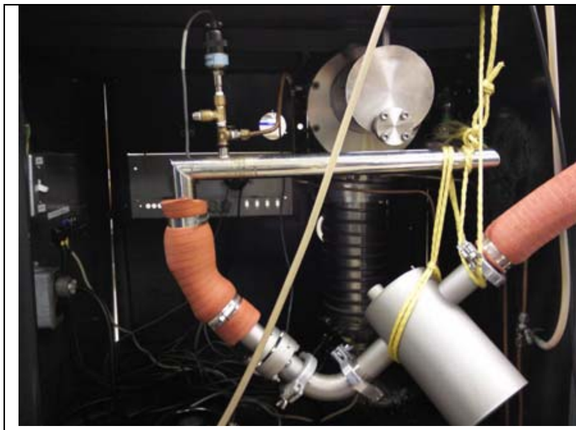	
Mechanical pump oil absorber	
	
Painted control pannel with	
	
Sandblasting the components inside chamber	

Reference

[1] W. Shockley and H. J.Queisser, 'Detailed Balance Limit of Efficiency of p-n function Solar Cells', Journal of Applied Physics, Vol. 32(3), pp.510-519, (1961)

[2] T. Trupke, M. A. Green and P. Wurfel, J. Appl. Phys., Vol.92 (7), pp.4117-4122, (2002)

[3] P. Wurfel, 'The chemical potential of radiation', J. Phys. C, Solid State Phys., Vol.15, pp.3967-3986, (1982)

[4] Alan L. Fahrenbruch and Richard H. Bube, 'Fundamentals of Solar Cells', Academic Press, 559p., (1983)

[5] A. Mehrotra, A. Freundlich, and A. Alemu, "Optimized device design for radiation resistant and high dislocation solar cells for space", Photovoltaic Specialist Conference (PVSC), 35th IEEE, pp. 2574-2577, (2010)

[6] A. Mehrotra, A. Freundlich, 'Superior radiation and dislocation tolerance of IMM space solar cells', Proc. Photovoltaics Specialist Conference, 38th IEEE, pp.3150-3154, (2012)

[7] M.A. Green, K. Emery, Y. Hishikawa, W. Warta and E. D. Dunlop, 'Solar cell efficiency tables (version 45)' , prog. Photovolt: Res. Appl. Vol.23(1), pp.1-9, (2015)

[8] E. Rosencher, 'Optoelectronics', equation (7.25), (2002)

[9] J.I. Pankove, 'Optical Processes in Semiconductors', Courier Dover Publications, 422p., (1971)

[10] L.Y. Voon, L.C. Wilatzen, M. Willatzen, 'The k p Method Electronic Properties of Semiconductors', Springer-Verlag Berlin Heidelberg, ISBN 978-3-540-92871-3, 445 pgs (2009)

Lekhnath Bhusal, PhD dissertation 'Short Period Strain Balanced GaAsN/InGaN Supperlattice Lattice Matched to InP for Mid-Infrared Photovoltaics' (2006)

[11] H.H. Hassan, 'Interband Optical Absorption in Thin Semiconducting Quantum Well Wires', J. Vac. Sci. Technol. A Vacuum, Surfaces, Film., Vol.3 (1), pp 22, Jan, (1985)

[12] W. Masselink, P. Pearah, J. Klem, and C. Peng, 'Absorption coefficients and Exciton Oscillator Strengths in AlGaAs-GaAs Superlattices', Physics Review B, no. Dec., (1985)

[13] M. Dignam and J. Sipe, 'Exciton States in Coupled Double Quantum Wells in a Static Electric Field', Physics Review B, no. Feb., (1991)

[14] A. Alemu, A. Freundlich, ‘Resonant thermotunneling design for high-performance single-junction quantum-well solar cells’, Photovoltaics, IEEE Journal of, Vol.2 (3), pp 256-260, (2012)

[15] G. Vijaya, A. Freundlich, ‘Modeling of single junction anisotype dilute nitride multi quantum well solar cell for improvement in efficiency’, Photovoltaic Specialists Conference (PVSC), IEEE 39th, pp 1089-1091, (2013)

[16] http://sundoc.bibliothek.uni-halle.de/diss-online/08/08H130/t3.pdf , last access Sept. 3rd, 2015

[17] F. Dimroth, M. Grave, P. Beutel, U. Fieldeler et. al. ‘Wafer bounded four-junction GaInP/GaAs/GaInAsP/GaInAs concentrator solar cells with 44.7% efficiency’, Progress in Photovoltaics: Research and Applications, Vol.22 (3), pp 277-282 (2014)

[18] T. Tibbits, P, Beutel, M, Grave, C, Karcher, et. al., ‘New efficiency frontiers with wafer-bounded multi-junction solar cells’ , presented at the 29th European PV Solar Energy Conference and Exhibition, 22-26, 2014, Amsterdam, The Netherlands

[19] P. Patel, D. Aiken, D. Chumney, A. Cornfeld, et. al. ‘Initial results of the monolithically grown six-junction inverted metamorphic multi-junction solar cell’, 38th IEEE photovoltaic specialist conference, Vol.2, pp1-4 (2012)

[20] J.Y. Chen, K.W. Sun, ‘Enhancement of the light conversion efficiency of silicon solar cells by using nanoimprint anti-reflection layer’, Solar Energy Materials and Solar Cells, Vol.94, pp. 629–633, (2010)

[21] Z.N. Yu, H. Gao, W. Wu, H.X. Ge, S.Y. Chou, ‘Fabrication of large area subwavelength antireflection structures on Si using trilayer resist nanoimprint lithography and liftoff’, Journal of Vacuum Science and Technology B, Vol.21, pp. 2874–2878, (2003)

[22] K. Hadobás, S. Kirsch, A. Carl, M. Acet, E.F. Wassermann, ‘Reflection properties of nanostructure-arrayed silicon surfaces’, Nanotechnology, Vol.11, pp. 161–164, (2000)

[23] C.L. Cheung, R.J. Nikolić, C.E. Reinhardt, T.F. Wang, ‘Fabrication of nanopillars by nanosphere lithography’, Nanotechnology, Vol.17, pp. 1339–1343, (2006)

[24] W. Li, L. Xu, W.M. Zhao, P. Sun, X.F. Huang, K.J. Chen, ‘Fabrication of large-scale periodic silicon nanopillar arrays for 2D nanomold using modified nanosphere lithography’, Applied Surface Science, Vol.253, pp. 9035–9038, (2007)

[25] R.Y. Zhang, B. Shao, J. R. Dong, K. Huang, Y. M. Zhao, S. z. Yu, and H. Yang, ‘Broadband quasi-omnidirectional antireflection AlGaInP window for III-V multi-junction solar cell through thermal dewetted Au nano template’, Opt. Mat. Exp, Vol.2 (2), pp 173-182, (2012)

[26] L.K. Yeh, K.Y. Lai, G.J. Lin, P.H. Fu, H.C. Chang, C.A. Lin, J.H. He, ‘Giant efficiency enhancement of GaAs solar cells with graded antireflection layers based

on syringe-like ZnO nanorod arrays', Advanced Energy Materials, Vol.1 (4), pp.506-510, (2011)

[27] K.Q. Peng, S.T. Lee, 'Silicon nanowaires for photovoltaic solar energy conversion', Advanced Material, Vol.23(2), pp.198-215, (2010)

[28] S.J. An, J.H. Chae, G.C. Yi, and G. H. Park, 'Enhanced light output of GaN-based light-emitting diodes with ZnO nanorod arrays', Applied Physics Letter Vol.92, pp.121108-121110, (2008)

[29] J. K. Kim, S. Chhajed, M. F. Schubert, E. F. Schubert, A. J. Fischer, M. H. Crawford, J.Cho, H. Kim, C. Sone, 'Light-extraction enhancement of GaInN light-emitting diodes by graded-refractive-index indium tin oxide anti-reflection contact', Advanced Material, Vol.20 (4), pp.801-804, (2008)

[30] X. Zhu, L. Wang and D. Yang, 'Investigations of random pyramid texture on the surface of single-crystalline silicon for solar cells', Proceedings of ISES Solar World Congress, pp.1126-1130, (2007)

[31] T.G. Chen, B.Y. Huang, Y.Y. Huang, E.C. Chen, P.C. Yu, and H.F. Meng, 'Fabrication and device modeling of micro-textured conductive polymer / silicon heterojunction solar cells', Photovoltaic Specialists Conference (PVSC), 38th IEEE, pp.3143-3145 (2012)

[32] J. M. Gee, R. Gordon and H. F. Laing, 'Optimization of textured-dielectric coatings for crystalline-silicon solar cells', Photovoltaic Specialists Conference, 25th IEEE, pp.733-736, (1996)

[33] E.S. Marstein et al. 'Acidic texturing of multicrystalline silicon wafers', Photovoltaic Specialists Conference (PVSC), 31st IEEE, pp.1309-1312, (2005)

[34] http://coefs.uncc.edu/jahudak/files/2011/08/AnisotropicSiEtch.pdf

[35] C.G. Bernhard, 'Structural and functional adaptation in a visual system', Endeavour Vol.26, pp.79-84, (1967)

[36] D.G. Stavenga, S. Foletti, G. Palasantzas, and K. Arikawa, 'Light on the moth-eye corneal nipple array of butterflies', Proc. R. Soc. B, Vol.273, pp.661-667, (2006)

[37]Y. Wu, Y. Cao, 'Fabrication of CaN Nanopillar Arrays Using Self-Assembly Ni Nanodots as the Mask', Micronanoelectronic Technology, Vol.50 (12), pp 765-769, (2013)

[38] W. Xu, P. Zuo, L. Dai, et.al., 'light output improvement of InGaN/GaN leds by self-assembled Ag nano-particles and SiNx surface roughening', Solid-State and Integrated Circuit Technology (ICSICT), 12th IEEE International Conference on, pp 1-3, print ISBN 978-4799-3296-2, (2014)

[39] P. Shang, S. Xiong, Q. Deng, L, Shi, M. Zhang, ‘Disordered antireflective subwavelength structures using Ag nanoparticle on fused silica windows’, Applied Optics, Vol.53 (29), pp. 6789-6796, (2014)

[40] J.W. Leem, Y. Yeh, and J.S. Yu, ‘Enhanced transmittance an hydrophilicity of nanostructured glass substrates with antireflective properties using disordered gold nanopatterns’, Optics Express, Vol.20 (4), pp 4056-4066, (2012)

[41] J.W. Leem, K.S. Chung, J.S. Yu, ‘Antireflective properties of disordered Si SWSs with hydrophobic surface by thermally dewetted Pt nanomask patterns for Si-based solar cells’, Current Applied Physics, Vol.12 (1) pp. 291–298, (2012)

[42] H. Sai, H. Fujii, K. Arafune, Y. Ohshita, M. Yamaguchi, Y. Kanamori, H. Yugami, ‘Antireflective subwavelength structures on crystalline Si fabricated using directly formed anodic porous alumina masks’, Applied Physics Letters, Vol.88, p 201116, (2006)

[43] J. Liu, M. Ashmkhan, B. Wang, T. Yi, ‘Fabrication and reflection properties of silicon nanopillars by cesium chloride self-assembly and dry etching’, Applied Surface Science, Vol.258 (22), pp8825-8830, (2012)

[44] C.H. Chiu, P.C. Yu, H.C. Kuo, C.C. Chen, T.C. Lu, S.C. Wang, S.H. Hsu, Y.J. Cheng, and Y.C. Chang, ‘Broadband and omnidirectional antireflection employing disordered BaN nanopillars’, Optics Express, Vol.16 (12), pp.8748-8754, (2008)

[45] A.M Chadha, W.D Zhou, E.D Cline, ‘Design criteria for nanostructured omni-directional antireflection coatings’, Photovoltaic Specialist Conference (PVSC), 38th IEEE, paper NO.738, (2012)

[46] Y. Wang, N. Chen, X. Zhang, X. Yang, Y. Bai, M. Cui, Y. Wang, X. Chen, and T. Huang, 'Ag surface plasmon enhanced double-layer antireflection coatings for GaAs solar cells', Jounals of Semiconductors, Vol.30 (7), pp.072005-5(2009)

[47] J.B. Schneider, ‘Understanding the FDTD Method’, http://www.eecs.wsu.edu/~schneidj/ufdtd/ufdtd.pdf, last access Aug. 16, 2015

[48] M. Born, E. Worf, ‘Principles of Optics’, Cambridge University Press, ISBN 0-521-642221, 952p., (1999)

[49] H. Haidner, P. Kipfer, W. Stork, and N. Streibl, 'Zero-order gratings used as an artificial distributed index medium', Optik, Vol.89, pp.107-112, (1992)

[50] M.W. Farn, 'Binary gratings with increased efficiency,' Appl.Opt., Vol.21, pp.4453-4458, (1992)

[51] E. Noponen, A. Vasara, J. Turunen, J.M. Miller, and M.R. Taghizadeh, 'Synthetic diffractive optics in the resonance domain,' J. Opt. Soc. Am. A, Vol.9, pp.1206-1213, (1992).

[52] C.H. Sun, P. Jiang, B. Jiang, 'Broadband moth-eye antireflection coatings on silicon', Applied Physics Letter, Vol.92, pp.061112-061114, (2008)

[53] G.R. Zhou, X. Li, N.N. Feng, 'Design of deeply etched antireflective waveguide terminators', IEEE Journal of quantum electronics, Vol.39 (2), pp 384-391, (2003)

[54] Y.F. Huang, S. Chattopadhyay, Y. Jen, C.Y. Peng, T.A. Liu, Y.K. Hsu, C.L. Pan, H.C. Lo, C.H. Hsy, Y.H. Chang, C.S. Lee, K.H. Chen, L.C. Chen, 'Improved broadband and quasi-omnidirectional anti-reflection properties with biomimetic silicon nanostructures', Nature Nanotechnology, Vol.2 (12), pp.770-774, (2007)

[55] Y.J. Hung, S.L. Lee, K.C. Wu, Y. Tai, and Y.T. Pan, 'Antireflective silicon surface with vertical-aligned silicon nanowires realized by simple wet chemical etching processes', Opt. Express, Vol.19 (18), pp.15792-15802 (2011)

[56] W. Zhou, M. Tao, L. Chen, and H. Yang, 'Microstructured surface design for omnidirectional antireflection coatings on solar cells', Journal of Applied Physics, Vol.102 (10), pp.103105-103113, (2007)

[57] http://refractiveindex.info/ , last access date 03/02/2012

[58] M.G. Moharam, E.B. Gtann, D.A. Pommet, 'Formulation for stable and efficient implementation of the rigorous coupled-wave analysis of binary gratings', J. Opt. Soc. Am, Vol.12 (5), pp.1068-1076, (1995)

[59] W. Zhou, M. Tao, L. Chen, H. Yang, 'Microstructured surface design for omnidirectional antireflection coatings on solar cells', Journal of Applied Physics, Vol.102(10), pp.103105-103105-9, (2007)

[60] E. Yablonovitch, G. D. Cody, 'Intensity enhancement in textured optical sheets for solar cells', IEEE transactions on electron devices, Vol.29 (2), pp.300-305, (1982)

[61] S. Liu, D. Ding, S. R. Johnson, and Y.H. Zhang, 'Approaching single-junction theoretical limit using ultra-thin GaAs solars with optimal optical designs', IEEE 38th Photovoltaic Specialists Conference (PVSC), pp. 2082-2087, (2012)

[62] http://www.horiba.com/scientific/products/optics-tutorial/diffraction-gratings/ last access Aug 20, 2015

[63] G. K. Vijaya, A. Alemu, A. Freundlich, "Dilute Nitride Multi-quantum Well Multi-junction Design: A Route to Ultra-Efficient Photovoltaic Devices", Proc. SPIE 7933, Physics and Simulation of Optoelectronic Devics XIX, (2011)

[64] T. Inoue, K. Watanabe, et.al, "Enhanced Light Trapping in Multiple Quantum Wells by Thin Film Structure and Backside Grooves with Dielectric Interface", 40th IEEE Photovoltaic Specialists Conference, article# 812-P47, (2014)

[65] Z. Yu, A. Raman, et. al, "Fundamental Limit of Light Trapping in Grating Structures", Optics Express, vol.18, issues3, pp. A3660A380, (2010)

[66] M. A. Green, "Lambertian Light Trapping in Textured Solar Cells and Light-Emitting Diodes: Analytical Solutions", progress in Photovoltaics: Research and Applications, vol.10, issue 4, pp. 235-241, (2002)

[67] M.P. Lumb, C.G. Bailey, J.G.J. Adams, G. Hillier, F. Tuminello, V C. Elarde, and R.J. Walters, 'Extending the 1-D Hovel Model for Coherent and Incoherent Back Reflections in Homojunction Solar Cells', IEEE Journal of Quantum Electronic, Vol. 49 (5), pp462-470, (2013)

[68] W.J. Dauksher, N.V. Le, E.S. Ainley, et. al, 'Nano-imprint lithography: Templates, imprinting and wafer pattern transfer', Microelectronic Engineering, Vol. 83 (4-9), pp 929-932(2006)

[69] A. M. Carroll, 'Chapter One – Pattern Generators for Reflective Electron-Beam Lithography (REBL)', Advances in Imaging and Electron Physics, Vol. 188, pp 1-23, (2015)

[70] Y.C. Lee, C.C. Chang, Y.Y. Chou, 'Fabrication of broadband anti-reflective sub-micron structures using polystyrene sphere lithography on a Si substrate', Photonics and Nanostructures - Fundamentals and Applications, Vol. 12(1), pp 16-22, (2014)

[71] G.A.C. Jones, P.D.Rose, E.H. Linfield, D.A. Ritchie, 'GaAs/AlGaAs device fabrication using MBE growth and in situ focused ion beam lithography', Physica B: Condensed Matter, Vol. 227 (1-4), pp 264-267, (1996)

[72] T. Shiokawa, P.H. Ki, M. Hamagaki, et. al, 'Microstructures of GaAs fabricated by finely focused ion beam lithography', Microelectronic Engineering, Vol. 9 (1-4), pp 277-279, (1989)

[73] Q. Xie, M.H. Hong, H.L. Tan, G.X. Chen, et.al 'Fabrication of Nanostructures with Laser Interference Lirhography', Journal of Alloys and Compunds, Vol 449, issue 1-2, pp 261-264, (2008)

[74] F.J. Duarte, J.A. Piper, 'Dispersion Theory of Multiple-Prism Beam Expanders for Pulsed Dye Lasers', Optics Communications Vol.43 (5), pp 303-307 (1982)

[75] http://www.newport.com/Laser-Beam-Expanders/141075/1033/info.aspx?xcid=bing-ppc-0102#tab_Overview, last access May 16, 2015

[76] http://www.thorlabs.com/NewGroupPage9.cfm?ObjectGroup_ID=1580 , last access May 16,2015

[77] http://www.edmundoptics.com/technical-resources-center/lasers/beam-expanders/ , last access May 16, 2015

[78] V. Berger, O. Gauthier-Lafaye, and E. Costard, 'Photonic band gaps and holography', Joural of Aplied Physics, Vol.82 (1), pp. 60-64 (1997)

[79] S. Yang, M. Megens, J. Aizenberg, P. Wiltzius, P.M. Chaikin, and W. B. Russel, 'Creating Period Three-dimensional Structures by Multibeam Interference of Visible Laser', Chemistry of Materials, Vol.14 (7), pp.2831-2833, (2002)

[80] http://www.newport.com/Pellicle-Beamsplitter/141118/1033/info.aspx#tab_Overview , last access May 16, 2015

[81] http://www.newport.com/Polka-Dot-Beamsplitters/372843/1033/info.aspx, last access May 17, 2015

[82] http://search.newport.com/i/1/q1/products/q2/Beamsplitters/x1/pageType/x2/section/q3/Cube+Beamsplitters/x2/section/x3/chapter/nav/1/, last access May 17, 2015

[83] M. Ellman, A. Rodriguez, N. Perez, M. Echeverria, Y.K. Verevkin, C.S. Peng, et.al, 'High-power Laser Interference Lithography Porcess on Photoresist: Effect of Laser Fluency and Polarization', Applied Surface Science, Vol.255 (10), pp 5538-5541, (2009)

[84] http://www.microchem.com/PDFs_Dow/S1800.pdf. Last access time May 6, 2015

[85] DAVID C. HAYS, 'Selective Etching of Compound Semiconductors', http://pearton.mse.ufl.edu/theses/david_hays_sel_etching_of_compound_semi.pdf

[86] http://www.monzir-pal.net/Instrumental%20Analysis/Lectures/Lecture%201-20/L10.pdf , last access May 28, 2015

[87] http://www.newport.com/Getting-Light-into-a-Monochromator/383722/1033/content.aspx , last access May 29, 2015

[88] http://www.horiba.com/fileadmin/uploads/Scientific/Documents/Mono/triax.pdf , last access May 29, 2015

[89] http://refractiveindex.info/?shelf=main&book=Au&page=Rakic , lass access May 28, 2015

[90] http://refractiveindex.info/?shelf=main&book=Al&page=Rakic , lass access May 28, 2015

[91] http://refractiveindex.info/?shelf=main&book=Ag&page=Rakic , lass access May 28, 2015

[92] A. Alemu, A. Freundlich, 'Resonant thermotunneling design for high-performance single-junction quantum-well solar cells', Photovoltaics, IEEE Journal of Vol.2 (3), pp 256-260, (2012)

[93] A. L. Fahrenbruch, R. H. Bube, 'Fundamentals of Solar Cells', Acamemic Press, pp.559, (1983)

[94] M. P. Lumb, C. G. Bailey, J. G. J. Adams, et al, ‘Extending the 1-D Hovel Model for Coherent and Incoherent Back Reflections in Homojunction Solar Cells’, IEEE Journal of Quantum Electronic, Vol. 49 (5), pp.462-470, (2013)

[95] W. Wang, A. Freundlich, ‘Optimizing the Design of 2D Subwavelength ARC Gratings for Multijunction III-V Concentrator Cells’, in 38th IEEE Photovoltaic Specialists Conference, 2012, article# 621-I18

[96] X. Li, P. Li, et. al, ‘Integrated Optical Nanostructures for Wide-angle Antireflection and Light Trapping in III-V Solar Cells’, in 40th IEEE Photovoltaic Specialists Conference, 2014, pp. 2238 - 2242

[97] C. O. McPheeters, E. T. Yu, ‘Computational analysis of thin film InGaAs/GaAs quantum well solar cells with back side light trapping structures’, optics express, Vol.20, No. S6, pp. A864-A878, (2012)

[98] T. Inoue, K. Watanabe, et.al, ‘Enhanced Light Trapping in Multiple Quantum Wells by Thin Film Structure and Backside Grooves with Dielectric Interface’, 40th IEEE Photovoltaic Specialists Conference, 2014, article# 812-P47